Radioactive Molecular Beams

at CERN-ISOLDE

Dissertation

zur Erlangung des Grades

"Doktor der Naturwissenschaften"

im Promotionsfach Kernchemie

am Fachbereich Chemie, Pharmazie und Geowissenschaften

der Johannes Gutenberg-Universität

in Mainz

Jochen Ballof

geb. in Wiesbaden

Mainz, den 12.10.2021

Gutachter

1. Berichterstatter:
2. Berichterstatter:

Datum der mündlichen Prüfung:

This project has received funding from the CERN doctoral students program and the European Unions Horizon 2020 research and innovation program under grant agreement No 654002.

Abstract

The present thesis addresses aspects of molecular beam developments for thick-target radioactive ion beam facilities such as CERN-ISOLDE. At these facilities, an intense and energetic driver beam impinges on a target. Radioisotopes are produced in a target matrix from which they require to diffuse into an ion source. On their way, numerous encounters with structural materials and the target material occur, which enable desired and undesired chemical interactions. The extracted ions are separated by their mass-to-charge ratio and supplied to various experiments for investigations *e.g.* in nuclear structure, reactions and applications.

The motivation to extract radioisotopes as molecular beams is multifold. Firstly, the elements with the highest melting and boiling points (refractory elements) require embedding in a volatile carrier molecule to enable their transport to the ion source. Secondly, a common issue are isobaric contaminations which come along with the isotope of interest after mass separation. They can render impossible the intended user experiments. A powerful tool to produce and purify these beams is the extraction as molecular sideband which synthesizes volatile compounds *in-situ* and shifts the mass as seen by the mass separator away from the contamination. Finally, a field of investigation on radioactive molecules themselves was recently arising.

This thesis is based on four publications which cover different facets of molecular beam developments. The first publication concerns the redesign and implementation of the ISOLDE yield database which provides valuable information of available beams and demonstrates the need for molecular beam developments. This implementation also contains new data and models to predict ion beam yields based on measured data. The first extraction of radioactive boron beams at a thick-target ISOL-facility is discussed in the second publication. Boron is a reactive and refractory element which cannot be extracted in elemental form. Its release properties from multi-walled carbon nanotubes are described. The measured yield of ^{8}B is presented along with predictions for yields of ^{12}B and ^{13}B, based on the derived release model. As an example for beam purification by molecule formation, the third publication provides investigations by online and offline measurements towards a reliable extraction of carbonyl selenide sidebands.

The investigations towards extraction of transition metals as carbonyl complexes are a major contribution to this thesis. Most of the refractory transition metals are not available as ISOL beam since no suitable carrier molecules to enable their transport have been identified yet. This is often due to the harsh conditions in the target an ion source unit that typically operates at high temperatures. It was studied by simulation, calculation and exploratory experiments, if carbonyl compounds could be used within a cold target concept. To avoid slow diffusion processes, the recoil momentum in fission and spallation reactions is exploited. Transition metal carbonyl compounds (*e.g.* $Mo(CO)_6$) form *in-situ* upon their thermalization in a carbon monoxide containing atmosphere already at ambient pressure and temperature. However, these are delicate compounds which easily decompose when exposed to heat, electron bombardment or plasma. The included publication presents first exploratory experiments with an electron beam induced arc discharge ion source operated at ambient pressure. In contrast to classical thermionic electron production, electrons are liberated by a laser from a cold ion source.

The addendum of the thesis documents experimental results towards ionization of the fragile carrier molecule $Mo(CO)_6$ with available ISOLDE ion sources. Their ionization efficiency turned out insufficient and underlines the need for development of a cold electron impact ion source, as proposed in the publication. Moreover, an experimental setup has been built and tested to study the formation of neutral transition metal carbonyl complexes at ISOLDE. The included documents describe its purpose, mode of operation and management of involved risks.

Contents

Acronyms

ALTO	Linear Accelerator and Tandem	6
ANL	Argonne National Laboratory	7
ARIEL	Advanced Rare IsotopE Laboratory	6
BME	Boltzmann Master Equations	25
CARIBU	Californium Rare Isotope Breeder Upgrade	7
CARIF	China Advanced Rare Ion beam Facility	6
CARR	China Advanced Research Reactor	6
CCP	Capacitively Coupled Plasma	37, 38
COLLAPS	COLlinear LAser SPectroscopy	9
COMIC	COmpact MIcrowave and Coaxial	16, 84, 114
CRIS	Collinear Resonance Ionization Spectroscopy	9
DPM	Dual Parton Model	26
DPMJET	Dual Parton Model and JETs	25
EBIS	Electron Beam Ion Source	9, 70
ECR	Electron Cyclotron Resonance	5, 16, 37, 38, 57, 83, 84
ECRIS	ECR Ion Source	15
EDX	Energy-Dispersive X-ray spectroscopy	114, 115
FAIR	Facility for Antiprotons and Ion Research	4
FEBIAD	Forced-Electron Beam Induced Arc-Discharge	13, 14, 36, 38
FLUKA	FLUktuierende KAskade	25
FRS	FRagment Separator	24
GANIL	Grand Accélérateur National d'Ions Lourds	4, 15
GDHM	Geometry Dependent Hybrid Model	26
GINC	Generalized Intra-Nuclear Cascade	26
GPS	General Purpose Separator	8, 40, 42
GSI	Gesellschaft für Schwerionenforschung	4, 24, 82
HFIR	High Flux Isotope Reactor	7
HIE-ISOLDE	High Intensity and Energy ISOLDE	9

HPGe	High Purity Germanium detector	43
HRS	High Resolution Separator	8, 40, 42
IAEA	International Atomic Energy Agency	24
ICP	Inductively Coupled Plasma	37, 38
IDS	ISOLDE Decay Station	9
IGISOL	Ion Guide Isotope Separator On Line	7
IMF	Intermediate Mass Fragments	24
INC	Intra-Nuclear Cascade	22–24, 26
INFN	Istituto Nazionale di Fisica Nucleare	25
IPNO	Institute of Nuclear Physics at Orsay	5
IRENA	Ionization by Radial Electrons Neat Adaptation	6
ISAC	Isotope Separator and ACcelerator	6, 12
ISIS	ISolde Irradiation Station	9
ISOL	Isotope Separation OnLine	3, 4, 26, 27, 30, 31, 81, 105
ISOLDE	Isotope Separator OnLine DEvice	2
JGU	Johannes Gutenberg - Universität Mainz	14, 82
LCP	Light Charged Particles	24
LINAC	LINear ACcelerator	4
LISE	Ligne d'Ions Super Epluchés	4
LIST	Laser Ion Source and Trap	13
LNL	Laboratori Nazionali di Legnaro	6
LPSC	Laboratoire de Physique Subatomique et de Cosmologie de Grenoble	16
MCP	MicroChannel Plate detector	41
MECRIS	Mono ECR ISOLDE	16
MEDICIS	MEDical Isotopes Collected from ISOLDE	9
MIVOC	Metal Ions from VOlatile Compounds	84, 109
MWCNT	MultiWalled Carbon NanoTubes	12, 57
MYRRHA	Multi-purpose hYbrid Research Reactor for High-tech Applications	6
PE	Polyethylene	71
PEANUT	PreEquilibrium Approach to NUclear Thermalization	25
PSB	Proton Synchrotron Booster	8, 33
PTFE	PolyTetraFluoroEthylene	111–113
Q-COMIC	Quartz COmpact MIcrowave and Coaxial	16
QMA	Quadrupole Mass Analyzer	41
REX	Radioactive Beam EXperiment	9
RF	Radio Frequency	15, 111–114
RGA	Residual Gas Analyzer	41, 111, 114, 115

RIB	Radioactive Ion Beam	2
RILIS	Resonant Ionization Laser Ion Source	13
RIPS	RIKEN Projectile-fragment Separator	4
RISP	Rare Isotope Science Project	6
rQMD	relativistic Quantum Molecular Dynamics	25
SC	Synchrocyclotron	8, 33
SCK•CEN	Studiecentrum voor Kernenergie • Centre d'Étude de l'énergie Nucléaire	6
SEM	Secondary Electron Multiplier	41
SPES	Selective Production of Exotic Species	6
SPIRAL	Système de Production d'Ions Radioactifs Accélérés en Ligne	4, 15
SRIM	Stopping and Range of Ions in Matter	28
STF	STopping Force	27, 28
Super-FRS	Superconducting FRagment Separator	4
Ti:Sa	Titanium Sapphire laser	14
TISOL	TRIUMF Isotope Separator On-Line	12
TISS	Target and Ion Source System	9, 10, 26
TRIGA	Training, Research, Isotopes, General Atomic	14
TRIUMF	TRI University Meson Facility	6, 83
VADIS	Versatile Arc Discharge Ion Source	13–15, 84, 108, 110, 116, 117

Symbols

A	Mass number	23
a	Screening parameter in internuclear potentials	28
α	Power function exponent of release efficiency [s]	33
α_l	Weighting parameter of fast and slow decay of the release delay function	33
a_s	Characteristic dimension parameter [m]	29
β	Ionization enhancement factor for surface ionization	12
C	Concentration of a species [m^{-3}]	29
C_g	Conductance (gas flow) [$m\,s^{-3}$] (unless noted otherwise)	109
D	Diffusion constant [$m^2\,s^{-1}$]	29, 30, 32
d	Gap length, *e.g.* distance between the plates of a vacuum diode [m]	35, 36
D_0	Pre-exponential factor of the Arrhenius expression for diffusion [$m^2\,s^{-1}$]	30
d_{foil}	Foil thickness [m]	32
ΔH_{ads}	Enthalpy of adsorption [$kJ\,mol^{-1}$]	30, 32
e	Elementary charge $e \approx 1.602 \times 10^{-19}$ C	28, 34–36, 39
E_a	Activation energy [$J\,mol^{-1}$]	30
ϵ_0	Vacuum permittivity $\epsilon_0 \approx 8.854 \times 10^{-12}\,F\,m^{-1}$	34, 35
ϵ_{feb}	Ionization efficiency of a FEBIAD source	39
ϵ_{form}	Efficiency of molecule formation (chemical yield)	47
ϵ_{ion}	Ionization efficiency	47, 109, 111, 114
ϵ_{irr}	Efficiency accounting for irreversible losses in radioactive ion beam yield	47
ϵ_{surf}	Surface ionization efficiency	12
ϵ_{rel}	Release efficiency of an radioactive beam in a target and ion source assembly	27, 32, 33, 47
$\mathcal{E}_{rel}^{dif}$	Release efficiency of an radioactive beam in a target and ion source assembly in the diffusion controlled regime	32
$\mathcal{E}_{rel}^{ef}$	Release efficiency of an radioactive beam in a target and ion source assembly in the effusion controlled regime	32
f	Fraction of extracted ions in the FEBIAD model proposed by Penescu	39, 40
f_{rem}	Fraction of isotopes remaining in a solid after a heat treatment	29, 32

g_0	Statistical weight of atomic states	12
Γ_i	Decay width of channel i	24
g_i	Statistical weight of ion states	12
I	Logarithmic mean excitation energy per electron [J]	28
IP^*	First effective ionization potential [eV]	12
IP	First ionization potential [eV]	12
I_{prim}	Primary beam current [µA]	47
j_{2d}	Child-Langmuir limited current for a two-dimensional emitter [$\mathrm{A\,m^{-2}}$]	36
j_B	Bohm current density [$\mathrm{m\,s^{-1}}$]	36
j_{crit}	Maximum current density that can be transported in a short pulse over a gap without virtual cathode formation [$\mathrm{A\,m^{-2}}$]	35
j_e	Electron current density [$\mathrm{A\,m^{-2}}$]	36
$j_{e,cl}$	Child-Langmuir-limited current density for electrons [$\mathrm{A\,m^{-2}}$]	35, 36
j_i	Ion current density [$\mathrm{A\,m^{-2}}$]	35, 36, 39
J_x	Flux of particles in x-direction [$\mathrm{m^{-2}\,s}$]	29
$\mathrm{k_B}$	Boltzmann constant $\mathrm{k_B} \approx 8.617 \times 10^{-5}\,\mathrm{eV\,K^{-1}}$	12, 34, 36, 39
λ	Decay constant of an radioisotope [$\mathrm{s^{-1}}$]	32, 47
λ_D	Debye length [m]	34, 35, 39
λ_f	Fast decay time constant of the release function [$\mathrm{s^{-1}}$]	33
λ_{ion}	Ionization length [m]	110
λ_r	Rise time constant of the release delay function [$\mathrm{s^{-1}}$]	33
λ_s	Slow decay time constant of the release function [$\mathrm{s^{-1}}$]	33
m_e	Electron mass [kg]	28, 36
m_i	Mass of an ion [kg]	35, 36, 39, 110
μ_0	Delay parameter of diffusion [$\mathrm{s^{-1}}$]	32
N_{e}	Number density of electrons [$\mathrm{m^{-3}}$]	28, 39
N_{n}	Number density of neutrals [$\mathrm{m^{-3}}$]	39
n_e	Electron density in a plasma [$\mathrm{m^{-3}}$]	17, 34–36
n_{e0}	Unperturbed electron density in the plasma bulk [$\mathrm{m^{-3}}$]	34, 36
n_{ed}	Electron density on the discharge axis [$\mathrm{m^{-3}}$]	39
n_i	Ion density in a plasma [$\mathrm{m^{-3}}$]	34, 35
n_{i0}	Unperturbed ion density in the plasma bulk [$\mathrm{m^{-3}}$]	34
n_{in}	Neutrals admitted to the ion source per unit time [$\mathrm{s^{-1}}$]	39
ν_0	Delay parameter of effusion [$\mathrm{s^{-1}}$]	32
v_B	Ion velocity at the sheath edge (Bohm velocity) [$\mathrm{m\,s^{-1}}$]	36
v_i	Ion velocity [$\mathrm{m\,s^{-1}}$]	110
ω_{RF}	RF driver frequency [Hz]	38
$p(t)$	Normalized release time distribution function of a stable isotope (delay function)	32, 33, 42, 47
p	Gas pressure [Pa]	38
p_{extr}	Pressure at the extraction side of the offline 1 separator [mbar]	41, 109–112
Φ	Electric potential [V]	34–36
ϕ	Work function [eV]	12, 13
Φ_s	Screening function in nuclear stopping	28
P_i	Probability of de-excitation via channel i	24

$p_v(t)$	Effusion delay function of a stable isotope	32
p_{vap}	Saturation vapour pressure [mbar]	109, 112
Q_{pV}	pV-flow rate of a gas [$\text{Pa}\,\text{m}\,\text{s}^{-3}$] (unless noted otherwise)	109
R	Universal gas constant, $R \approx 8.314\text{J}\,\text{mol}^{-1}\,\text{K}$	30
r	Distance, *e.g.* between two point charges [m]	28
ρ_{ie}	Space charge [$\text{C}\,\text{m}^{-3}$]	34
R_{ioniz}	Ionization rate per unit volume [m^{-3}]	39
S	Total (linear) stopping force [N]	27
S_{el}	(Linear) electronic stopping force [N]	28
v_i	Ion velocity [$\text{m}\,\text{s}^{-1}$]	28
σ_{ion}	Ionization cross section [m^2]	39
s_m	Maximum size of the oscillating RF sheath [m]	37, 38
T	Temperature [K]	12, 30, 110
t	Time [s]	29, 47
$t_{1/2}$	Half-life time of an radioisotope [s]	12, 32, 33
$t^0_{1/2}$	Half-life of transition from plateau to power-law in release efficiency plot [s]	33
t_{ads}	Time spent in adsorbed state during effusion [s]	47
τ_0	Period of oscillation perpendicular to the surface [s]	30
τ_{a}	Mean adsorption sojourn time (single encounter) [s]	30–32
τ_d	Characteristic diffusion time [s]	29
τ_{f}	Mean time of flight between two collisions [s]	32
τ_p	Pulse duration [s]	35
t_c	Tapestation collection time [second]	42
T_{cath}	Cathode temperature of an ion source [°C]	109
t_d	Tapestation delay time [second]	42
t_{diff}	Time required for diffusion [s]	47
T_e	Electron temperature in a plasma [K]	17, 34, 36, 39
t_{eff}	Time spent in flight during effusion [s]	47
T_i	Ion temperature in a plasma [K]	34
t_m	Tapestation measurement time [second]	42
T_{res}	Evaporation chamber temperature [°C]	109
t_t	Tapestation transport time [second]	42
t_v	Vacuum transit time [s]	35
U	Potential difference [V]	35
u_0	Unperturbed ion velocity [$\text{m}\,\text{s}^{-1}$]	36
$\mathcal{V}$	Atom-atom internuclear potential	28
V_0	Amplitude of the voltage across an RF sheath [V]	37, 38
v_e	Electron velocity [$\text{m}\,\text{s}^{-1}$]	39
v_F	Fermi velicity	28
V_{source}	Volume of the ionization region [m^3]	39, 40
χ	Mean number of wall collision	32
x	Path of a particle in a stopping medium [m]	29
X_{cl}	Normalized pulse length	35
Y	Radioactive ion beam yield [s^{-1}]	46, 47
Y_0	Normalized in-target production rate of an isotope [μC^{-1}]	47
Z	Atomic number	23, 26, 28

List of Figures

1 Introduction - Radioactive Ion Beams

Contents

The development of techniques for radioactive nuclide production builds the foundation for investigations in various fields of science and their applications, reaching from fundamental nuclear physics to cancer treatment. A nuclide (or an isotope)[1] is an atomic species defined by the number of protons and neutrons residing in its nucleus.

In 1911, Rutherford discovered the latter in his famous scattering experiment [1]. At first, only primordial isotopes and their decay products have been available for studies. In 1934, the first artificial production of isotopes could be demonstrated by Curie and Joliot in Paris by irradiation of light targets (B, Mg, Al) with α-particles obtained from a polonium source [2]. Since the advent of nuclear reactors, nuclear explosions and particle accelerators, the number of known isotopes is rapidly increasing. Today, more than 4000 isotopes of 118 elements have been discovered, out of which only 254 are considered as stable [3–5]. A significantly higher number of isotopes is predicted to exist (around 7000 [6]) and many of these are yet to be discovered.

While chemical elements are organized in the periodic table based on their electron configuration, the visualization of nuclides in the nuclide chart is well established. Typically, the isotopes are arranged such that the number of protons is increasing along the vertical axis and the number of neutrons along the horizontal one. Thus, all isotopes of the same element are contained in an row. A nuclear chart of known isotopes

[1] The term isotope originally referred to nuclides of same atomic but different mass number. Since nowadays the term is used synonymously to nuclide, this work adapts the common terminology.

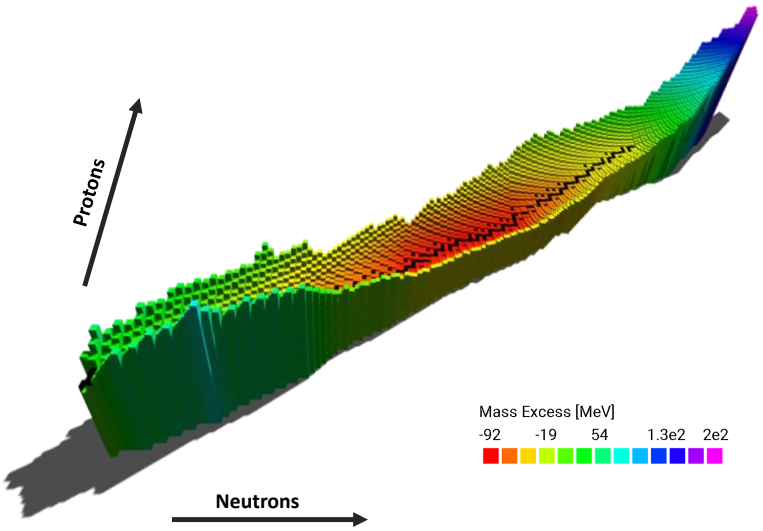

Figure 1.1: Three-dimensional nuclide chart showing on the third axis the mass excess [7] and illustrating the valley of β-stability. Stable isotopes are shown in black at the very bottom of the valley. Adapted from [8,9].

is shown in fig. 1.1. The chart also illustrates the mass excess, *i.e.*, the difference between the mass of the nucleus and the sum of the respective number of neutron and proton masses, which is related via the equivalence of mass and energy to the binding energy. Less stable isotopes have lower binding energies and a bigger mass excess. As can be seen from fig. 1.1, the stable isotopes are situated along the so-called valley of β-stability.

The generation of ever new radioactive isotopes in higher yields and improved purity advances our understanding of the atomic nucleus and the nuclear landscape. To achieve this goal efforts must be undertaken in the development of new and improvement of existing techniques for radioactive isotope production and beam generation.

The remaining part of this chapter gives a brief overview of techniques and facilities for Radioactive Ion Beam (RIB) generation in general, and the Isotope Separator OnLine DEvice (ISOLDE) facility in particular.

1.1 Radioactive ion beam facilities

A recent review by Y. Blumenfeld *et al.* about facilities and methods for RIB production is available in [10]. Two methods are commonly used for radioactive isotope production: i) induced nuclear reactions, *e.g.* by a driver beam impinging on a target and ii) the collection of isotopes from spontaneous fission sources. After production of a nuclide, it has to be separated from unwanted byproducts and transported away from the harsh production environment. The figures of merit of an RIB facility as defined in [11,12] are:

- The *diversity* of available beams
- The beam *intensity* which depends on the production rate of the desired isotopes and efficiency of all downstream processes. Always included are beam transport

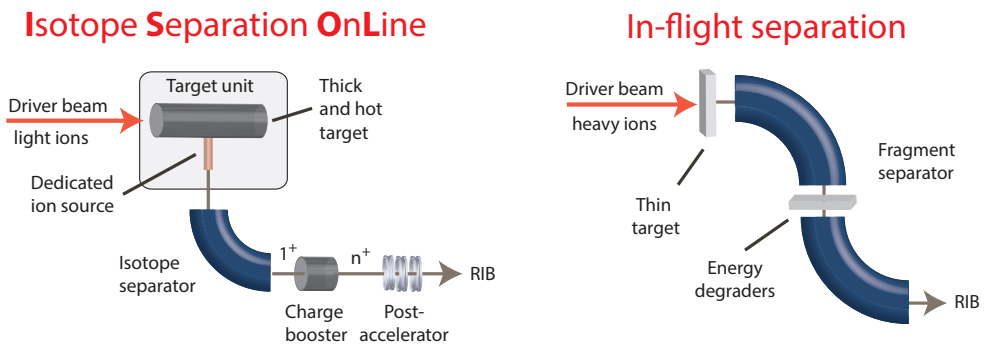

(a) The ISOL meathod

(b) In-flight separation

Figure 1.2: Comparison of ISOL and in-flight separation methods. Within the (a) ISOL-method, a thick target is bombarded with a proton or light-ion beam. The radioisotopes are stopped inside the target and have to diffuse out of the material into a dedicated ion source. If the energy of the secondary beam of ca. 60 kV is not sufficient, a post-acceleration stage is required. (b) The in-flight separation technique requires swift heavy ions to impinge on a thin target. The produced radioisotopes are not thermalized, and separated in a fragment separator. Re-acceleration is typically not required. See text for details.

and separation, often also ionization and diffusion processes.

- The beam *quality*, for instance the absence of unwanted ion components (beam purity) and beam-optical properties (emittance)
- The yearly *availability* of the facility
- The level of ion beam degradation over time, often related to ageing of the target material or ion source in ISOL-type facilities

Two complementary approaches for the production and separation of radioactive ion beams exist: In-flight separation and Isotope Separation OnLine (ISOL). Within this work, the term ISOL is restricted to thick-target facilities wherein the nuclear reaction products are thermalized inside a condensed target material.

1.1.1 In-flight separation

Within the In-flight separation method (see [13] for a review), the nuclear reaction products are not thermalized in a thick target. A primary beam is focused on a thin target of few g/cm^2 or less from which the reaction products emerge by their typically large forward momentum. The nuclides are produced as energetic ions and separated based on their momentum to charge ratio (magnetic rigidity). The beam emittance may be poor, however, post-acceleration of nuclides is typically not required due to their large momentum. Since chemical processes, diffusion or dedicated ionization and post-acceleration steps do not play a role, the efficiency can reach up to 100%. A significant advantage of this method is its short delay time, which allows to extract very short-lived isotopes (below µs).

A wide range of isotopes is available with this technique. Exploited reaction mechanisms are mostly fragmentation or fission of fast projectiles. Neutron deficient isotopes are produced in projectile fragmentation reactions, the neutron number varying with the atomic weight of the target material. Neutron-rich isotopes are produced by pro-

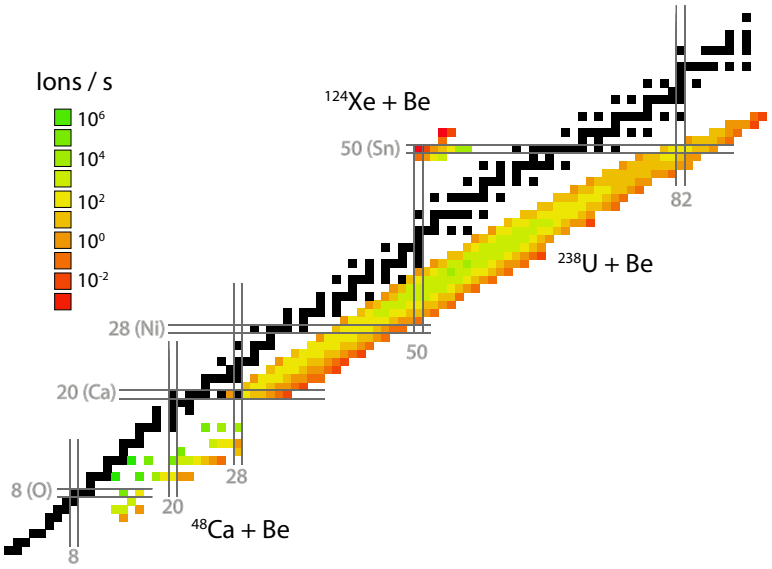

Figure 1.3: Beam intensities of selected isotopes available at the BigRIPS in-flight separator which is part of the RIKEN radioactive ion beam factory [14].

jectile fission, and even more exotic isotopes are available in fusion reactions followed by recoil separation. Among the existing In-flight facilities are the RIPS [15] and BigRIPS [16] separators located at RIKEN (Tokyo, Japan), the FRS separator [17] at GSI (Darmsadt, Germany) and the LISE spectrometer [18] at GANIL (Caen, France). Beam yields of selected isotopes currently available at the BigRIPS separator are shown in fig. 1.3. The reactions ^{124}Xe + Be and ^{48}Ca + Be are shown as example for projectile fragmentation, and ^{238}U + Be for fission. The heavy ion beam energy was 345 MeV u^{-1} and maximum primary beam intensities as given in [14] were assumed.

Within the FAIR project, extending the existing GSI facilities, the Super-FRS is currently under construction [19, 20]. Predicted production rates for FAIR are discussed in [21]; up to a factor of 10^4 of improvement in radioactive ion beam intensities over the FRS is expected [10]. The facilities at GANIL are also being upgraded and vastly extended within the SPIRAL2 project. The superconducting LINAC will deliver heavy ion beams of up to 14.5 MeV u^{-1} and allow the production of heavy nuclei by fusion-evaporation and light neutron rich nuclei via transfer reactions.

1.1.2 Thick-target ISOL method

The Isotope Separation OnLine (ISOL) method emerged in the 1950s after pioneering experiments in which short-lived krypton isotopes could be extracted form a 10 kg uranium oxide target and separated by their mass-to-charge ratio [22, 23]. The new inventive step was the simultaneous (*i.e.* "online") production, extraction and separation of radioisotopes. In contrast to the in-flight separation method, the produced isotope ions are fully thermalized and neutralized inside the target material, from which they need to diffuse out and be re-ionized in a dedicated ion source. Due to the large target thickness, high in-target production rates can often be achieved. However, the migration through the target material is time-consuming and strongly depends on the chemical

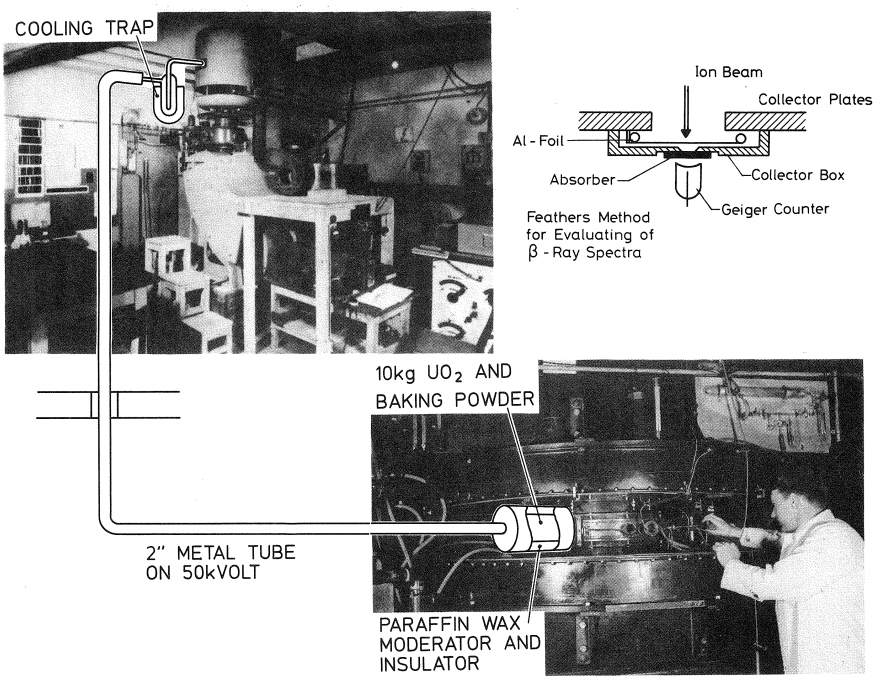

Figure 1.4: The first ISOL experiment in Copenhagen [24]. Volatile radioisotopes were produced in an uranium oxide target mixed with baking soda (bottom right) and fed into a separator (top left). Radiative decomposition of baking soda yielded volatile species to support the transport of radioisotopes. *Reprinted by permission from Springer Nature : Springer-Verlag US, On-Line Mass Separators by Helge L. Ravn, Brian W. Allardyce © 1989.*

properties of the compound.

With the ISOL-method, isotopes are typically obtained in their ground state and investigation in related properties can be readily achieved. Investigations in excited states are feasible by post-acceleration. The dedicated beam formation in ion sources and accelerators results in beam optical properties which are superior to beams of in-flight facilities.

The major facilities in Europe are ISOLDE [25,26] at CERN (near Geneva, Switzerland), SPIRAL 1 [27,28] at GANIL (Cean, France) and ALTO [29,30] at IPNO (Orsay, France). ISOLDE is the oldest of these and offers the largest variety of beams. It is supplied by 1.4 GeV protons allowing to exploit high energy spallation, fragmentation and fission reactions. Low-energy (few MeV) neutron-induced fission products are available through secondary spallation neutrons obtained from a proton-to-neutron converter [31]. At ISOLDE more than 1000 different isotopes are available from a variety of target materials and ion sources [32]. Post-acceleration up to ca. $10\,\mathrm{MeV\,u^{-1}}$ is available via the HIE-ISOLDE super-conducting LINAC.

At SPIRAL 1, nuclides are mostly produced via projectile fragmentation of swift heavy ions (up to $95\,\mathrm{MeV\,u^{-1}}$) on a carbon target. An Electron Cyclotron Resonance (ECR) ion source is coupled to the target and allows the extraction of volatile elements as multicharged ions. Isotopes of the elements He, Ne, Ar, Kr, N, O and F are available as beam. Before SPIRAL 2, the CIME cyclotron allowed the post-acceleration up to $20\,\mathrm{MeV\,u^{-1}}$. The SPIRAL 1 facility currently undergoes a comprehensive upgrade program which

includes the usage of heavier target materials (till Nb), hot transfer between target and ion source, new types of ion sources (surface and FEBIAD) and a new charge breeder [33–36]. In addition, a new technique is being developed to exploit fusion-evaporation reactions. The primary beam impinges on a thin target inducing fusion reactions. The evaporation residues recoil out of the target and are thermalized in a catcher from where they have to diffuse into the ion source [37].

After invention of the ISOL technique in Copenhagen (Denmark), the first extraction of condensible elements was achieved in Orsay by coupling the Synchro-cyclotron (155 MeV protons) to an online isotope separator [38]. Today, the ALTO-facility is equipped with an electron LINAC operating at 50 MeV to induce photo-fission processes. Uranium carbide is used as target material and a variety of ion sources, including resonant laser ionization and the radial electron impact ion source IRENA, are available [39].

Outside of Europe, the ISAC facility [40] located at TRIUMF (Vancouver, Canada) provides a variety of radioactive isotope beams. It is supplied by an intense beam with up to 100 µA of 500 MeV protons from the cyclotron driver. Similar to ISOLDE, a variety of target materials (light materials till uranium) and ion sources is available. Two accelerators are installed for post-acceleration: the first stage provides acceleration up to 1.8 MeV u^{-1} and a second stage at least 6 MeV u^{-1} for ions below 150 u. The new ARIEL facility will extend the capabilities of ISAC in the future. Two new target stations are under construction, which can be equally supplied by protons from the cyclotron or a new 500 kW, 50 MeV electron driver to produce isotopes by photo-production and photo-fission. Along with the new target stations, new mass-separators and beam lines will be introduced that also allow ion transport to the ISAC facility.

Due to the ever increasing demand in radioactive ion beams, a number of new facilities is currently under construction. In Europe, these include the SPES project [41] at LNL (Legnaro, Italy) aiming at extracting and post-acceleration of fission products produced with an high-power proton beam of up to 700 µA at 40 MeV. The target stations are designed for a power deposition of up to 8 kW. The planned ISOL@MYRRHA facility at SCK•CEN (Mol, Belgium) will use a small fraction (up to 5%) of the protons delivered by the existing MYRRHA installation to produce ISOL beams. The project is divided in three phases. In the first phase, proton beams of 100 MeV will be produced. Phase 3 aims at (up to 200 µA) at 600 MeV and would allow to produce a wide range of isotopes [42]. In Asia, a facility even exceeding these beam currents is being constructed at RISP (Daejeon, Korea) [43] which will be supplied by 500 µA protons at an energy of 70 MeV, leading to a power deposition of 35 kW in the uranium carbide target. The first phase of the project aims at 10 kW power deposition, 143 µA current and 70 MeV beam energy. In China, the CARIF project foresees a research reactor CARR as intense fission source, providing 2×10^5 fissions per second.

1.1.3 Gas-cell facilities

Besides the big research centers discussed above, some smaller facilities deserve special attention since they bridge the gap between ISOL and in-flight facilities. These are the facilities using gas-stopping cells. In these facilities, fission fragments are thermalized in a gas (few hundred mbar or less) but not neutralized due to the higher ionization

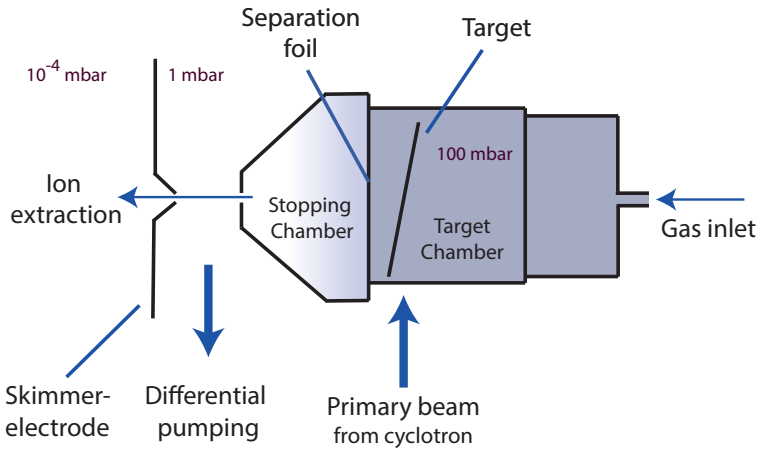

Figure 1.5: Early version of the IGISOL ion guide, simplified and adapted from [44].

potential of the stopping gas. The ions are guided by electrostatic and radio-frequency fields to the outlet of the stopping cell where they are separated from the gas by differential pumping. With this method, the extraction of short-lived non-volatile elements can be achieved that cannot readily diffuse out of an ISOL target. The advantage of the method, its chemical universality [44], is a drawback at the same time because extracted beams are typically not pure [45].

In Europe, the IGISOL facility [46] in Jyväskylä, Finland provides beams since the 1980s. The facility was evolving during time, and today a 30 MeV proton beam with a current of 140 µA is provided by the MCC-30/15 cyclotron [47]. The same accelerator is also capable of providing deuterons, and heavier ions can be provided by the K-130 cyclotron. By adaptation of the stopping cell to the kinematics of the nuclear reactions, isotopes are available from charged-particle induced fission, neutron induced fission [48], fusion-evaporation and deep inelastic transfer reactions [49].

A sketch of the IGISOL fission ion guide is shown in fig. 1.8. The primary beam is focused on a tilted target in the target chamber. Fission fragments recoil out of the target and propagate through the separation foil into the stopping chamber, where they are thermalized and reach a charge state of 1^+ by charge exchange with the gas. The ions are electrostatically extracted. The injected gas expands after leaving the stopping chamber and is removed in differential pumping sections. A foil between target and stopping chamber prevents the beam-induced plasma near the target from extending to the stopping chamber, where it would cause unwanted neutralization processes. In newer versions, the skimmer electrode has been replaced by a sextupole ion guide [50].

The CARIBU facility [45] located at ANL (Argonne, Il, USA) is another gas-catcher facility. Radionuclides are obtained from a ^{252}Cf (ca. 1 Ci) spontaneous fission source which was produced by electroplating of material from the High Flux Isotope Reactor (HFIR) in Oak Ridge. In contrast to IGISOL, also post-acceleration of up to 10 MeV u^{-1} is available via a LINAC. The spacious stopping cell has an inner diameter of 50 cm and a length of ca. 1.2 m. In addition to an electrostatic field that pushes the ions towards the extraction nozzle, the full cell is covered by a radio-frequency (RF) field. The complex system consists of more then 1000 electrodes and prevents diffusion of

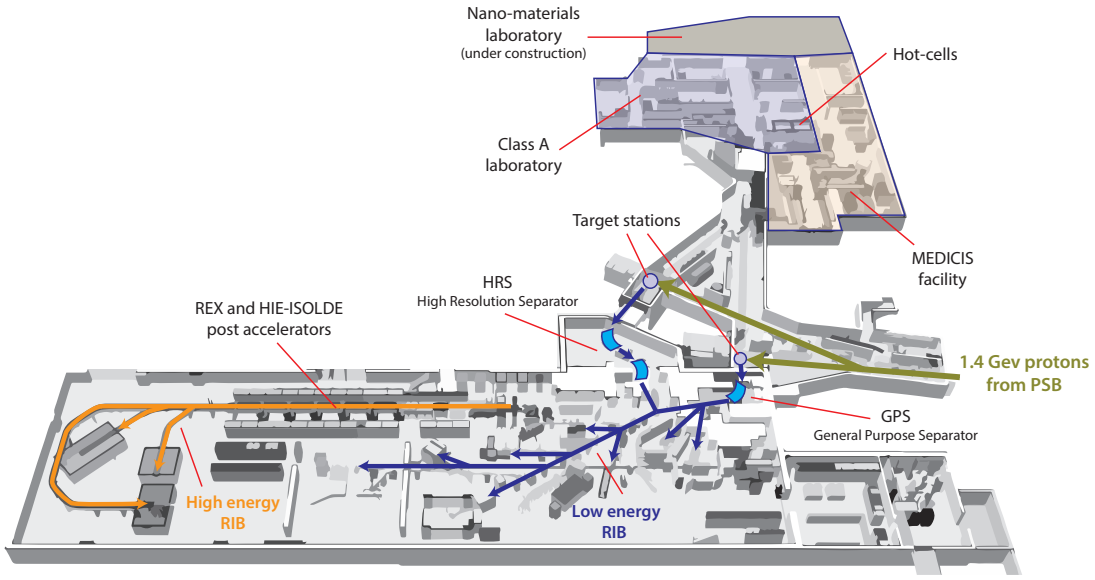

Figure 1.6: The ISOLDE facility

ions to the walls.

1.2 The ISOLDE facility and its target assembly

The ISOLDE facility is one of the oldest experiments at CERN. After the pioneering experiments in Copenhagen and Orsay, it was identified that the Synchrocyclotron (SC) accelerator at CERN is a well-suited driver for a dedicated ISOL facility. Its 600 MeV proton beam allowed to exploit spallation reactions for isotope production. In 1967 the erection of the facility was completed and its first beam was delivered to an experiment [51, 52]. After decommissioning of the SC, an improved version of ISOLDE was built that now includes two independent target stations and separators. It was connected to the Proton Synchrotron Booster (PSB). Today, the pulsed proton beam supplied to ISOLDE has an energy of 1.4 MeV and can reach a current of ca. 2 µA, which equals about half of all protons supplied by the PSB. In the future, an upgrade of intensity and energy to 6 µA and 2 GeV is discussed.

A sketch of the current ISOLDE facility is shown in fig. 1.6. The two target stations are connected to two independent separators of different conceptual design. The General Purpose Separator (GPS) consists of a single magnet allowing separations with a resolution of $m/\Delta m = 800$. It allows to extract beams at three different masses simultaneously and is easy to operate [53]. The High Resolution Separator (HRS) is made up of two separation magnets and has a resolution of up to $m/\Delta m = 6000$. The beamlines of GPS and HRS merge into a central beamline. Radioactive ion beam yields can be measured with the ISOLDE tape station [54] which is installed close to the junction point in the central beamline (CA0). It is further described in section 2.4.2 and the process of yield measurements is outlined in section 4.2.

Many experiments exploit directly the low energy (30 kV to 60 kV) RIBs, as supplied

by the target stations. These include *e.g.* nuclear decay spectroscopy at the ISOLDE Decay Station (IDS), mass measurements (ISOLTRAP), Collinear Resonance Ionization Spectroscopy (CRIS) and COLlinear LAser SPectroscopy (COLLAPS). Post-acceleration is available via the linear accelerators of Radioactive Beam EXperiment (REX) and High Intensity and Energy ISOLDE (HIE-ISOLDE). Before injection in the post-acceleration stage, the low-energy beams are bunched and fed into the REX-Electron Beam Ion Source (EBIS) to boost the charge state.

For the handling of open radioactive sources, a dedicated lab is available that is classified according to the swiss authorities as Type 'A'. The MEDical Isotopes Collected from ISOLDE (MEDICIS) faclilty [55] aims at production of radioisotopes for medical applications. Most of the protons hitting an ISOLDE target pass it without significant loss in energy. MEDICIS makes use of the protons which were otherwise lost to the beam dump. The MEDICIS target is placed between the HRS ISOLDE target and the beam dump. A rail conveyor system allows to recuperate the target and to move it to a dedicated MEDICIS iosotope separator where longer-lived isotopes are extracted and typically implanted in a metallic foil. In contrast to the ISOLDE target stations, services like water cooling, heating or electrical connectivity are not available to a MEDICIS target unit during irradiation. Recently, the parabiotic extension ISolde Irradiation Station (ISIS) was installed to the GPS target station that allows material irradiations, similar to the MEDICIS concept. A laboratory dedicated to the handling of nano-materials, some of which have shown to be very reactive, is currently under construction.

1.2.1 The ISOLDE target unit

The ISOLDE target unit is installed on a target station which is commonly called Frontend. A Frontend is the interface between beamline and target unit. Frontends provide all necessary services to target units: water-cooling, electrical connectivity, gases and RF signals. The Frontends are replaced on a regular basis due to aging in the harsh environment close to the proton beam. The latest Frontend upgrade included two additional gas-lines (three in total), and one additional RF connector (two in total) [56].

A target unit is tailored to the desired radioactive ion beam and combines three components: i) a target container which confines the target material ii) the ion source and iii) a transfer line connecting target container and ion source. The components are integrated into an aluminum vacuum vessel that is equipped with a gate valve. After installation on the Frontend, the valve is opened and an extraction electrode is moved close to the ion source. The target unit is kept at a positive voltage of 30 kV to 60 kV to accelerate positively charged ions towards the grounded extraction electrode and beamlines. In the case of negative beam extraction, the polarity of the target is adapted accordingly.

The assembly is also called Target and Ion Source System (TISS) and is the heart of an ISOL facility. A skech is shown in fig. 1.7a and a photo taken during installation on the Frontend in fig. 1.7b. Due to radiation and contamination risks, manual intervention on or near Frontends is avoided during the operation period. The target units are handled by industry-style robots and the installation on the Frontend is completed fully remotely.

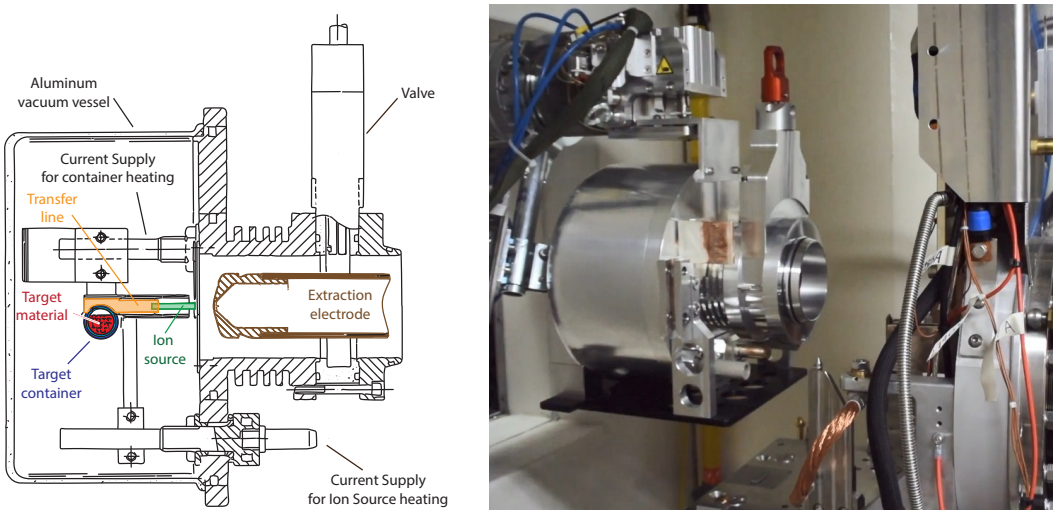

(a) Schematic representation of an early ISOLDE target unit (adapted from [24])

(b) Photo of a target unit during installation on the frontend

Figure 1.7: The ISOLDE target unit

1.2.2 Target materials

The engineering of material characteristics (especially its microstructure) is among the hot topics in ISOL beam development. The requirements a target material has to meet are multifold: i) the material needs to have a sufficiently high production rate for the radioisotope of interest, ii) the diffusion of isotopes in the material must be fast, iii) adsorption times of the radionuclide should be low, iv) the material must be stable at high temperatures which are typically necessary for fast diffusion and v) it needs to be chemically inert towards the structural materials of the TISS and the desired radionuclide.

Recent reviews about target materials for ISOL beams are given in [57,58] and broader discussions also covering chemical aspects can be found in [59,60]. Practically all target materials are operated at elevated temperatures (up to 2200 °C) to promote diffusion inside the material and reduce adsorption times on surfaces. The number of radioisotopes produced inside the target material scales with its density, however, less dense materials (*e.g.* high open porosity or thinner foils) show often superior release properties. A certain target unit is typically used for a period of at least several days up to a few weeks. It is a common issue of almost all target materials that over this time, the extracted RIB yield often decreases. In many cases this is attributed to a degradation of the target material. Due to the limited lifetime of radioisotopes, their released fraction strongly depends on the diffusion time which in turn depends on the grain size of the target material. The latter increases with time (sintering), promoted by heating and radiation damage induced by the primary beam [61]. Target materials can be classified according to their state of matter and chemical composition.

Molten targets have the highest possible density and are often made of low-melting metals like lead or tin. The temperature of operation is mostly close to the melting point of the metal. The diffusion time is typically long [62] and only scales weakly with temperature, in contrast to solid materials [60]. In some cases, the mechanical

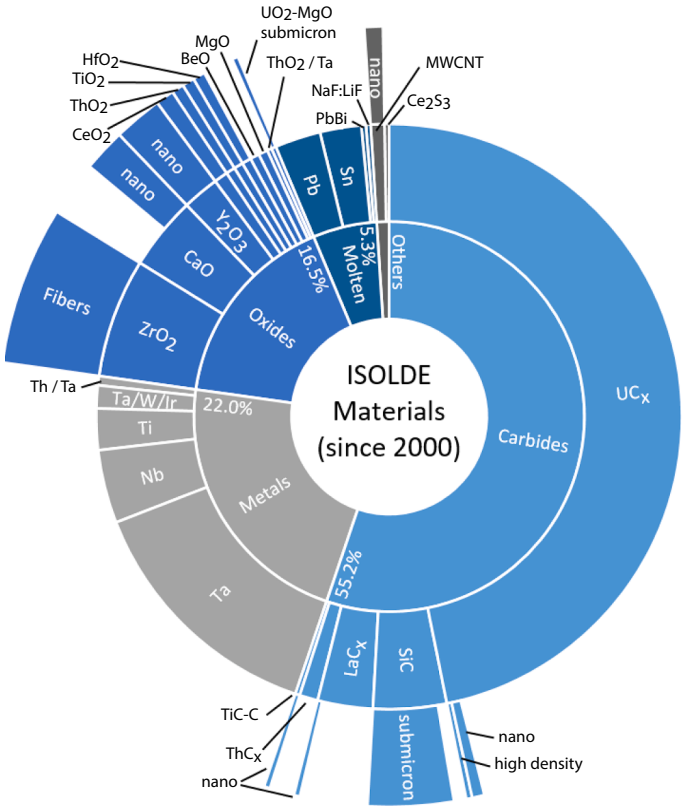

Figure 1.8: Target materials used at ISOLDE since 2000. Adapted from [57] by permission from Elsevier and J.P. Ramos.

shaking induced by magnets has been found to reduce diffusion times [63]. Recently, a prototype equipped with a forced circulation loop and shower to create small droplets has been developed [64] and tested [65, 66]. An advantage of this target class is the absence of target material degradation, allowing extended usage times.

Metal powder has been considered in the past but was discarded due its susceptibility to sintering. Commonly, rolled metallic foils are used which are embossed to contain small spikes. These minimize the contact surface between the layers and reduce sintering. Typically, the most refractory metals are considered for foil targets. Tantalum is among the frequently used metal foil targets for the production of lanthanides. Pressed powders are the most frequently used target materials. Oxides are widely used but are prone to sintering. As for the metal foils, a successful approach to control sintering is to minimize the contact surface. Micron-sized fiber materials, *e.g.* yttria-stabilized zirconia, have proven to be reliable [67]. As shown in the case of calcium oxide, a rigorous temperature control can be decisive to prevent fast sintering [68, 69]. Many metal carbides have refractory properties, among these uranium carbide which is the most versatile material. The uranium carbide target is produced from uranium oxide in a reaction with excess carbon (graphite). The latter forms a separate phase that reduces sintering [70].

A more recent development is the emergence of nanostructured target materials. Due to their small grain size, diffusion is fast and particularly short-lived isotopes profit

from this development [12]. The first attempt to exploit nanostructured materials was a sodium zeolite [71] used at the TISOL facility [72] at TRIUMF, a predecessor of ISAC. Increased yields were reported for ^{16}N ($t_{1/2} = 7.13\,\mathrm{s}$). At ISOLDE, a sub-micron sized silicon carbide target material was developed [73] and with the development of a novel calcium oxide target in 2011, the first nanometric material has found its way into the facility which showed high yields for exotic isotopes *e.g.* ^{31}Ar ($t_{1/2} = 15.1\,\mathrm{ms}$) [68]. The development of nanometric uranium carbide [58], titanium carbide [74], yttria [73] and the carbon allotrope MWCNT [75] followed.

1.2.3 Ion sources

For radioactive isotope beam extraction, the efficiency of an ion source is a key figure, due to the very limited number of produced isotopes in the target. Several high-efficiency ion sources have been developed in the last decades. The choice of ion source must be adapted to the physical and chemical properties of the desired species and consideration of selectivity requirements. The relevant ionization phenomena can be divided into three groups: i) surface ionization, *i.e.*, ionization in hot cavities ii) electron impact ionization which is also the most relevant ionization process in plasma and iii) resonant laser ionization.

Surface ionization

Alkaline and alkaline earth metals have low ionization potentials (IP) and ionization often takes place readily on contact with a hot metal surface of high work function ϕ. In the ionization process, an electron is transfered from the atom to the metal via quantum tunneling [76]. The ionization process is described by the Saha-Langmuir equation [77,78]. In tubular cavities, multiple collisions between neutral species and the ionizer surface occur. Also, the probability of ion extraction from the tubular cavity needs to be considered. In [79,80], the following expression for the ionization efficiency ϵ_{surf} has been derived:

$$\epsilon_{\mathrm{surf}} = \frac{\beta \exp\left(\dfrac{\phi - IP^*}{\mathrm{k_B}T}\right)}{1 + \beta \exp\left(\dfrac{\phi - IP^*}{\mathrm{k_B}T}\right)}, \tag{1.1}$$

where T is the temperature and $\mathrm{k_B}$ the Boltzmann constant. The effective ionization potential $IP^* = IP - \mathrm{k_B}T \ln(g_i/g_0)$ takes into account the statistical weights of ion g_i and atom states g_0. The ionization enhancement factor β is related to the effective number of collisions and survival probability of the ions.

Besides alkaline (earth) metals, the method can also be applied to other low-ionization potential ($IP \lesssim 7\,\mathrm{eV}$ [79]) elements, like the elements of the lanthanide series. As can be seen in Eq. 1.1, the ionization efficiency strongly depends on the temperature. Commonly, tantalum ($\phi = 4.25\,\mathrm{eV}$ [81]), tungsten ($\phi = 4.55\,\mathrm{eV}$ [81]) and rhenium ($\phi = 4.72\,\mathrm{eV}$ [81]) ionizers operated at temperatures of 2000 °C to 2400 °C [59] are used. Efficiencies for low-ionization potential elements are typically well above 10% and can almost reach 100% in some cases. Besides elements, also low-ionization potential molecules can be ionized, *e.g.* barium, strontium and calcium fluorides [82].

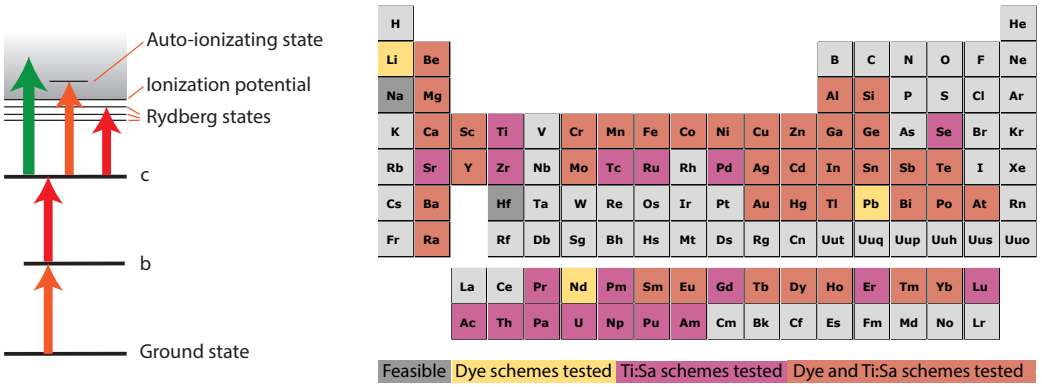

(a) Pathways (adapted from [83]) (b) Available RILIS elements [87]

Figure 1.9: The ISOLDE RILIS (a) The different pathways of ionization, including ionization via auto-ionization states, non-resonant ionization from an excited state or via Rydberg states (see text). (b) RILIS elements available with dye lasers or Titanium Sapphire lasers (Ti:Sa).

Resonant laser ionization

The Resonant Ionization Laser Ion Source (RILIS) [83] is the most frequently used ion source at ISOLDE. In 2018, RILIS was used during 60% of all shifts. The ionization method provides, in contrast to all other available methods, element sensitivity due to the unique electronic structure of elements. Possible pathways for excitation are shown in fig. 1.9a. Transitions from (typically) the ground state to excited states (b and c in fig. 1.9a) are step-wise initiated by absorption of photons of specific frequency. From here, three possible pathways lead to efficient ionization: i) non-resonant ionization with a powerful laser; ii) resonant ionization to an auto-ionizing state and iii) resonant ionization to a Rydberg state, *i.e.*, a state close to ionization energy, followed by collisional or field ionization.

Auto-ionizing states are bound states above the ionization potential which can be reached by excitation of two or more electrons. Due to the reliability and efficiency, auto-ionizing states are often the preferred pathway, nonetheless not all atoms possess these. The ionization via Rydberg states suffers from a lack of reproducibility and is not routinely practiced, also due to limited laser capabilities [83].

The combination of element-sensitive ionization and mass separation would in principle allow the extraction of a pure beam, only containing the isotope of interest. However, in practice, the laser ionization takes place in a hot cavity, susceptible to surface ionization. The elevated temperature is in many cases necessary to avoid sticking of condensable elements to the walls which would delay the extraction process or even render it impossible.

The hot cavity also has characteristics that are favourable for ion survival and extraction. The latter equally applies to surface ion sources. Heating leads to thermionic emission of electrons, as described by the Richardson-Dushman equation [84]. The walls of an otherwise empty ionizer are left with a positive potential that confines ions in the center of the cavity and prevents recombination by collision with the surface of the ionizer (see [85] for a more sophisticated discussion). In addition, an increasing electrical potential along the ion source and transfer line, pushes the ions towards the

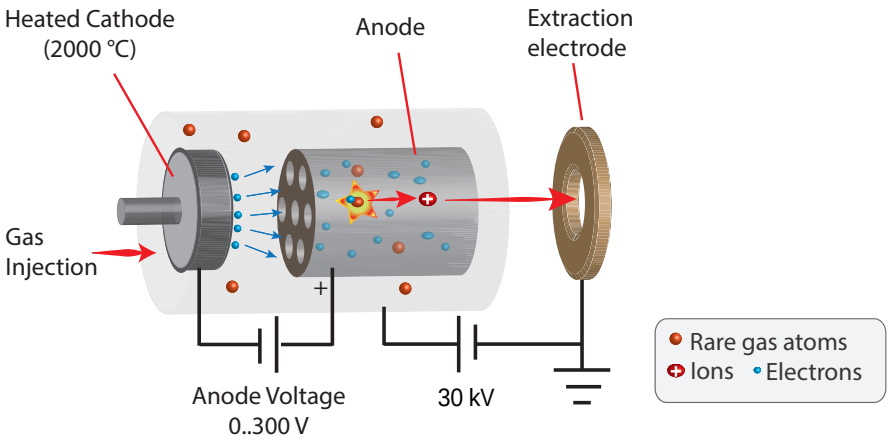

Figure 1.10: Electron impact ionization (simplified schematic)

extraction side. Recently, it was shown that this effect can be amplified by application of an axial magnetic field which increases the electron density [86].

A series of developments has been made to suppress unwanted surface-ionized contaminants. These include the use of low-work function (ϕ) materials and the development of the Laser Ion Source and Trap (LIST) [88] which allows laser ionization free of hot surfaces in an RF ion-guide after strong suppression of surface ions by an electrostatic repeller.

Forced electron beam sources

The Versatile Arc Discharge Ion Source (VADIS) depicted in fig. 1.10 is commonly used at ISOLDE and based on the concept of the Forced-Electron Beam Induced Arc-Discharge (FEBIAD) ion source. Electrons are released from a resistively heated tantalum cathode (ca. 2000 °C) and accelerated through a grid towards the anode body which is typically biased between 100 V and 200 V. The electrons are weakly focused by an axial magnetic field (< 300 G) and forced on helical orbits which reduces electron flux transverse to the magnetic field. Thus, the electron lifetime and density are increased. Ions are formed in collisions of neutral atoms or molecules with electrons. The ion source is held at a voltage of 30 kV to 60 kV, so that the ions are accelerated towards the grounded extraction electrode.

The FEBIAD-concept was introduced in the 1970s by Kirchner and Roeckl and tested on-line at the TRIGA reactor at the Johannes Gutenberg - Universität Mainz (JGU) [89]. Besides the better stability in operation, its major improvement compared to the earlier Nielsen source and its derivatives [90, 91], is the introduction of a grid close to the cathode which allows to extract higher electron currents thermionically emitted by the cathode. In earlier versions, the major fraction of electrons was obtained from a plasma that ignited only at a threshold gas pressure well above 1×10^{-4} mbar. In later versions of the FEBIAD ion source, the heating filament of the cathode was replaced by a ruggedized (electron-beam welded) tantalum part that was heated along with the transfer line in a common electrical curcuit [92]. Further geometry and material opti-

mizations followed which led in some cases to an efficiency increase of one order of magnitude [93]. The improved model was named VADIS and ion sources of this series carry 'VD' in their name, in contrast to the earlier FEBIAD ('MK') series. The option to provide a voltage different from the anode potential to its end-cap (named anti-cathode by Kirchner *et al.*) was rediscovered to improve the extraction of laser-ionized species [94–96], leading to a setup similar to the FEBIAD MK3 model. Electron impact ion sources and related phenomena are discussed in greater detail in section 2.3.

Via electron-impact ionization, all species can be ionized. This includes noble gases and molecules which are not efficiently accessible by laser ionization and mostly not available by surface ionization. The universality, *i.e.*, the lack of selectivity is a drawback at the same time. Some selectivity can be obtained by choosing an electron energy favourable for the ion of interest and adverse for the conataminant. However, since these differences are often small, the suppression effect is not typically exploited in on-line operation and comes, especially if higher charge states need to be used, at the price of highly reduced efficiency. In some cases, the decomposition of molecules could be achieved by higher anode voltages, so that the elemental beam is preferentially populated [97, 98]. Often the VADIS is combined with a filtering transfer-line (section 1.2.4), which, *e.g.*, provides pure beams for many noble gases or condenses selectively alkali matals on a quartz surface. It was also suggested to purify beams by chemoselective trapping in a pulsed source [99, 100]. As will be discussed in Chapter 5, a powerful technique for beam purifaction is the selective formation of molecules. By attaching the isotope of interest to a molecular carrier, the mass-to-charge ratio changes and the species can be separated electromagnetically.

Radio-frequency heated plasma sources

Especially for the production of volatile atom and molecular beams, Radio Frequency (RF)[2] plasma ion sources have been considered. Despite this chapter focusing on the ISOLDE facility, it is worth mentioning that the SPIRAL facility at GANIL used an ECR Ion Source (ECRIS) as principle mean of ionization. A review about ECRIS for radioactive ion beam production can be found in [101].

In plasma ion sources, a buffer gas (typically a noble gas) is introduced at a constant flow rate and ignited by RF injection. In contrast to (forced) electron beam sources, plasma sources are typically not resistively heated and are believed to offer favourable properties for the ionization of molecules (like carbon monoxide). Due to cold operation, thermal decomposition of these molecules on the walls of the ionizer, as it would occur in forced electron beam sources, can often be avoided. However, molecule decomposition in the plasma can occur and its confinement is often limited.

The design of an RF-heated ion source for ISOLDE is challenging due to a series of contradictory requirements. Sources need to be efficient, radiation-hard, compact and tolerant to the gas-load peaks produced on beam impact on the target material. The required infrastructure (RF generation, transmission and connectivity) is by far more complex than the simple electric connectivity required for other source types and the operation (*e.g.* plasma ignition) can be troublesome. Most plasma sources have in common that a magnetic confinement of the plasma is required. The RF power is coupled into the source by antennas close to the plasma chamber or through a wave

[2] Within this work, the term radio frequency is used for the frequency range from 20 kHz to 300 GHz, *i.e.* also including the microwave region.

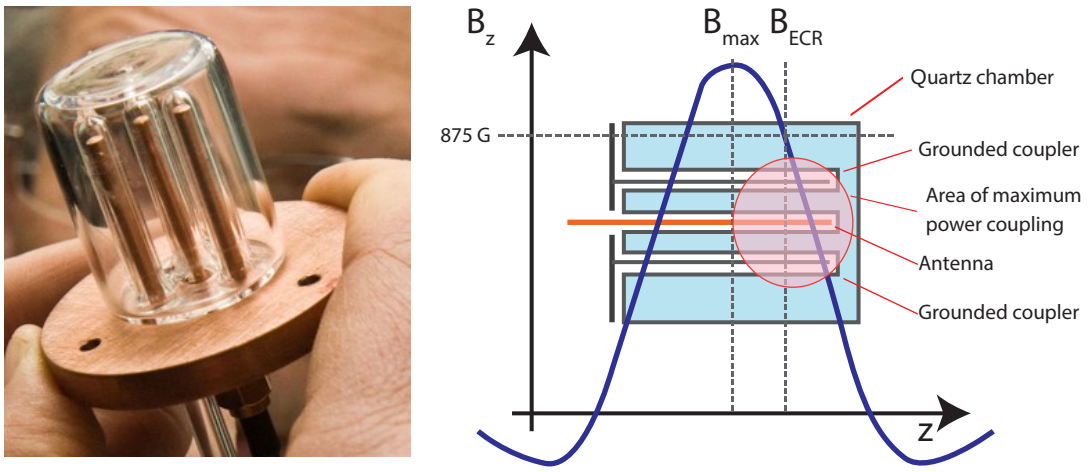

(a) Photo (b) Magnetic field

Figure 1.11: The COMIC ion source (a) Photo of the ion source, not showing the permanent magnet array. (b) Schematics and magnetic field arrangement

guide.

The first RF-plasma ion source operated at ISOLDE was the Minimono source [102,103] that was adapted from its predecessor at GANIL [104, 105]. It was equipped with permanent magnets in multipole configuration providing electron confinement [106]. The magnetic field was progressively decreasing from 0.2 T to 0 T in the center of the plasma chamber. The required field for the ECR at 2.45 GHz is 87.5 mT. In offline tests, Ionization efficiencies of up to 55% (Xe) [102] have been measured, and 4% and 14% for the ionization of CO and CO_2 [103]. In on-line tests, the gas burst on proton impact caused an efficiency decrease by one order of magnitude [101], however, short-lived ^{9}C ($T_{1/2} = 123$ ms) [75] could be extracted.

Due to concerns regarding the radiation-hardness of the permanent magnets, the development of the radiation hard source Mono ECR ISOLDE (MECRIS) was launched [107]. The permanent magnet array was replaced by two coils in Helmholtz configuration, thus lacking a radial confinement. Compared to the Minimono source, only low electron densities could be reached. Offline measurements report efficiencies of 5% to 10% for xenon, which were comparable to the FEBIAD MK7 (cold transfer line) source used at that time (2004).

Aiming at efficient extraction of volatile molecules, the Quartz COmpact MIcrowave and Coaxial (Q-COMIC) ion source was tested at ISOLDE [108,109]. It is based on the COMIC source developed at LPSC Grenoble [110]. As the previously described sources, the COMIC ion source operates at 2.45 GHz. A photo and sketch of the magnetic field are shown in fig. 1.11. The source is equipped with an array of permanent magnets, designed such that the maximum of the magnetic field is located in the center of the source. ECR conditions are met in the region between center and outlet hole. Due to the magnetic mirror effect, ions created in this region are longitudinally guided towards the plane of the outlet hole. The plasma chamber is made of quartz to provide chemical compatibility for oxide formation. The highest measured ionization efficiency was

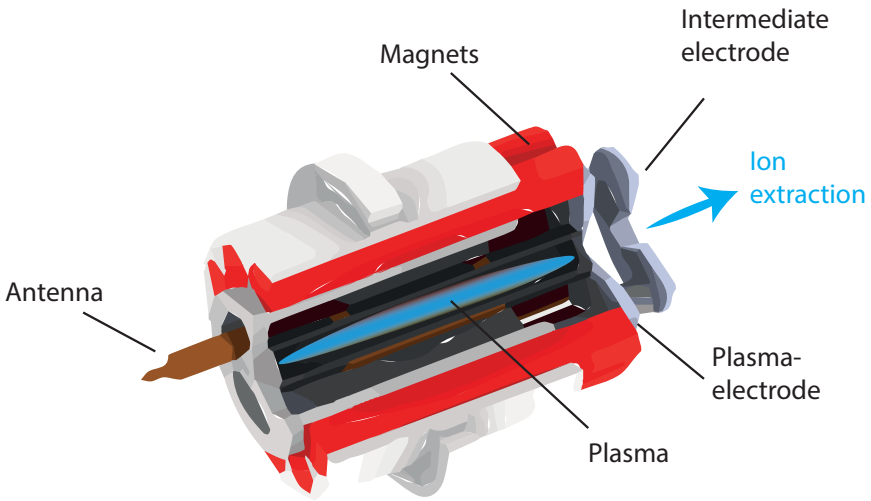

Figure 1.12: The Helicon ion source

claimed to be 75% (Xe), however, the ionization efficiency for CO_2^+ did not exceed 0.2%. The low ionization efficiency was tentatively attributed to breaking of the molecule, as the dissociation energies of CO_2 and CO bonds are only 5 eV and 11 eV [111], respectively, but the ionization potential is 14 eV [112]. The mean electron energy of the COMIC source is expected to be ca. $T_e \approx 1$ eV with an decreasing tail towards higher energy (Maxwellian or Lorentzian distribution) [113].

The Helicon ion source (*cf.* fig. 1.12) was developed with the goals of higher efficiency than the COMIC source could provide and tolerance to the pressure fluctuations which ECR sources suffer from [114]. The source contains a magnetized plasma driven by a 20 MHz to 200 MHz transmitter. The design is based on the concept of energy coupling through a helicon wave in the magnetized plasma. This coupling mode promises a high level of ionization and electron density. Efficiencies of 1% and 2.5% for CO_2^+ and CO^+, respectively, are reported [115]. In contrast to the COMIC source, helium buffer gas was found to yield the highest efficiency for molecular beams. The plasma density was estimated to be $n_e \approx 1 \times 10^{17}\,\mathrm{m}^{-3}$ based on the extracted maximum current. It was deduced that the density is not sufficient for the generation of a helicon wave. Very likely, the plasma was coupled inductively. Further detail about plasma sources is given in section 2.3.

1.2.4 Transfer lines

The transfer line, connecting ion source and target container, does not only provide a confined pathway for the neutral radioisotopes produced in the target to diffuse into the ion source but is also used as chromatographic column to delay the transport of unwanted species. An overview of ion source and transfer line combination is given in table 1.1 [92, 93, 116–119].

The simplest transfer line is implemented in the "hot-plasma" source (VD5) and in most cases also applied for hot cavities. The ion source is connected via a hot tantalum transfer tube to the target container. It is designed with the goal to transport all species

Table 1.1: Ion sources and transfer lines for the VADIS and FEBIAD-type ion sources. Materials of the transfer lines in contact with the radioisotopes, the typical temperature of the transfer line and the number of anodes in the ion source are given. The cathode temperature of the ion source is typically ca. 2000 °C for all sources listed below. Identifiers starting with 'MK' were introduced in the FEBIAD series, 'VD' refers to a version of the VADIS source.

Name	**Transfer line Material**	**Transfer line Temp. / °C**	**Source Anodes**	**Field of application**
Warm plasma *MK3*	steel	200 - 400	2	for molten metal targets *not used anymore*
Hot plasma *VD5/MK5*	Ta	2000	1	non-volatile species
Warm plasma *MK6*	steel	200 - 400	1	medium volatile species *e.g.* separation of Cd/Hg
Cold plasma *VD7/MK7*	Cu	20 (RT)	1	very volatile species *e.g.* noble gases, BF_3, CO
Cold quartz	Ta and quartz	300 - 800	1	Suppression of contaminants *e.g.* alkaline metals with high adsorption on quartz
Hot quartz	quartz	700 - 1100	1	
Cold chimney helix insert	Ta and steel	350 - 550	-	molten targets, retains vapor *e.g.* Pb target
Hot chimney helix insert	steel	up to 1000	-	molten targets, retains vapor *e.g.* Sn target

effusing out of the target container to the ion source. Thus, it does not provide additional selectivity. The hot transfer tube is required for species exhibiting relatively high melting or boiling points.

The "warm-plasma" sources (MK3 and MK6) are equipped with a stainless steel block, offering temperatures in the range from 200 °C to 400 °C. The transfer line was designed to transmit relatively volatile elements (Zn, Cd, Hg) and retain vapours from the hot target. For very volatile species (*e.g.* noble gases or carbon monoxide), the VD7 source is used. It condenses all non-volatile elements in a water-cooled copper block, kept at ca. 30 °C.

To avoid spilling of liquid metals from molten targets into the ion source and also retain unwanted metal vapors in the target, a dedicated transfer line was designed [62]. It contains a helix structure to condense metal vapors before reaching the ion source. Designs for three different temperature ranges have been developed, tailored to the properties of La, Sn ad Hg [119].

The quartz-transfer lines allow to suppress contaminants which show stronger adsorption than the species of interest [117, 118]. Two versions are available and cover the

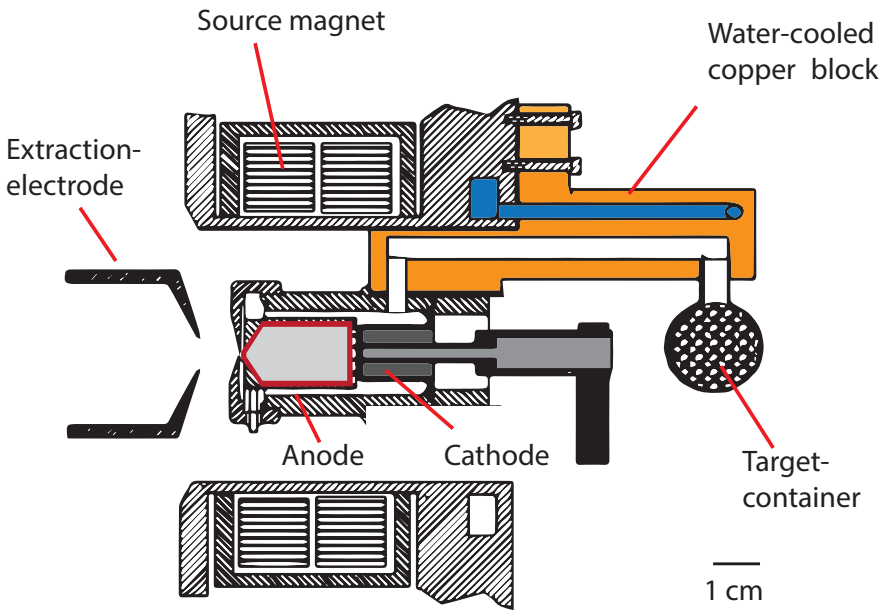

Figure 1.13: The MK7 assembly. Target container and ion source are connected via a water-cooled transfer line.

temperature range from 300 °C to 1100 °C. Often the quartz line is applied to suppress alkaline metals, a common class of contaminants due to their susceptibility to efficient surface ionization.

2 Models and tools used in this thesis

Contents

The development of new molecular beams is addressed in this work. This chapter presents models and tools used to derive efficiencies for each step of the ISOL-process: in-target production in nuclear reactions, transport of radioactive isotopes via diffusion and effusion, and ionization. The in-target production was studied numerically with the help of established and benchmarked codes. Models for diffusion and effusion are presented which together define the fraction and time-structure of the release. The latter are important properties for conditions experienced at ISOLDE where the proton beam is pulsed. Ionization will be discussed with respect to the used ion sources, which are radio frequency-driven plasma sources and electron beam induced arc-discharge sources.

2.1 Radioactive nuclide production

2.1.1 Fundamentals

The ISOLDE facility is served with pulses of 1.4 GeV protons which initiate high-energy reactions inside the target nuclei. At this energy, the wavelength of the incident proton is less than the average distance between the nucleons. Their interaction energy is also significantly smaller than the projectile energy. Under these conditions, the reaction is governed by collisions of the incident proton with single nucleons inside the nucleus and described by the Intra-Nuclear Cascade (INC) model as shown in fig. 2.1 [120–122].

The proton propagates like a free particle in the nuclear medium which is treated as a Fermi gas. Secondary particles with typically large forward momentum form in collisions. Their energy spectrum reaches up to the incident particle energy. The secondaries in turn, initiate new cascades until they either emerge from the nucleus or their energy has decreased to an extent that the particle can be considered as absorbed. In the latter case, the remaining energy contributes to the excitation energy of the nucleus. Some collisions are forbidden by quantum effects, mainly Pauli blocking. The nucleons not involved in the collision occupy certain quantum states which are not available anymore as final states of incident particle or its collision partner. As a result, the effective collision cross section is reduced. The cascade extinguishes within a duration in the order of only 1×10^{-22} s. The remaining nucleus is left in an excited state, defined by its mass and atomic number, velocity, angular momentum and excitation energy. Besides nucleons, also pions are involved in nuclear cascades and can escape the nucleus despite their high interaction cross section. In contrast to low-energy collisions, the reaction between a high-energy projectile and target nucleus does not result in a well-defined compound nucleus but an ensemble of different compound nuclei.

The further progress of the reaction is depicted in fig. 2.2. In the second stage of the process, the nucleus undergoes several deexcitation steps. The most important channels are i) evaporation ii) fission and iii) fragmentation. In evaporation reactions single nucleons and light particles are emitted from the nucleus. The evaporation residues of high-energy reactions are often referred to as spallation products.[1] The highest production cross sections are found on the low-mass side in the vicinity of the target

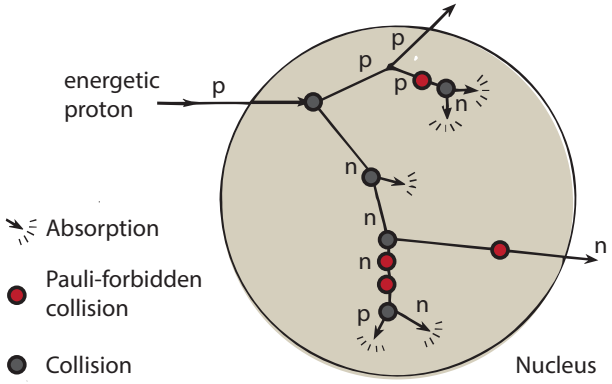

Figure 2.1: The intra-nuclear cascade (INC) model. Adapted from [120].

[1] The term spallation was first used by G.T. Seaborg in 1937 [123]. It can be derived from the verb to spall, meaning to chip nucleons of a nucleus [122]. The term can be used either in a general way for high-energy reactions including all deexcitation channels or refer to the evaporation channel only. In this work, spallation refers to the evaporation channel only.

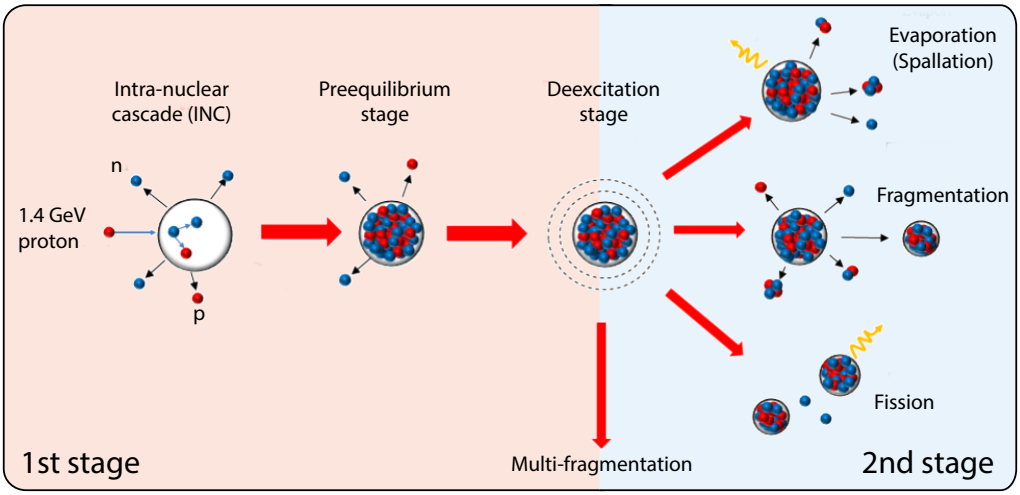

Figure 2.2: High-energy nuclear reactions. Adapted from [124].

nucleus. They decrease steeply with increasing mass difference. With higher energy of the projectile and higher excitation energy of the compound nucleus, the distribution turns broader.

Fission plays an important role in high-energy reactions of heavy targets like uranium. In every step of the deexcitation process, fission is in competition with evaporation. The probability of fission (fissility) is proportional to Z^2/A, due to the increase in long-range Coulomb repulsion over short-range attractive forces in heavier elements. Despite the high energy of the projectile, the excitation energy of the compound nucleus is sometimes as low as a few tens of MeV only. In this case, the deexcitation follows the rules for low-energy fission processes with often double-humped asymmetric mass distribution. At elevated excitation energies, shell effects are washed out so that the symmetric fission channel dominates. Fission products are typically found on the neutron-rich side of the nuclear chart and have their maximum yields in the intermediate mass range.

At even higher excitation energies (some hundreds of MeV for uranium) fragmentation reactions emerge. This channel is responsible for the high production cross section of nuclides in the low mass range but also extends to the fission-dominated intermediate masses. Besides the discussed deexcitation modes, the hot nucleus can also break up due to thermal instabilities leading to multifragmentation. The duration of the deexcitation step with 1×10^{-18} s is significantly longer than the INC. Between the intranuclear cascade and the deexcitation stage, newer models implement a preequilibrium stage which is entered when all excited nucleons have reached an energy below a given threshold (typically a few tens of MeV).

2.1.2 Computational tools

A comprehensive overview of simulation codes can be found in [122] and a recent review article [123]. Benchmark results of several codes are provided by the IAEA [125]. The main simulation tools used in this work are ABRABLA [126, 127] and FLUKA [128,129] which will be briefly described. From a users perspective, the major difference between these codes is that FLUKA is a particle-tracking code allowing to implement

complex target geometries while ABRABLA considers a single encounter between a projectile and a target nucleus. As a direct consequence, FLUKA considers secondary reactions, *e.g.*, between neutrons produced in one projectile-target collision and another target nucleus (sometimes referred to as int**er**-nuclear cascade).

ABRABLA

The ABRABLA code was developed at GSI and its name can be derived from the included models of abrasion and ablation. The abrasion (ABRA) model is a first stage model developed for peripheral nucleus-nucleus collisions at high energies [130]. In contrast to the INC-model, it is a macroscopic model. The geometrically overlapping region between the colliding nuclei is defined as participator (or "hot fireball"), while nucleons in spectator regions keep moving with their initial velocity. The treatment of nucleon-nucleus-interactions was added by integration of the BURST model [131], which is based on parameterization of results obtained from an INC-code [126].

The deexcitation stage is treated within the statistical model in the ABLA07 code [127]. After the thermal equilibrium is reached, the nucleus expands. If its excitation energy exceeds ca. 5 MeV per nucleon, the result of the expansion is a fast break-up of the nucleus (multifragmentation) due to its negative incompressibility in this regime. The expansion even increases the pressure and results in the simultaneous emission of clusters and several nucleons. For excitation energies below ca. 5 MeV per nucleon, a single compound nucleus is assumed.

In the further deexcitation of the fragments, ABLA considers emission of neutrons, Light Charged Particles (LCP), Intermediate Mass Fragments (IMF), fission and gamma rays with their respective decay width Γ_{neutron}, Γ_{LCP}, Γ_{IMF}, Γ_{fission} and Γ_{gamma}. The probability of deexcitation P_i via channel i is given by the ratio of its decay width Γ_i over the total decay width Γ_{tot},

$$P_i = \frac{\Gamma_i}{\Gamma_{\text{tot}}}, \text{ where } \Gamma_{tot} = \Gamma_{\text{neutron}} + \sum_{\text{LCP}} \Gamma_{\text{LCP}} + \Gamma_{\text{Gamma}} + \Gamma_{\text{fission}} + \sum_{\text{IMF}} \Gamma_{\text{IMF}}. \tag{2.1}$$

The sums run over all possible particles that can be emitted.

The code was applied to for the interpretation of experiments at the FRagment Separator (FRS) located at GSI. Instead of focusing an energetic proton beam on a steady target, heavy projectiles (up to uranium) were sent on a liquid hydrogen target [132]. A comparison with results obtained at ISOLDE is available in [133]. ABLA was also implemented in several transport-codes [122] *e.g.* in the Geant4 package which also supports INC models [134].

FLUKA

The multi-purpose FLUktuierende KAskade (FLUKA) Monte-Carlo code was developed at CERN and INFN and is based on three dimensional particle tracking. In contrast to cross-section codes, it allows to predict energy- and angle-differential particle fluences in a complex geometry. The production yields of residual nuclei can equally be obtained along with expected dose rates. However, the kinetic energy of low-energy fission fragments is not readily available.

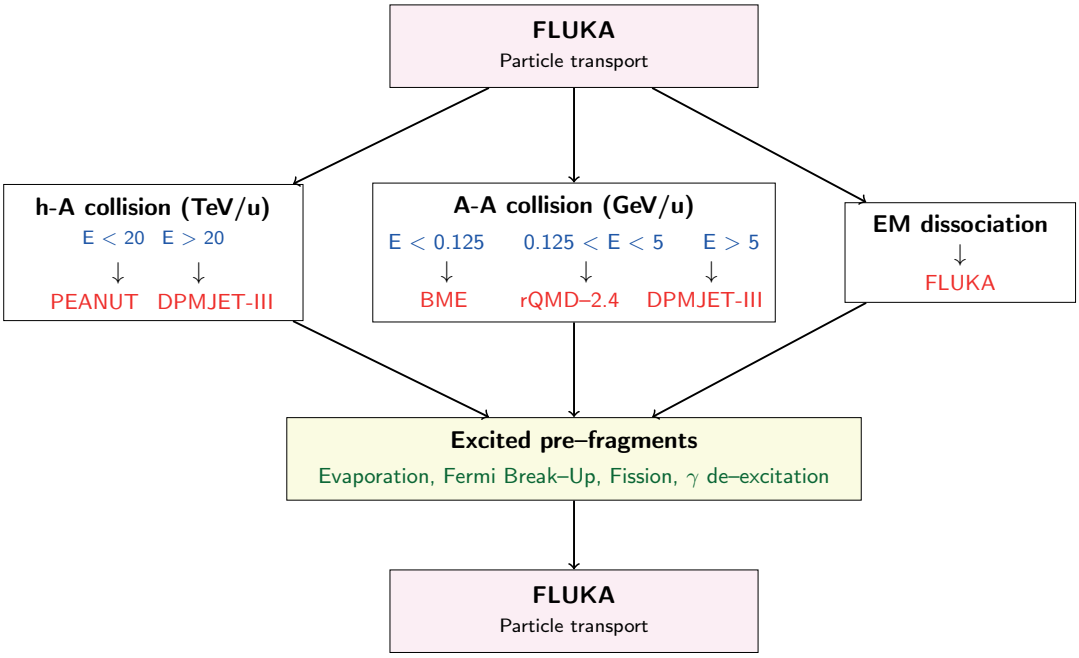

Figure 2.3: Schemetic program sequence of FLUKA, including the different event generators for hadron-nuclus (h-A) and nucleus-nucleus (A-A) reaction. Reproduced from [140].

FLUKA covers hadron-hadron, hadron-nucleus and nucleus-nucleus interactions from the threshold up to an energy of 10 PeV. Besides heavy ions, sixty different particles can be transported [135].

The included models are discussed in [121, 136–140] and the program sequence is schematicially shown in fig. 2.3. The models can be categorized by applicable energy range and type of interaction. At the highest energies, which are out of the scope for ISOLDE, the Dual Parton Model and JETs (DPMJET) interface is used. For ion-ion collisions (A-A) below ca. 5 GeV the relativistic Quantum Molecular Dynamics (rQMD) event generator and at even lower energies the Boltzmann Master Equations (BME) module is used.

The PreEquilibrium Approach to NUclear Thermalization (PEANUT) model is most relevant for residual production at ISOLDE and covers hadron-nucleus interaction over a wide energy range (up to 20 TeV). Its implementation follows a sequence of four sequential steps:

Step 1: Glauber-Gribov cascade and high energy collisions

Coupling of Glauber multiple scattering to a Dual Parton Model (DPM) (for energies above ca. 5 GeV)

Step 2: Generalized Intra-Nuclear Cascade

For lower (< 100 MeV to 200 MeV) and higher (> 2 GeV to 3 GeV) energies, the plain INC model needs to be extended. These extended models are referred to as Generalized Intra-Nuclear Cascade (GINC) models. This stage runs until all nucleons are below a smooth threshold of ca. 50 MeV and all particles (mostly pions) but nucleons have been emitted or absorbed.

Step 3: Preequilibrium emission

The preequilibrium stage bridges the end of the INC to the begin of the deexcitation stage. The FLUKA implementation follows an exciton model called Geometry Dependent Hybrid Model (GDHM). An exciton is either a particle above the Fermi-surface or a hole below the surface. In nucleon-nucleon collisions the nucleus proceeds through a chain of several steps. At each step the probability of particle emission is evaluated. Following the "never come back" approximation, the number of excitons increases while the chain progresses. The end of the chain (*i.e.* equilibrium) is reached if the excitation energy is below any emission threshold, or if the excitation number is sufficiently high compared to single particle level density and excitation energy.

Step 4: Deexcitation

The deexcitation stage considers evaporation, fission, gamma-ray emission and fragmentation (break-up). The implementation for evaporation follows the Weisskopf-Ewing description of the statistical model. Emission probabilities depend on the level densities of the final (and initial) nucleus. Fission can significantly contribute for heavier ($Z > 70$) nuclei and is equally considered in a statistical approach describing the way to the saddle point where the fission barrier is overcome and the system irreversibly separates. In addition, a Fermi Break-up model is included which is of particular importance for light nuclei.

At ISOLDE, the FLUKA code is widely used to optimize the geometry of the TISS. It has proven especially useful for the development of proton-to-neutron converter assemblies, where energy differential particle-fluence maps play an important role. Obtained particle fluences have been benchmarked with experimental data [141, 142] and are in agreement over a wide range. Besides residual isotope production, the code is also used for radio-protection and engineering applications. The energy deposited in target-beam interactions can be estimated by FLUKA and requires consideration especially for dense targets or highly intense driver beams.

2.2 Transport phenomena

The various transport phenomena involved in the ISOL process are schematically illustrated in fig. 2.4. Each phenomenon contributes to the radioactive ion beam yield, as will be discussed in Chapters 3 and 4. The produced isotope is an ejectile of a nuclear reaction and posseesses a certain momentum, often referred to as recoil momentum. Its kinetic energy depends strongly on the production channel. Due to the large Coulomb forces between nascent fission fragments at scission, kinetic energies in the order of some tens of MeV to even above 100 MeV can be found in uranium fission. The resulting ranges are in the order of µm in the target material. The recoil energy in spallation reactions is significantly lower (typically tens of keV to few MeV). However, it was pointed out that the spallation recoil momentum could contribute to high yields observed in target nanomaterials [69]. After thermalization and neutralization, the isotope ion has to propagate through condensed (solid or liquid) matter till it reaches a boundary to open space (*e.g.*, the grain boundary). The following diffusion through

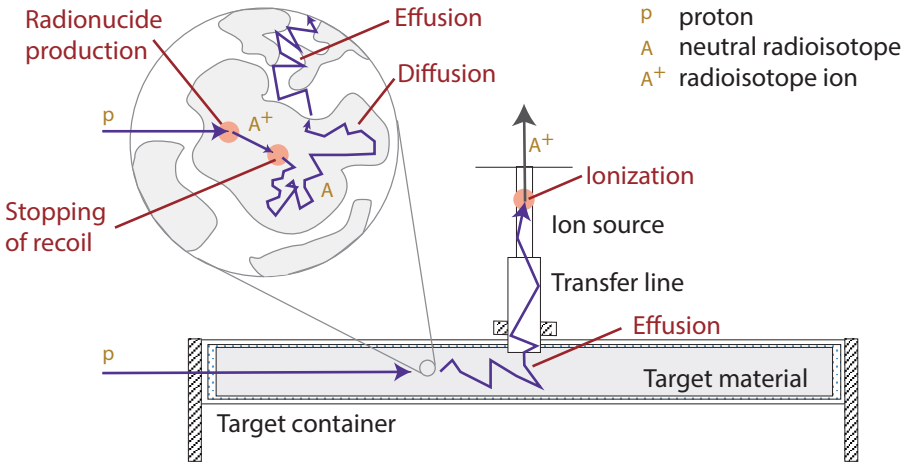

Figure 2.4: Schematic repesentration of transport processes in the ISOL process. Adapted from [73,74].

open space towards the ion source is often referred to as effusion. Due to the limited lifetime of radioisotopes, the transport time translates directly into an efficiency, the so-called release efficiency ϵ_{rel}, which accounts for decay losses.

2.2.1 Transport of ions in matter

The recoil momentum is typically neglected in models describing the efficiency of ISOL beam production. However, it plays an important role in the target concept introduced in Chapter 6. A detailed discussion on ion transport in matter is available, *e.g.*, in [143–145]. While propagating through a material, the ion successively loses its energy in interactions with the medium. The energy loss can be quantified with the concept of a retarding STopping Force (STF)[2] , $S = -\mathrm{d}E/\mathrm{d}x$. It depends on mass and charge of the ion, its velocity and the stopping medium. The range of an ion can be obtained by integration. As proposed by Bohr already in 1913, the different velocities (and associated time scales) of electron and nuclei propagation allow to separate their respective contributions [147].

Nuclear Stopping

The nuclear stopping force can be estimated by consideration of elastic collisions between the incident ions and the target nuclei screened by their electron shell. The calculation is based on the atom-atom interatomic potential $\mathcal{V}$ for which several models have been proposed. They have in common that a Coulomb term ($\propto Z_1 Z_2/r$) is multiplied by a screening function Φ_s,

$$\mathcal{V}(r) \propto \frac{Z_1 Z_2}{r} \Phi_s(a, r), \tag{2.2}$$

where Z_1 and Z_2 are the atomic numbers of the involved nuclei which are typically treated as point charges. The screening function depends on the distance between the point charges r and the screening radius a. The developers of the Stopping and Range of Ions in Matter (SRIM) application [148], commonly used to estimate STF and ranges, have derived an analytic function that is based on a fit of selected interatomic potentials which were calculated for a set of atom-atom pairs.

[2] Historically, the term Stopping Power is used for the same quantity. However, it was pointed out that the actual unit is that of a force [146].

Electronic Stopping

Energy transferred to the electrons (inelastic energy loss) is considered in the electronic STF. The derivation of expressions for the electronic contribution to the STF is more complex than its nuclear counterpart. The involved particles continually change during the stopping process, *e.g.*, the charge state of the incident ion depends on its energy. According to an early theory of Bohr, electrons having an orbital speed smaller than the speed of the ion are efficiently removed. Also the electron density in the target is affected by the ion due to polarization. The electronic stopping can be mathematically treated first for light ions (H, He) and then scaled to heavy ions. The models have evolved with time, starting with the early work of Bohr in 1913 that was extended by Bethe and Bloch. The (classic) Bohr-Theory is based on consideration of target electrons as collection of harmonic oscillators. Within the Bethe-Bloch theory, the issue is treated quantum-mechanically with the help of the perturbation theory. The non-relativistic Bethe equation yields the electronic stopping force S_{el} for an incident ion of velocity v_i and charge Ze in a medium with electron number density N_e as

$$S_{el} = \frac{4\pi N_\mathrm{e} Z^2 e^4}{m_e {v_i}^2} \ln \frac{2 m_e {v_i}^2}{I}, \tag{2.3}$$

where I is the logarithmic mean excitation energy per electron which can be derived from the dipole oscillator strength. The equation generally holds for swift light ions. In later work (*e.g.*, Lindhard stopping), the electrons in the stopping medium are treated as plasma (Fermi gas with velocity v_F), so that collective phenomena can be taken into account.

Other energy loss mechanism

Nuclear stopping typically dominates at low energies and electronic stopping at elevated energies. In some cases (very high ion energies or stopping of electrons), radiative energy loss due to Bremsstrahlung needs to be considered. In common terminology, energy loss due to nuclear reactions (*i.e.*, nonelastic nuclear interactions) is not typically classified as contribution to the stopping force [149, 150]. However, for ion energies above $10\,\mathrm{MeV\,u^{-1}}$ they can significantly contribute [148] or even become the dominating loss mechanism.

2.2.2 Diffusion

Diffusion is a process of particle transport from one part of a system to another driven by a difference in concentration. From a thermodynamics point of view, the transport is favored due to the associated increase in entropy. The particles continuously move along random trajectories due to their thermal energy. After reaching a homogeneous distribution, the net particle flux vanishes. However, a selected tracer particle still follows its random movement. The analog process of conductive heat transfer can be described by a similar model.

The Fick equations lay the foundations for a mathematical treatment of diffusion phenomena. The first Fick law states that the diffusive flow J_x through a section of unit

area perpendicular to the space coordinate x is proportional to the gradient of concentration C. The proportionality constant is the diffusion constant D.

$$J_x = -D\frac{\delta C}{\delta x} \tag{2.4}$$

The second Fick law is often referred to as the differential diffusion equation and introduces a time-dependence. It can be derived from the continuity equation accounting for mass conservation. A change in concentration over time is related to the inflow or outflow of particles as

$$\frac{\delta C}{\delta t} = -\frac{\delta J_x}{\delta x}. \tag{2.5}$$

From Eq. 2.4 and 2.5 follows the second Fick law (Eq. 2.6), assuming that the diffusion constant does not depend on the concentration.

$$\frac{\delta C}{\delta t} = D\frac{\delta^2 C}{\delta x^2}. \tag{2.6}$$

Solutions of the second order partial differential equation have been obtained, *e.g.*, in [151] under the boundary condition that i) once at the surface, the diffusing isotope desorbs rapidly and does not diffuse back into the bulk material and ii) the initial distribution of isotopes is homogeneous. The fraction of isotopes remaining in the solid for foils ($n = 1$), fibers ($n = 2$) and particles ($n = 3$) at time t is given by

$$f_{\mathrm{rem}}(\hat{t}) = \frac{2n}{\pi^2}\sum_{m=1}^{\infty} c_m^{-1}\mathrm{e}^{-c_m\hat{t}}, \tag{2.7}$$

with $c_m = (m - 1/2)^2$ for foils, $(j_{0,m}/\pi)^2$ for fibers and m^2 for particles, where $j_{0,m}$ is the mth positive root of the Bessel function of order zero and $\hat{t} = t/\tau_d$. The characteristic diffusion time $\tau_d = {a_s}^2/(\pi^2 D)$ depends on the diffusion constant and the parameter a_s which accounts for the geometrical size.

The diffusion constant strongly depends on the combination of diffusing species and the host medium. Its temperature dependence in solids follows an Arrhenius-type exponential expression. The displacements can be described as jumps between lattice positions which require a certain activation energy E_a. The exponential term reflects the fraction of species that have sufficient energy. It is combined with a pre-exponential term D_0, which is equal to the diffusion coefficient at infinite temperature.

$$D = D_0 \exp\left(-\frac{E_a}{\mathrm{R}T}\right) \tag{2.8}$$

Solid state diffusion is usually a slow process at room temperature. To reach sufficiently short diffusion times for the extraction of radioisotopes, the operation of target materials close to their melting point is often required. As can be seen from Eq. 2.7 and the definition of the characteristic diffusion time, the size of the particles also plays an important role.

Diffusion experiments with radio-tracers are often conducted in a series of heat treatments of a sample and the determination of the released (or remaining) fraction of isotopes. The temperature is successively increased for each treatment. As a result of the first heat treatment, the distribution of the radioisotopes is not uniform anymore. A method to correct for the disturbed profile was proposed in [152].

2.2.3 Effusion and adsorption

Effusion is the diffusive flow of particles through an orifice in a gas phase and as such a special case of diffusion. In the context of ISOL targets, the term diffusion usually refers to the diffusion through condensed matter only. Effusion covers the transport through open space from the surface of the target material to the ion source. The distinction is made due to the different approaches required for modeling of the phenomena. In powder or fiber targets, an additional regime is involved. The particle flow between the grains of the material (inter-grain diffusion, bulk diffusion or volume diffusion) is an effusion-like process which can either be categorized as part of the diffusion process, part of the effusion process or as an independent phenomenon. A discussion about inter-grain diffusion and its modeling can be found in [153].

Due to the low pressure ($< 1 \times 10^{-3}$ mbar) inside the target and ion source assembly, which is required for efficient operation of the ion source, the mean free path between particles of the effusing species is long compared to the structural dimensions of the setup. Thus, the probability of a collision between two diffusing particles is low and the flow regime is non-viscous. The diffusing particle undergoes numerous collisions with surfaces on its way to the ion source. On each encounter, it changes from a free state to an adsorbed state for a time predicted by the Frenkel equation [154, 155],

$$\tau_a = \tau_0 \, e^{\frac{-\Delta H_{ads}}{RT}}, \tag{2.9}$$

where τ_0 is the period of oscillation perpendicular to the surface and ΔH_{ads} the adsorption enthalpy which is assumed to equal the negative desorption enthalpy. As the diffusion coefficient, the sticking time per encounter (or sojourn time) τ_a depends exponentially on the temperature. The enthalpy of adsorption is related to the macroscopic quantity of sublimation enthalpy that is a measure for the strength of interaction between the atoms in the bulk material lattice and the volatility of the compound. Both quantities are compiled in fig. 2.5. The maxima are found near elements with maximum number of free valences [156]. As will be discussed in Chapters 3, 4 and 6, the adsorption behavior determines if an element can be extracted from an ISOL target.

The number of wall encounters a particle suffers on its way to the ion source can be obtained by simulation codes for molecular flow. Typical numbers have been obtained in [153] and reach from 1×10^3 to 1×10^8, depending on target material and geometry.

2.2.4 Release from an ISOL target

The fraction of isotopes which decay in the target material before their release is expressed in the release efficiency. While release from an ISOL target has been discussed

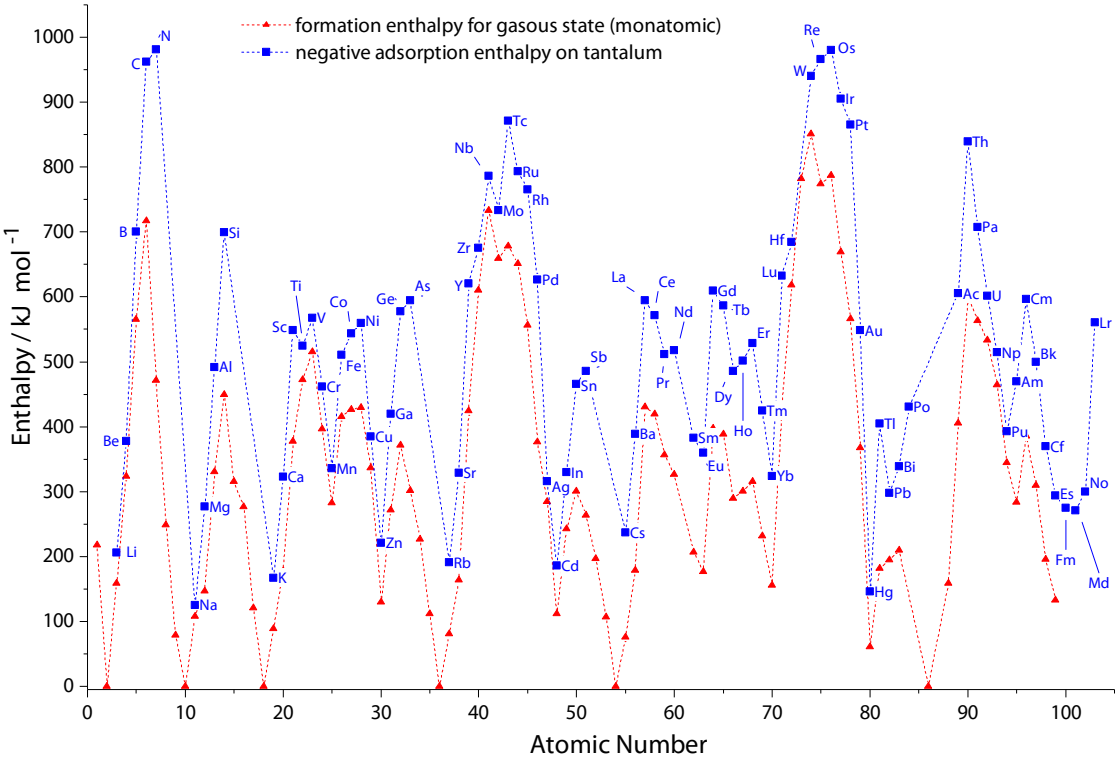

Figure 2.5: Enthalpy of formation of the the gasous monatomic elements, which equals their sublimation enthalpy [156], in comparison to the adsorption enthalpy on tantalum calulated with the Eichler-Miedema model [157]. The trends are a measure for the volatility of the elements. Values taken from [81, 158–160]. The formation enthalpy of nobles gases equals zero by definition. Connecting lines serve to guide the eye only.

already in the 1960s [161], Kirchner proposed expressions for release efficiencies of foil targets [162] considering diffusion and effusion.

Kirchner release model

Each isotope that has been produced in the target material follows its individual trajectory to the ion source with the associated release time t. The distribution function of these release times for a stable isotope is given by the delay function $p(t)$ which is normalized to unity. Folding the delay function with a factor accounting for decay, yields the release efficiency ϵ_{rel} as fraction of radioisotopes with decay constant λ that have reached the ion source before their decay.

$$\epsilon_{\mathrm{rel}} = \int_0^\infty p(t)\, \mathrm{e}^{-\lambda t} \mathrm{d}t. \tag{2.10}$$

The delay function for diffusion can be obtained from Eq. 2.7. If effusion is fast compared to diffusion (diffusion controlled regime), the release efficiency of an isotope with half-life $t_{1/2}$ from foils of thickness d_{foil} is given by

$$\mathcal{E}_{\mathrm{rel}}^{\mathrm{dif}} \approx 0.76\sqrt{\mu_0\, t_{1/2}}, \text{ with } \mu_0 = \frac{\pi^2 D}{{d_{\mathrm{foil}}}^2}, \tag{2.11}$$

which holds for $\mu_0 t_{1/2} \lesssim 0.3$.

If the radioisotope undergoes strong interactions with the target material or structural materials ($-\Delta H_{\text{ads}} \gtrsim 350\,\text{kJ}\,\text{mol}^{-1}$), effusion needs to be considered as major contribution to the release efficiency. The delay time of effusion through an orifice $p_\nu(t)$ is given by

$$p_\nu(t) = \nu_0\, \text{e}^{\nu_0 t}, \text{ with } {\nu_0}^{-1} = \chi\,(\tau_\text{a} + \tau_\text{f})\,, \tag{2.12}$$

where χ is the number of collisions, τ_a the mean sojourn time on each wall collision and τ_f the mean time of flight between two collisions.[3] If only effusion is considered, the fraction of isotopes remaining in the target structure is obtained as $f_\text{rem} = \text{e}^{-\nu_0 t}$ and the release efficiency of effusion computes to

$$\mathcal{E}^\text{ef}_\text{rel} = \frac{\nu_0}{\nu_0 + \lambda} \approx 1.44 \nu_0 t_{1/2} \text{ for } \nu_0 t_{1/2} \lesssim 0.2. \tag{2.13}$$

In the combined case of effusion and diffusion, the overall release efficiency is obtained as product of diffusion and effusion contribution $\epsilon_\text{rel} = \mathcal{E}^\text{dif}_\text{rel}\ \mathcal{E}^\text{ef}_\text{rel}$. Since the effusion follows the diffusion, the delay function for the combined case can be obtain by convolution as

$$p(t) = \int_{t'=0}^{t} p_\mu(t')\ p_\nu(t - t')\ \text{d}t'. \tag{2.14}$$

Fit functions by Lukic *et al.* and Lettry *et al.*

The model proposed by Kirchner allows to deduce diffusion coefficients, if sufficient information about the target material structure is known. However, often more simple functions are required for extrapolation of the half-live dependence of release fractions. The latter is of importance for the extrapolation of measured yield data to more exotic isotopes.

Lukic *et al.* proposed an expression for the release fraction with two parameters. For short half-lives, the release efficiency is expected to follow a power-law expression of type $\epsilon_\text{rel} \propto {t_{1/2}}^\alpha$. The value of α indicates the type of interaction. For pure diffusion from foils $\alpha = 1/2$ is expected (Eq. 2.11). In the effusion limited case $\alpha = 1$ (Eq. 2.13), and in the combination of both $\alpha = 3/2$. At longer half-lives, a plateau in a double logarithmic plot of release efficiency versus half-live is found. The half-life at the transition between plateau and power-law (free fit parameter) is $t^0_{1/2}$ and the full expression proposed by Lukic *et al.* is

$$\epsilon_\text{rel} = \frac{1}{1 + \left(t_{1/2}(t^0_{1/2})\right)^{-\alpha}}. \tag{2.15}$$

After the ISOLDE facility moved from the SC to the PSB, the driver beam was no longer continuous but pulsed. The pulse structure allows to directly measure the delay function $p(t)$. The so called release-curves are typically fitted with a three-exponential function as proposed by Lettry *et al.* [163].

$$p(t) = N\left(1 - \text{e}^{-\lambda_r t}\right)\left[\alpha_l \text{e}^{-\lambda_f t} + (1 - \alpha_l)\text{e}^{-\lambda_s t}\right] \tag{2.16}$$

The function contains three time constants which account for one rise component (λ_r) and two decay components (λ_s and λ_f) which are weighed by parameter α_l. The normalization factor N is chosen such that $\int_{t=0}^{\infty} p(t)\text{d}t = 1$.

[3] In refs. [118,142], a second effusion time constant was introduced and validated with experimental data. The second parameter considers not only diffusion through an orifice but through a transfer line.

2.3 Ionization

A general overview about ion sources for radioactive beam extraction was already given in section 1.2.3. This section will give further detail about plasma phenomena and electron impact ionization. To goal of this section is to give phenomenological descriptions and most equations will be presented without their derivation.

2.3.1 Plasma phenomena

Many characteristics of ion sources can be explained by plasma physics. This includes the maximum ion current of the source, the maximum electron flux of a cathode and also the energy of electrons, *i.e.*, their temperature. Thus, in this section, a very brief description of plasma phenomena is given, listing the key parameters. Concise information about plasma physics in the context of ion sources can be found in [76,164,165] and a more general discussion, *e.g.*, in [166]. Properties of RF-plasma are discussed in [167] and helicon plasma in [168–170]. The following summary is based on these texts.

Plasma is considered as the fourth state of matter, besides the solid, liquid and gaseous state. A plasma is characterized by the presence of charged species which interact via electric (or magnetic) forces in a collective manner. The charged particles are typically ions of varying charge state and electrons. In addition, neutrals (atoms, molecules, radicals) can be present in a plasma. According to the principle of charge neutrality of a classical plasma, negative and positive charges cancel each other (almost) out over a certain range, so that the bulk plasma appears neutral. However, deviations from quasi-neutrality appear locally (*e.g.* in the plasma sheath). In so-called non-neutral plasma (*e.g.* electrons or ions in traps), the trap potential ensures confinement and has the role of the missing counter charges.

Debye length and shielding

One of the collective phenomena of a plasma is its capability to shield electric fields. If an additional charge is placed inside a plasma, the trajectories of electrons and ions adapt to the charge. Assuming the charge is positive, electrons are attracted and ions[4] are repelled. The capability of the plasma to adapt to the charge depends on its electron and ion temperature T_e which defines the stiffness of the electron and ion trajectories. Thus, the screening is less efficient at higher energies. Quantitatively, the length of shielding is described by the Debye length λ_D. It can be derived with the help of the Poisson equation which relates the electric potential Φ to the distribution of charge density (space charge) ρ_{ie} via its 2nd derivative as

$$\Delta\Phi = \frac{\rho_{ie}}{\epsilon_0}. \tag{2.17}$$

The combined Debye length of electrons and ions is given by

$$\frac{1}{{\lambda_D}^2} = \frac{e^2\, n_e}{\epsilon_0\, \mathrm{k_B} T_e} + \frac{e^2\, n_i}{\epsilon_0\, \mathrm{k_B} T_i}, \tag{2.18}$$

[4] For the sake of simplicity, 'ion' in this section, refers to a singly charged positive ion.

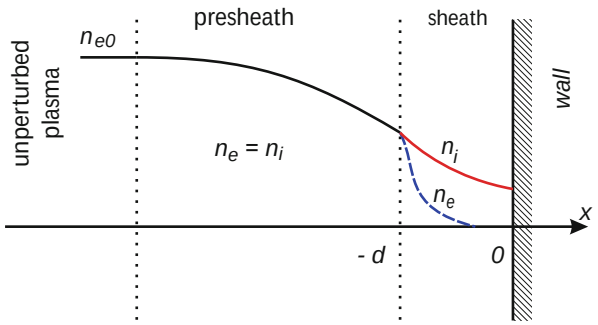

Figure 2.6: Electron and ion densities in the plasma sheath. In the unperturbed plasma, electron and ion densities are equal $n_{e0} = n_{i0}$. In the sheath, the neutrality of the plasma is violated. See text for details. Adapted from [166].

where T_e and T_i are the electron and ion temperatures and n_e and n_i their respective densities. The Debye length in comparison to geometrical dimensions can be interpreted as condition for plasma formation. Since the quasi-neutrality can be violated within the Debye length, the physical dimension of a plasma must be at least several Debye lengths.

The plasma sheath and the Child-Langmuir law

In the following, some aspects of the boundary between the unperturbed plasma bulk and a confining wall are discussed. In fig. 2.6, the densities of electrons n_e and ions n_i in the boundary region are illustrated . In the bulk of the plasma, the charge neutrality condition is fulfilled, *i.e.* $n_e = n_i$. However, electrons leave the plasma bulk at the boundary faster as ions, due to their higher velocity. The negative charge accumulates at an isolated (floating) wall and limits further electron loss. Taking the wall as reference for the potential, the plasma bulk gains a positive potential. The region between the wall and the region of charge-neutrality is called plasma sheath. The boundary between the latter is referred to as sheath edge ($x = -d \approx -\lambda_D$ in fig. 2.6). The transition region of an unperturbed plasma and the plasma sheath is called presheath.

The Child-Langmuir law was originally introduced for space-charge limited electron currents in a vacuum diode. It can be derived as steady-state condition for ion flow to a wall, which is negatively biased by an external voltage. The ion current density j_i is given by

$$j_i = \frac{4}{9}\epsilon_0 \sqrt{\frac{2e}{m_i}} \frac{U^{3/2}}{d^2}, \tag{2.19}$$

where the potential difference $U = \Phi(-d) - \Phi(0)$ and m_i is the ion mass. To estimate the real current flow through the sheath, also the Bohm current (discussed later in this section) needs to be considered. Furthermore, the application of an external voltage affects the width of the sheath.

The space charge-limitation is a key parameter in the design of ion sources and illustrated in fig. 2.7. An electron current of density j_e is emitted from a cathode thermionically ($x = 0$, $\Phi(0) = 0$) and accelerated towards an anode at $x = -d$ biased at $\Phi(-d) = U$. If the emitted current exceeds the Child-Langmuir limit, an electron cloud builds up

near the cathode which forms a negative potential well. The behavior is referred to as virtual cathode formation, since the jammed electrons act as cathode.

If the charge transport through a gap is not continuous, but pulsed in a way that the pulse length τ_p is short compared to its transit time through the gap t_v, equation 2.19 needs to be adjusted. In [171] expressions have been derived to estimate the maximum current j_{crit} that can be transported without virtual cathode formation. Within the equivalent diode approximation,

$$j_{\mathrm{crit}} = 2\frac{1-\sqrt{1-3/4{X_{\mathrm{cl}}}^2}}{{X_{\mathrm{cl}}}^3} j_{e,cl}, \text{ with } X_{\mathrm{cl}} = \frac{2\tau_p}{3t_v}. \tag{2.20}$$

Expressions have been derived in [172] that take into account a two-dimensional shape of an electron emitter. For a circular emission surface of radius R, the Child Langmuir-limited current is given by

$$j_{2d} = j_{e,cl}\left(1+\frac{d}{4R}\right). \tag{2.21}$$

The Bohm criterion

The Bohm criterion defines the speed of ions at the sheath edge. The criterion has to be met for the formation of a stationary sheath. From the perspective of the plasma, the ion speed u_0 required to penetrate into the sheath must be equal to or greater than the Bohm velocity v_B, *i.e.*

$$u_0 \geq v_B = \sqrt{\frac{\mathrm{k_B}T_e}{m_i}}. \tag{2.22}$$

From the perspective of the presheath, further conditions to the velocity apply. The role of the quasi-neutral presheath is to accelerate ions to gain sufficient energy to enter the sheath region. It can be shown that only ions below the Bohm speed are accelerated, so that the inequality of Eq. 2.22 resolves, and the ion speed at the sheath edge is given by the Bohm speed. The equation allows to estimate the ion flux through the sheath (the

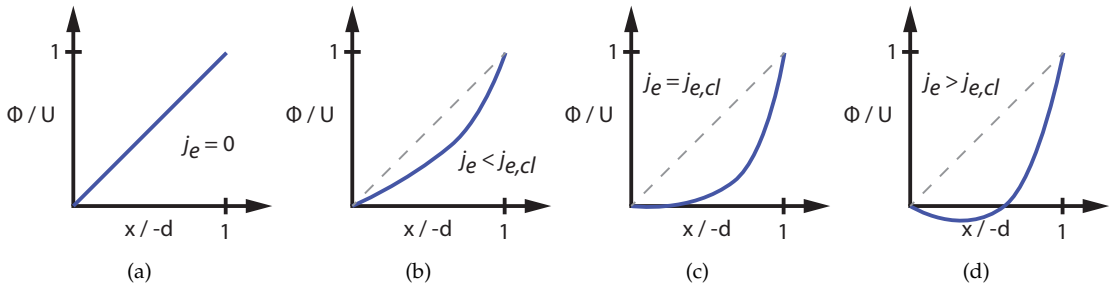

Figure 2.7: Potential distribution for different electron current densities j_e emitted from a cathode at $x = 0$ and accelerated towards an anode at position $x = -d$ and voltage U in different current regimes: (a) without electron flow, (b) below Child-Langmuir limit, (c) at Child-Langmuir limit and (d) virtual cathode formation beyond the Child-Langmuir limited current $j_{e,cl}$.

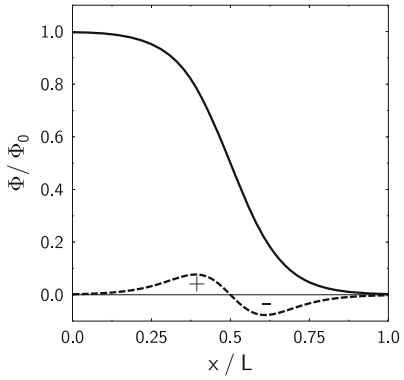

Figure 2.8: Space charge and potential in a double layer. Reproduced from [166].

Bohm current) as

$$j_B = en_e(-d)v_B = en_{e0}\exp\left(\frac{e\Phi(-d)}{k_B T_e}\right)v_B \approx n_{e0}\,e^{1/2}\,v_B \approx 0.61e\,n_{e0}\sqrt{\frac{k_B T_e}{m_i}}. \qquad (2.23)$$

The comparison of a non-space charge limited current from a plasma ion source with Eq 2.23 allows to estimate the electron density of a plasma, if the temperature can be estimated. The equation holds a for collisionless ionization-free plasma.

Double layers

A double layer consists of an accumulation of positive and negative charges residing next to each other. It can form, *e.g.*, near the electron-emitting cathode of an ion source. If the electron emission is space charge limited, an electron cloud forms near the cathode. Accelerated electrons produce positive ions in collisions with neutrals. The ions are attracted by the negative potential in front of the cathode and form a double layer. Space charge and potential follow the Poisson equation (Eq. 2.17) as illustrated in fig. 2.8. The ratio of electron and ion currents penetrating a strong ($\Phi_{max} \gg k_B T_e/e$) double layer is given by the Langmuir criterion for a strong double layer as

$$\frac{j_e}{j_i} = \sqrt{\frac{m_i}{m_e}}. \qquad (2.24)$$

In predecessors of the FEBIAD ion sources, *i.e.*, before the introduction of a grid, the electron current emitted from the cathode was given by Eq. 2.24. As can be seen from the equation, a flow of ions to the cathode is necessary to allow electrons emitted from the cathode to penetrate the double layer (bipolar flow). After introduction of the grid, the distance between cathode and anode was significantly shortened, and the electron flux from the cathode is described by Eq. 2.19 [89].

Coupling of RF plasmas

In RF plasma ion sources, energy is transferred from RF fields to the electrons in the plasma. Three different coupling mechanisms have been identified: i) capacitive coupling, ii) inductive coupling and iii) coupling by waves, *e.g.*, helicon or ECR. The type

of coupling has an impact on plasma parameters (*e.g.*, density and temperature) and depends on the design of the setup (especially antenna geometry) but also on operating conditions, like gas pressure and RF power.

Capacitively Coupled Plasma (CCP) and Inductively Coupled Plasma (ICP) are illustrated in fig. 2.9. A CCP forms by applying an RF voltage (typically in the range 10 MHz to 500 MHz) to two parallel plates placed in a gas-filled (1×10^{-1} mbar to 1×10^{-4} mbar) chamber. Typically, the time required for ions to react is long compared to the oscillation of an RF field. However, electrons do react, and adapt to the RF field. With the electrons, the sheath adapts and forms the oscillating RF sheath. However, the sum of the sheath lengths at opposite plasma boundaries is constant. The sheath size s_m scales with the voltage V_0 across the plasma, the gas pressure and strongly with the RF frequency ω_{RF}.

$$s_m \propto \left(\frac{V_0}{p{\omega_{\mathrm{RF}}}^4} \right)^{1/5} \tag{2.25}$$

The capacitive coupling deposits energy mostly within the RF sheath by electron heating and ion acceleration towards the electrodes but also in the inertia of electrons in the plasma bulk. The plasma density that defines the maximum ion flux (*cf.* Eq. 2.23) scales with RF power and so does the voltage across the plasma. At a given plasma density, the sheath voltage can be reduced by increasing the driver frequency ω_{RF}. The plasma potential of CCP is relatively high compared to ICP, which leads to beam impurities by sputtering on the walls.[5] Thus, CCP is not commonly used for ion sources.

With inductive coupling, higher plasma densities can be achieved and the coupling is more efficient. The working principle is similar to that of a transformer (fig. 2.9b). An antenna (coil) is placed close to a plasma and supplied with an RF current. A current is induced in the plasma representing the secondary coil of the transformer. An electromagnetic wave emitted from an antenna weakens exponentially during penetration into a conductor. Thus, its range is limited to the skin of the conductor. However, the skin depth (typically a few centimeters) is wider than the plasma sheath, so that energy deposition in ICP reaches further into the plasma bulk than in CCP.

The coupling by helicon waves extends even deeper into the plasma. In magnetized plasma, low-frequency electro-magnetic waves can propagate through the plasma. Helicon waves propagate axially to the applied magnetic field and efficiently couple their energy into the electrons of the plasma bulk.

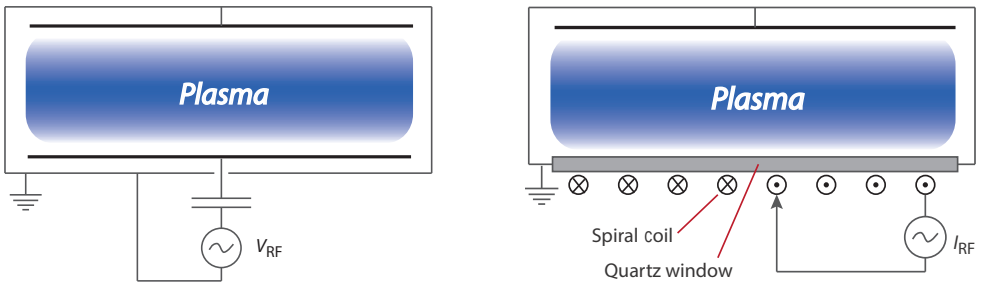

(a) capacitively coupled plasma (b) inductively coupled plasma

Figure 2.9: Schematics of capacitive and inductive plasma coupling. Adapted from [166, 167].

[5] Electrons in the high-energy tail of an ECR plasma can also lead to unwanted contamination.

The energy coupling mechanisms are also named E-mode for capacitive coupling, H-mode for magnetic coupling and W-mode for helicon coupling. An ion source designed for the H mode, will first ignite in E-mode. The antenna does not only couple inductively but also capacitively. The transition from E-mode to H-mode requires a certain plasma conductivity, so that (in the transformer model) a current can be injected into the plasma. The mode transition typically appears by increasing the RF power. The mode change can be seen by jumps in plasma parameters, like density and luminosity. Similar considerations hold for W-transitions, which also require a certain plasma density. Helicon sources are subject to E-H-W transitions.

2.3.2 Ionization efficiency of FEBIAD ion sources

To date, the models available for FEBIAD ion sources do not yet provide a full description of the ion source. Particularly, a model adjusted to the requirements of molecular beams has not yet been proposed. Often, the most-simple case of a chemically inert noble gas is considered.

A first FEBIAD model was provided by its inventors Kirchner and Roeckl. Based on the electron current measured on the outlet plate (5% to 70% of the extracted electrons), they concluded that despite the high primary electron current, the high ionization efficiency cannot exclusively be explained by electron impact ionization [89]. The measured efficiency exceeded values expected by electron impact ionization by more than an order of magnitude. As discussed in [173,174], also other effects, like instabilities below a threshold pressure, contributed to their classification as arc-plasma source. Based on a model for electron beam generated plasmas [175], the ion current was claimed to follow the propagation through a single sheath, similar to the Bohm current (Eq. 2.23)

$$j_i \approx 0.4 e n_{\mathrm{ed}} \sqrt{\frac{2 \mathrm{k_B} T_e}{m_i}}, \tag{2.26}$$

where n_{ed} is the electron density on the discharge axis.

In the work by Penescu [176], a global model for the ionization efficiency based on operation parameters was set up. It was pointed out that the FEBIAD plasma is controlled by the electron beam produced by cathode emission. The Debye shielding length (Eq. 2.18) is dominated by electrons and it computes to $\lambda_D \approx 2\,\mathrm{mm}$ at a typical cathode temperature of 2000 °C. It was estimated that a distance of $3.5\lambda_D$ is required to shield the applied anode potential (ca. 150 V) due to the low ion energy which is assumed to be equal to the ion source temperature. Thus, in a typical FEBIAD ion source of ca. 6 mm radius, the potential is not fully shielded. The proposed model is based on the assumption that ions are not confined in a plasma and follow the the potential distribution in the source. The ionization efficiency ϵ_{feb} is given by the ionization rate per unit volume R_{ioniz}, the ionization volume V_{source}, the rate of neutrals admitted to the source n_{in} and a factor f accounting for the fraction of extracted ions and second order effects.

$$\epsilon_{\mathrm{feb}} = \frac{R_{\mathrm{ioniz}} V_{\mathrm{source}}}{n_{\mathrm{in}}} f, \text{ where } R_{\mathrm{ioniz}} = N_{\mathrm{n}}\, N_{\mathrm{e}}\, \sigma_{\mathrm{ion}}(v_e)\, v_e \tag{2.27}$$

The rate of ionization is calculated under assumption of a neutral gas inside the source with density N_{n} and electron density N_{e} as extracted from the cathode. The relative

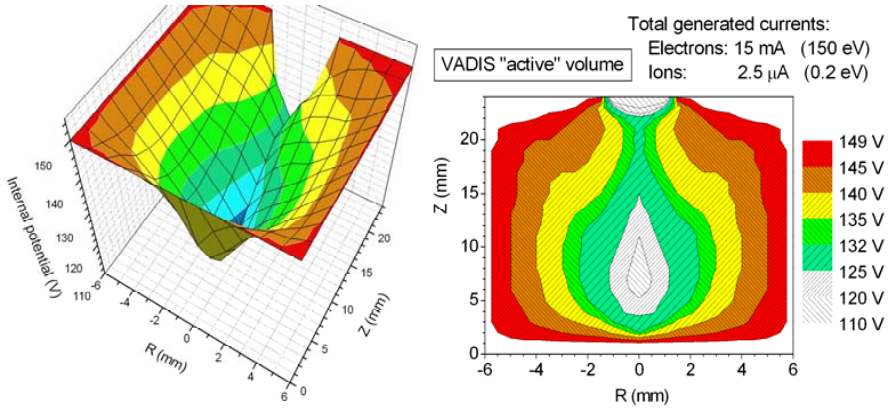

Figure 2.10: Potential distribution inside the VADIS source. Reprocuded from [176].

speed of ions and electrons is approximated with the electron velocity v_e on which also the ionization cross section σ_{ion} depends.

Due to the space charge of the electron beam, the potential in the center of the anode body is depressed. The field imposed by the extraction electrode penetrates only to a certain extent into the source so that a field distribution as shown in fig. 2.10 develops. Only ions produced in certain regions (the active volume) can be extracted. The ratio of active volume to total ionization volume V_{source} builds the foundation for the interpretation of the extraction factor f.

Due to the complex mixture of processes in the ion source, the factor f depends not only on physical and chemical properties of the desired isotope and the structural materials of the ion source but also on operational parameters like temperature, gas composition and pressure, anode voltage and the applied magnetic field. The model was verified for noble gases in a wide range of operational conditions.

Recently, further insights into the FEBIAD ion source could be gained by extensive Particle-in-Cell simulations by Martinez Palenzuela *et al.* [94, 95] and Milan *et al.* [177]. The magnetic field could be shown to generate unique electrical field maps, depending on the magnetic field strength but also on ion population and electron energy. An experimentally observed oscillation of the ion current while varying the magnetic field strength could be reproduced in simulations.

2.4 Experimental setups

2.4.1 The Offline separator

Two offline isotope separators are available at ISOLDE. The separators are used for beam development and quality control of target units prior to their installation on the GPS or HRS Frontends. The older device (Offline 1) was previously described, *e.g.*, in [176]. Offline 2 is a new installation currently undergoing commissioning [178]. Exposure of the setups to radioisotopes is typically avoided so that studies are limited to stable isotopes. In contrast to their online counterparts, the devices exhibit a higher level of flexibility regarding experimental installations and control software. Within this

work, only the Offline 1 separator was used which is described below.

Figure 2.11 provides an overview of the beam extraction part of the separator. The ions generated in the source of the target unit are extracted by a puller electrode that is held at a mechanically adjustable distance from the ion source. The ion beam passes a set of electrostatic steering elements which allow realigning. The Einzel lens focuses the beam before entering the separation magnet (60°). The total (non-separated) beam current can be obtained from a Faraday cup placed between Einzel lens and magnet. After separation by mass-to-charge ratio, the beam arrives in a diagnostic box which is equipped with a Faraday cup and a horizontal scanner. Additionally, other detectors like MagneToF or MicroChannel Plate detector (MCP) can be installed for low intensity beams or single-ion-counting. The transmission from the first to the second Faraday cup is typically in the order of 75%.

The setup is capable of separating masses of up to ca. 300 u at a beam energy of 30 keV. The composition of the residual gas in the vacuum system could be obtained from a Residual Gas Analyzer (RGA) that combines its own ion source, a Quadrupole Mass Analyzer (QMA), a Faraday cap and a Secondary Electron Multiplier (SEM) ion detector.

The frontend of the Offline separator is shown in fig. 2.12. For experiments discussed in Chapter 6 and Appendix A, the injection of vapors of volatile metal compounds was required. The setup was built of stainless steel tubing and chambers. The evaporation chamber is connected via a leak valve to a target injection line. A second leak valve allowed to regulate the flow rate of gases (typically noble gases, NF_3, SF_6, CF_4, CO or CO_2) into the common injection line. Via manually controlled 3-way-valves, the gas injection could be switched to a calibrated leak for efficiency measurements. The gas injection is limited by the pumping capabilities of the vacuum system. At the extraction side, the pressure (p_{extr}) is measured by Penning and Pirani gauges between the extraction electrode and the Einzel lens. Typically, a pressure of lower than 1×10^{-5} mbar is required to safely operate the high-voltage system and efficiently operate the ion source. The maximum for gas injection is in the order of 1×10^{-4} mbar L s^{-1}.

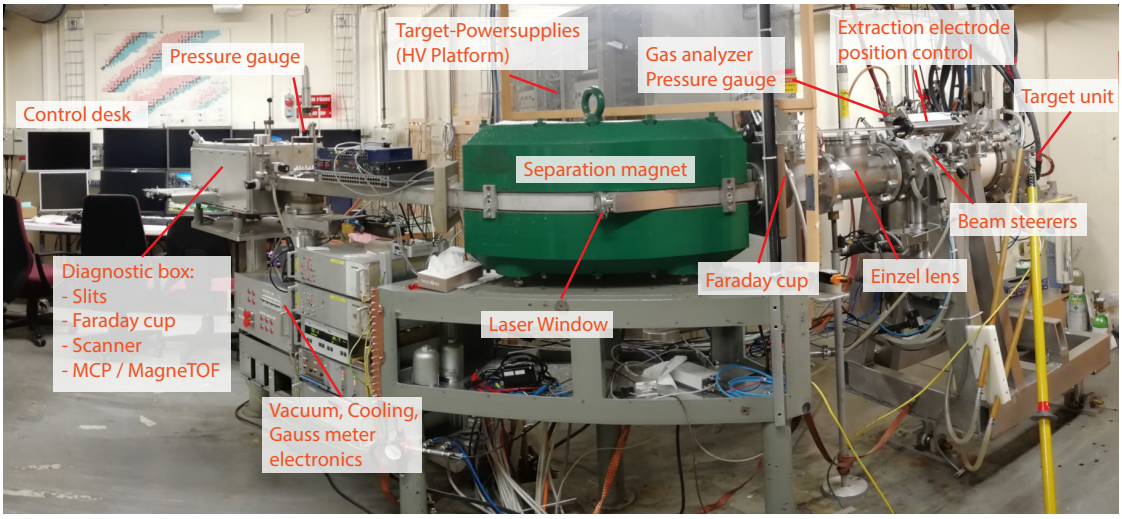

Figure 2.11: The ISOLDE offline separator - Beam extraction

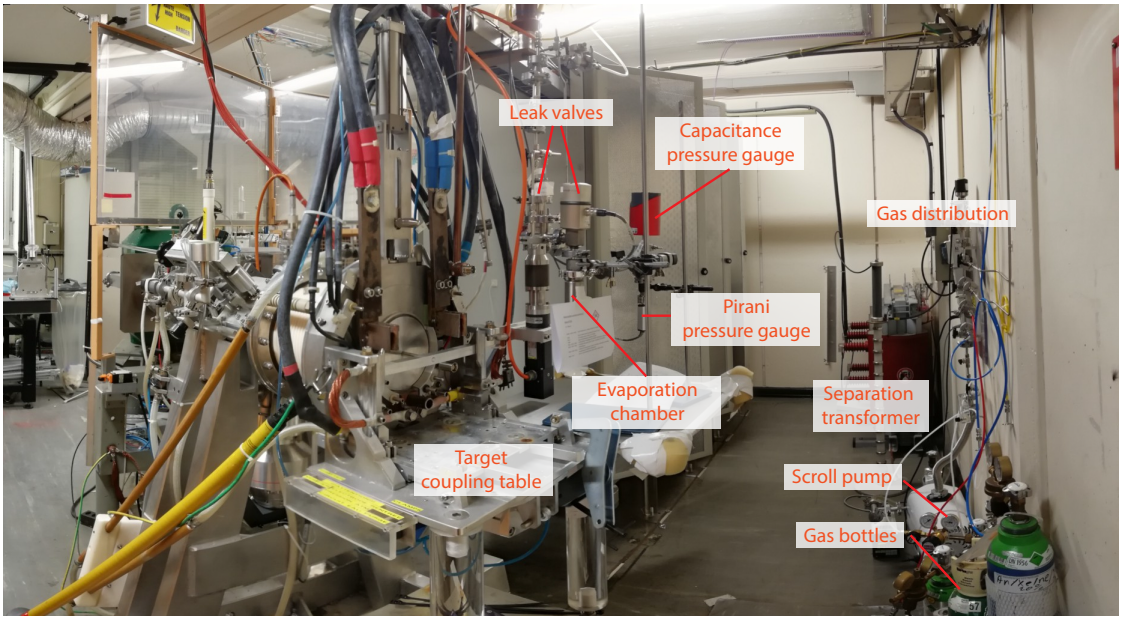

Figure 2.12: The ISOLDE offline separator - Evaporation setup

2.4.2 The ISOLDE tape station

The ISOLDE tape station is located downstream the junction point of GPS and HRS beamlines. It is used as reference device to measure radioactive ion beam yields and the delay function $p(t)$. A brief description is provided in [54] and the process of yield measurements is also outlined in Chapter 3. The tape station was recently replaced by a new model [25] which is yet to be commissioned.

A sketch of the tape station is shown in fig. 2.13. With the help of a an electrostatic element, the radioactive ion beam can be deflected towards the tape. After collection of activity on the aluminized Mylar tape for a period of t_c, the tape is transported within $t_t = 0.9\,\mathrm{s}$ to the measurement position where the activity is measured for a duration of t_m. The start of each collection and measurement cycle can be synchronized to an arriving proton pulse. The delay between proton pulse and start of the collection can also be set (t_d). An upstream deflector (so-called beam gate) prevents the beam from reaching the tape station before t_d. The timing parameters (t_d, t_c and t_m) are controlled by software. They need to be adjusted such that a sufficient amount of activity can be registered but the response of the detector is still linear to the activity. At high counting rates ($> 20\,000\,\mathrm{s}^{-1}$), the scintillation detector approaches saturation. The delay function can be sampled by a series of measurements with small collection time and variation of the delay time.

Two detectors are available at the tape station. It is equipped with a plastic scintillator in 4π geometry for beta counting. In addition, a High Purity Germanium detector (HPGe) allows to disentangle mixtures of radioisotopes by gamma spectroscopy.

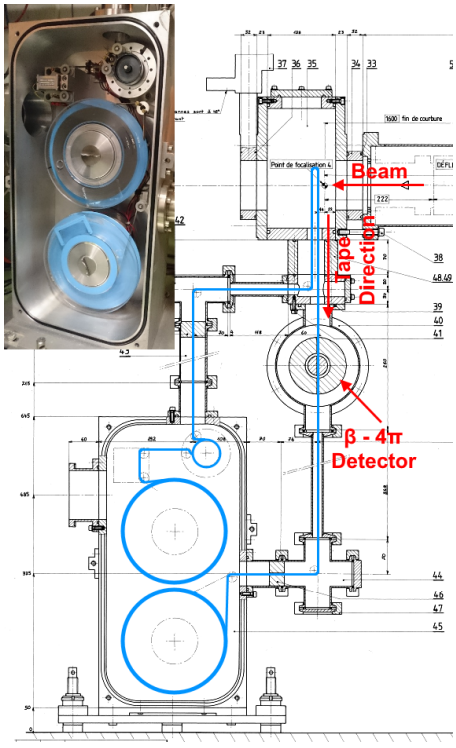

(a) ISOLDE Tape Station with tape represented in blue

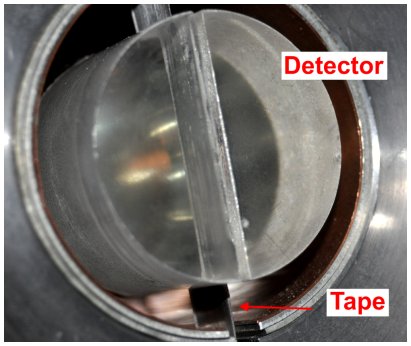

(b) ISOLDE Tape Station Beta detector

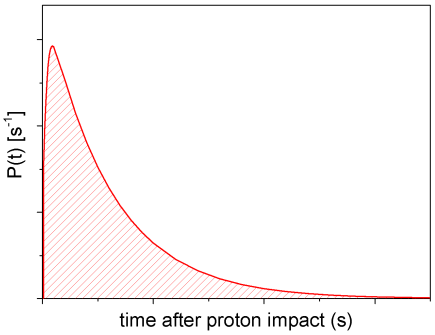

(c) Representation of the pulse shape of a radioactive ion beam after proton impact

Figure 2.13: The ISOLDE tape station and typical shape of the delay function $p(t)$. Reproduced from [74] by permission from J.P. Ramos.

3 The ISOLDE Yield database

Contents

The ISOLDE yield database provides information about available beam yields and is an important tool for experiment planning. Within this thesis, the application and database were completely re-developed and equipped with models and data to predict beam intensities of isotopes which could not yet be measured. The included yields demonstrate the strength of the ISOL-method, its limitations and the requirements for molecular beam developments.

3.1 Available beams at ISOLDE

At ISOLDE, more than 1000 isotopes of 74 different chemical elements are available. The variety of elements is often visualized in the ISOLDE chart of nuclides. The chart extends from the light element helium to elements in the vicinity of the target material. Nuclear reaction cross-sections define its theoretical upper boundary. With few exceptions, only isotopes lighter than the target material are produced. Since macroscopic quantities (typically at least tens of grams) of target material are required, the heaviest available target material is uranium. Within the range from the lightest to the heaviest elements, gaps in the spectrum of available elements appear. The gaps emerge due to the refractory character of certain elements.

Already early it was concluded that the formation of a volatile carrier molecule is required to extract elements with high adsorption enthalpies on the surfaces of the target and ion source assembly [179]. As discussed in sect. 2.2.3, the adsorption enthalpy correlates to the boiling points of the elements. An ISOLDE nuclide chart along with the melting and boiling point of the elements is shown in fig. 3.1. In some cases, refractory elements like boron [75, 180] or carbon [103] could be extracted as molecular beam, which are often referred to as (molecular) sidebands. As can be seen in fig. 3.1, the three biggest gaps in the nuclide chart correspond to the 4d (Zr to Pd) and 5d (Ta to Pt) transition metals and the early actinide series. Work within this thesis contributed to the successful extraction of boron (Chapter 4) and the proposal to a concept for the extraction of 4d and 5d refractory transition metals (Chapter 6).

The radioactive ion beam intensity Y at ISOLDE depends on the normalized production

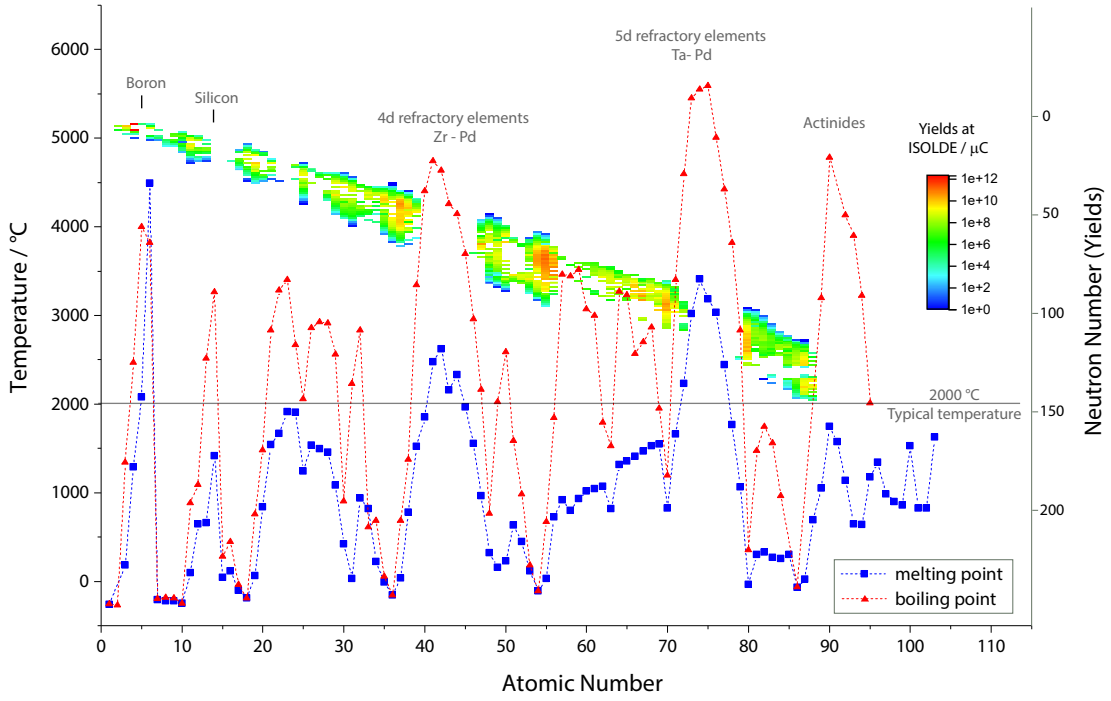

Figure 3.1: Boiling and melting point of the elements and available beams at ISOLDE as recorded in the yield database. Isotopic nuclides are shown along the vertical axis. Type of plot proposed by S. Rothe.

rate of the desired isotope in the target Y_0, the driver beam current I_{prim} and a set of efficiency parameters accounting for decay during release ϵ_{rel}, ionization ϵ_{ion} and further losses ϵ_{irr}, *e.g.* due to irreversible chemisorption. In the case of molecular beams, the chemical yield ϵ_{form} also needs to be considered.

$$Y = Y_0 \; I_{\text{prim}} \; \epsilon_{\text{rel}}(\lambda) \; \epsilon_{\text{ion}} \; \epsilon_{\text{form}} \; \epsilon_{\text{irr}} \tag{3.1}$$

The release efficiency depends on the time an isotope requires to propagate from the target material to the the ion source. The propagation time of a single isotope t is given by the sum of time required for diffusion in condensed state matter t_{diff}, the in-flight time of effusion t_{eff} and the time spent in the adsorbed state t_{ads}.

$$t = t_{\text{diff}} + t_{\text{ads}} + t_{\text{eff}} \tag{3.2}$$

Folding the normalized distribution function $p(t)$ of propagation times for a stable $(\lambda = 0)$ isotope with a factor accounting for decay, yields the release efficiency as

$$\epsilon_{\text{rel}} = \int_0^\infty p(t) \; \mathrm{e}^{-\lambda t} \mathrm{d}t. \tag{3.3}$$

It is typically assumed that only the release efficiency depends on the half-life of the radioisotope. This assumption allows to predict the yield of an isotope, if i) the delay function $p(t)$ and intensity Y_0 of a different isotope of the same element could be measured under same experimental conditions and if ii) its production yield could be determined in simulations. As discussed in the following publication, the functionality has been implemented in the ISOLDE yield database web application.

3.2 Contributions

Within this thesis, I have designed and implemented the new database, user-interfaces and application programming interface which led to a first operational release. Further development work includes contributions by A. Molander under my supervision, as outlined in [181]. A comprehensive set of simulations for in-target production was setup, conducted and analyzed by J.P. Ramos. The following article was written by myself and I was following through the peer-review process.

Contents lists available at ScienceDirect

Nuclear Inst. and Methods in Physics Research B

journal homepage: www.elsevier.com/locate/nimb

The upgraded ISOLDE yield database – A new tool to predict beam intensities

J. Ballof[a,b,*], J.P. Ramos[a,e], A. Molander[a,c,d], K. Johnston[a], S. Rothe[a], T. Stora[a], Ch.E. Düllmann[b,f,g]

[a] CERN, 1211 Geneva 23, Switzerland
[b] Johannes Gutenberg – Universität Mainz, Institut für Kernchemie, Fritz-Strassmann-Weg 2, 55128 Mainz, Germany
[c] University of Helsinki, FI-00014 Helsinki, Finland
[d] Helsinki Institute of Physics, P. O. Box 64, FI-00014 Helsinki, Finland
[e] KU Leuven, Instituut voor Kern- en Stralingsfysica, B-3001 Leuven, Belgium
[f] GSI Helmholtzzentrum für Schwerionenforschung, 64291 Darmstadt, Germany
[g] Helmholtz-Institut Mainz, 55099 Mainz, Germany

ARTICLE INFO

Keywords:
CERN
ISOLDE
Radioactive beams
Database
Yields
Yield prediction
Cross sections
FLUKA
ABRABLA
Release efficiency
Production Yield
In-target production

ABSTRACT

At the CERN-ISOLDE facility a variety of radioactive ion beams are available to users of the facility. The number of extractable isotopes estimated from yield database data exceeds 1000 and is still increasing. Due to high demand and scarcity of available beam time, precise experiment planning is required. The yield database stores information about radioactive beam yields and the combination of target material and ion source needed to extract a certain beam along with their respective operating conditions. It allows to investigate the feasibility of an experiment and the estimation of required beamtime. With the increasing demand for ever more exotic beams, needs arise to extend the functionality of the database and website not only to provide information about yields determined experimentally, but also to predict yields of isotopes, which can only be measured with sophisticated setups. For the prediction of yields, in-target production and information about release properties of target materials must be known. While the former were estimated in a simulation campaign using FLUKA and ABRABLA codes, the latter is available from measurement data as already stored in the database. We have compiled the information necessary to predict yields, and made available a yield prediction tool as web application. This currently undergoes extensive testing and will be available as powerful tool to the ISOLDE user community.

1. Introduction

The ISOLDE facility is one of the oldest experiments at CERN and has been continuously upgraded over the years [1]. Today, it offers online production, extraction and separation of more than 1000 radioisotopes of 74 different chemical elements from thick targets, which are typically made of pressed powders, metallic foils, or molten materials. Within the target and ion source unit, the target materials are enclosed in a tantalum container, and are coupled to a transfer line and ion source, which are also selected out of a variety of different types of sources and lines.

In earlier days, a comprehensive collection of yield data was available in the ISOLDE Users' guide compiled by H.-J. Kluge [2]. Later, an online yield database was developed to provide information about yields to users and technical teams [3–5]. It is now fully redesigned, upgraded using state-of-the-art technologies, extended in its functionality and new yield data were included. The database and web application [6] not only store experimental yield information, but also provide release properties, in-target production cross sections estimated by means of time consuming and computationally expensive Monte-Carlo simulations and algorithms to predict yields of isotopes which have not yet been measured.

2. Beam production at ISOLDE

The isotope extraction and beam production from thick targets is a multistage process. The radioisotopes are produced upon impact of the primary 1.4-GeV proton beam on a target material. The atoms then need to diffuse out of the target material and into the ion source, where they are ionized, extracted electrostatically and transported ion

* Corresponding author at:CERN, 1211 Geneva 23, Switzerland.
E-mail address: Jochen.Ballof@cern.ch (J. Ballof).

https://doi.org/10.1016/j.nimb.2019.05.044
Received 31 January 2019; Received in revised form 24 April 2019; Accepted 14 May 2019
Available online 24 May 2019
0168-583X/

optically to an electromagnetic dipole for separation by mass to charge ratio.

An efficiency is associated to each step of the process. The first factor contributing to the radioactive ion beam yield Y is the in-target production N_0. Efficiencies for beam transport to the focal plane of the magnet, ionization and chemical efficiency can be summarized in an overall efficiency parameter ϵ_f. The half-life dependent release efficiency ($\epsilon_{release}$) is governed by diffusion and effusion processes and takes into account the time passing between production and release. A more detailed discussion of efficiency parameters can be found e.g. in Ref. [7].

Each atom follows its individual path to reach the ion source, and the distribution function for the time needed to follow these trajectories is defined by the release density function $p(t)$ [8,9] The release efficiency of an isotope with decay constant λ is obtained by folding the release density function $p(t)$ with a factor to account for decay losses.

$$Y = N_0 \ \epsilon_{release} \ \epsilon_f, \text{ where } \ \epsilon_{release} = \int_0^\infty p(t) e^{-\lambda t} \, dt \tag{1}$$

The release density function is normalized such, that $\int_0^\infty p(t)\,dt = 1$. The efficiency parameter ϵ_f and the distribution function $p(t)$, which describes the release of a stable nuclide, depend on the chemical element, operating conditions and typically only to negligible extend on the isotope. Hence, it is only required to experimentally determine the parameters ϵ_f and $p(t)$ once for each chemical element in a defined target and ion source system at given operating conditions. Knowing the two parameters and the in-target production rates of isotopes, allows to predict yields for the full isotopic chain (cf. Eq. (1)). The isotope for the measurement of $p(t)$ must be chosen such, that the tail of the experimentally obtained radioactive release curve $p_\lambda(t) = p(t)\,e^{-\lambda t}$ is not governed by radioactive decay.

From elementary diffusion and effusion processes, expressions for the delay function $p(t)$ have been obtained, e.g. by Kirchner et al. [8]. However, these expressions depend on numerous parameters, such as target material properties, target geometry and operation conditions. In addition, the expressions are often difficult to fit to experimental data. For practical purposes, the experimental data is often fitted to the three exponential function given in Eq. (2)[11], where A_L is a normalization parameter, t_{rise}, t_{fall1} and t_{fall2} are time constants describing the curve shape, and α is a weighting coefficient.

$$p(t) = \frac{1}{A_L}(1 - e^{-t \ln(2)/t_{rise}}) \cdot (\alpha \, e^{-t \ln(2)/t_{fall1}} + (1 - \alpha) e^{-t \ln(2)/t_{fall2}}) \tag{2}$$

A typical release curve of stable neon is shown in Fig. 1, along with calculated release efficiencies for short-lived radioisotopes. At the time of writing, release curves for 427 yield entries are available in the yield database.

A common procedure to assess a yield, is based on the measurement of a release curve, as shown in Fig. 1. ISOLDE is supplied with protons from the proton synchrotron booster (PSB), which arrive as narrow pulses of only a few microseconds length and typically contain up to 3×10^{13} protons. The proton pulse impinges on the target at $t = 0$. After a certain delay time $t = t_{delay}$, electrostatic deflectors allow the radioactive beam emitted from the ion source to pass downstream the beamline and to the tape of the tape station, in which it is implanted for a defined collection time $t_{collect}$. After the end of the collection ($t = t_{delay} + t_{collect}$), the radioactive ion beam transport is prevented by electrostatic deflectors, and the tape is forwarded to move the collected activity to the measurement position, where it is counted by calibrated detectors. Taking into account the decay during tape transport, the number of ions per second extracted at $t = t_{delay} + 0.5\,t_{collect}$ is obtained. Repeating the procedure whilst varying the delay time t_{delay} allows to sample a full release curve of the radioactive beam. The yield in the focal center of the separation magnet is obtained by integration of the non-normalized release curve, and correcting for losses by beam transport from magnet to tape station. Beam losses are estimated by measurement of stable beam with Faraday Cups placed along the beamlines. The procedure is

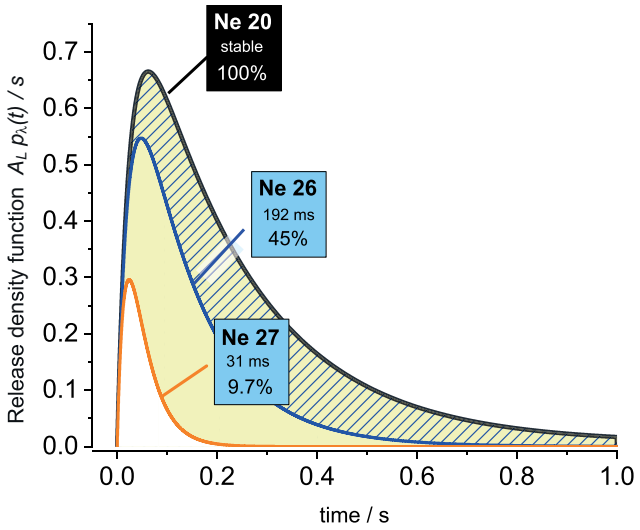

Fig. 1. Typical non-normalized release curves $A_L\,p(t)$ of stable neon, and release curves $A_L\,p_\lambda(t) = A_L\,p(t)\,e^{-\lambda t}$ of radioactive isotopes. The release efficiencies are given in percent and have been calculated according to Eq. (1). Parameters t_{rise}, t_{fall1}, t_{fall2} and α (cf. Eq. (2)) taken from Ref. [10]. The normalization parameter A_L has to be chosen such, that $\int_0^\infty p(t)\,dt$ computes to unity.

summarized in Ref. [3], and more detail about pulse shapes, yield calculation and efficiencies is given in Lit. [26].

3. In-target production

The in-target production rates N_0 of all common target materials were assessed by means of an extensive simulation campaign. High statistics of up to 1×10^9 primary particles are needed to achieve reliable production rates also for exotic nuclides. Two simulation codes have been used to investigate the production rates. The ABRABLA code [12] is commonly used at ISOLDE and was already used and benchmarked for 600 MeV and 1.0 GeV proton beam [13]. Per each simulation run, the code yields radionuclide production cross sections at a defined driver beam energy and target nuclide, and is therefore ideally suited for simple geometries and a beam directly impinging on the target, where secondary reactions do not contribute significantly. The cross section estimates are obtained at the initial energy of the proton beam, not taking into account energy losses in the target. The particle transport code FLUKA [14,15] allows the definition of complex geometries and calculates multiple particle interactions with matter using various integrated physics models. The definition of a geometry has especially proven useful for target units equipped with a neutron spallation source, the so called proton-to-neutron converter [16,17].

The codes were used to simulate isotope production with common and prospective target materials at proton beam energies of 0.6, 1.0, 1.4 and 2.0 GeV, to take into account historic driver beam energies delivered by the Synchrocyclotron (SC) along with the early, present and future beam energies of the Proton Synchrotron Booster (PSB), which supplies ISOLDE [18]. Besides the prediction of exotic nuclide yields, the simulation data allows the estimation of release efficiencies if experimental yields of several isotopes of the same chemical element are available. Thus, it gives insight into release properties of targets and ion sources used for the past 60 years at ISOLDE. The data enabled us to conduct a systematic study of isotope production at the planned upgraded driver beam energy of 2.0 GeV, for beams delivered after the upgrade.

4. Technical implementation

All software components have been developed compatible to the CERN centrally provided IT infrastructure services to ensure reliability

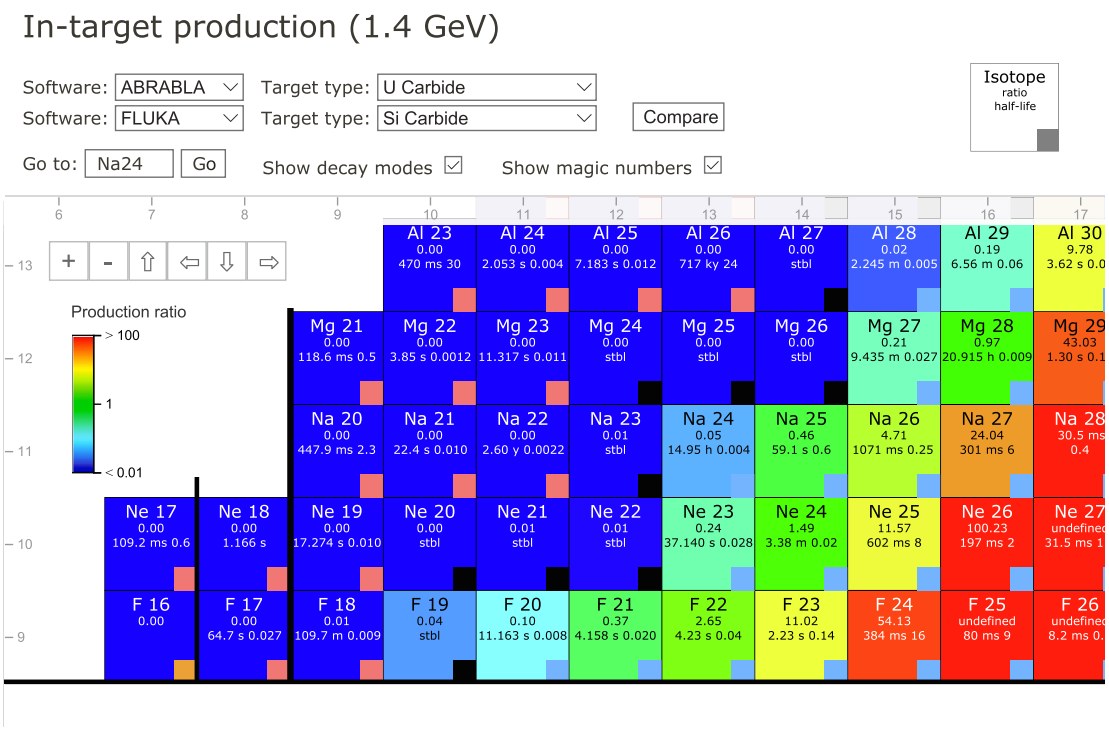

Fig. 2. Cut-out of the interactive nuclide chart, which is used in the web application to visualize in-target production and radioactive beam yields. The example is meant to demonstrate the capabilities of the software and shows the relative in-target production rates of two different target materials estimated by simulations using two different codes. The background color represents the production ratio, and the inset rectangle the decay mode of the isotope. In addition, half-life information is given.

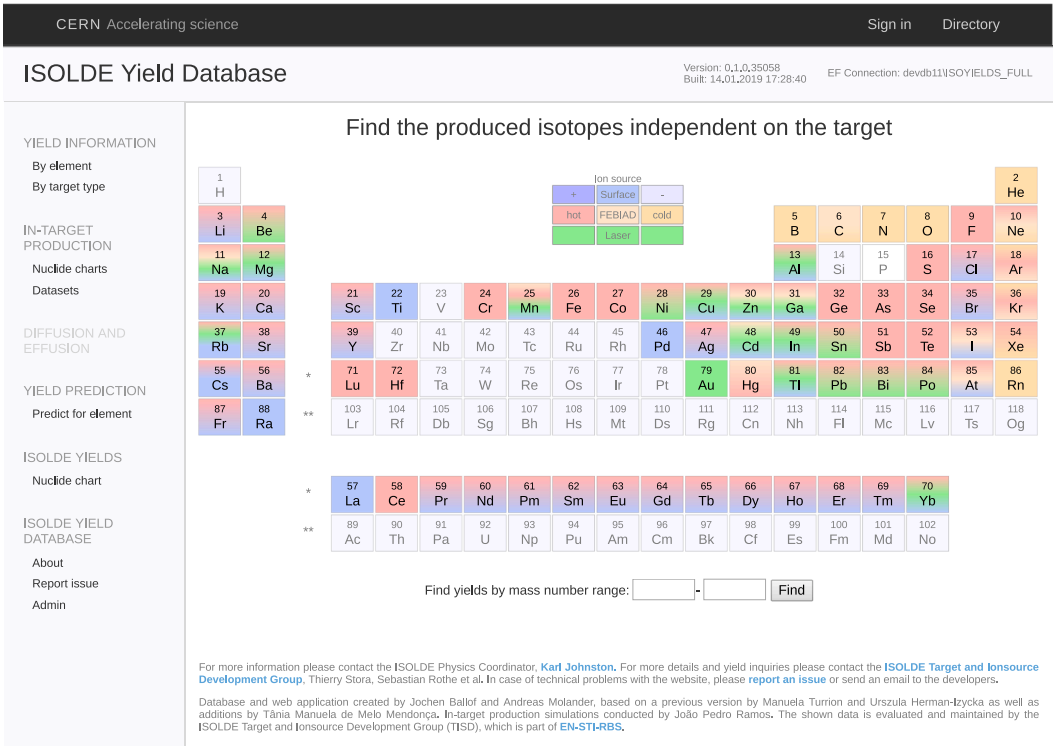

Fig. 3. The web frontend of the ISOLDE yield database, showing available beams in the periodic table of elements. The frontend is available at http://cern.ch/isolde-yields.

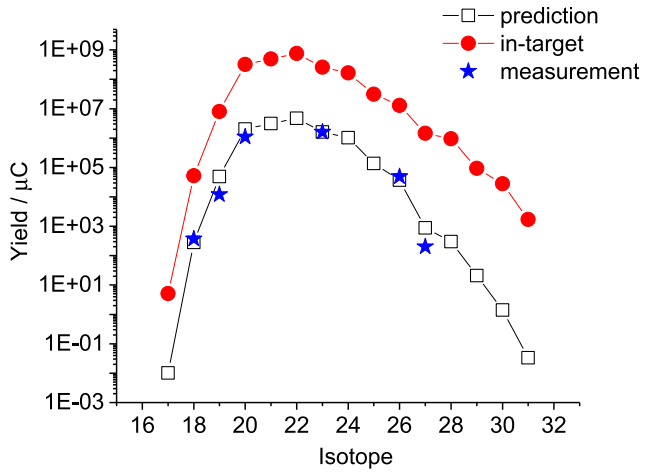

Fig. 4. Exemplary plot showing measured yields, in-target production along with yield predictions of neon isotopes from a uranium carbide target [10,6].The experimental yield for ^{23}Ne was used as reference point to calculate ϵ_f. The in-target production yields were taken from ABRABLA.

and long-term support. The Oracle Database 11 g [19], which is widely used at CERN, serves as underlying data provider for all high-level applications.

4.1. Database

The database stores experimentally obtained radioactive ion beam yields which were typically measured using the ISOLDE tapestation and taken from publications. The yields are stored along with information about the used target-unit, such as type of ion source, target material, thickness and operational conditions, and are given as yield in the focal plane of the magnet. Within this work, the structure of the database was completely redesigned and further normalized to ease maintenance and allow data storage for the upgraded functionality. A measured yield is linked to a defined target unit, which in turn is associated with a target material, made up of a nuclide mixture in defined stoichiometry. A set of new tables was added to store in-target production data obtained in simulations. For each target material nuclide, one ABRABLA run is necessary. The total in-target production cross section of a target material is then calculated by combining the estimated cross sections obtained in multiple ABRABLA runs and the thickness (areal density) of the target unit. In addition, FLUKA simulation results are available. Here the full target geometry and nuclide inventory is covered by one simulation. Release curve parameters are required to calculate release efficiencies (cf. Eq. (2)) and are available in a table linked to the table holding information about measured yields. At the time of writing, ca. one million production cross sections estimated by simulation codes are available, also indicating the production channel (like fission or spallation) for ABRABLA data. Besides storing published yield information, the database was extended to maintain data of yield measurements, typically taking place before each physics run. Within the 2018 operating period, new yields have been introduced, which are now available to advanced users.

4.2. User and application programming interfaces

Two new user-interfaces have been developed. One interface is implemented as website and displays data to users. For fast data manipulation, a rich client solution is under development. A prototype application implemented using Microsoft Access is already provided to users as RemoteApp by Microsoft Remote Desktop services (RDS) [20] to allow a rich client experience but avoiding at the same time the need of local software installation on client computers.

4.2.1. Web application

In contrast to earlier versions, the new web application [6] (Fig. 3) is not based on Oracle integrated web solutions and Java applets, but implemented in C# under Microsoft ASP.NET [21] to gain a higher degree of flexibility in development. User authentication is accomplished by Single Sign On (SSO) services, widely used at CERN. The Microsoft Entity Framework [22] allows object-relational mapping and rapid development of data driven applications. With the new application, further details about production conditions of yields are given, which include among other attributes, target and ion-source temperatures and release curves. The latter are provided as parameters (cf. Eq. (2)) and plot to visualize the time structure of the release. Besides adding yield details, an interactive nuclide chart was developed using the JavaScript library D3.js [23], which is capable of displaying an overview chart of all beams at ISOLDE as well as in-target production yields for each target material [24]. For easy comparison between target materials or different driver beam energies, the plotting of ratios between different data sets is also available (cf. Fig. 2). The functionality to predict yields for not yet measured isotopes is also included in the web application. It allows the user to predict yields for the full chain of isotopes of a certain element. The desired target material, proton beam energy and simulation software are selected by the users. The application then searches for reference point candidates in the database, which serve as source for the calculation of the efficiency parameter ϵ_f. The actual reference point is selected by the user, and prediction results are displayed as table and plot. A typical plot is shown in Fig. 4. Half-life data of nuclides is necessary to calculate release efficiency. An import function for NUBASE evaluation data [25] allows to continuously update the data with new and modified entries.

4.2.2. Rich client application

The prototype desktop application allows fast and direct access to the data layer. It is intended to be used for data manipulation and queries by advanced users. Functionality has been included to calculate yields obtained during routinely performed measurements for each unit, which are either conducted at the ISOLDE tape station or derived from Faraday Cup readings. The tape station is equipped with scintillation counter and high purity germanium detector and used as reference method to determine yields.

4.2.3. Application programming interface

Following user requests to link their own systems to the yield database, a REST-interface based on the ASP.NET Web API is available. The solution integrates nicely into Entity Framework and enables us to rapidly develop programming interfaces. The data is delivered as JSON or XML data. The interface is also used to provide data to the CRIBE (Chart of Radioactive Ion Beams in Europe) project, which aims at providing an overview of available and future radioactive ion beams at all facilities in Europe [27].

5. Conclusions and outlook

Within a complete redevelopment of the website and restructuring of the underlying database we have added a set of new functions to the ISOLDE yield database application. Now, it does not only provide available yield information, but is also capable to predict yields at the prospective proton beam energy of 2.0 GeV, which is an option of the driver beam upgrade under consideration. Yield predictions for exotic isotopes, which could only be measured with sophisticated setups, are now available. To achieve the latter, a comprehensive simulation campaign was conducted. The results of the simulation data are made available to users. At the time of writing the application is available to advanced users and undergoes extensive testing before release on the ISOLDE web page. In the future, we plan to further extend the functionality of the database and develop interfaces for data exchange between asset management and control applications. The inclusion of

yields reported by facility users and an extension of the simulation campaign are in preparation. The added simulation data will cover cross sections of materials which have not yet been used at ISOLDE, and will also be verified against new versions of the simulation codes.

Acknowledgments

We would like to thank T.M. Mendonça for her comprehensive revision of available yield information, evaluation of user requirements, and work towards the redesign of the webpage, R. S. Augusto for support regarding the FLUKA code, as well as A. Kelic-Heil and J. Klimo for ABRABLA support. We also thank M. Rey Regulez, I. Posada Trobo and the CERN IT staff for fast and reliable hosting of database and web application and acknowledge continuous support. Regarding the implementation of the CRIBE interface, we appreciate the fruitful collaboration with M. Celary and M. Fadil (GANIL). Moreover, we thank M. J. García Borge, G. Neyens and the members of the ISOLDE physics group for their support and valuable input. This project has received funding from the European Union's Horizon 2020 research and innovation program under grant agreement No 654002.

References

[1] R. Catherall, W. Andreazza, M. Breitenfeldt, A. Dorsival, G.J. Focker, T.P. Gharsa, G.T. J, J.-L. Grenard, F. Locci, P. Martins, S. Marzari, J. Schipper, A. Shornikov, T. Stora, The isolde facility, J. Phys. G: Nucl. Part. Phys. 44 (9) (2017) 094002 URL: http://stacks.iop.org/0954-3899/44/i=9/a=094002.

[2] H.J. Kluge, ISOLDE users' guide, CERN Yellow Reports: Monographs, CERN, Geneva, 1986 URL: http://cds.cern.ch/record/170359.

[3] M. Turrión, M. Eller, R. Catherall, L. Fraile, U. Herman-Izycka, U. Köster, J. Lettry, K. Riisager, T. Stora, Management of isolde yields, Nucl. Instrum. Methods Phys. Res., Sect. B 266 (19) (2008) 4674–4677, https://doi.org/10.1016/j.nimb.2008.05.144 proceedings of the XVth International Conference on Electromagnetic Isotope Separators and Techniques Related to their Applications.http://www.sciencedirect.com/science/article/pii/S0168583X08007994.

[4] M. Turrión, M. Borge, O. Tengblad, Database for ISOL-production optimization with web access, Nucl. Phys. A 746 (2004) 441–444, https://doi.org/10.1016/j.nuclphysa.2004.09.062.

[5] The ISOLDE yield database – Classic version, 2018. http://isoyields-classic.web.cern.ch, [Online; accessed 14-December-2018].

[6] The ISOLDE yield database – Development version, 2018. http://isoyields2.web.cern.ch, [Online; accessed 14-December-2018].

[7] U. Köster, How to produce intense and pure ISOL beams, Prog. Part. Nucl. Phys. 46 (1) (2001) 411–412, https://doi.org/10.1016/S0146-6410(01)00148-X URL: http://www.sciencedirect.com/science/article/pii/S014664100100148X.

[8] R. Kirchner, On the release and ionization efficiency of catcher-ion-source systems in isotope separation on-line, Nucl. Instrum. Methods Phys. Res., Sect. B 70 (1–4) (1992) 186–199.

[9] T.E. Cocolios, B.A. Marsh, V.N. Fedosseev, S. Franchoo, G. Huber, M. Huyse, A.M. Ionan, K. Johnston, U. Köster, Y. Kudryavtsev, M. Seliverstov, E. Noah, T. Stora, P.V. Duppen, Resonant laser ionization of polonium at rilis-isolde for the study of ground- and isomer-state properties, Nucl. Instrum. Methods Phys. Res., Sect. B 266 (19–20) (2008) 4403–4406, https://doi.org/10.1016/j.nimb.2008.05.142.

[10] U. Bergmann, G. Auböck, R. Catherall, J. Cederkäll, C. Diget, L. Fraile, S. Franchoo, H. Fynbo, H. Gausemel, U. Georg, T. Giles, H. Jeppesen, O. Jonsson, U. Køster, J. Lettry, T. Nilsson, K. Peräjärvi, H. Ravn, K. Riisager, L. Weissman, J. Äystö, Production yields of noble-gas isotopes from isolde UCX/graphite targets, Nucl. Instrum. Methods Phys. Res., Sect. B 204 (2003) 220–224, https://doi.org/10.1016/S0168-583X(02)01921-3 14th International Conference on Electromagnetic Isotope Separators and Techniques Related to their Applications.http://www.sciencedirect.com/science/article/pii/S0168583X02019213.

[11] J. Lettry, R. Catherall, P. Drumm, P. Van Duppen, A. Evensen, G. Focker, A. Jokinen, O. Jonsson, E. Kugler, H. Ravn, et al., Pulse shape of the isolde radioactive ion beams, Nucl. Instrum. Methods Phys. Res., Sect. B 126 (1–4) (1997) 130–134.

[12] A. Keli, M.V. Ricciardi, K.-H. Schmidt, Abla07 – towards a complete description of the decay channels of a nuclear system from spontaneous fission to multi-fragmentation, in: Joint ICTP-IAEA Advanced Workshop on Model Codes for Spallation Reactions Trieste, Italy, February 4–8, 2008, 2009. arXiv:0906.4193.

[13] S. Luki, F. Gevaert, A. Keli, M. Ricciardi, K.-H. Schmidt, O. Yordanov, Systematic comparison of isolde-sc yields with calculated in-target production rates, Nucl. Instrum. Methods Phys. Res. Section A 565 (2) (2006) 784–800, https://doi.org/10.1016/j.nima.2006.04.082 URL: http://www.sciencedirect.com/science/article/pii/S0168900206007005.

[14] A. Ferrari, P.R. Sala, A. Fass, J. Ranft, FLUKA: a multi-particle transport code (program version 2005), CERN Yellow Reports: Monographs, CERN, Geneva, 2005 URL: http://cds.cern.ch/record/898301.

[15] T. Böhlen, F. Cerutti, M. Chin, A. Fassó, A. Ferrari, P. Ortega, A. Mairani, P. Sala, G. Smirnov, V. Vlachoudis, The fluka code: developments and challenges for high energy and medical applications, Nucl. Data Sheets 120 (2014) 211–214, https://doi.org/10.1016/j.nds.2014.07.049 URL: http://www.sciencedirect.com/science/article/pii/S0090375214005018.

[16] R. Catherall, J. Lettry, S. Gilardoni, U. Köster, Radioactive ion beams produced by neutron-induced fission at isolde, Nucl. Instrum. Methods Phys. Res., Sect. B 204 (2003) 235–239, https://doi.org/10.1016/S0168-583X(02)01915-8 14th International Conference on Electromagnetic Isotope Separators and Techniques Related to their Applications.http://www.sciencedirect.com/science/article/pii/S0168583X02019158.

[17] T. Stora, E. Noah, R. Hodak, T.Y. Hirsh, M. Hass, V. Kumar, K. Singh, S. Vaintraub, P. Delahaye, H. Franberg-Delahaye, M.-G. Saint-Laurent, G. Lhersonneau, A high intensity 6he beam for the beta-beam neutrino oscillation facility, EPL (Europhysics Letters) 98 (3) (2012), https://doi.org/10.1209/0295-5075/98/32001.

[18] K. Hanke, Past and present operation of the CERN PS booster, Int. J. Mod. Phys. A 28 (13) (2013) 1330019, https://doi.org/10.1142/s0217751x13300196.

[19] Oracle Corporation Website, 2018.http://www.oracle.com, [Online; accessed 13-December-2018].

[20] Remote Desktop Services, 2018.https://docs.microsoft.com/en-us/windows-server/remote/remote-desktop-services/welcome-to-rds/, [Online; accessed 15-December-2018].

[21] Microsoft ASP.NET documentation, 2018.https://docs.microsoft.com/en-us/aspnet/, [Online; accessed 14-December-2018].

[22] Microsoft Entity Framework documentation, 2018.https://docs.microsoft.com/en-us/aspnet/, [Online; accessed 14-December-2018].

[23] M. Bostock, D3 – Data Driven Documents JavaScript library, 2010 – 2017.https://d3js.org/, [Online; accessed 15-December-2018].

[24] A. Molander, Development of the ISOLDE Yield Database, CERN Summer Student Programme Report.http://cds.cern.ch/record/2636715.

[25] G. Audi, F.G. Kondev, M. Wang, W. Huang, S. Naimi, The NUBASE2016 evaluation of nuclear properties, Chin. Phys. C 41 (3) (2017) 030001, , https://doi.org/10.1088/1674-1137/41/3/030001.

[26] J. Lettry, R. Catherall, P. Drumm, P.V. Duppen, A. Evensen, G. Focker, A. Jokinen, O. Jonsson, E. Kugler, H. Ravn, Pulse shape of the isolde radioactive ion beams, Nucl. Instrum. Methods Phys. Res., Sect. B 126 (1–4) (1997) 130–134, https://doi.org/10.1016/s0168-583x(96)01025-7.

[27] M. Fadil, CRIBE JRA Eurisol, First Periodic Scientific Report, 2018.https://eurisol-jra.in2p3.fr/?page_id=79, [Online; accessed 15-December-2018].

4 Molecular beams as means of in-situ volatilization

Contents

In many cases, elements can be extracted in atomic state from a target and efficiently ionized. However, for certain elements this is either impossible or unwanted. The former holds for elements with high melting or boiling points and the latter is particularly relevant if severe isobaric contaminations are present in the mass separated beam which would render user experiments impossible. This chapter provides a general overview about radioactive molecular beam production and includes the publication about the first extraction of radioactive boron beams by the ISOL method as example for the extraction of a refractory element by *in-situ* volatilization (or chemical evaporation).

4.1 Production of molecular beams

The motivation for the extraction of radioisotopes as molecular beam can be multifold. Besides previously mentioned volatilization of refractory elements, molecular sidebands can shift the mass of a radioisotope as seen by the mass separator. The latter technique is of interest if substantial isobaric impurities are present on the atomic mass. Such a case is discussed in Chapter 5. Recently, also interest in experiments arose in which the molecule itself is subject of the study, *e.g.* by optical spectroscopy [182]. The latter might even facilitate the exploration of particle physics beyond the standard model [183].

For most applications, the radioactive molecule is formed in the target and ion source unit, but also molecular beam production from ion traps [184], beam coolers [185] or gas catchers [186] has been reported. In the foremost case, which this thesis is addressing, the molecule typically needs to be stable in a high-temperature environment. This requirement limits the suitable compounds to only a few classes, which are mostly binary halides, oxides or sulfides.

A general introduction about chemistry in the target and ion source unit, recommended materials and sideband formation was given by Freeman and Sidenius at the second conference on ion sources in 1972 [187,188]. The authors also provided a comprehensive list of candidate compounds. More recent reviews and contributions are available by Kirchner [189], Köster [59, 190, 191], Kronenberg [98], Franberg [103] and Seiffert [75]. A periodic table visualizing radioactive molecular beams as reported in literature is shown fig. 4.1. The references have been compiled in table 4.1.

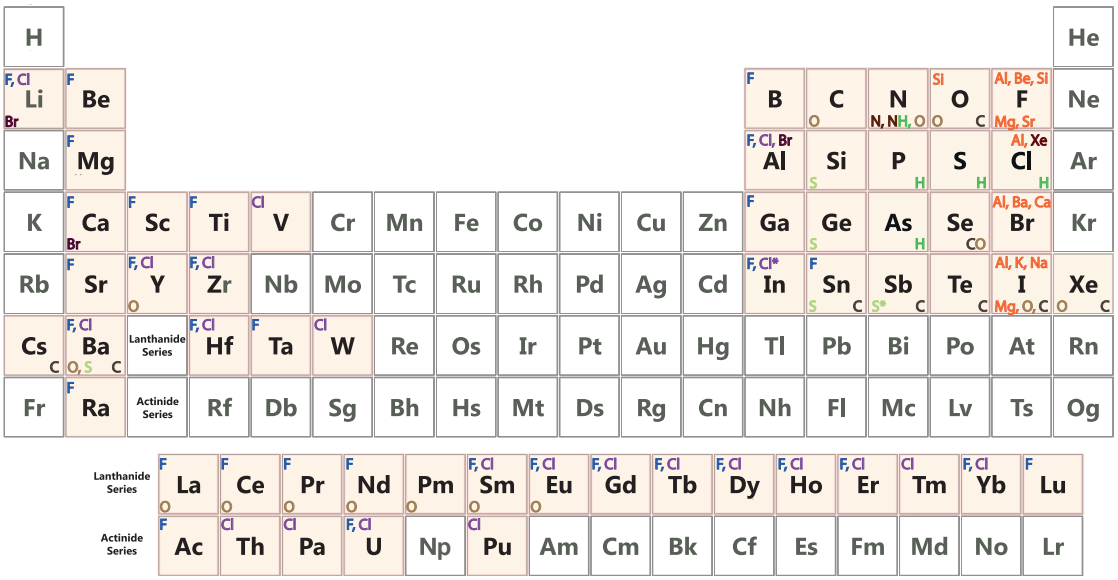

Figure 4.1: Radioactive molecular beams produced at ISOL facilities. Tracer experiments leading to online developments are also included. The asterisk (*) denotes proposed intermediates. References are given in table 4.1.

Table 4.1: Extracted radioactive molecular beams and beam development with stable tracers. The radiogenic reactant or volatilized tracer is shown in bold. The stoichiometry is not given.

Fluorides		**Chlorides**		**Chalcogenides**	
AcF	[192]	Al**Cl**	[193]	**Ba**O	[204]
AlF	[82]†, [193]	**Ba**Cl	[190]	**Ba**S	[190]†
Al**F**	[192–197]	**Dy**Cl	[219]†	**C**O	[59, 67, 116, 196, 222, 223] [68, 75, 103, 191]
BF	[82]†, [75, 180], *this work*	**Er**Cl	[219]†		
BaF	[82]†, [59, 63, 82, 194, 198–204]	**Eu**Cl	[219]†		
BeF	[82]†, [97, 194]	**Gd**Cl	[219]†	C**O**	[224]
Be**F**	[205]	H**Cl**	[220]	**Ce**O	[200, 225, 226]
CaF	[82]†, [59, 97, 201]	**Hf**Cl	[219]†	**Dy**O	[211]
CeF	[206]†, [202]	**Ho**Cl	[219]†	**Eu**O	[226]†
DyF	[206]†	**In**Cl	[63, 221]‡	**Ge**S	[189]†, [190, 193, 197, 227], *this work*
ErF	[206]†	**Li**Cl	[211]		
EuF	[206, 207]†, [194]	**Pa**Cl	[219]†	**I**O	[204]
GaF	[202]	**Pu**Cl	[219]†	**La**O	[200, 225, 226]
GdF	[206]†	**Sm**Cl	[219]†	**Lu**O	[211]
HfF	[59, 97, 191, 192, 208–210]	**Tb**Cl	[219]†	**N**O	[103]
HoF	[206, 207]†	**Th**Cl	[219]†	**Nd**O	[200], [226]†
InF	[202], *this work* ‖	**Tm**Cl	[219]†	**O**O	[223]
LaF	[206, 207]†, [199, 202, 203]	**U**Cl	[219]†	**Pm**O	[200], [226]†
LiF	[211]	**V**Cl	[98]	**Pr**O	[200], [226]†
LuF	[206]†, [59, 97, 192, 210]	**W**Cl	[219]†	**Sb**S	[189]†‡
		Xe**Cl**	[190]	**Si**S	[193]
MgF	[82]†	**Y**Cl	[179]	Si**O**	[211]
Mg**F**	[211]	**Yb**Cl	[219]†	**Sm**O	[226]†
NdF	[206]†	**Zr**Cl	[179]§	**Sn**S	[189]† [190, 193, 197, 228]
PrF	[206, 207]†, [202]			**Tb**O	[211]
RaF	[59, 183, 194, 212–214]			**Xe**O	[204]
ScF	[59, 97, 192]			**Y**O	[225]
Si**F**	[215]			**Yb**O	[211]
SmF	[206]†				
SnF	[202]			**Others**	
SrF	[82]†, [97, 192, 199–202] [59, 194, 196, 204, 216]			Al**Br**	[67, 202, 227, 229], *this work*
				Al**I**	[192, 202, 229]
SrF	[216]			**As**H	[220]
TaF	[191]†, [199, 208, 217]			Ba**Br**	[230]
TbF	[206]†			**Ba**C	[204]
TiF	[75]			Ca**Br**	[194, 231]
UF	[97, 194]			CO**Se**	[59, 67, 190, 192, 196, 227], *this work*
YF	[59, 97, 192, 196, 202, 209]				
YbF	[206]†, [210]			**Cs**C	[204]
ZrF	[202]§, [173, 191, 199, 209, 218]			H**S**	[220]
				IC	[204]
				K**I**	*this work* ‖
				LiBr	[211]
				Mg**I**	*this work* ‖
				NN	[59, 103, 196, 222, 223, 232, 233]
				NNH	[232, 233]
				Na**I**	[173]
				PH	[220]
				SbC	[204]
				SnC	[204]
				TeC	[204]
				XeC	[204]

† Offline experiments with tracers ‡ Faster release or higher yields observed with reactive gas injection, proposed intermediates. § Claimed to be not reproducible or partially doubted by other authors [98].
‖ Observed from a magnesium-uranium oxide target (not published).

4.1.1 Requirements for molecular beam formation

A reaction partner is required to synthesize a molecule. The reactant can be either a gas (*e.g.* CF_4), vapour of a volatile liquid (*e.g.* CCl_4), or can be obtained by decomposition or evaporation of solids in an oven (*e.g.* sulfur, aluminum). In some cases, the reactant is obtained from the target material itself or trace impurities in the target and ion source unit. Reaction mechanisms and sources of reactants are not always understood. If the production cross sections are sufficiently high, the reactant can also be produced in nuclear reactions [216]. The latter route is usually unwanted due to a dilution effect. The desired isotope is distributed among several sidebands of different mass which reduces the total yield at a given mass.

Several conditions have to be met for efficient formation of a molecular sideband: i) the introduced reactant needs to be either sufficiently inert towards structural materials and target material or form an intermediate product that arrives in the target container and is available for reactions, ii) the carrier molecule must be stable at operational temperature and chemically inert towards structural materials and target material, iii) the formation of the carrier compound must be favoured kinetically and thermodynamically, iv) the carrier compound must be sufficiently volatile and v) the compound must be suited for efficient ionization. Due to typically high temperatures, the rate of chemical reactions is fast, however kinetic aspects might play a crucial role if the element itself is volatile and extracted before a molecule can be formed [189].

4.1.2 Available molecular beams

The history of molecular beam development dates back to the 1960s. The first *in-situ* volatilization experiment (also referred to as chemical evaporation) was reported by Sidenius and Skilbreid in 1961 [219]. The authors presented a method for efficient ionization of rare earth elements with what would later become known as the CCl_4-method. Lanthanum oxides were introduces into the discharge chamber of an arc-discharge ion source and extracted as chlorides from a CCl_4 plasma with up to 22% efficiency. Günther Herrmann discussed rapid chemical separations and compiled volatile compounds for all elements known at that time [234]. In 1971, Weber, Herrmann and Trautmann reported on the release of refractory fission products (Mo, Tc, Zr) from an uranium tetrafluoride target [235] and in 1973 the first online radioactive molecular beams (ZrF_3^+) were extracted at the JGU TRIGA reactor in collaboration with the a GSI On-line separator group using a tape transport system developed by the ISOLDE group [218]. The production of the fluoride compound was achieved by evaporation of a stable ZrF_4 carrier into the UF_4 target. The pulsed neutron beam and tape transport system even allowed to measure the delay function of noble gases and iodine radioisotopes.

At ISOLDE, Ravn *et al.* discovered that alkaline earth elements obtained from metal targets form fluoride sidebands already with trace impurities of fluorine, while alkaline elements remain in the atomic state [198]. The discovery allowed to supply pure beams of barium isotopes. The stability of similar sidebands could be improved by injection of carbon tetrafluoride [97, 202]. Hoff *et al.* also reported that not only radiogenic metals can be extracted as halides but also radiogenic halides can be extracted as aluminium compounds via the aluminum vapour method [202]. The fluorination method was also

succesfully applied to other elements, *e.g.*, the early transition metals, lanthanides and actinium [97, 192, 202]. The extraction of selenium as carbonyl selenide (COSe), an homologue to carbon dioxide [192], is so far the only ternary radioactive molecule that was reported to be extracted from an ISOL target. The formation of oxides allowed, *e.g.*, the extraction of carbon [116] and also lanthanides often appear in the oxide sideband [190]. Pure beams of the intermediate group 14 elements Si, Ge and Sn were first reported by Stracener *et al.* who extracted these elements as sulfides. Faster release of the molecules compared to the elemental form was observed [189, 190, 193, 197]. Indications for hydride beams of phorphorous, arsenic and sulfur were reported by Jardin *et al.* from an ECR ion source [220]. With a high temperature setup allowing operation beyond 2500 °C, even typically non-volatile carbide compounds could be extracted by Hellström *et al.* [204].

4.1.3 Boron beams

Radioactive boron beams are the most recent addition to the index of available molecular beams. As discussed in the article, the extraction as atom is considered impossible at thick-target ISOL facilities due to its refractory character and reactivity. The extraction of boron as fluoride had already been been proposed in 1972 by Freeman and Sidenius [187]. More detailed considerations were presented by Köster *et al.* proposing ionization with either a FEBIAD or an ECR ion source from graphite, calcium fluoride or platinum matrix [191]. Promising release data from MultiWalled Carbon NanoTubes (MWCNT) and molecule formation experiments were conducted by Seiffert and led to a first online experiment in which indication for ^{8}B could be found [75]. In a second online run with only minor modification to the target an ion source unit, radioactive boron beams $^{8}BF_x$ with $0 \leq x \leq 3$ could be unambiguously identified in alpha-gamma coincidence measurements.

4.2 Contributions

The development of boron beams has been initiated within the work of Ch. Seiffert as reported in [75]. Within this thesis, a second online run with an improved production and detection setup was performed. The data obtained in the second online run was analyzed by myself and a release model (Eq. 1 and 4 to 7 of the publication) was proposed within this thesis. Ch. Seiffert prepared a publiction draft covering most of the aspects reported in [75]. The remaining text was written by myself. Correspondence with the journal and following the peer-review process were also done by myself. O. Tengblad, R. Lica and M. Madurga Flores have built and operated the alpha-gamma-spectroscopy setup used in the second run. M. Delonca, Y. Martinez Palenzuela, T.M. Mendonca, J.P. Ramos, S. Rothe and F. Wienholtz participated in the measurements of the second or later online runs.

Eur. Phys. J. A (2019) **55**: 65
DOI 10.1140/epja/i2019-12719-1

THE EUROPEAN PHYSICAL JOURNAL A

Regular Article – Experimental Physics

Radioactive boron beams produced by isotope online mass separation at CERN-ISOLDE

J. Ballof[1,3,a], C. Seiffert[1,2], B. Crepieux[1], Ch.E. Düllmann[3,7,8], M. Delonca[1], M. Gai[6], A. Gottberg[1,b], T. Kröll[2], R. Lica[1,11], M. Madurga Flores[1], Y. Martinez Palenzuela[1,9], T.M. Mendonca[1], M. Owen[1], J.P. Ramos[1,4], S. Rothe[1], T. Stora[1,c], O. Tengblad[10], and F. Wienholtz[1,5]

[1] CERN, 1211 Geneva 23, Switzerland
[2] Technische Universität Darmstadt, Schlossgartenstr. 9, 64289 Darmstadt, Germany
[3] Johannes Gutenberg - Universität Mainz, Institut für Kernchemie, Fritz-Strassmann-Weg 2, 55128 Mainz, Germany
[4] Laboratory of Powder Technology, École Polytechnique Fédérale de Lausanne (EPFL), Lausanne, CH-1015, Switzerland
[5] Universität Greifswald, Domstraße 11, 17489 Greifswald, Germany
[6] LNS at Avery Point, University of Connecticut, Groton, CT 06340, USA
[7] GSI Helmholtzzentrum für Schwerionenforschung, 64291, Darmstadt, Germany
[8] Helmholtz-Institut Mainz, 55099 Mainz, Germany
[9] KU Leuven, Instituut voor Kern- en Stralingsfysica, B-3001 Leuven, Belgium
[10] Instituto de Estructura de la Materia, CSIC, Serrano 113 bis, ES-28006 Madrid, Spain
[11] "Horia Hulubei" National Institute of Physics and Nuclear Engineering, RO-077125, Bucharest, Romania

Received: 26 August 2018 / Revised: 31 January 2019
Published online: 13 May 2019

Communicated by K. Blaum

Abstract. We report on the development and characterization of the first radioactive boron beams produced by the isotope mass separation online (ISOL) technique at CERN-ISOLDE. Despite the long history of the ISOL technique which exploits thick targets, boron beams have up to now not been available. This is due to the low volatility of elemental boron and its high chemical reactivity which make the definition of an appropriate production target unit difficult. In addition, the short half-lives of all boron radioisotopes complicate tracer release studies. We report here on dedicated offline release studies by neutron capture and alpha detection done with implanted ^{10}B in prospective target materials, as well as molecule formation and ionization tests, which suggested the use of multiwalled carbon nanotubes (CNT) as target material and injection of sulfur hexafluoride SF_6 to promote volatile boron fluoride formation. Two target units equipped with an arc discharge electron impact ion source VADIS coupled to a water cooled transfer line to retain non-volatile elements and molecules were subsequently tested online. The measured yield of these first ^{8}B ISOL beams increases in the series $^{8}BF_3 < {}^{8}BF < {}^{8}B < {}^{8}BF_2$, reaching a maximum yield of 6.4×10^4 $^{8}BF_2{}^{+}$ ions per μC of protons.

1 Introduction

At CERN-ISOLDE [1] more than 1000 radioisotopes of 74 different chemical elements can be delivered to a large spectrum of experimental setups for investigations in nuclear structure, atomic physics and applications. These isotopes are produced by the ISOL (Isotope mass Separation OnLine) method inside a combined target and ion source unit upon impact of the 1.4 GeV proton driver beam from the PS-Booster. The yield of radioactive isotopes which can be extracted from ISOL-like facilities is strongly dependent on the half-life and the chemical properties of the desired element. For some elements (*e.g.*, Na, K) extraction efficiencies from ISOL targets can be close to 100%, while for other elements their extraction has proven difficult or even impossible up to now, despite decades of research in this field. Examples for isotopes with low extractable yields are refractory or chemically very reactive elements such as boron, tungsten or rhenium. The reasons why yields can be very low is apparent from the extraction process itself [2]. After isotope production typically through fission, fragmentation or spallation nuclear reactions, the neutral isotopes have to diffuse to the surface of

[a] e-mail: jochen.ballof@cern.ch
[b] *Present address:* TRIUMF, 4004 Wesbrook Mall, Vancouver, BC V6T 2A3, Canada.
[c] e-mail: thierry.stora@cern.ch (corresponding author)

the target material grain where they can evaporate or react to form more volatile molecules, in the case of a molecular extraction. During the subsequent migration through the target setup towards the ion source, the isotope experiences numerous interactions with the surrounding target and structural material. At each interaction losses due to chemical reactions or irreversible sticking on the surfaces can occur. In the case of boron these losses are so large, that no Radioactive Ion Beam (RIB) was produced by the ISOL method until now, although many possibilities are offered by different combinations of targets and ion sources operated in facilities such as ISOLDE at CERN. In the present article, we introduce the different developments made, and the description of the target unit obtained for the delivery of ^{8}B as molecular ion beam [3]. Finally we report on the online results obtained at ISOLDE with the prepared target unit.

2 ISOL beam extraction processes

The extractable yield Y of isotopes produced in an ISOLDE target unit can be estimated by folding the extraction probability of a single isotope weighted by the number of initially produced isotopes N_0 per μC of primary beam with the distribution function $p(t)$ of extraction times in the investigated setup:

$$\begin{aligned} Y &= \int_0^\infty N(t)\, p(t)\, \mathrm{d}t, \quad \text{where} \\ N(t) &= N_0\, e^{-\lambda t}\, \epsilon_{\mathrm{irrev}}\, \epsilon_{\mathrm{form}}\, \epsilon_{\mathrm{ion}}, \quad \text{and} \\ t &= t_{\mathrm{diff}} + t_{\mathrm{ads}} + t_{\mathrm{eff}}. \end{aligned} \tag{1}$$

Here, λ is the decay constant of the isotope, t_{diff} is the diffusion time out of the material, t_{ads} the delay due to sticking on surfaces, t_{eff} the time of flight through the target container and into the ion source and $\epsilon_{\mathrm{irrev}}$ is the transport efficiency considering chemical losses and irreversible adsorption on surfaces. $N(t)$ is the yield of extracted isotopes, which need time t to propagate from the target material to the ion source. The expression holds for pulsed and continuous primary beam. However, modified expressions for facilities using a continuous driver beam are typically used, which give the radioactive beam intensity as number of radioactive ions per second. If the vapor pressure of a desired element is too small at achievable temperatures, extraction as a more volatile molecule is necessary. The formation efficiency for a particular molecular sideband is given by ϵ_{form}. Finally, ϵ_{ion} gives the ionization efficiency.

Diffusion in solid grains of the target material as well as effusion processes through open space are responsible for the shape of the distribution function $p(t)$, which holds for a stable, non-decaying isotope [4].

The initial number of produced isotopes N_0 is determined by the production cross section, proton beam intensity and number of target atoms. Since in most cases, the geometry of the target is predefined, a high target material density is favorable to increase N_0. However, a high density might be adverse for the diffusion of the isotope out of the material. A high porosity and small grain size is desired to allow fast and efficient diffusion and migration out of the target material [5]. If isotopes need to be extracted as molecules, the target setup can be equipped with additional gas injection lines, which allows to provide reaction partners for the formation of volatile carrier molecules. To minimize the losses due to sticking and chemical reaction of the reaction products, each of the materials used in the entire target and ion source assembly has to be considered separately.

Although the variety of available setups and advances in target materials production allows the extraction of isotopes of a large range of elements, no beams of radioactive boron were extracted at any thick-target ISOL facility prior to the development reported here. The experimental interest in beams of ^{8}B is manifold: besides interest in studying the proton halo structure [6] or high lying resonances of ^{9}C, which become accessible by elastic scattering of ^{8}B on a proton target [7], beams of boron would be ideal to investigate diffusion properties in semi conductors where boron is commonly used as a dopant [8]. Recently beams of ^{8}B were extracted at KVI at a rate of 7 ions per second [9] and at the thin-target facility IGISOL at a rate of 200 ions per second [10]. However, the yields available in these facilities are not sufficient for the above mentioned experiments, which require rates in the order of 5×10^{3} ions per second or above, and in some cases post acceleration of the beam. The relatively high production cross sections combined with the thick-target technologies available at ISOL facilities, like ISOLDE, open up new perspectives for physics experiments, if control over the boron release out of the target material and ionization can be gained.

In this work the factors important for the extraction (cf. eq. (1)) of radioactive boron (^{8}B, $T_{1/2} = 770\,\mathrm{ms}$) are investigated. This includes the choice of target material based on their production cross sections and the experimental determination of boron mobility in candidate targets, taking into account overall diffusion and effusion release processes. A dedicated offline release experiment was conducted exploiting the high neutron capture cross section of ^{10}B to determine which material allows a fast extraction and therefore high mobility. Since boron exhibits not only a high chemical reactivity but also a high boiling point, it needs to be extracted as molecular sideband. Upon reaction with a fluorinating agent, boron readily forms volatile and relatively inert fluorides. In comparison to other halogens, fluorine possesses only one stable isotope which allows to concentrate the molecular formation on a single isobar and therefore to achieve a higher mass separation efficiency. In a second step, the release of boron as boron fluorides (BF_x, $0 \leqslant x \leqslant 3$) was studied using an ISOLDE target setup and the offline isotope mass separator. This allowed to compare the measured beam composition with chemical equilibrium calculations performed under different conditions of SF_6 injection as well as the investigation of ionization behavior and influence of target parameters on the beam formation. Following up on the positive outcome of the preparatory experiments, a prototype target could be built, and beams of ^{8}B were produced online and characterized.

Table 1. Nominal densities [11] and typical material densities of prospective target materials for the production of boron radioisotopes at ISOLDE.

Material	Nominal density [g cm^{-3}]	ISOLDE density [g cm^{-3}]
CaO	3.34	0.38[a]
CNT	2.2[c]	0.4[b]
HfO_2	9.68	–
CaF_2	3.18	–
Y_2O_3	5.03	3.16[b]
Al_2O_3	3.99	–

[a] Value taken from ref. [5].
[b] Density of available materials, which were also used in the offline mobility studies (sect. 4).
[c] The theoretical density of graphite is given in the case of multiwalled carbon nanotubes (CNT).

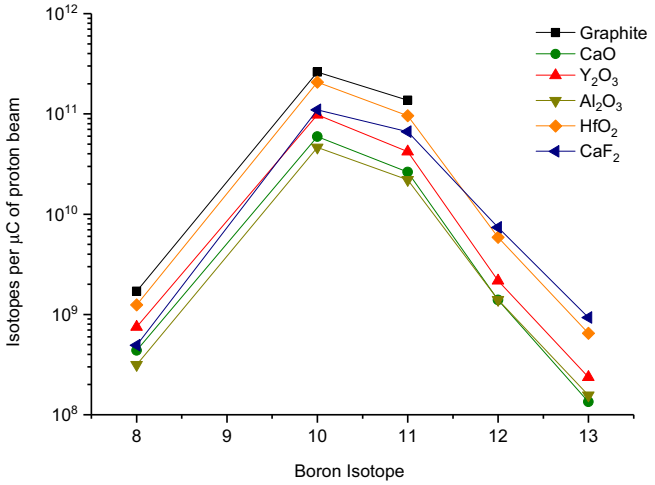

Fig. 1. In-target production yields of boron isotopes in potential target materials for the extraction of radioactive boron beams, obtained with the ABRABLA code. At ISOLDE, an average proton intensity of up to 2 μA is available. Nominal densities, as given in table 1 are assumed.

3 In-target isotope production

The in-target production of the desired isotope is the first parameter that needs to be considered for the development of new ISOL beams. The factors important for a high production rate are the production cross section σ for the particular isotope, the number of target nuclei and the number of protons impinging on the target. In this work, the production cross section of boron isotopes by bombarding a selection of target materials with 1.4 GeV protons was calculated using the ABRABLA code [12]. The selection of target materials is based on characteristics like melting point and chemical compatibility. Here the production cross sections were calculated for graphite, aluminum oxide, calcium oxide, calcium fluoride, hafnium oxide and yttrium oxide.

From the production cross section σ the number of produced isotopes N_0 which is used in eq. (1) can be calculated via the equation

$$N_0 = \sigma\, N_p\, N_T, \tag{2}$$

where N_p is the number of protons impinging on the target and N_T the areal density of target atoms, given by the dimensions of the target container and the density ρ of the target material. For the sake of comparison the nominal densities of the bulk materials were used for the calculation of the in-target production. As discussed in sect. 2 the practical densities of materials suitable for ISOL targets are lower to achieve a desired open porosity. Both densities are presented in table 1 and the in-target yields in isotopes per μC of proton beam according to eq. (2) are displayed in fig. 1, which take into account the dimensions of the cylindrical ISOLDE target container, having length and diameter of 20 cm and 2 cm, respectively [13].

4 Mobility of boron in potential target materials

The diffusion process is specific for every combination of target material and diffusing element. The diffusion coefficient D is a measure for the mean displacement of a particle per time unit and exponentially increases with the temperature as given by the Arrhenius equation [14]

$$D = D_0\, \mathrm{e}^{-Q/(\mathrm{R}\,T)}, \tag{3}$$

where D_0 is a temperature independent pre-exponential factor, Q the activation energy, R the universal gas constant and T the absolute temperature. The characteristic diffusion time is given by $\tau_D = a^2/(\pi^2 D)$ [15].

ISOLDE targets can be operated at temperatures up to about $T_{max} \approx 2500$ K. However, in many cases target materials start to degrade due to sintering effects already at lower temperatures which can result in an increase of the characteristic diffusion time and thereby reducing the yield of the extracted radioactive ions [5]. As diffusion is a slow process in comparison to migration through open space, a high open porosity and a small grain size are the desired characteristics of target materials. Determining diffusion coefficients is often difficult and requires sophisticated setups. For the production of radioactive ion beams the combination of both diffusion and migration through open space is important and can be summarized as the mobility of an element in the target.

In a first approximation, diffusion can be described by Fick's second law, and solutions for certain geometries and boundary conditions are provided in ref. [15]. Effusion effects are negligible for long heat treatment times (see sect. 7.1), and the fraction of isotopes remaining in the

solid after a heat treatment time t computes to

$$f(t) = \frac{2n}{\pi^2} \sum_{m=1}^{\infty} c_m^{-1} e^{-c_m t/\tau_D}, \qquad (4)$$

with $c_m = (j_{0,m}/\pi)^2$ for fibers ($n = 2$), and $c_m = m^2$ for spheres ($n = 3$). $j_{0,m}$ stands for the m-th positive root of the Bessel function of order zero and τ_D is the characteristic diffusion time. The latter can be deduced, if $f(t)$ was determined in an experiment. The solution of the diffusion differential equation given in eq. (4) was derived in ref. [15] under the boundary condition, that the diffusing species is uniformly distributed in the sample. However, after a heat treatment, the originally uniform distribution profile is disturbed due to depletion of the particle density near the edges of each grain. For subsequent heat treatments, the mean path a particle needs to travel to reach the surface of the grain, is longer compared to the original distribution. Within the mathematical procedure to correct for the disturbance of the profile, the two conducted heat treatments at different temperatures are replaced by one heat treatment at the higher temperature. The replacement procedure to derive the characteristic diffusion time for the second treatment, is adjusted such that the release fraction at the beginning and the end match the experimental treatment. For a discussion see ref. [16].

In earlier studies of boron diffusion in different materials by neutron depth profiling, more complex phenomena have been found. In certain matrices, accumulation of boron on the surface of the sample and propagation of the apparent inventory towards the surface of the sample were observed. The latter was attributed to the presence of radiation induced damage, introduced during the implantation process [17].

For this work the mobility of boron in different potential target materials was studied. The high cross section of 3.84 kb for the reaction $^{10}\mathrm{B}(n,\alpha)^7\mathrm{Li}$ at thermal neutron energies [18] offers an elegant way to determine the amount of boron tracers and therefore to study the mobility of boron in materials. The branching ratio and expected particle energies for this reaction are as follows [19, 20]:

$$^{10}\mathrm{B} + \mathrm{n}_{thermal} \xrightarrow{94\%} {}^7\mathrm{Li} + \alpha + \gamma \quad (0.84 \;\; 1.48 \;\; 0.48 \text{ MeV})$$
$$^{10}\mathrm{B} + \mathrm{n}_{thermal} \xrightarrow{6\%} {}^7\mathrm{Li} + \alpha \quad (1.01 \;\; 1.79 \text{ MeV})$$

The mobility of boron in three out of the six materials considered in the previous chapter was studied. We included yttrium oxide (Y_2O_3) as a representative class for the oxide materials as it had appropriate nanometric grain size and porosity, and two carbon allotropes namely graphite and multiwalled carbon nanotubes (CNT). To obtain reproducible and representative results, calcium oxide, for instance in the form of a nanoporous material, needs to be handled under inert gas atmosphere [5], and was therefore not considered for practical purposes. CaF_2 was neither considered following the outcome of chemical equilibrium calculations as discussed in sect. 5. Moreover, the mobility of boron in MgF_2 has already been studied, which might serve as surrogate for CaF_2 [21].

Samples for the three materials were prepared in pressed powder form (pellets) and 4×10^{16} atoms of ^{10}B, extracted as $BF_2{}^+$ from an ISOLDE target unit (cf. sect. 6) were implanted in each pellet at the ISOLDE offline mass separator at 50 kV extraction voltage. In the case of CNT and Yttria, the sample was biased additionally (-12 kV) to increase the implantation depth. Each sample was subjected to neutron irradiation with an intense ^{238}Pu-Be source of 1 Ci available from the CERN dosimetry service, and simultaneously the resulting α-particles (1.48 MeV) were detected using silicon detectors. A determination of the initial boron inventory with this method was done after preparation of each sample. Subsequently, the samples were heat treated to promote the diffusion process and the remaining fraction of boron atoms in the sample was determined. The heat treatment and measurement were repeated to a maximum temperature of 2000 °C, or until no boron could be detected anymore.

4.1 Materials

Multiwalled carbon nanotubes were supplied by *Nanocyl*, ref. NC3100, > 95% purity, 10 nm diameter, 1.5 μm length. Commercially available Yttria (*Alfa Aesar*, yttrium (III) oxide, 99.995% (REO) 25–50 nm APS Powder) and graphite (*Alfa Aesar*, ref. 40798, 325 mesh, < 44 μm) were used. The carbon materials have been characterized and results are provided in ref. [22].

4.2 Experimental setup and measurement

The detection of α-particles was achieved using an Ortec Alpha Aria spectrometer equipped with an Ortec silicon detector (450 mm^2, 100 μm depletion layer). The sample was placed at a distance of 5 mm to the detector and exposed to thermalized neutrons from the ^{238}Pu-Be source. The emerging fast neutrons were moderated by a 7 cm polyethylene (PE) block. In addition 15 cm of lead served as shielding to suppress background due to gamma radiation. After measurement of the α-particle rate, and subsequent deduction of the apparent boron inventory, the samples were heated in a tantalum furnace, similar to a standard target container [13].

To investigate the temperature dependence of the diffusion, samples were heated for 30 minutes in 5 (4 for CNT) steps, from room temperature to approximately 2000 °C. After each step, samples were exposed to the neutron source for approximately 50 hours and the emitted α-particles were recorded.

4.3 Results and discussion

A typical spectrum obtained from the silicon detector within a measurement time of 27 hours is shown in fig. 2.

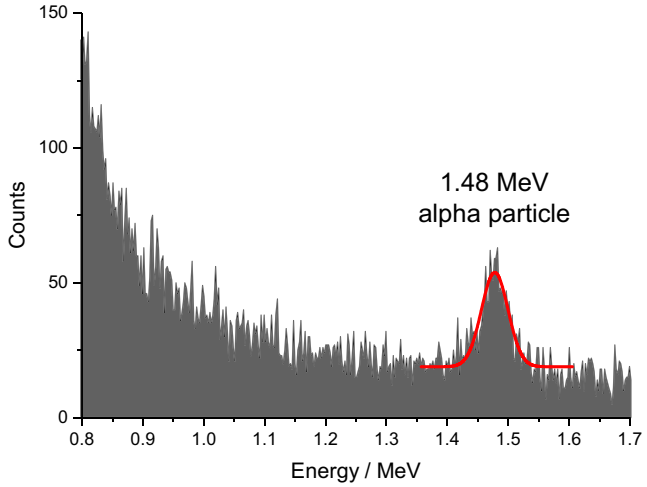

Fig. 2. Typical silicon detector spectrum obtained within a measurement time of 27 hours for the offline mobility studies. The peak arising from the 1.48 MeV alpha particle was fitted with a Gaussian function.

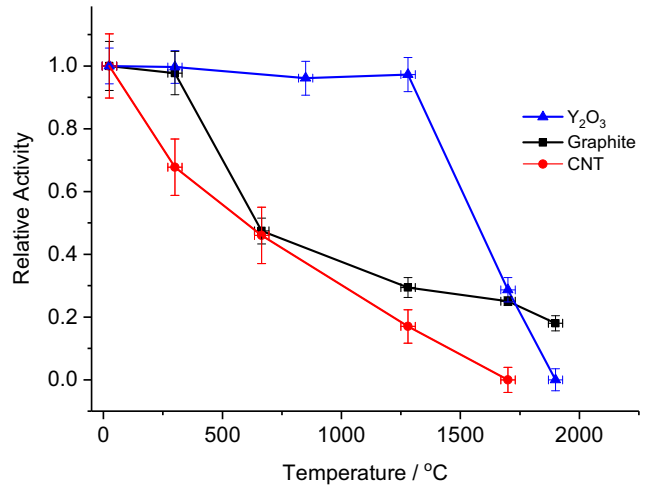

Fig. 3. Relative apparent boron inventory of the samples measured in the $^{10}\mathrm{B}(n,\alpha)^{7}\mathrm{Li}$ reaction, after successive offline mobility studies (see text).

Due to limited statistics, only the peak arising from the 1.48 MeV alpha particle is detectable. Peak center and area were obtained by fitting with a Gaussian function. Within the errors of the fits, which were less than ± 0.05 MeV for the peak center energy, we did not observe a reduction or increase of the alpha energy after subjecting the respective samples to the heat treatments. Hence we assume, that in-diffusion into deeper layers is not the primary reason for the depletion of the apparent boron inventory. Figure 3 shows the apparent boron inventory evolution of the samples obtained from the peak areas. To ease comparison, measurements are normalized to the initial implantation of each sample. The boron depletion is believed to be caused by its migration to the surface of the material, where it can desorb and is expected to be caught on parts of the tantalum oven or extracted as volatile species. Further studies would be necessary to fully explain the desorption process. We believe, that the desorption process is promoted by reactions with residual gases. Candidate compounds are oxides, oxohalides or halides. Oxygen is available as residual gas (5×10^{-5} mbar), and might react with boron to form boron monoxide or dioxide as intermediate carriers, which have been identified in other processes [23]. Halogens might be present as impurities in the oven or host material. A certain amount of fluorine was introduced during the sample preparation by implantation of $BF_2{}^+$.

It is obvious, that the diffusion behavior of boron significantly varies within the set of investigated host materials. Diffusion of boron in single crystals of graphite has been studied by Henning [24], who found almost 1000 times higher diffusion constants for diffusion parallel to the carbon layers compared to the diffusion perpendicular to the layers. At a temperature of 2291 °C, the diffusion constant was determined to be 3.9×10^{-10} cm^2/s, if diffusion occurs parallel to the carbon layers. Novak *et al.* investigated the diffusion in polycrystalline graphite and obtained diffusion coefficients as high as 3.1×10^{-6} cm^2/s at 2200 °C [25]. Despite our setup not allowing to derive diffusion constants, the cited values indicate fast diffusion and a strong dependence on the allotrope, which is reflected in the results shown in fig. 3. After the heat treatment at 700 °C the amount of boron in the graphite sample drops from almost 100% to about 50% of the initially implanted amount. Heating the graphite sample to 1300 °C causes an additional drop of remaining boron to 30%. Increasing the temperature further does not change the remaining amount significantly which suggests that the remaining boron is physically or chemically confined in the graphite matrix. The situation for multi-walled carbon nanotubes is slightly different. Similar to the graphite sample, significant fractions are released at relatively low temperatures with a decrease to approximately 65% after heating to a temperature of 300 °C. Further heating shows a faster decrease of boron in comparison to graphite. After heating to 1700 °C no remaining boron could be detected during measurements. Applying eq. (4) and a disturbed profile correction yields at the highest respective temperatures, a characteristic diffusion time of $\tau_D^{\mathrm{CNT}} = 8.6^{+3.5}_{-1.5} \times 10^2$ s for carbon nanotube fibers at 1700 °C, while a lower limit of 5 times this value was determined for the micron-sized graphite material at 1900 °C, which was treated as agglomeration of particles. The given errors are computed from the uncertainty in the release fraction. The application of eq. (4) requires, that boron is implanted uniformly in the material grain. For carbon nanotubes, an implantation depth of 177 nm was estimated by SRIM 2013 [26, 27]. Considering the nanometric structure, the condition of a uniform profile is assumed to be met (cf. table 2). However, in the case of the more dense and micron-sized graphite, boron is only implanted close to the surface. It is therefore assumed to be released faster in comparison to a uniform distribution, only allowing to give a lower limit of the characteristic diffusion time within the used model.

Table 2. Raw material and implantation characteristics, expected implantation depth and range of 1.48 MeV alpha particles used in the mobility study. The expected implantation depth and alpha range were obtained by SRIM [26, 27].

Material	Particle size	Implantation		Alpha
		energy	depth	range
CNT	9.5 nm × 1.5 μm[a]	62 keV	177 nm	22 μm
Graphite	5.3 μm[b] [22]	50 keV	35 nm	4.0 μm
Y_2O_3	67 nm[b,c] [28]	62 keV	51 nm	5.4 μm

[a] As given by the supplier.
[b] Particle size parameter obtained by specific surface area.
[c] Sintering is expected at elevated temperatures [28].

While diffusion in-between and through the walls of the nanotubes should be the same as for graphite, additional diffusion along and across the surface and through the capillaries of the tubes can be expected. This is a probable reason for the faster decrease of boron in the material [25, 29–31].

In the case of Yttria almost no change can be observed up to 1300 °C. The remaining amount of boron at this temperature is close to 100% of that initially implanted. However, heating the sample to 1700 °C shows a drop of 50%. After subsequent heating to 1900 °C no remaining boron was detectable during irradiation with neutrons. However, preliminary investigations show sintering at these temperatures [28], and simulations indicate possible decomposition in vacuum above 1900 °C [32]. Also taking into account the diffusion properties of boron in MgF_2 as given in ref. [21], multiwalled carbon nanotubes offer favorable diffusion characteristics.

5 Chemical equilibrium considerations

Besides production cross sections and diffusion inside the target material, chemical processes play an important role in the ISOL thick-target release processes. Boron does not only have a low volatility, but also exhibits a high reactivity towards many materials present in the target assembly. Hence, boron has to be extracted as part of a volatile molecule. The demands on the volatile compound are multi-fold. The formation should be fast, it needs to be stable at operation temperature, inert towards reaction with target materials and ionizable with sufficiently large cross sections.

After an evaluation of the known compounds we have chosen boron trifluoride as volatile carrier and sulfur hexafluoride as fluorinating agent. Both are gases at room temperature. Chemical equilibrium calculations with a set of target materials such as alumina, yttria, magnesium fluoride, calcium fluoride and carbon, have been conducted using the software package HSC 7 [32], based on the included thermodynamic data. The interactions with other materials present in the target assembly, like tantalum and molybdenum were also considered.

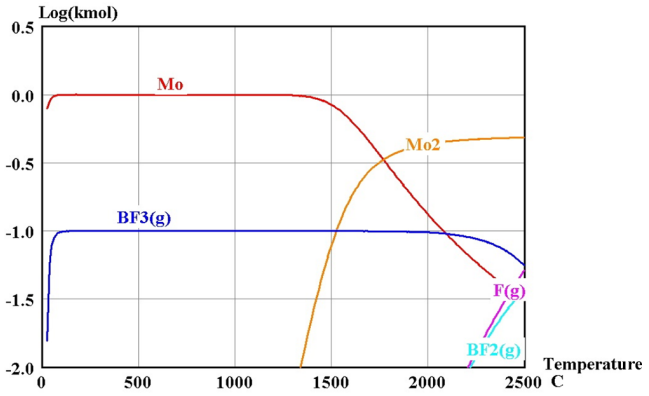

Fig. 4. Chemical equilibrium between molybdenum and BF_3.

The results of the calculation performed for molybdenum and BF_3 are shown as an example in fig. 4. It can be seen that within the calculated system gaseous boron trifluoride is stable even at high temperatures and does not form thermodynamically favoured compounds with molybdenum. Only at temperatures above 2200 °C the difluoride starts to build up and eventually becomes the dominating species well above 2500 °C. Similar results were obtained for the equilibrium between other construction materials and BF_3.

The common result for all calculations aiming at the formation of BF_3 in different target materials is that fluorine has to be available in excess. If this is not the case tantalum borides are expected to be formed. In the case of alumina, volatile molecules of BF_3 and BOF are formed in relatively narrow temperature ranges. Here, BF_3 can be expected from 800 °C to 1400 °C and BOF from 1400 °C to 2100 °C. Furthermore, calculations predict the formation of aluminum borides. The equilibrium with yttria indicates a dominant formation of BOF starting from 1500 °C. Below this temperature no volatile boron species is formed. For calcium fluoride as well as magnesium fluoride formation of boron fluoride is thermodynamically favoured. Unfortunately the temperature at which formation of BF_3 starts is, in both cases, higher than the boiling point of the material. For MgF_2 gaseous BF_3 appears above approximately 1400 °C, for the case of CaF_2 above 1600 °C.

The calculations indicate that BF_3 is not chemically retained in a carbon-based target material. This, along with the availability of carbon nanomaterials which allow fast diffusion made this selection our preferred choice. Also the very high specific surface favors volatilization by molecule formation with an injected gas.

6 Ionization behavior and extraction efficiency

The formation and ionization of boron fluoride ions, so-called sidebands, was tested at the ISOLDE offline separator by placing elemental boron powder in the target container of a typical ISOLDE target. The tantalum container was connected to a VADIS ion source [33] via a water

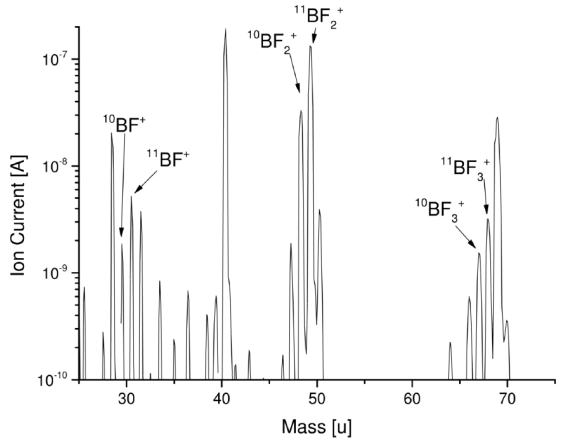

Fig. 5. Mass distribution of boron fluorides ions extracted from a solid boron sample which was placed in heated tantalum container. SF_6 was injected through a calibrated leak of 5×10^{-5} mbar L/s (air).

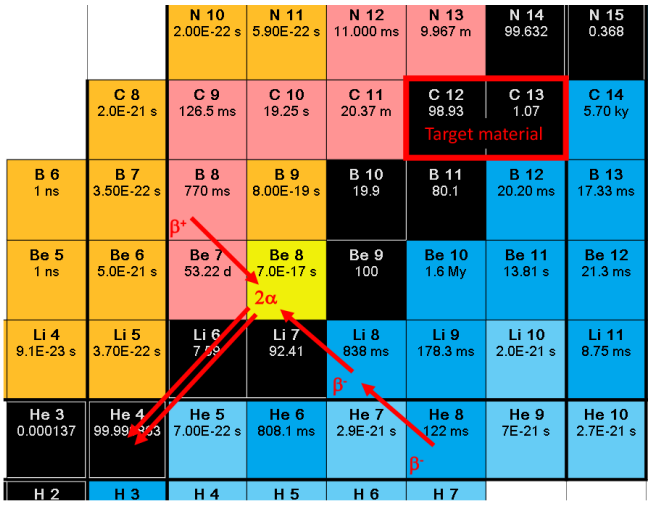

Fig. 6. Cutout of the nuclide chart showing the target material and selected nuclei produced in fragmentation reactions by impact of the 1.4 GeV proton beam and their decay modes. (Adapted from ref. [34]).

cooled copper transfer line and equipped with a calibrated leak of 5×10^{-5} mbar L/s (air) allowing the injection of SF_6. A typical mass spectrum of the extracted beam is shown in fig. 5. The predominant species is BF_2^+, which is expected to arise from dissociative ionization of BF_3. The container was gradually heated from about 100 °C to 1600 °C. The ion yield rises from lower temperatures to a maximum at about 1500 °C and drops again towards higher temperatures. In sect. 4 it was shown that fast diffusion of boron in graphite and CNT is expected in this temperature range, thus the extraction of boron fluoride from a CNT target is also expected.

Besides the dependency of the extracted boron fluorides current on temperature, the dependency on the amount of injected SF_6 was studied in the range from 1×10^{-5} to 5×10^{-5} mbar L/s (air). From equilibrium calculations a linear dependency of the BF_3 formation on available fluorine is expected. This correlation was confirmed in the measurements. The extracted ion current of BF_2^+ increases linearly with an increase of injected fluorine. Consequently, a high flow rate of injected sulfur fluoride leads to the most efficient extraction. However, the flow rate is limited by the target station gas pumping capabilities, which have to maintain a pressure below 5×10^{-5} mbar on the extraction side to ensure proper operation of the ion source and beam transport.

The calibrated leak allows to determine the combined efficiency for ionization, formation of the compound and transport from target container to ion source, which are ϵ_{ion}, ϵ_{form} and ϵ_{irrev} in eq. (1), respectively. The combined efficiency was evaluated to be 1.5%. While the release studies (sect. 4) were done on a time-scale much longer than the half-life of ^{8}B, making the assessment of the release efficiency difficult, these results lead us to expect that some fraction of the in-target yield would be produced as BF_2^+ molecular ions.

7 Online measurements

Two target units have been tested in three online runs at ISOLDE. Following the outcome of our preparatory experiments, we have chosen CNT as target material. The ABRABLA code predicts the formation of ^{8}B mainly by fragmentation of ^{12}C which is induced by impact of the 1.4 GeV proton beam. A water-cooled transfer line ensured that only volatile compounds like BF_3 could reach the VADIS ion source. A constant flow of SF_6 was applied through a calibrated leak.

The first target unit tested in 2014 was equipped with a calibrated leak of 3.7×10^{-5} mbar L/s (air). Measurements started at a target temperature of 1350 °C which was successively increased to a maximum of 2000 °C. The extracted radionuclides have been characterized with the ISOLDE tape station [35] located at the central beam line. The tape station allows measurements with a plastic scintillator in 4π geometry and a high purity germanium gamma detector.

As shown in fig. 6, ^{8}B is known to undergo $\beta^+2\alpha$ decay, the isobaric ^{8}Li, which is also produced in fragmentation reactions of ^{12,13}C, decays by $\beta^-2\alpha$ [36]. Therefore, the annihilation radiation allows to distinguish between both isobars. In the investigated temperature range the scintillation counter indicated activity on mass 8, reaching a maximum of $1 \times 10^4/\mu$C at 2000 °C. The half-life was determined to be 800 ± 100 ms. The annihilation peak in the gamma spectrum revealed, that 3% of the activity found by scintillation counts was originating from β^+ emitters, leading to a ^{8}B yield of $3 \times 10^2/\mu$C. Potential isobaric contaminants on mass 8 are ^{8}Li and ^{8}He. While lithium is expected to be retained in the water-cooled transfer line, the volatile helium nuclides are extracted as beam and reach the tape of the tape station. During tape transport from collection to measurement position (900 ms) ^{8}He mostly decays to ^{8}Li, the latter causing scintillator events while

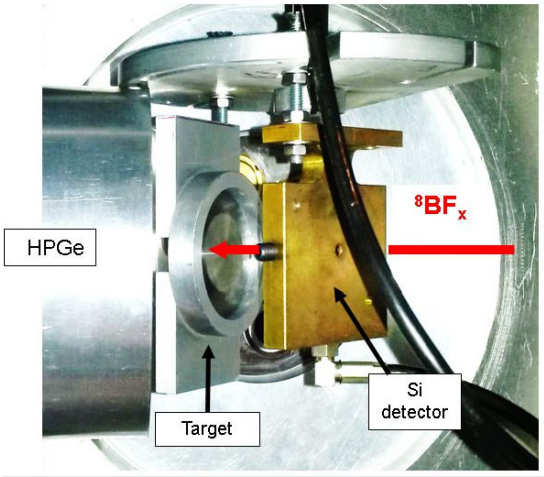

Fig. 7. In beam detection setup consisting of a silicon and high purity germanium detector.

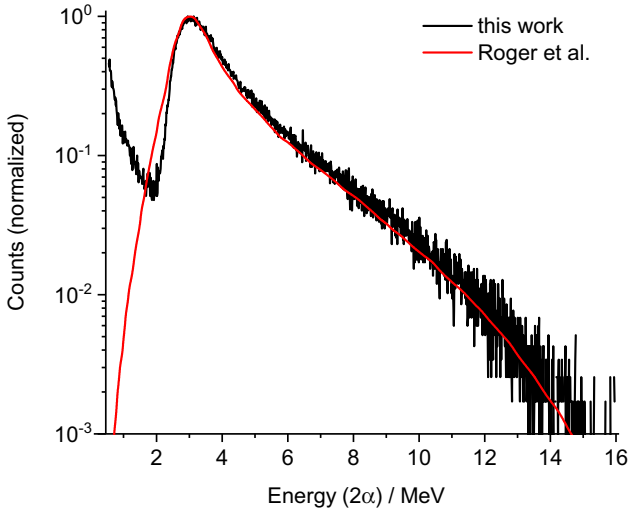

Fig. 8. Single alpha spectrum (black) recorded on the mass of $^8BF_2$ in comparison with two alpha spectrum taken by Roger *et al.* [9]. The respective energies of the single alpha spectrum have been multiplied by two to allow the comparison to the two alpha spectrum. The two alpha spectrum by Roger *et al.* is corrected for β summing and α detection efficiency. These minor corrections are not necessary for the identification of ^{8}B and therefore not included in this work.

the gamma radiation originating from the decay of ^{8}He is not seen. In contrast to offline studies, activity on the masses of ^{8}BF, $^8BF_2$, $^8BF_3$ as well as ^{8}BO, ^{8}BOC and ^{8}BOF could not be found. The detection limit for ^{8}B was calculated to be 75 ions per μC. The concurrent absence of stable SF_x and TaF_x ions, along with the absence of BF_x radioisotopes indicated that the formation of boron fluorides was limited by the availability of fluorine.

Therefore, we increased the size of the calibrated leak in the second unit to 1.8×10^{-4} mbar L/s. It contained 14.96 g of carbon nanotubes pressed to pellets of 15 mm diameter, yielding an areal density of 8.4 g/cm^2. In order to strengthen the argument that the measured activity is caused by ^{8}B we made use of an in-beam detection system (fig. 7) equipped with a silicon and a high purity germanium detector allowing the detection of alpha and gamma annihilation events in coincidence (15 μs window). In this experiment, the target was operated at 1500 °C as well as at 1750 °C. In contrast to the first measurement, beams of BF_x ($0 \leq x \leq 3$) radioisotopes could now be extracted and beams of stable sulfur fluorides were seen, indicating the availability of fluoride in the target. In agreement with the offline ionization tests, the yields were increasing in the series $^8BF_3 < {}^8BF < {}^8B < {}^8BF_2$. The yield found for $^8BF_2$ was calculated to be $6.4 \times 10^4/\mu$C at the target temperature of 1500 °C. As expected, ^{8}He was only found on mass 8 ($4.5 \times 10^3/\mu$C) and nearly all activity registered by the scintillator on the ^8BF_x masses could be assigned to a positron emitter.

Figure 8 shows a measured alpha spectrum in comparison with data obtained in a more sophisticated setup by Roger *et al.* [9] by implanting ^{8}B at a rate of 7 ions/s in a finely segmented double sided silicon micro strip detector (DSSD). Roger *et al.* applied a correction for contributions of β-particles and α-efficiency, which is not of importance for the unambiguous identification of ^{8}B, and therefore not considered in this work.

The high energy tails of both spectra are well in agreement. Minor deviations in the raising part of the spectra can be explained by the low energy threshold for α-particles in the setup, as well as electronic noise and contributions due to energetic β-particles. The consistence of both spectra along with registered annihilation radiation in coincidence with alpha events allows us to assign the activity to the decay of ^{8}B.

7.1 Release properties

The time-dependent release of $^8BF_2$ was studied with the scintillation counter of the ISOLDE tape station. In contrast to the offline mobility studies discussed in sect. 4, it was crucial to also consider effusion effects due to the significantly shorter time scale. A release curve is obtained by collecting a small fraction of the released ions at a well-defined time t after proton impact, determining the collected activity and repeating the procedure while varying t. Correcting this release curve by the decay losses during the extraction time t yields a release curve for a stable isotope of the same species $p(t)$, since the diffusion and effusion properties only depend on the chemical species and not on the isotope.

The release curve for a stable isotope $p(t)$ is given by a folding integral of effusion contribution $p_\nu \propto e^{-t/t_{\text{eff}}}$ [4] and diffusion contribution $p_\mu = -\mathrm{d}f(t)/\mathrm{d}t$. For an agglomeration of fibers $p(t)$ is given by

$$\begin{aligned} p(t) &= \frac{1}{A_K} \int_0^t p_\mu(t')\, p_\nu(t-t')\mathrm{d}t' \\ &= \frac{1}{A_K} \sum_{m=1}^{\infty} \frac{\mathrm{e}^{-c_m t/\tau_D} - \mathrm{e}^{-t/t_{\text{eff}}}}{\tau_D - c_m t_{\text{eff}}}\,, \end{aligned} \tag{5}$$

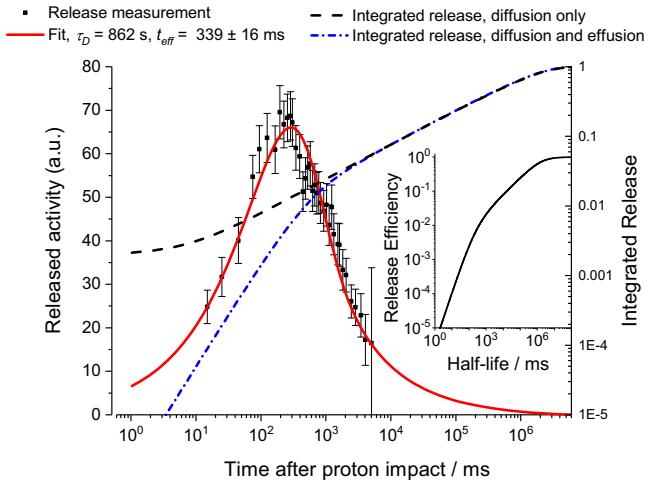

Fig. 9. Released activity *versus* time t after proton impact, measured with the scintillation detector of the ISOLDE tape station on the mass of $^{8}BF_2$ and corrected for the decay during release. Inset: release efficiency $y(T_{1/2})$, derived from the measured release curve and offline mobility studies (see text).

where the normalization parameter A_K is chosen such that $p(t)$ integrates to unity and computes to $A_K = \sum_{m=1}^{\infty} c_m^{-1}$. Folding the release function of the stable isotope $p(t)$ with the decay losses of a radioactive isotope ($T_{1/2}$) gives the fraction of released isotopes, the so called release efficiency y, which computes to

$$y(T_{1/2}) = \int_0^{\infty} p(t)\, \mathrm{e}^{-\ln(2)\, t/T_{1/2}}\, \mathrm{d}t = \frac{1}{A_K} \sum_{m=1}^{\infty} \frac{T_{1/2}^2}{(c_m T_{1/2} + \tau_D \ln(2))\,(T_{1/2} + t_{\mathrm{eff}} \ln(2))}\,. \quad (6)$$

The experimentally obtained release curve $p(t)$ is shown in fig. 9. The function following eq. (5) does not exhibit a strong constraint in the parameter τ_D. Therefore, the result obtained in the offline mobility studies was used, which is in agreement with the experimental data and allows us to determine the effusion time constant to be $t_{\mathrm{eff}} = 339 \pm 16$ ms. The expression used for the effusion contribution to the release function $p_\nu(t)$ holds for the effusion of uniformly distributed particles in a certain volume through a small orifice. However, the ISOLDE target container is connected via a transfer line to the ion source, which causes a delayed release. To account for the slower release, a second effusion time parameter leading to $p_\nu(t) \propto (1 - \mathrm{e}^{-t/t_{\mathrm{eff1}}})\, \mathrm{e}^{-t/t_{\mathrm{eff2}}}$ was introduced in [37] based on the result of Monte Carlo simulations and was applied in [38]. In the case analyzed here, the second parameter did not improve the fit significantly and was therefore discarded.

To justify that effusion processes were neglected at high temperatures within the deduction of τ_D from offline mobility experiments, fig. 9 shows the integrated release according to eq. (4), where effusion is not considered, as well as the integration of the experimental release curve fitted by eq. (5) and therefore taking into account effusion. It can be seen from fig. 9 that at the heat treatment time of 30 minutes (1.8×10^6 ms) effusion contributions are negligible. Also shown as insert in fig. 9 is a plot of the release efficiency (eq. (6)). The release efficiency of the investigated isotope ^{8}B computes to 1.7% ($T_{1/2}$ = 770 ms), the release efficiencies of the isotopes ^{12}B ($T_{1/2}$ = 20.2 ms) and ^{13}B ($T_{1/2}$ = 17.3 ms) are expected to be 0.029% and 0.023%, respectively. Comparing the measured yield weighted by the release fraction with the in-target production predicted by ABRABLA, indicates an overall efficiency for BF_2 molecular formation, ionization and transport of $\epsilon_{\mathrm{irrev}}\, \epsilon_{\mathrm{form}}\, \epsilon_{\mathrm{ion}} = 1.1\%$, which is close to the efficiency value of 1.5% obtained in offline studies. Assuming in-target production yields predicted by FLUKA [39], the same efficiency product computes to 0.15%. The availability of this information allows to predict yields of the more exotic boron isotopes ^{12,13}B, which are given in table 3.

For practical purposes, ISOLDE release curves are typically fitted with the three exponential function given in eq. (7) and discussed in ref. [40].

$$p(t) = \frac{1}{A_L}\left(1 - \mathrm{e}^{-t/t_{\mathrm{rise}}}\right) \cdot \left(\alpha\, \mathrm{e}^{-t/t_{\mathrm{fall1}}} + (1-\alpha)\, \mathrm{e}^{-t/t_{\mathrm{fall2}}}\right). \quad (7)$$

The release properties obtained from the curve fit have been evaluated to be as follows for the release of a stable isotope.

Ion	t_{rise}	α	t_{fall1}	t_{fall2}
$^{8}BF_2^+$	52 ms	0.20	253 ms	3015 ms

7.2 Further developments and outlook

Another test of the target unit took place in 2016 aiming at post-acceleration of the low energy ^{8}B beam at HIE-ISOLDE [41]. In 2017, the first ^{8}B ISOL beams were delivered to a physics experiment (IS633) [42], investigating the electron capture of ^{8}B into highly excited states in ^{8}Be using the ISOLDE decay station [43]. In 2018, the first accelerated ^{8}B beams (4.9 MeV/u) were delivered via HIE-ISOLDE to study reaction dynamics of proton-halo induced collisions [44]. Instead of sulfur hexafluoride, the fluorinating agent tetrafluoromethane (CF_4) was used to avoid a possible sulfur contamination of the target station. After injection of CF_4, a stable isobaric contamination on the mass of $^{8}BF_2$ of ca. 2 nA was found in the low energy beam, which exceeds the typical acceptance limit of the high energy setup for efficient operation. The recorded mass spectra show molybdenum fluoride beams, and indicate that the contamination is arising from doubly charged ^{92}Mo. Parts of the VADIS ion sources are build of molybdenum, thus serving as molybdenum source. The development of a molybdenum-free ion source could increase the efficiency and beam yields for HIE-ISOLDE.

Table 3. Measured ($^{8}BF_2$) and predicted ($^{12,13}BF_2$) yields of radioactive boron beams based on the release efficiency function $y(T_{1/2})$ deduced from the measured release curve of $^{8}BF_2$, the ionization and extraction efficiency as well as in-target production cross sections computed by Monte Carlo codes.

Boron isotope	8		12		13
Half-Life	770 ms		20.20 ms		17.33 ms
Release Efficiency	1.7%		0.029%		0.023%
Code	ABRABLA	FLUKA	ABRABLA	FLUKA	FLUKA
In-target production/μC	3.3×10^8	2.4×10^9	2.2×10^8	7.3×10^8	5.2×10^6
Beam yield/μC	6.4×10^4		7.1×10^{2} [a]	3.2×10^{2} [a]	1.9×10^{0} [a]

[a] Predicted yield, which was not yet experimentally confirmed.

8 Conclusions

Following the experimental and calculation strategy shown here, we successfully developed and tested a target unit for the production of exotic boron ISOL beams. By using multiwalled carbon nanotubes we could achieve high mobility of boron inside the grains of the target material, which leads to a fast extraction of boron and therefore relatively small losses due to decay during the diffusion process. The low volatility and high reactivity of boron, which hampers the release in its atomic form could be overcome by the extraction as volatile molecule. We have chosen fluorides as volatile carriers for boron, which are produced *in-situ* by injection of sulfur hexafluoride into the target container. The compound was ionized in an arc discharge electron impact VADIS ion source which was equipped with a water cooled copper transfer line to retain condensible elements and compounds. In online experiments yields of 6.4×10^4 $^{8}BF_2$ ions per μC of protons could be determined while an average proton intensity of up to 2 μA is available at ISOLDE [1]. The attainable yields drastically exceed yields reported to date from thin-target facilities and therefore pave the way for new physics experiments.

We would like to thank the radio protection staff of CERN DGS/RP-DC, P. Carbonez, A. Chantelauze and G. Lagneau, for hosting the setup used for offline mobility studies and the possibility to use the radioactive sources. We also acknowledge support from the ISOLDE operating staff for separator setup and support during the online experiment, the ISOLTRAP team for their effort to investigate the beam composition, as well as R. Dos Santos Augusto for support regarding the FLUKA code, and A. Kelic-Heil for ABRABLA support. This work has been partly supported by the Spanish CICYT through projects, FPA2015-64969-P, and by the European Union by means of the European Commission within its Seventh Framework Program (FP7) via ENSAR (Contract No. 262010). Further, this project has received funding from the European Union Horizon 2020 research and innovation program under grant agreement No. 654002. One of the authors, CS, acknowledges support by the German BMBF via the Gentner program and his local project 05P12RDCIA.

Author Contribution Statement

All the authors were involved in the preparation of the manuscript. All authors have read and approved the final manuscript.

Data Availability Statement This manuscript has no associated data or the data will not be deposited. [Authors' comment: All data generated during this study are contained in this published article.]

References

1. R. Catherall, W. Andreazza, M. Breitenfeldt, A. Dorsival, G.J. Focker, T.P. Gharsa, T. Giles, J.L. Grenard, F. Locci, P. Martins *et al.*, J. Phys. G: Nucl. Part. Phys. **44**, 094002 (2017).
2. U. Köster, P. Carbonez, A. Dorsival, J. Dvorak, R. Eichler, S. Fernandes, H. Frånberg, J. Neuhausen, Z. Novackova, R. Wilfinger *et al.*, Eur. Phys. J. ST **150**, 285 (2007).
3. C. Seiffert, *Production of radioactive molecular beams for CERN-ISOLDE*, Doctoral Thesis, Technische Universität Darmstadt, Germany (2014) `http://cds.cern.ch/record/2064456`.
4. R. Kirchner, Nucl. Instrum. Methods Phys. Res. Sect. B **70**, 186 (1992).
5. J. Ramos, A. Gottberg, T. Mendonça, C. Seiffert, A. Senos, H. Fynbo, O. Tengblad, J. Briz, M. Lund, G. Koldste *et al.*, Nucl. Instrum. Methods Phys. Res. Sect. B **320**, 83 (2014).

6. A. DiPietro, P. Figuera, A. Bonaccorso, M. Fisichella, J. Gomez-Camacho, M. Lattuada, M. Milin, A. Musumarra, M. Pellegriti, D. Santonocito *et al.*, Tech. Rep. CERN-INTC-2010-063. INTC-I-126, CERN, Geneva (2010) `https://cds.cern.ch/record/1298251`.
7. M. Pellegriti, P. Descouvemont, A. DiPietro, P. Figuera, M. Fisichella, M. Lattuada, M. Milin, A. Musumarra, V. Scuderi, D. Torresi *et al.*, Tech. Rep. CERN-INTC-2010-069. INTC-I-127, CERN, Geneva (2010) `https://cds.cern.ch/record/1298603`.
8. Sacavm Lisbon Leuven Göttingen Porto Durban CERN Collaboration, EC-SLI Collaboration (U. Wahl, L. Amorim, J.P. Araujo, K. Bharuth-Ram, J.G. Correia, M.R. da Silva, S. Decoster, H. Hofsäss, M. Nagl, L. Pereira *et al.*), Tech. Rep. CERN-INTC-2010-077. INTC-I-130, CERN, Geneva (2010) `https://cds.cern.ch/record/1298732`.
9. T. Roger, J. Büscher, B. Bastin, O.S. Kirsebom, R. Raabe, M. Alcorta, J. Äystö, M.J.G. Borge, M. Carmona-Gallardo, T.E. Cocolios *et al.*, Phys. Rev. Lett. **108**, 162502 (2012).
10. O.S. Kirsebom, S. Hyldegaard, M. Alcorta, M.J.G. Borge, J. Büscher, T. Eronen, S. Fox, B.R. Fulton, H.O.U. Fynbo, H. Hultgren *et al.*, Phys. Rev. C **83**, 065802 (2011).
11. J.R. Rumble (Editor), *CRC Handbook of Chemistry and Physics: A Ready-Reference Book of Chemical and Physical Data*, 99th edn. (Taylor & Francis, 2018).
12. A. Kelic, M.V. Ricciardi, K.H. Schmidt, *ABLA07 - towards a complete description of the decay channels of a nuclear system from spontaneous fission to multifragmentation*, in *Proceedings of the Joint ICTP-IAEA Advanced Workshop on Model Codes for Spallation Reactions, Trieste, Italy, February 4-8, 2008* (IAEA, 2008) arXiv:0906.4193.
13. T. Bjørnstad, E. Hagebø, P. Hoff, O. Jonsson, E. Kugler, H. Ravn, S. Sundell, B. Vosicki, Nucl. Instrum. Methods Phys. Res. Sect. B **26**, 174 (1987).
14. W. Callister, *Materials Science and Engineering: An Introduction* (John Wiley & Sons, New York, 2007).
15. M. Fujioka, Y. Arai, Nucl. Instrum. Methods Phys. Res. Sect. B **186**, 409 (1981).
16. H. Fechtig, S. Kalbitzer, *The Diffusion of Argon in Potassium-Bearing Solids* (Springer Berlin Heidelberg, Berlin, Heidelberg, 1966) pp. 68–107.
17. D. Fink, L. Wang, Radiat. Effects Defects Solids **114**, 343 (1990).
18. D. Brown, M. Chadwick, R. Capote, A. Kahler, A. Trkov, M. Herman, A. Sonzogni, Y. Danon, A. Carlson, M. Dunn *et al.*, Nucl. Data Sheets **148**, 1 (2018).
19. A. Göpfert, F.J. Hambsch, H. Bax, Nucl. Instrum. Methods Phys. Res. Sect. A **441**, 438 (2000).
20. L.W. Weston, J.H. Todd, Nucl. Sci. Eng. **109**, 113 (1991).
21. J. Vacik, V. Hnatowicz, J. Cervena, S. Posta, U. Köster, G. Pasold, AIP Conf. Proc. **1099**, 836 (2009).
22. J. Ramos, A. Senos, T. Stora, C. Fernandes, P. Bowen, J. Eur. Ceramic Soc. **37**, 3899 (2017).
23. G. Heller, *Gmelin Handbook of Inorganic and Organometallic Chemistry - B Boron Compounds, 4th Supplement, Boron and Oxygen* (Springer Berlin Heidelberg, 1991) `https://doi.org/10.1007/978-3-662-06150-3`.
24. G. Henning, J. Chem. Phys. **42**, 1167 (1965).
25. Y.V. Novak, T.V. Pyrkova, A.F. Kuteinikov, Khimiya Tverdogo Topliva **16**, 127 (1982).
26. J.F. Ziegler, M. Ziegler, J. Biersack, Nucl. Instrum. Methods Phys. Res. Sect. B **268**, 1818 (2010).
27. J.F. Ziegler, *SRIM The Stopping Range of Ions in Matter*, `http://www.srim.org` (2018) (accessed 24 August 2018).
28. J.P. Ramos, *Thick solid targets for the production and on-line release of radioisotopes: the importance of the material characteristics - A Review*, in preparation.
29. A.I. Skoulidas, D.M. Ackerman, J.K. Johnson, D.S. Sholl, Phys. Rev. Lett. **89**, 185901 (2002).
30. A. Noy, J. Phys. Chem. C **117**, 7656 (2013).
31. G.A. Perkova, A.V. Demin, E.F. Chalykh, Y.M. Kachanov, Khimiya Tverdogo Topliva **5**, 163 (1976).
32. A. Roine, *HSC Chemistry 7.1*, `http://www.hsc-chemistry.net` (2010) (accessed 19 July 2015).
33. L. Penescu, R. Catherall, J. Lettry, T. Stora, Rev. Sci. Instrum. **81**, 02A906 (2010).
34. Nucleonica GmbH, *Nucleonica Nuclear Science Portal*, `www.nucleonica.com` (2017) version 3.0.65.
35. M. Turrión, M. Eller, R. Catherall, L. Fraile, U. Herman-Izycka, U. Köster, J. Lettry, K. Riisager, T. Stora, Nucl. Instrum. Methods Phys. Res. Sect. B **266**, 4674 (2008).
36. W.T. Winter, S.J. Freedman, K.E. Rehm, J.P. Schiffer, Phys. Rev. C **73**, 025503 (2006).
37. E. Bouquerel, *Atomic beam merging and suppression of alkali contaminants in multi body high power targets: Design and test of target and ion source prototypes at isolde*, Doctoral Thesis (2009).
38. T. Stora, E. Noah, R. Hodak, T.Y. Hirsh, M. Hass, V. Kumar, K. Singh, S. Vaintraub, P. Delahaye, H. Franberg-Delahaye *et al.*, EPL **98**, 32001 (2012).
39. A. Ferrari, P.R. Sala, A. Fass, J. Ranft, *FLUKA: A multi-particle transport code (program version 2005)*, CERN Yellow Reports: Monographs (CERN, Geneva, 2005) `http://cds.cern.ch/record/898301`.
40. J. Lettry, R. Catherall, P. Drumm, P. Van Duppen, A. Evensen, G. Focker, A. Jokinen, O. Jonsson, E. Kugler, H. Ravn *et al.*, Nucl. Instrum. Methods Phys. Res. Sect. B **126**, 130 (1997).
41. Y. Kadi, Y. Blumenfeld, W.V. Delsolaro, M.A. Fraser, M. Huyse, A.P. Koufidou, J.A. Rodriguez, F. Wenander, J. Phys. G: Nucl. Part. Phys. **44**, 084003 (2017).
42. M. Borge, J. Cederkall, P. Diaz Fernandez, L. Fraile, H. Fynbo, A. Heinz, J. Jensen, H. Johansson, B. Jonson, O. Kirsebom *et al.*, Tech. Rep. CERN-INTC-2016-052. INTC-P-482, CERN, Geneva (2016) `http://cds.cern.ch/record/2222324`.
43. ISOLDE-IDS Setup, `http://isolde-ids.web.cern.ch/isolde-ids/#setup` (2018) (accessed 31 July 2018).
44. A. Di Pietro, P. Figuera, J. Ballof, A. Bonaccorso, J. Cederkall, T. Davinson, J. Fernandez Garcia, M. Fisichella, M. Garcia Borge, J. Gomez Camacho *et al.*, Tech. Rep. CERN-INTC-2016-018. INTC-P-463, CERN, Geneva (2016) `https://cds.cern.ch/record/2120157`.

5 Molecular beams as means of beam purifaction

Contents

A common issue of mass-separated beams is that the isotope of interest is accompanied by isobars, *i.e.*, isotopes of different elements of same mass number. This chapter provides a brief overview of means to purify ISOL beams and includes a publication about extraction of carbonyl selenide beams.

5.1 Purification of ISOL beams

Selectivity plays a role at each step of the ISOL process. To avoid overloading downstream processes, measures to control purity should be implemented as early as possible in the process chain from target material to the user experiment [59].

Selectivity can be achieved by choice of i) projectile and target material, ii) carrier species, iii) transfer line, iv) ion source and iv) (high-resolution) mass-separation. Depending on the application, further purity can be reached with a second separation step [190]. For online operation, this could be break-up of molecules in the EBIS and subsequent mass separation [236]. For offline-processing, wet-chemical separation is available [234].

Aspects regarding target material, projectile (*e.g.* proton-to-neutron converter), transfer line and ion source have already be discussed in Chapter 1 and are briefly summarized below. If the species of interested is more volatile than the contaminant, the latter can be retained on the transfer line by temperature controlled adsorption. Resonant laser ionization is element specific, however surface ionized contaminants remain largely unsuppressed. Laser ion sources with suppression of surface ions have been developed but come at the cost of significantly reduced ionization efficiency [88].

To apply separation by chemoselective sideband formation, all prerequisits for molecular beam extraction, as discussed in Chapter 4, have to be met for the species of interest. An additional requirement emerges for the contaminant. At least one of the prequisits must not be fulfilled for the latter [189]. The isobaric contaminant typically belongs to a different group in the periodic table of elements, so that chemical properties differ. For example, alkali elements do not form fluoride sidebands in contrast to the alkaline earth elements. Or, as shown in the article below, arsenic does not efficiently form sulfide sidebands, while germanium sulfide is efficiently extracted. Often, the presence or absence of sidebands can be explained by thermodynamic stability of the molecuar species, see, *e.g.*, ref. [190] for stability of sulfides in comparison to extracted sidebands. The thermodynamic stability (equilibrium composition of a system) can be predicted with codes like HSC [237], if thermodynamic data (enthalphy, entropy of formation, heat capacity) are available.

5.2 Carbonyl selenide beams

The compound COSe was first synthesized sufficiently pure for characterization by Pearson and Robinson in the early 1930s [238]. At room temperature, it was described as colourless evil-smelling gas that easily decomposes when exposed to humidity, light or comes into contact with porous materials like charcoal [239]. The first synthesis was achieved by passing dried carbon monoxide over heated selenium. The yield was found to depend on the materials of the apparatus, the flow rate of carbon monoxide and the temperature. Glemser and Risler report yields of ca. 10 vol.−% COSe in carbon monoxide with selenium kept at 780 °C [239]. Other synthesis routes with higher yields were described, *e.g.*, via aluminium selenide and phosgene (carbonyl chloride) [239] or from selenium and carbon monoxide in the presence of amines at ambient temperature and pressure [240]. Purcell and Zahoorbux studied the decomposition of the compound [241]. The equilibrium COSe $\rightleftharpoons$ CO + Se was found to shift towards CO and Se at

lower temperatures and at 140 °C no formation but only decomposition was found on a glass surface covered by the deposited selenium film. Fluctuations in the measured rate constant were attributed to catalytic effects of the surface, which vary due to the allotropic complexity of selenium.

Carbonyl selenide as volatile carrier for selenium fission recoils was reported and identified by Baldwin *et al.* [242]. The compound forms *in-situ* upon thermalization of recoils in carbon monoxide. While selenium fission recoils were reported to form COSe in low yields (ca. 0.02%), selenium produced in (n, γ)-reactions (lower kinetic energy) did not form COSe. Wachsmuth *et al.* report an efficiency of 10% for the transport of selenium fission products thermalized in helium gas containing 600 ppm carbon monoxide [243]. It was also reported that the volatile selenium compound could be decomposed at temperatures above 800 °C in a quartz tube. In a similar experiment, yields of 6.3% were found, even after transport through a 80 m-long Polyethylene (PE) capillary [244].

Thermochemical data that would allow the calculation of chemical equilibrium compositions (*e.g.*, enthalpy and entropy of formation) is not available for COSe. However, spectroscopic studies indicate that the stability of homologue compounds decrease in the order CO_2 > COS > COSe > COTe [245,246]. This is in agreement with the efficiency for compound formation of recoils. Carbonyl sulfide is formed in high yields [247], lower yields are obtained for COSe [242] and COTe could not be produced by thermalization of fission recoils [242].

While carbonyl selenide beams could be extracted at ISOLDE from zirconia targets [192], the mechanism of molecule formation remains unclear. In particular, the source of carbon could not yet be identified. Its depletion is suspected to cause decreasing intensities of COSe beams which vanish after few days of operation. The article presents online and offline studies towards molecule formation. Earlier work suggested that injection of oxygen or carbon dioxide could promote molecule formation. The results presented in the article below indicate that neither carbon dioxide nor carbon monoxide or oxygen promote formation of carbonyl selenide in the investigated setup. Introduction of excess graphite into the ion source could also not prevent the depletion of the carbonyl selenide sidebands. In contrast, injection of carbon tetrafluoride gas could partially recover the vanished sideband.

5.3 Contributions

Within this thesis, experiments towards COSe formation with trace quantities of stable isotopes have been conducted at the Offline 1 separator and online experiments yielding radioactive isotopes were conducted at ISOLDE. The offline and online measurements towards molecule formation were conducted and analyzed by myself. The publication was prepared in collaboration with K. Chrysalidis, who reported about resonant laser ionization of selenium. The article was jointly written by K. Chrysalidis and myself according to the individual contributions.

Eur. Phys. J. A (2019) **55**: 173
DOI 10.1140/epja/i2019-12873-4

THE EUROPEAN PHYSICAL JOURNAL A

Regular Article – Experimental Physics

Developments towards the delivery of selenium ion beams at ISOLDE

K. Chrysalidis[1,2,a], J. Ballof[1,3,b], Ch.E. Düllmann[3,4,5], V.N. Fedosseev[1], C. Granados[1], B.A. Marsh[1], Y. Martinez Palenzuela[1,6], J.P. Ramos[1], S. Rothe[1], T. Stora[1], and K. Wendt[2]

[1] CERN, 1211 Geneva, Switzerland
[2] Institut für Physik, Johannes Gutenberg-Universität, 55099 Mainz, Germany
[3] Institiut für Kernchemie, Johannes Gutenberg-Universität, 55099 Mainz, Germany
[4] Helmholtz-Institut Mainz, 55099 Mainz, Germany
[5] GSI Helmholtzzentrum für Schwerionenforschung, 64291, Darmstadt, Germany
[6] KU Leuven, Instituut voor Kern- en Stralingsfysica, 3001 Leuven, Belgium

Received: 24 April 2019 / Revised: 15 August 2019
Published online: 14 October 2019

Communicated by K. Blaum

Abstract. The production of selenium ion beams has been investigated at the CERN-ISOLDE facility via two different ionization methods. Whilst molecular selenium (SeCO) beams were produced at ISOLDE since the early 1990s, recent attempts at reliably reproducing these results have so far been unsuccessful. Here we report on tests of a step-wise resonance laser ionization scheme for atomic selenium using the ISOLDE Resonance Ionization Laser Ion Source (RILIS). For stable selenium an ionization efficiency of 1% was achieved. During the first on-line radioisotope production tests, a yield of $\approx 2.4 \times 10^4$ ions/μC was measured for $^{71}Se^+$, using a ZrO_2 target with an electron impact ion source. In parallel, an approach for extraction of molecular carbonyl selenide (SeCO) beams was tested. The same ion source and target material were used and a maximum yield of $\approx 3.6 \times 10^5$ ions/μC of $^{71}SeCO^+$ was measured.

1 Introduction

CERN-ISOLDE is an isotope separation on-line facility [1, 2], where isotopes can be produced, then ionized and extracted within one apparatus, often in a selective (isotope purity) and efficient (up to several percent overall efficiency) process. This method provides the means to supply ion beams of exotic isotopes, far from stability, with half-lives as low as several ms [3]. For this purpose, protons, provided by the CERN Proton Synchrotron Booster (PSB) with an energy of 1.4 GeV, impinge on a thick target. Reaction products created by spallation, fragmentation or fission are then evaporated from the target material and ionized. The target and ion source assembly is situated on a 20–60 kV high voltage platform and is resistively heated causing the reaction products to diffuse through the target material and effuse into the ion source. Once the atoms or molecules have been ionized, they are extracted by the grounded extraction electrode situated downstream of the ion source. The temperature of ion source and target container are controlled by two separate electrical circuits, allowing to independently adjust the temperatures within a wide range.

Three main methods are used at ISOLDE to produce ion beams: thermal ionization on a hot metal surface, electron impact ionization in a FEBIAD-type (Forced Electron Beam Induced Arc Discharge) ion source or VADIS (Versatile Arc Discharge Ion Source) [4], and laser resonance ionization. The laser-atom interaction can take place in different environments: a hot cavity surface ion source [5], a radio-frequency ion guide LIST (Laser Ion Source and Trap) [6] or a VADIS operated at reduced anode voltage [7,8].

Several attempts have been made to produce selenium beams at ISOLDE in the past, namely for Coulomb excitation studies using post-accelerated ^{70}Se [9]. Such an experiment requires a beam purity in the order of 90%. Due to the abundance of isobaric contaminants expected at the desired atomic masses, un-selective FEBIAD ionization of elemental selenium is not expected to yield the required purity for the proposed Coulomb-excitation experiment using HIE-ISOLDE [10,11]. Even the element selective RILIS process might not yield the required purity, since selenium ($Z = 34$) is located half-way between the

[a] e-mail: katerina.chrysalidis@cern.ch (corresponding author)
[b] e-mail: jochen.ballof@cern.ch

surface ionizable elements gallium ($Z = 31$) and rubidium ($Z = 37$). Isobars of one of these elements tend to be produced at comparable or higher yields for most Se isotopes. Thus all neutron-rich Se isotopes ($A > 80$) produced from GeV proton-induced fission of any type of U or Th target will likely suffer from isobaric Rb, while spallation-produced neutron-deficient Se isotopes up to about ^{73}Se will suffer from isobaric Ga. In some cases the isobars are stable (^{67,69}Ga and ^{85,87}Rb), allowing decay spectroscopy studies. However, these isobars will still affect any type of experiment that is disturbed by stable contaminants, due to ion load limitations (such as ion beam bunching and charge breeding before post-acceleration). However, for the molecular beam ^{x}SeCO^{+}, fewer contaminant isobars are expected, which are mainly ^{27}Al^{x+1}Br^{+} [12] and $^{x-4}$Ge^{32}S^{+}.

In a past experiment, contamination from isobaric ^{72}Ga^{+} was avoided by extracting selenium in the form of a SeCO^{+} beam, through the use of a FEBIAD-type ion source. The SeCO^{+} was subsequently broken up inside the Electron Beam Ion Source (EBIS) of the REX-ISOLDE and the resulting Se^{n++}-ions were post-accelerated. The disadvantage of this approach is that a significant amount of the ions of interest are lost, due to the distribution among different molecular fractions [13]. Furthermore, many low-energy experiments at ISOLDE, which are situated upstream of the EBIS, are not readily able to make use of molecular beams (solid state physics implantations, collinear laser spectroscopy, etc.). These experiments would profit from the production of elemental Se^{+} beams. The Resonance Ionization Laser Ion Source (RILIS) [14], which is the most commonly used ion source at ISOLDE, can provide this alternative and generate an element-selective way of ionizing selenium.

2 Laser ionization of selenium atoms

2.1 Atomic structre of selenium

Selenium belongs to the chalcogens (oxygen group) along with oxygen (O), sulfur (S), tellurium (Te) and polonium (Po). Chalcogens have six valence electrons and relatively high ionization energies, which decrease with increasing atomic number. They are therefore not efficiently surface ionized in the typical Ta, W or Re surface ion source at maximum temperatures of around 1800–2500 °C. At ISOLDE, laser ionization schemes for Te and Po have been developed and applied in past experiments [15,16].

The information on the atomic level structure of Se atom available in [17] is mostly based on the spectral data obtained in [18,19]. The electronic configuration of the Se atomic ground state is [Ar]$4s^2 4p^4\,{}^3$P with $J = 2$. The state [Ar]$4s^2 4p^4\,{}^3$P forms a triplet as shown in fig. 1. An estimation of thermal population of these states can be derived from Boltzmann distribution calculations. At $T = 2000\,°$C (used for the measurements, see sect. 4), 83% of the ^{3}P$_2$ state is populated, whilst the ^{3}P$_1$ and ^{3}P$_0$ states are populated with 14% and 3% respectively. The lowest-lying energy level accessible via a single-photon transition is the

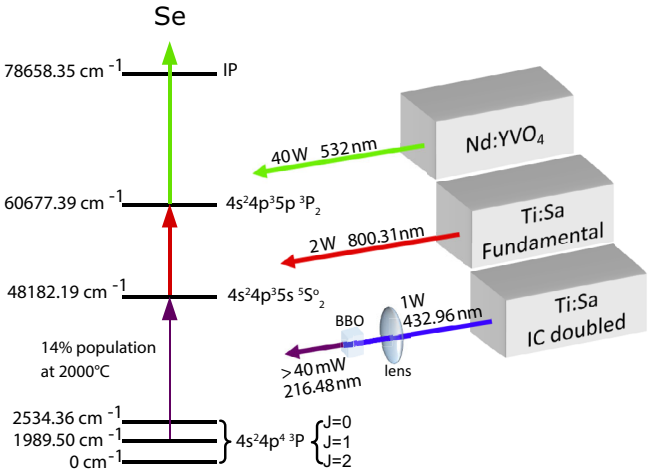

Fig. 1. Ionization scheme for atomic selenium alongside the RILIS lasers which provided the excitation steps with their respective powers. The first step is provided by intra-cavity (IC) frequency doubling a Ti:Sapphire laser and subsequent frequency doubling of this blue output in a single pass through a BBO crystal to generate UV light at 216.5 nm. The Ti:Sapphire lasers are pumped by frequency doubled Nd:YAG lasers at 532 nm. Typical pulse lengths are $\approx$ 50 ns. The Nd:YVO$_4$ is a BLAZE laser from *Coherent*. The population for the metastable level used for the chosen first step excitation is given. Level configurations and energies are from [17], vacuum wavelengths are given.

$4s^2 4p^3 5s\,{}^5$S$^o_2$ state at an energy of 48182.19 cm^{-1}. Excitation to this state can be achieved either from the ground state ^{3}P$_2$ (207.55 nm$_{\mathrm{vac}}$) or from the first metastable state ^{3}P$_1$ (216.48 nm$_{\mathrm{vac}}$). The transition from the ground state is the preferred option for optimal ionization efficiency due to the thermal population distribution.

2.2 RILIS laser set up and ionization scheme development

The current status of the ISOLDE RILIS is described in detail in reference [14]. Typically 2-3 tunable, pulsed (10 kHz repetition rate) laser beams are temporally and spatially overlapped inside the ion source cavity and tuned to an element-specific multi-step resonance ionization scheme. The optimal ionization scheme is typically determined for each element by a dedicated resonance ionization spectroscopy study. An ideal ionization scheme is one that combines maximum efficiency with a convenient (reliable, easy to set up and maintain) laser configuration.

For generating the first excitation step, an attempt was made to produce 207.55 nm$_{\mathrm{vac}}$ light by 4th harmonic generation using a Ti:sapphire laser with an intra-cavity second harmonic generation (SHG) and focusing its $\approx$ 1 W blue output with a 150 mm focal length lens, into a $6 \times 5 \times 4$ mm BBO crystal (type 1 SHG - angle 79.7°, supplied by CRYSTECH INC). Although up to 50 mW at 207.55 nm$_{\mathrm{vac}}$ was achieved, destructive absorption of

Table 1. Second step transitions investigated during the ionization scheme development for selenium, with the first step set to 216.48 nm_{vac}. The relative ion beam intensities achieved using these second steps, compared to the most efficient ionization scheme using the $4p^3 5p\,^3P_2$ state are given. The expected laser power transmission to the ion source is ≈ 70% for the non-resonant step at 532 nm. The 5 new transitions that were found are marked in bold.

2nd step ΔE [cm^{-1}]	E_{total} [cm^{-1}]	3rd step	rel. int.
12495.20	60677.39	532 nm	1
24901.15	73082.34	scan for AI	
24912.21	73094.40		5×10^{-3}
24870.10	73052.29	532 nm	7×10^{-3}
24860.73	73042.92		3×10^{-2}
24435.99	72618.18		1×10^{-5}
17376.5(2)	**65558.7(2)**		
17380.4(2)	**65562.6(2)**		
17422.0(2)	**65604.2(2)**	532 nm	1×10^{-5}
17744.5(2)	**65926.7(2)**		
17795.5(2)	**65977.7(2)**		

this wavelength in the BBO crystal occurred within minutes. The severe loss of 4th harmonic generation efficiency therefore renders this approach impractical.

Therefore, the metastable state with the estimated population of 14% was used for the measurements described in this work (see fig. 1). The clear disadvantage is an expected loss in efficiency of a factor ≈ 6, due to the lower thermal population at 2000 °C compared to the ground state. The required wavelength of 216.48 nm_{vac} was generated by 4th harmonic generation of a Ti:sapphire laser operating at 865.92 nm_{vac}. The same method described above, this time with a BBO crystal at 69.7°, was used.

For the initial verification of the laser beam position and overlap, transitions known from the literature [18] were tested as second steps. An additional laser, operating at 532 nm with a power of 40 W (10 kHz repetition rate and 17 ns pulse length), was used for non-resonant ionization into the continuum. The power of this laser was stable for all measurements listed in table 1 and the position inside the ion source remained fixed through the use of an active beam stabilization system. The first of the second-step transition tested leads to the $4s^2 4p^3 5p\,^3P_2$ level at a total energy of 60677.388 cm^{-1}, corresponding to a required transition wavelength of ≈ 800.31 nm_{vac}. The alternative transition to the $4s^2 4p^3 5p\,^3P_1$ state was not tested due to the lower J quantum number of this state. The lower occupancy of this level $(2J + 1)$ is expected to result in a reduced maximum ionization efficiency [20]. Several other transitions that can be found in literature were tested and are listed in table 1. The relative intensities compared to the ionization pathway via the $4s^2 4p^3 5p\,^3P_2$ level were of the order of 1×10^{-5}–3×10^{-2}. No further investigations into these states were performed since, based on previous experience, it is not reasonable to expect that a transition to an autoionizing state from these levels would yield more than a factor 3–5 enhancement in ionization efficiency [21].

Therefore, a search for new second-step transitions was performed by scanning the second step laser wavelength in the range of 720–920 nm and 558–592 nm. These scans were carried out using respectively a grating-based Ti:sapphire laser and a Rhodamine 6G dye laser available at the RILIS laser laboratory. In the range covered by the Ti:sapphire laser, no second-step transitions were found. The wavelength scan of the dye revealed five resonances, which could not be attributed as transitions from the $4s^2 4p^3 5s\ ^5S_2^o$ state to any of the higher levels tabulated in [17]. Since each of those resonances was observable only under presence of the laser beam at 216.48 nm_{vac}, it is reasonable to conclude that new excited levels, linked by the optical transitions with the $4s^2 4p^3 5s\ ^5S_2^o$ state, were found. The transitions and respective levels are listed in table 1. It is worth to mention that the table of lines observed in the arc spectrum of selenium (see [18]) contains four lines with frequencies very close to the newly found transitions (17376.46 cm^{-1}, 17380.37 cm^{-1}, 17421.99 cm^{-1} and 17795.41 cm^{-1}). However, the authors of [18] did not designate these transitions to the level used in our work. Neither of the transitions resulted in a sufficiently intense ion rate to be considered as a part of a favorable ionization scheme.

2.3 Laser ionization efficiency measurement

The RILIS efficiency is measured as the percentage of a calibrated-mass sample that is extracted and detected as an ion beam during optimal RILIS conditions. A sample with a calibrated amount of selenium (natural abundance) atoms (in standard solution of 5% HNO_3 on Ta foil) was inserted into one of the resistively heated capillary ovens, referred to as "mass markers" [22]. This was attached to the transfer line of the empty target container, as is schematically depicted in fig. 2. The sample was gradually evaporated over > 5 hours and the ion current was measured using a Faraday cup during this time. Integrating this measurement over the evaporation time reveals the total number of ions that reach the detection point (after extraction and mass separation).

The efficiency was determined to be ≈ 0.6%. Due to instabilities in the UV generation for the first step excitation, the power of this step was deliberately limited to 40 mW by moving the 4th harmonic generation crystal away from the focus of the intra-cavity generated blue light. Absorption-induced damage to the crystal is then reduced, resulting in a more stable operation. When reducing the power of the first step from ≈ 80 mW (on the laser table) to 40 mW, a drop in ion current of factor 2 was observed. If the UV light is kept at 80 mW, a correction with a factor of 2 can be applied to the calculated result from the data. Previously the RILIS at ISOLDE (or TRIUMF respectively) has been operated over extensive periods with UV light of comparable wavelengths, *e.g.* for ionization of Zn (65 mW on the table at 213.9 nm) or Sb (40 mW on the table at 217.6 nm) respectively (see

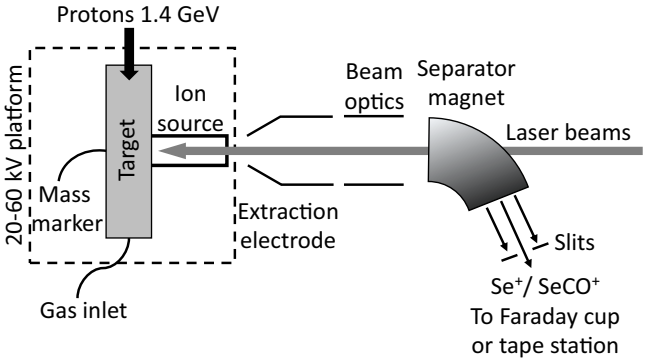

Fig. 2. Schematic view of the experimental set up (not to scale) of the target and ion source. Laser beams were directed into the ion source through a window in the mass separator vacuum chamber. The gas inlet for the production of molecular Se beams was attached to the side of the target container and the mass marker to the back of the transfer line. More details are given in the text.

also [23], table 4). Thus, stable operation with at least 65 mW of UV light can be guaranteed, leading to the efficiency value of 1%.

No uncertainty is quoted for the efficiency measurement since only a single measurement was performed. Nevertheless, this type of ISOL efficiency measurement is known to be susceptible to fluctuations due to several contributing factors such as an accumulation of the sample in cold spots of the target/ion source assembly, losses of a portion of the sample in preparation and initial target heating. The value should therefore be considered as a lower limit. Should reliable production of 207.5 nm_{vac} for a first step transition from the ground state become feasible, a laser ionization efficiency of about 10% can be expected, due to the higher thermal population of this state.

3 Production of molecular selenium

Molecular selenium beams were first reported in 1992 by Hagebø *et al.* [24] who operated a ZrO_2 fiber target equipped with a FEBIAD source under an additional oxygen partial pressure of 7×10^{-4} mbar. The selenium was extracted as carbonyl selenide (SeCO) and allowed spectroscopic studies on the isotopes ^{67,68}Se. However, the exact mechanism of molecular formation remained unclear. Parts of the ion source assembly were proposed as source of carbon which was likely emitted by the graphite grid of a FEBIAD MK5 ion source [25]. Also the source of oxygen remained unclear since the absence of SeCO beams was not confirmed prior to oxygen injection, and after discontinuing the oxygen injection, the SeCO beams did not deplete. A partial pressure of free oxygen is expected from the hot oxide target material itself. Despite this intrinsic presence of oxygen, the influence of additional oxygen supply was tested in 2016 at ISOLDE. Air, containing ca. 21% oxygen, was injected through a calibrated leak of 3.7×10^{-5} mbar L s^{-1} into a zirconia fiber target, as shown schematically in fig. 2. After injection, the radioactive ion yields of $^{67}Ge^{32}S^+$ and $^{71}SeCO^+$ decreased by factors of ten and two, respectively. A more recent suggestion is that SeCO formation is fostered by injection of carbon dioxide gas, which decomposes to carbon monoxide and oxygen at typical operation temperatures of the target and ion source. This in turn, would open up the classic synthetic route for carbonyl selenide (SeCO) [26].

The production mechanism of the compound inside the target unit was investigated, since issues regarding the stability of ion beam extraction had been observed. A steep decrease in the yields of carbonyl selenide was found, the most likely cause being a depletion of the carbon or oxygen source. To investigate the formation mechanism, tests at the ISOLDE off-line mass separator [27] were performed using target unit #605 which was equipped with a VADIS ion source [4], ZrO_2 fibers inside the tantalum target container and an oven supplying selenium. The setup allowed to study the influence of operation parameters on SeCO formation, which could be determined as the ratio between the extracted beams of $^{nat}Se^+$ and $^{nat}SeCO^+$. Target container and ion source cathode temperatures have been deduced from a calibration curve obtained by variation of the applied heating current, while monitoring the temperature with a pyrometer. The temperature of the ion source was measured at the cathode of the ion source assembly. Whilst varying the ion source cathode temperature in the range from 1960 to 2100 °C did not significantly affect the SeCO formation, a substantial influence of the target container temperature on the SeCO formation was observed. At low temperatures, the extraction is shifted towards the atomic selenium. The target unit was additionally equipped with a calibrated leak to introduce 99% isotopically enriched $^{13}CO_2$ into the ion source. The rate of the leak was initially chosen to be 2.5×10^{-5} mbar L s^{-1} and was later increased to 1.0×10^{-4} mbar L s^{-1} and 1.2×10^{-3} mbar L s^{-1}. The corresponding ^{13}CO partial pressures of 4.0×10^{-5}, 1.6×10^{-4} and 1.9×10^{-3} mbar, respectively, are expected to form in the ion source, based on the conductance estimation in the molecular flow regime and assuming, that CO_2 quantitatively breaks up to CO, in agreement with the Boudouard equilibrium.

The presence of ^{13}C inside the ion source could be verified in the extracted beams. For the largest leak rate, 177 nA of $^{12}CO^+$ and 2330 nA of $^{13}CO^+$ were measured, while the current on the mass of $^{13}CO^+$ was below 3 nA before injection of $^{13}CO_2$. Despite the expectations, the extracted $^{nat}SeCO$ beams are dominated by the ^{12}C isotope, and $^{nat}Se^{13}CO$ could not be unambiguously identified in the mass spectrum. Thus, the results indicate that the injected carbon dioxide does not serve as primary carbon source for carbonyl selenide formation. Furthermore, the formation of SeCO is significantly affected by the target temperature, as discussed in more detail in sect. 4.

An elementary analysis by electron-dispersive X-ray spectroscopy (EDS) did not show carbon above the detection limit of typically 0.1% in the zirconia target material itself. While the result shows, that no important carbon fraction is present in the material, a contribution of carbon *e.g.* originating from the decomposition of minor

amounts of zirconium carbide at elevated temperatures cannot be excluded. Another source of carbon are the structural parts of the target assembly, which is obvious from intense CO^+ beam typically extracted from freshly assembled target units without charge in the target container.

So far, injection of tetrafluoromethane (CF_4) was found to regenerate radioactive SeCO beams after depletion of the sideband, albeit at a lower yield. Further investigations are ongoing.

4 On-line yield measurements with ZrO_2 as target material

Two different target units (#605 and #612) with Yttria-stabilized zirconia fibers as target material were used for carbonyl selenide ion beam production. The target material was supplied by Zircar Zirconia Inc., PO BOX 287 87 Meadow Road, NY 10921 Florida, type ZYBF-5, lot #30D-96. Both target units were equipped with FEBIAD-type ion sources. Due to the decreasing production of SeCO during operation of the first target unit #605, it was investigated if the carbon inventory of the original FEBIAD MK5 source [25] can be exploited to foster SeCO formation. The earlier FEBIAD sources contained graphite parts (accelerating grid, outer ring of outlet plate), which were found responsible for a substantial carbon monoxide beam at elevated temperatures. These parts have been replaced by molybdenum within the development of the VADIS ion source [27]. Therefore for target unit #612 the molybdenum grid of the VADIS source was replaced by a graphite grid. Other than this part, the ion sources were identical. To minimize the reduction of the carbon inventory during offline conditioning, the heating time of the target before online operation was minimized for unit #612. This resulted in an initial CO^+ current of 540 nA for target unit #612, which was ca. five times the value of target unit #605, measured under comparable conditions.

Due to this additional supply of carbon, an enhancement of molecular formation of SeCO was therefore expected for the second target, unfortunately, this was not the case. Additionally, a comparison between a VADIS-ionized molecular beam of $SeCO^+$ and a resonantly laser ionized atomic beam in VADLIS mode (running with an anode voltage < 10 V) [7] was made with target #605. For the VADLIS measurements laser powers were optimized for efficiency, meaning that the first step was operated at 80 mW.

Yields of radioactive species for both target units were measured using gamma-ray spectroscopy with the ISOLDE tapestation [28], located at the central beamline, which is equipped with a plastic scintillator and a high purity germanium detector. The obtained yields strongly depend on the history of target heating and temperatures during the measurement. The yields for the different ionization mechanisms are given in fig. 3, alongside the temperature dependence and time evolution in fig. 4. Due to

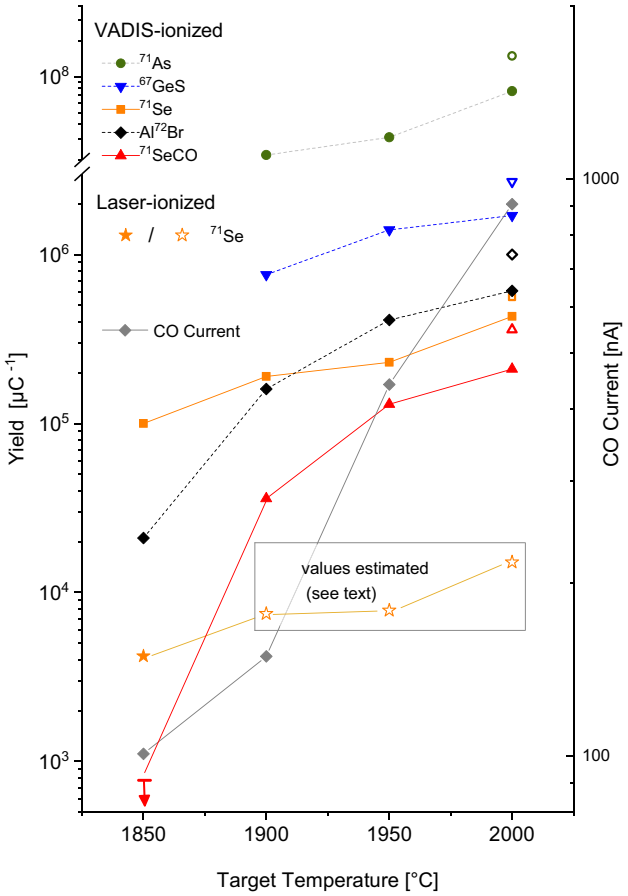

Fig. 3. Radioactive ion beam yields obtained from target #605 [ZrO] at the beginning of the run in dependence of the target container temperature. Open symbols represent measurements at an ion source cathode temperature of 2100 °C, otherwise the ion source cathode temperature was 2050 °C. The yield of laser-ionized $^{71}Se^+$ was only measured at a target temperature of 1850 °C, laser-ionized yields at higher temperatures were estimated by eq. (1). See text for details.

limited availability of beam time, the yield of laser ionized selenium could only be measured at the target temperature of 1850 °C. Contrarily, significant yields of molecular species were only present at higher target temperatures. It is well established that the fraction of radioactive species released from the target material before their decay typically increases with target temperature (see *e.g.* [29]). For prospective users of laser-ionized selenium beams, it is of interest to estimate the yield at higher temperatures. Thus, an estimation of expected laser-ionized selenium yields is required, which also allows a comparison of electron-impact and laser ionization yields. Within the given order of intensity (< 1 pA), the radioactive beam intensity scales linearly with the amount of neutrals introduced into the ion source. The latter equally holds for laser and electron impact ionization. Measurements with the FEBIAD source allow an estimation of the increase in atomic selenium injected into the ion source. In the FEBIAD source two major ionization channels

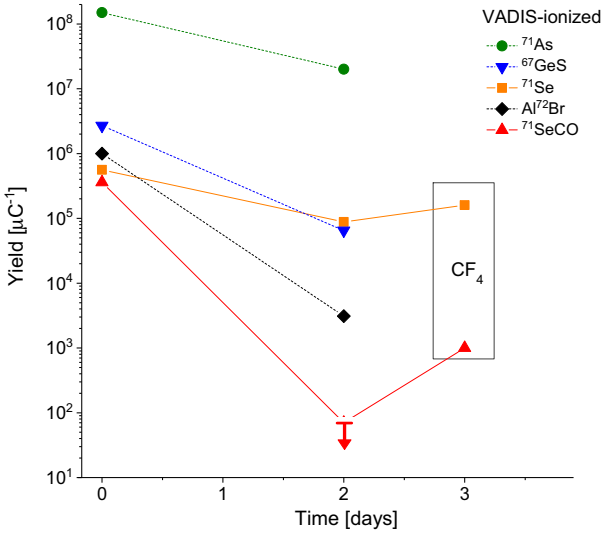

Fig. 4. Evolution of yields: After two days, the yield of $^{71}SeCO^+$ decreased below the detection limit of ≈ 200 ions/μC. Injection of CF_4 (after 3 days) could partially recover the beam. The connecting lines between the data points were inserted to guide the eye.

are expected to contribute to the extracted atomic Se^+ beams. Besides ionization of atomic selenium, an additional contribution is given due to dissociative ionization of selenium containing molecules. A search for selenium containing molecules other than SeCO including ^{71}SeO, ^{71}SeC, ^{71}SeF, $^{71}SeF_2$, $^{71}SeF_3$, $^{71}SeBr$, $^{71}SeCl$ and $^{71}SeAl$ remained unsuccessful. The dimer Se_2 as well as SSe have not been measured, however, the compounds are not predicted to be stable by the software package HSC above 1500 °C [30]. Thus, we assume that besides ionization of atomic selenium, only dissociative ionization of carbonyl selenide significantly contributes to the extracted Se^+ beams. The dissociative ionization can be expressed as $SeCO + e^- \rightarrow Se^+ + CO + 2e^-$. To the best of our knowledge, partial ionization cross sections of SeCO have not yet been reported. Within the offline studies prior to online operation of target units #605 and #612, the ratio of stable $^{nat}SeCO^+$ to $^{nat}Se^+$ beams was measured. The highest ratio found was, $^{nat}SeCO^+$ having twice the intensity of $^{nat}Se^+$ at an Anode voltage of 170 V. The ratio of injected neutral Se and SeCO is not known. However, from this measurement, it can be concluded, that no more than one third of the SeCO is extracted as atomic selenium ion beam. The value is in agreement with a fragmentation pattern published by Marquart *et al.* [31], which was measured at an electron energy of 70 eV. The neutral flow of atomic selenium $n_{Se}(T)$ at temperature T, can be conservatively estimated from the beam currents I of Se^+ and $SeCO^+$ as

$$n_{Se}(T_2) = \frac{I_{Se}(T_2) - 1/3 I_{Se}(T_2)}{I_{Se}(T_1) - 1/3 I_{Se}(T_1)} n_{Se}(T_1). \qquad (1)$$

Yields of laser-ionized selenium scaled using eq. (1) are included in fig. 3.

Additionally the observed contaminants for different masses of the atomic and molecular beams are given in the same fashion. A significantly higher yield (factor 35) was achieved when using electron impact ($SeCO^+$) compared to laser (Se^+) ionization. The drawback of this method, as can be concluded from the overview given in fig. 3, is the high amount of contamination after installation of the target, which was at least one order of magnitude higher than that of the species of interest. A potential contamination of sulfur is also indicated by a peak pattern in the stable beam mass spectrum in the range from 60 to 62 amu. This is the dominant beam of a freshly prepared unit, and matches the pattern of carbonyl sulfide (SCO). However, after two days the intensity of the $AlBr^+$ and GeS^+ contaminants reduced by factors of 300 and 40, respectively, whilst atomic Se^+ is only reduced by a factor of 3.5 (cf. fig. 4). The reduction of yields with operation time of the target is a common behavior of thick target units, and often attributed to a degradation of the target material during operation at elevated temperatures [32]. The precise origin of the decreasing yields in the given target and ion source setup along within the discrepancy in the values has not been studied. A depletion of a molecular sideband can be caused by a lack of one species necessary to form the sideband. For example, outgassing of aluminum prevents formation of $AlBr^+$. Assuming continuous release of atomic selenium from the target material, the depletion of the SeCO sideband might be caused by depletion of the precursor compounds. Additionally, competitive reactions, like formation of carbonyl sulfide instead of carbonyl selenide, might contribute to a depletion of the sideband. Nevertheless, if control over molecular formation of SeCO can be achieved, the extraction of molecular selenium might provide a relatively pure beam. The yield evolution of target unit #605 is shown in fig. 4. Two days after installation of the target unit #605, ^{71}Se yields above the detection limit of 200 ions/μC could not be measured anymore on the mass of $^{71}SeCO$. However, two hours after injection of CF_4 at a flow rate of 2.3×10^{-5} mbar L s^{-1} the yield of $^{71}SeCO^+$ was found to have recovered to $1.0 \times 10^3/\mu$C. Eight hours after the beginning of CF_4 injection, a yield of $1.6 \times 10^3/\mu$C was found. Thus, the vanishing of the $^{71}SeCO^+$ sideband is not related to sintering of the target material, which is in many other cases a common mechanism for material degradation.

5 On-line yield measurements with Ta foils as target material

Attempts were also made to extract selenium from a previously irradiated tantalum foil target (#565), which had no mass markers attached to it. It was equipped with a Ta surface ion source operated at 2150 °C with the target temperature set to 2100 °C. Calculations with ABRABLA [33] suggest that the production rate for ^{70}Se is a factor of ≈ 80 less than for ZrO_2. Although, as no SeO formation is expected, the increased proportion of atomic

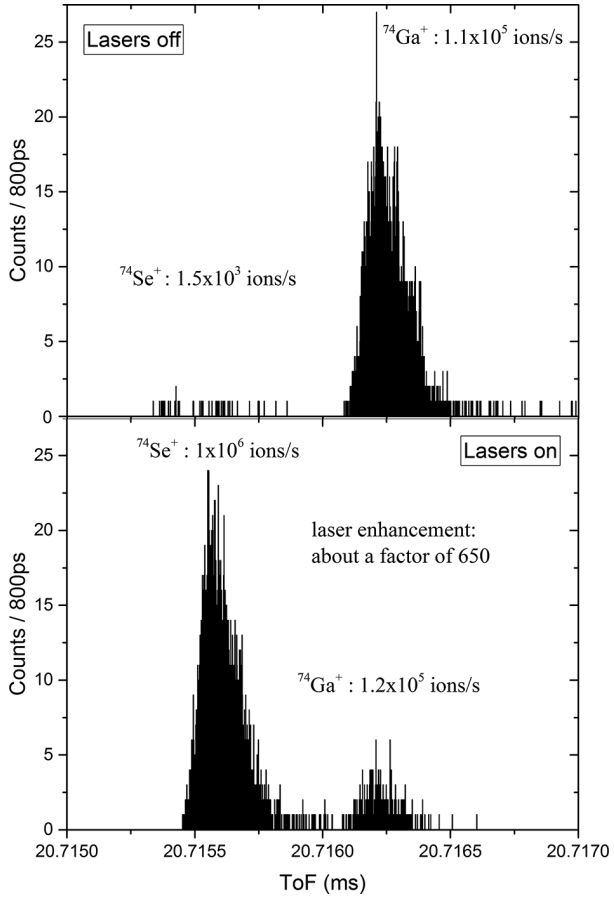

Fig. 5. $A = 74$ ion beam measured with the ISOLTRAP MR-ToF MS without and with laser ionization using a Ta foil target (#565). The measurements were 30 and 3 ms long respectively. The enhanced laser-ionized fraction of the beam (above the surface-ionized Se^{+} and isobars) is clearly visible. The graphs were provided by F. Wienholtz.

selenium available for laser ionization combined with the standard surface ion source could lead to similar yields. With the lasers set to the according transitions (powers before launch: 1st step 80 mW, 2nd step 2 W, 3rd step 40 W), no signal above the Faraday cup detection limit was observed for any of the stable selenium isotopes. The only signal seen was with use of the multi-reflection time-of-flight mass spectrometer (MR-ToF MS) [34], which is capable of single ion counting. With this, stable $^{74}Se^{+}$ (radiogenic, produced in the target material) was observed, but attempts at detecting radioactive species failed. Due to the very limited amount of time for this measurement, which prohibited further optimization attempts, no conclusion about the reason for the low yield can be drawn. The high sensitivity of the MR-ToF MS allowed the measurement of both laser- and surface-ionized selenium. The enhancement factor for laser over surface ionization was 650, and is clearly visible in fig. 5. Also visible is the isobaric contamination composed of $^{74}Ga^{+}$, which was less intense than the laser-ionized selenium.

6 Conclusion

A RILIS ionization scheme for selenium has been tested off-line and on-line at ISOLDE, yielding an efficiency of $> 1\%$ in a hot-cavity ion source. This value is expected to reach up to 10% if a reliable means of accessing the ground state atomic population is achieved. Laser-ionized radiogenic selenium production was investigated for ZrO_2 and Ta foil targets during on-line tests at ISOLDE. In the case of the ZrO_2 targets the RILIS-mode of the VADLIS was compared with standard electron impact ionization of either elemental or molecular (SeCO) selenium. The $^{71}Se^{+}$ ion beam produced by electron impact ionization was dominated by a $10\times$ more intense background of electron-impact ionized $^{71}As^{+}$. Whilst in RILIS mode the production of $^{71}Se^{+}$ was free of radioactive isobaric contamination (no detection of $^{71}As^{+}$), a loss of factor ≈ 35 in the ion rate was observed compared to electron impact ionization. Taking into account non-optimal conditions of laser ionization (low population of starting level) and assuming overcoming the technical difficulty of producing stable emission of laser light at 207.5 nm, the expected yield of laser-ionized selenium could reach the same order of magnitude as was obtained using the electron impact ionization.

For the Ta-foil target, RILIS ions were observed but the extracted ion rates were negligible, remaining below the Faraday cup detection limit. The molecular SeCO beams, extracted from the ZrO_2 targets, could neither provide the required yields and purity. Additionally the observed drop of molecular formation during the period of the measurements showed that further investigations into the production of these beams need to be made.

7 Outlook

For a better understanding of the molecular formation, the underlying chemical processes will be investigated by thermodynamic simulations and in a dedicated experimental setup. Moreover, target materials which favor atomic Se production should be tested in combination with the standard hot-cavity RILIS configuration. Should additional time for laser ionization scheme development become available, further investigations for identifying transitions to autoionizing states can be made to improve the laser ionization scheme efficiency. Scanning the range of either the frequency-doubled dye or Ti:sapphire lasers would provide access to an unexplored energy range of the continuum.

We would like to thank F. Wienholtz and the ISOLDE ISOLTRAP team for the conduction of MR-ToF measurements, and their persistent support during the online tests. We also acknowledge support and separator setup by the ISOLDE operating staff. This project has received funding from the European Union's Horizon 2020 research and innovation program under grant agreement No. 654002.

Data Availability Statement This manuscript has no associated data or the data will not be deposited. [Authors' comment: All data can be made available by the authors upon reasonable request.]

References

1. M.J.G. Borge, B. Jonson, J. Phys. G **44**, 044011 (2017).
2. R. Catherall *et al.*, J. Phys. G **44**, 094002 (2017).
3. U. Köster *et al.*, in *Exotic Nuclei and Atomic Masses (ENAM 98)* (ASCE, 1998) pp. 989–994.
4. L. Penescu *et al.*, Rev. Sci. Instrum. **81**, 02A906 (2010).
5. V.I. Mishin *et al.*, Nucl. Instrum. Methods B **73**, 550 (1993).
6. D.A. Fink *et al.*, Nucl. Instrum. Methods B **344**, 83 (2015).
7. T. Day Goodacre *et al.*, Nucl. Instrum. Methods B **376**, 39 (2016).
8. Y. Martinez Palenzuela *et al.*, Nucl. Instrum. Methods B **431**, 59 (2018).
9. A. M. Hurst *et al.*, Phys. Rev. Lett. **98**, 072501 (2007).
10. D. Doherty, J. Ljungvall, Technical report CERN-INTC-2014-057. INTC-P-423 (2014).
11. N. Orce *et al.*, Technical Report CERN-INTC-2012-067. INTC-P-368 (2012).
12. U. Köster *et al.*, Nucl. Instrum. Methods B **204**, 303 (2003).
13. F. Wenander, JINST **5**, C10004 (2010).
14. V.N. Fedosseev *et al.*, J. Phys. G **44**, 084006 (2017).
15. T. Day Goodacre *et al.*, Nucl. Instrum. Methods A **830**, 510 (2016).
16. T.E. Cocolios *et al.*, Nucl. Instrum. Methods B **266**, 4403 (2008).
17. NIST database, extracted January (2017).
18. J.E. Ruedy, R.C. Gibbs, Phys. Rev. **46**, 880 (1934).
19. C. Morillon, J. Vergès, Phys. Scr. **10**, 227 (1974).
20. V.N. Fedosseev *et al.*, Opt. Spectrosc. **57**, 552 (1984).
21. T. Day Goodacre *et al.*, Nucl. Instrum. Methods A **830**, 510 (2016).
22. H.L. Ravn, S. Sundell, L. Westgaard, Nucl. Instrum. Methods **123**, 131 (1975).
23. B. Marsh, *Contribution to the CAS-CERN Accelerator School: Ion Sources, Senec, Slovakia, 29 May - 8 June 2012*, `https://cds.cern.ch/record/1445287` (CERN, 2013).
24. E. Hagebø *et al.*, Nucl. Instrum. Methods B **70**, 165 (1992).
25. S. Sundell, H. Ravn, Nucl. Instrum. Methods B **70**, 160 (1992).
26. T.G. Pearson, P.L. Robinson, J. Chem. Soc. (Resumed), pp. 652–660 (1932).
27. L. Penescu, *Techniques to produce and accelerate radioactive ion beams*, PhD Thesis, Bucharest, Polytechnic Inst (2009).
28. M. Turrión *et al.*, Nucl. Instrum. Methods B **266**, 4674 (2008).
29. R Kirchner, Nucl. Instrum. Methods B **70**, 186 (1992).
30. A. Roine, HSC Chemistry 7.1. `http://www.hsc-chemistry.net` (2010) (online; accessed 19 July 2015).
31. J.R. Marquart, R.L. Belford, H.A. Fraenkel, Int. J. Chem. Kinet. **9**, 671 (1977).
32. J.P. Ramos, Nucl. Instrum. Methods B, `https://doi.org/10.1016/j.nimb.2019.05.045`.
33. A. Kelic *et al.*, arXiv:0906.4193 (2009).
34. R.N. Wolf *et al.*, Nucl. Instrum. Methods A **686**, 82 (2012).

6 The carbonyl concept for the most refractory beams

Contents

The most refractory elements (*i.e.*, elements with high melting and boiling points) are located in the center of the d-block. These elements, like molybdenum or tungsten, are often used as structural materials of the target and ion source system. Their extraction as ISOL beam from a thick target requires formation of a volatile carrier molecule. For the majority of refractory elements, it was so far unsuccessful. In this chapter, a concept tailored to the refractory 4d and 5d metals is proposed. Recently, it was discovered that these elements efficiently form carbonyl compounds at ambient temperature and pressure. The concept presented in the publication draft is based on calculations, simulations and proof-of-concept experiments towards a cold electron-impact ion source.

6.1 Extraction of refractory transition metals

While this section focuses on refractory transition metals[1] , a general introduction and review of molecular ion beam formation is provided in section 4.1. In fig. 6.1, the volatility of the elements is illustrated. It is typically assumed that a vapour pressure of at least 1×10^{-2} mbar is required to enable suffienctly fast transport of radioisotopes [191].As shown in the figure, the central transition metals make up the biggest agglomeration of refractory elements in the periodic table.

Attempts to extract refractory elements are among the first experiments with radioactive molecular beams. It was shown that molybdenum and technetium can be extracted by a nitrogen stream at atmospheric pressure from an irradiated uranium tetrafluoride target at temperatures below 800 °C [235]. However, attempts to efficiently ionize the volatile compounds (probably fluorides or oxyfluorides) remained unsuccessful [173]. Besides fluorides, oxides have been proposed as carriers [187]. The volatilization of Mo, Tc, Ru, Re and Os as oxides was demonstrated from molten silver and gold samples under a partial pressure of 1×10^{-3} mbar to 1×10^{-2} mbar of oxygen and water vapours [248]. Their efficient ionization in an ISOL setup is not reported. It has been argued that in both cases, the molecules are not sufficiently stable in the target and ion source system. In particular, hot tantalum surfaces often promote breakup of the compounds [98, 191].

Four of the thirteen refractory transition metals were successfully extracted as ISOL beam. Hafnium beams could be produced at ISOLDE from a tantalum / tungsten metal foil target and injection of CF_4 [210]. Zirconium extraction is reported in pioneering experiments from a GSI-JGU collaboration [173,218] in the 1970s and from ISOCELE [209]. The extraction of ZrF_x was reported from uranium deposited on a graphite cloth [202] but could not be confirmed in later experiments from a uranium carbide target [97, 98]. At TRIUMF, the extraction of long-lived ^{99m}Tc from a tantalum carbide target is reported [211]. At the ISOCELE facility, short-lived tantalum isotopes with half-lives in the order of seconds could be extracted as fluorides [217] in the mid 1980s. Since the

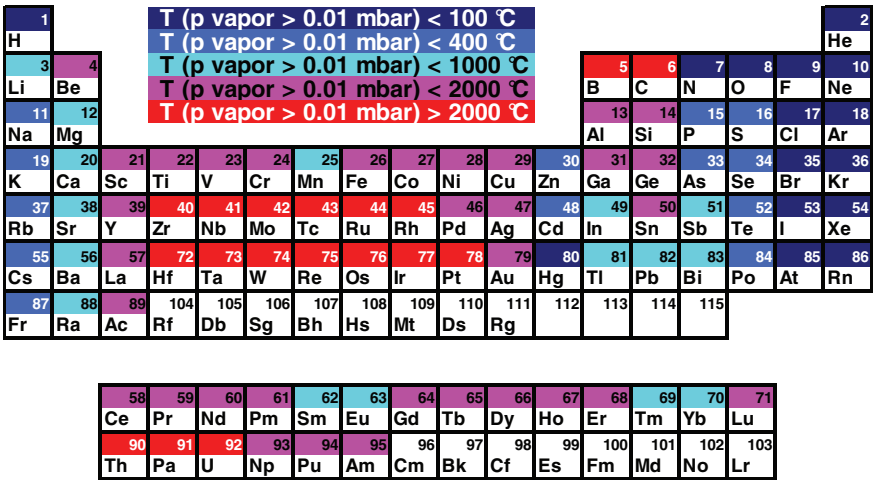

Figure 6.1: Periodic table of elements showing the temeratures required to reach a vapour pressure of more than 1×10^{-2} mbar. The pressure is an indication for sufficiently fast transport of radioisotopes in the target and ion source system. Reproduced from [191].

[1] For the sake of simplicity, refractory transition metals in this chapter refers to transition elements that require more than 2000 °C to reach a vapour pressure of 1×10^{-2} mbar.

characteristics and operating procedures of modern ISOL facilities differ significantly from the ISOCELE concept, it is not certain if the exploited methods can be applied nowadays. The target material at ISOCELE was integrated in the ion source and the separator allowed relatively high ion currents of up to 2 mA which allowed the evaporation of a significant amount of target material during operation [249]. The exchange of the extraction electrode was forseen after each run [209], which would not be feasible at ISOLDE due to the radiation levels in the area and its impact on the availability of ISOLDE as demanded user facility. More recently, the transport time of tantalum has been estimated in an ISOLDE target and ion source unit, indicating that an extraction of long-loved tantalum radioisotopes might be feasible [191]. However, in online experiments with tantalum / tungsten foil targets supplied with CF_4, radioactive tantalum beams could not be extracted. A possible reason might be the loss of radiogenic tantalum in exchange reactions with stable tantalum [210].

Recent proposals for the extraction of refractory transition metals have been provided by Köster *et al.* [191] and Kronenberg *et al.* [98]. Köster *et al.* argue that most refractory elements could be extracted as oxides or fluorides. To avoid their decomposition on the hot tantalum surfaces of FEBIAD ion sources, the development of an ECR ion source equipped with a hot plasma chamber is proposed by the authors. Few elements (*e.g.*, Os, Ru) form highly volatile oxides wich would even be compatible with cold plasma sources. Besides slow diffusion, some difficulties associated with this approach are the previously encountered instability of ECR sources with a pulsed driver beam (*cf.* sect. 1.2.3) and the proximity of the proposed hot plasma chamber and the heat-sensitive permanent magnet array. Kronenberg *et al.* propose to investigate zirconium sulfide sidebands from a uranium sulfide target or zirconium fluoride from a UF_3 target and addition of stable carrier [98]. The extraction of molybdenum and technetium is proposed in the oxide sideband from a thoria target. Ionization is not discussed in depth, however, for a vanadium oxychloride sideband, its collection on a cold spot and subsequent ionization by sputtering is proposed. While ion sources involving sputtering techniques have been developed for negative beams [250], their efficiency for positive beams remains unclear.

6.2 The carbonyl method

Within this thesis, the feasibility of a novel approach for molecular sideband formation is investigated. Recently, it was discovered that highly volatile carbonyl compounds of transition metals form at ambient temperature and pressure upon thermalization of fission recoils in a carbon monoxide-containing atmosphere [251]. The refractory transition elements Mo, Tc, Ru, Rh, W, Re, Os and Ir are known to form carbonyl compounds [252] and could possibly be extracted with the same method. These compounds are thermally unstable complexes similar to most organometallic compounds[2] . Comments on the use of organometallic compounds in ion sources were made by Freeman and Sidenius who advised against their usage in high temperature ion sources [187].

They point out that chemical equilibrium systems should be chosen instead, in which the metal ions can reform the molecule after breakup. In cold ECR ion sources for the production of intense stable beams, carbonyl compounds were successfully used within the Metal Ions from VOlatile Compounds (MIVOC) method [254].

[2] It can be argued that the carbon monoxide ligand is inorganic and as such carbonyl complexes are not metal-*organic* compounds. However, due to similar chemical behavior, transition metal carbonyls are typically discussed along with classical organometallic compounds *e.g.*, [252]. It was pointed out that *'Together with being a subfield of organic chemistry, organometallic chemistry can thus also be seen as a subfield of coordination chemistry in which the complex contains an M–C bond (*e.g., *$Mo(CO)_6$*)'* [253].

Within this thesis, modified and standard VADIS ion sources and the cold plasma ion sources Helicon and COMIC were tested for compatibility with carbonyl compounds. The measured ionization efficiencies from these sources were not sufficient (*cf.* Appendix A). Promising results were obtained in preliminary experiments with a cold electron-impact ion source in which electrons were liberated by a laser. Results from the latter, simulations for radioisotope production, stopping of recoils in a gas atmosphere and cryogenic gas separation of carbonyl compounds from the more volatile carbon monoxide gas are provided in the article below. The simulation results and extrapolation of experimental data allow the definition of parameters for an experimental setup and the estimation of radioactive beam yields which are provided for the model cases $^{105}Mo(CO)_6$ and $^{174}W(CO)_6$.

6.3 Contributions

The project was proposed and supervised by Ch.E. Düllmann, T. Stora and A. Yakushev. The simulations were set up, conducted and analyzed by myself, with support as outlined in the acknowledgments. The experiments towards cold electron-impact ionization were conducted in collaboration with K. Chrysalidis, D. Leimbach, B.A. Marsh, A. Ringvall-Moberg and S.G.Wilkins, who also provided and operated the laser system. The experimental data was analyzed by myself. E. Granados contributed in discussions regarding photo-cathode development. The article draft was written by myself and submitted for publication.

A concept for the extraction of the most refractory elements at CERN-ISOLDE as carbonyl complex ions

J. Ballof[1,2 a], K. Chrysalidis[1], Ch.E. Düllmann[2,3,4], V. Fedosseev[1], E. Granados[1], D. Leimbach[1,5], B.A. Marsh[1], J.P. Ramos[1 b], A. Ringvall-Moberg[1,7], S. Rothe[1], T. Stora[1 c], S.G. Wilkins[1,8], and A. Yakushev[3,4]

[1] CERN, Systems Department, 1211 Geneva 23, Switzerland
[2] Johannes Gutenberg - Universität Mainz, Department for Chemistry, TRIGA-site, Fritz-Strassmann-Weg 2, 55128 Mainz, Germany
[3] GSI Helmholtzzentrum für Schwerionenforschung, 64291, Darmstadt, Germany
[4] Helmholtz-Institut Mainz, 55099 Mainz, Germany
[5] Johannes Gutenberg - Universität Mainz, Department for Physics, Staudingerweg 7, 55128 Mainz, Germany
[6] École Polytechnique Fédérale de Lausanne (EPFL), Laboratory of Powder Technology, CH-1015, Switzerland
[7] University of Gothenburg, Department of Physics, Gothenburg, Sweden
[8] University of Manchester, School of Physics and Astronomy, Manchester M13 9PL, United Kingdom

Abstract. We introduce a novel thick-target concept tailored to the extraction of refractory 4d and 5d transition metal radionuclides of molybdenum, technetium, ruthenium and tungsten for radioactive ion beam production. Despite the more than 60-year old history of thick-target ISOL mass-separation facilities like ISOLDE, the extraction of the most refractory elements as radioactive ion beam has so far not been successful. In ordinary thick ISOL targets, their radioisotopes produced in the target are stopped within the condensed target material and have to diffuse through a solid material. Here, we present a concept which overcomes limitations associated with this method. We exploit the recoil momentum of nuclear reaction products for their release from the solild target material. They are thermalized in a carbon monoxide-containing atmosphere, in which volatile carbonyl complexes form readily at ambient temperature and pressure. This compound serves as volatile carrier for transport to the ion source. Excess carbon monoxide is removed by cryogenic gas separation to enable low pressures in the source region, in which the species are ionized and hence made available for radioactive ion beam formation. The setup is operated in batch mode, with the aim to extract isotopes having half-lives of at least several seconds. We report parameter studies of the key processes of the method, which validate this concept and which define the parameters for the setup. This would allow for the first time the extraction of radioactive molybdenum, tungsten and several other transition metals at thick-target ISOL facilities.

PACS. 29.38.-c Radioactive Beams

1 Introduction

The Isotope mass Separation OnLine (ISOL) technique was used already in 1951 to extract radioactive krypton isotopes from a 10 kg uranium oxide target, which was placed between the coils of a cyclotron magnet and irradiated by neutrons. The direct connection of the target to an ion source allowed simultaneous production and extraction of volatile species, and is today considered as the birth of the ISOL technique [1,2]. Modern ISOL targets use less material (see ref. [3] for a recent review), but their areal densities are typically above several g/cm^2. The thick target is both a blessing and a curse: the number of radioactive atoms produced inside the target scales with its thickness, translating into high yields for volatile elements like mercury. At CERN-ISOLDE, which is supplied by 1.4 GeV protons from the Proton Synchrotron Booster (PSB), extractable yields for ^{197}Hg from a molten lead-bismuth target have been measured to be as high as 5×10^9 ions per μC of protons, while the mean proton current for molten targets can reach up to 1.5 μA [4,5,6].

Issues arise, if i) the desired element is either chemically reactive and froms strong bonds to the target or to structural materials of the target and ion source system, ii) the diffusion of the element in the target material is slow, or iii) if the effusion through open space from the target to the ion source is hindered due to long sticking times at each wall encounter. The mean sojourn time τ

[a] e-mail: jochen.ballof@cern.ch
[b] Present address: SCK CEN, Boeretang 200, 2400 Mol, Belgium
[c] e-mail: thierry.stora@cern.ch

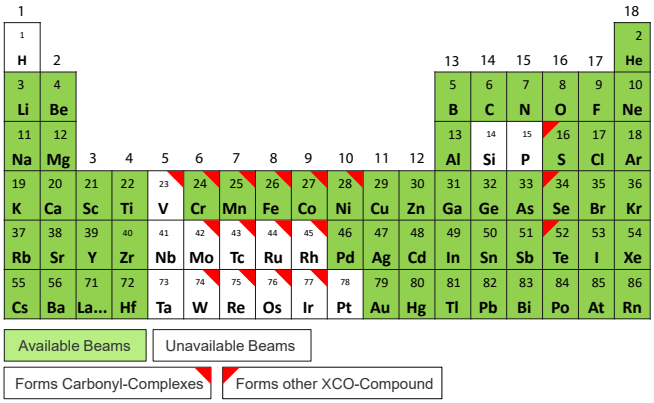

Fig. 1. Periodic table of elements showing available and not yet available thick-target ISOLDE-beams of short-lived isotopes ($T_{1/2} < 1\,\mathrm{h}$), in comparison with the elements forming carbonyl compounds [7,8,9]. S, Se and Te form compounds of type XCO (X= S, Se, Te), analogous to CO_2. Only the first six rows of the periodic table rows are shown.

for a single wall collision can be estimated by the Frenkel equation [10,11],

$$\tau = \tau_0 \, \mathrm{e}^{-\Delta H_{\mathrm{ads}}/(\mathrm{R}T)}, \qquad (1)$$

where R is the universal gas constant, τ_0 the period of vibration perpendicular to the surface in the adsorbed state and ΔH_{ads} the enthalpy of adsorption, which is a measure of the interaction strength between a single atom, molecule or ion and a surface. Hence, τ_0 is a property of the adsorbent only, while ΔH_{ads} depends on adsorbent and adsorbate. The latter can often be correlated to the macroscopic sublimation enthalpy of the adsorbent, characterizing the interaction between atoms or molecules of the same kind, which in turn is related to the vapour pressure of the compound. Hence, the vapour pressure is a measure for the mobility of a species during effusion processes for a given surface [12]. As can be seen from Eq. 1, the mean sojourn time depends exponentially on the temperature. Elements suffering from low vapour pressure and high boiling point are called refractory, and their extraction as ISOL beam provides a substential challenge. Volatile carrier molecules need to be formed, to enable transport of these elements to the ion source. From there they are either extracted as a molecular beam even as elemental ion beam, due to dissociation in the ion source. The process is called *in-situ* volatilization, chemical evaporation or extraction as molecular sideband. Reviews by Köster *et al.* give an excellent overview of the method and its limitations [13,14]. A recent development, not yet listed therein, is the successful extraction of the refractory and chemically reactive element boron as fluoride [15]. The elements for which short-lived isotope beams ($T_{1/2} < 1\,\mathrm{h}$) are available from thick-target ISOL facilities are shown in fig. 1. The most volatile elements, like noble gases, can already be extracted at low target temperatures. As both the sticking times and the diffusion processes inside the target material depend exponentially on the temperature, it is possible to extract most of the elements with the ISOL technique, if the target is operated at elevated temperatures. Therefore, the ISOLDE target container is made of tantalum and is designed to be heated restively to a maximum temperature of ca. 2250 °C.

As illustrated in fig. 1, many transition metals are not yet available as ISOL radioactive ion beam. This region of the periodic table contains the most refractory elements like molybdenum, tantalum, tungsten and rhenium. These are at the same time the construction materials of the typical target and ion source unit. So far, it was only possible to extract tantalum as TaF_5 [9,16], which is compatible with the structural materials of a FEBIAD ion source. Long-lived $^{99\mathrm{m}}$Tc ($T_{1/2} = 6\,\mathrm{h}$) could be extracted in elemental form from a tantalum carbide target equipped with a hot rhenium cavity by resonant laser ionisation. The online extraction of short-lived Tc isotopes is not reported [17]. Suitable sidebands for the remaining 4d and 5d refractory metals have not yet been found.

The requirements for volatile carriers are multifold. The compound should form easily upon reaction of a produced radioactive atom and a reaction partner, which is either present in the target and ion source system or introduced via injection of reactive gases. The latter can be either directly injected into the target or produced *in-situ* by heating a small solid sample which is connected to the target via a tube.

After formation of the isotope carrier compound, it has to travel from the target container via a transfer line to the ion source. On its way numerous wall encounters occur. Hence, the compound must be chemically inert towards the materials present in the target and ion source system. High temperatures are often beneficial for fast diffusion and volatile compound formation. However, it can be adverse to the desired chemical stability of the carrier molecule. This is especially the case, if decomposition is favored by thermodynamics, but could be inhibited kinetically, *i.e.* by slower reaction rates at lower temperatures. Moreover, if decomposition is required for beam purification purposes, catalytic processes at low temperatures can be considered.

After eventually reaching the ion source, the compound needs to be ionized efficiently. For the extraction of the 4d and 5d transition metals of groups 6 to 9, which the present article is addressing, the extraction as fluoride or oxide has been discussed [13,9,16]. Both compound classes suffer from limited compatibility with the materials present in target and ion sources. This especially holds for tantalum, which forms strong bonds to oxygen and fluorine, thus decomposing the volatilized oxygen or fluor-containing molecules upon impact.

Another issue arises from the target material. Typically uranium carbide targets are used at ISOLDE to produce heavy elements, fission products and light neutron-rich fragments. The reductive environment and the presence of carbon in the material are adverse to oxidation reactions. The material structure of uranium oxide has only limited thermal stability and is prone to fast sintering, which increases the diffusion time. To follow a classical approach for the extraction of the refractory metal

beams, the development of a new target material, ideally a target and transfer line free from metallic surfaces, and the integration of an efficient ECR (Electron Cyclotron Resonance) ion source would be required, due to catalytic decomposition of the volatile carrier on metallic surfaces and the given source temperatures. However, even after the implementation of all of these developments, the issue of slow diffusion in the target material remains. Hence, we propose a new target concept to bypass the limitations of a more classical high-temperature approach.

2 The target concept

To overcome operation at high temperatures, a novel target concept is proposed, allowing target operation at ambient temperature and pressure. The new concept aims at producing and extracting radioisotopes with half-lives of at least one to ten seconds in a batch-mode.

The recoil momentum allows ejectils of nuclear reactions to propagate through and emerge from thin metallic foils. In the proposed concept, the recoils are thermalized in a reactive gas and form volatile compounds *in-situ* (cf. fig. 2). A compound class that appears well suited for *in-situ* volatilization is that of metal carbonyl

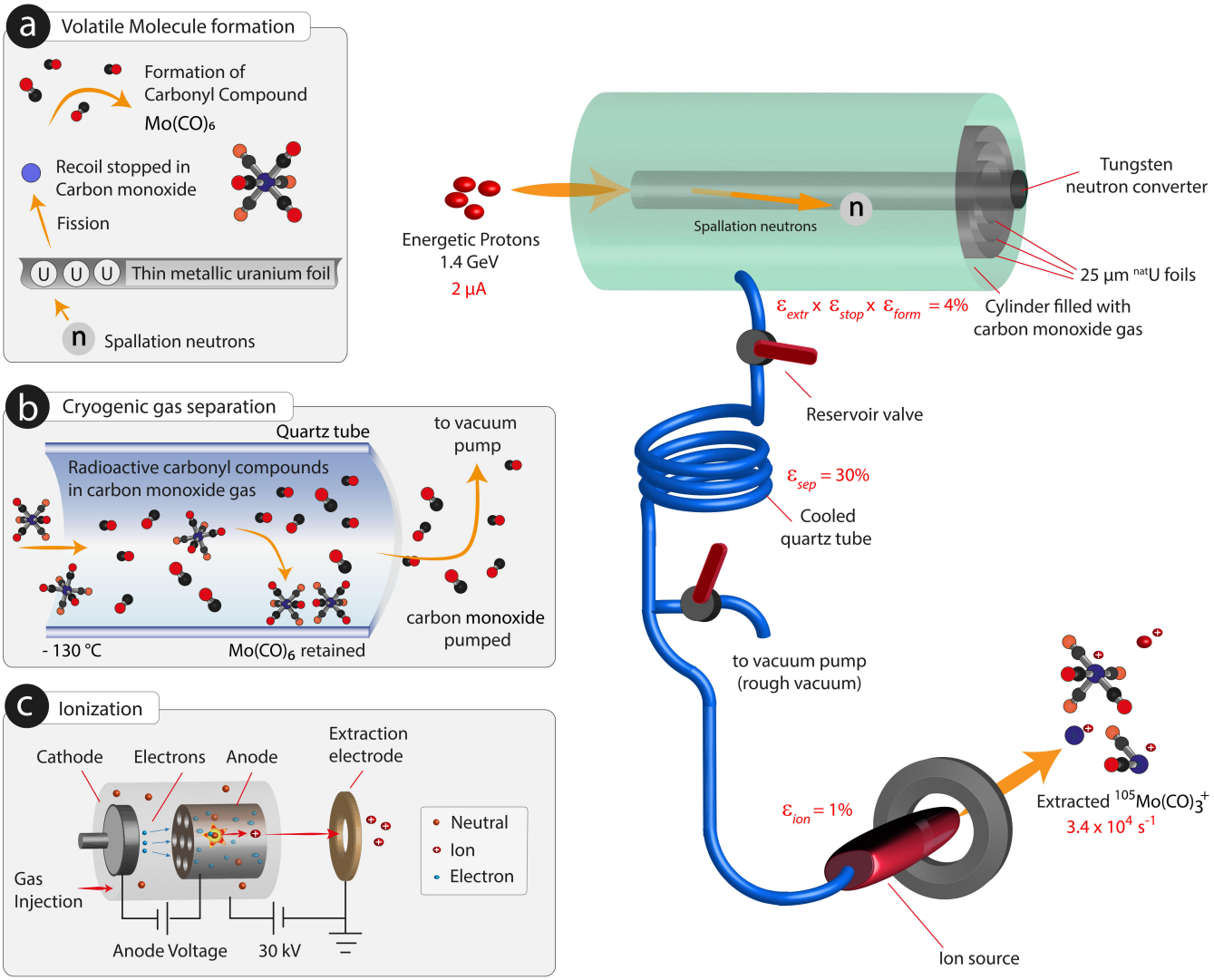

Fig. 2. Target concept for the extraction of refractory transition metals from a metallic foil target, shown exemplarily for the extraction of ^{105}Mo from uranium foils. Highly energetic protons impinge on a tungsten neutron converter and produce spallation neutrons. (a) The neutrons induce fission in the uranium foils and fission recoils emerge from the foil and are thermalized in carbon monoxide. Upon thermalization molybdenum hexacarbonyl complexes form readily. (b) The excess carbon monoxide is removed by cryogenic gas separation and the carbonyl complexes are fed into the ion source. (c) Electron impact ionization is proposed to ionize molybdenum hexacarbonyl. Electrons emerging from a cathode are accelerated through a grid into a cylindrical anode where ionization takes place in collisions between neutral molecules and electrons. The ion source is kept at a potential of 30 kV and ions are extracted through the grounded extraction electrode. Further details are given in the text.

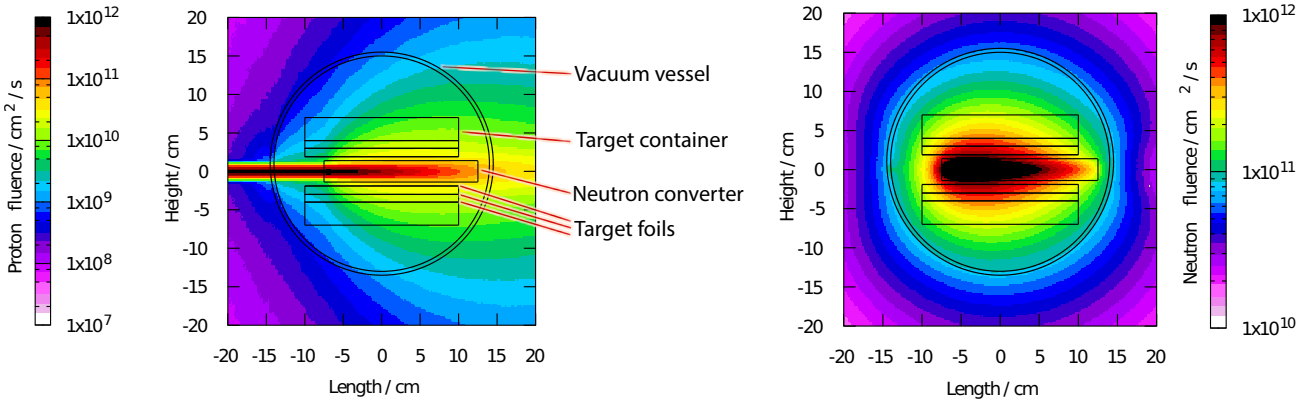

(a) Proton fluence (b) Neutron fluence

Fig. 3. (a) Proton and (b) neutron fluences at irradiation with 1×10^{13} protons per second obtained by FLUKA for the uranium foil geometry described in the text. The proton beam arrives from the left on the neutron converter. A sketch of the target is shown in fig. 2.

complexes. As can be seen in fig. 1, nine out of fifteen transition metals, of which beams are not yet available, form volatile carbonyl compounds. Already in 1961, the extraction of molybdenum from uranium oxide by formation of a volatile carbonyl compound was demonstrated [18]. Baumgärtner and Reichhold irradiated a mixture of U_3O_8 and $Cr(CO)_6$ with neutrons and were able to extract molybdenum hexacarbonyl by sublimation. Later, nuclear reaction products where thermalized in a chromium hexacarbonyl catcher, from which they could be evaporated as carbonyl compound [19]. However, a catcher made of $Cr(CO)_6$ is incompatible with an ion source as used in ISOL target units, due to its high volatility [20]. Recently, it was shown by Even *et al.* that volatile carbonyl complexes readily form at ambient temperature and pressure by thermalizing fission fragments of suitable elements in a carbon monoxide-containing atmosphere [21,22]. Within our concept, the formation of the volatile compound is

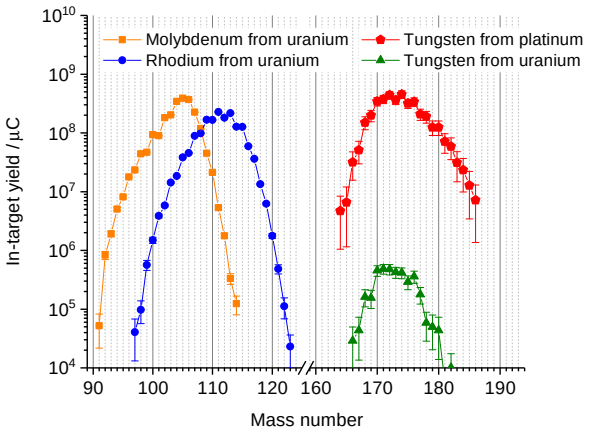

Fig. 4. In-target production for selected elements obtained by FLUKA. The error bars correspond to statistical errors of the simulation. The target geometry parameters are listed in Tab. 1.

followed by removal of the reactive gas by cryogenic gas separation [23], as illustrated in fig. 2b. The system is evacuated while the carbonyl compounds are retained in a cooling trap.

After excess gas removal, the cooling trap is allowed to warm up to release the volatile compounds, which are then fed into the ion source and ionized in collisions with electrons. In the following sections, the feasibility of the concept is investigated by means of proof-of-principle experiments of individual steps of the full procedure and numerical simulations. Molybdenum and tungsten were used as model case for the studies.

Despite their potential as volatile carriers, transition metal carbonyl complexes are delicate compounds, and decomposition in beam-induced plasmas and at elevated temperatures is expected [24,25,26,27]. In addition, impurities (*e.g.* oxygen or humidity) in the reactive gas reduce the chemical yield [28].

The topics addressed in the following sections aim at an order-of-magnitude estimation of radioactive ion beam yields that could be achieved. The average expected radioactive ion beam yield N computes to

$$\begin{aligned} N &= N_0^{\mathrm{batch}} \times \epsilon \times \nu_{\mathrm{batch}}, \text{where} \\ N_0^{\mathrm{batch}} &= \frac{I_p\, N_0}{\lambda} \left[1 - \mathrm{e}^{-\lambda\, t_{\mathrm{irr}}}\right], \text{and} \\ \epsilon &= \epsilon_{\mathrm{extr}} \times \epsilon_{\mathrm{stop}} \times \epsilon_{\mathrm{form}} \times \epsilon_{\mathrm{sep}}(\lambda) \times \epsilon_{\mathrm{ion}}, \text{ with} \end{aligned} \tag{2}$$

the in-target production yield by nuclear reactions N_0, the fraction of isotopes propagating through foils ϵ_{extr}, and of those stopped in the gas ϵ_{stop}, the formation of the volatile carrier molecule ϵ_{form}, the conditions required for removal of excess carbon monoxide gas and the associated efficiency ϵ_{sep} as well as the ionization efficiency of carbonyl complexes ϵ_{ion}. The number of isotopes N_0^{batch} with radioactive decay constant λ is produced per batch within the irradiation time t_{irr} at steady proton current I_p. The repetition frequency of the batch operation is ν_{batch}. Decay during separation is included in the efficiency fac-

tor $\epsilon_{\mathrm{sep}}(\lambda)$. In the following sections, each parameter is explained and its numerical value is studied in detail. The considerations are based on the target concept shown in fig. 2 and target geometries listed in table 1.

2.1 In-target production

To avoid direct exposure to the intense proton beam, a spallation neutron source made of tungsten is proposed. The latter is commonly found in ISOLDE target units and called proton-to-neutron converter [29,30,31]. This converter is concentrically surrounded by uranium or platinum target foils, which are placed inside a carbon monoxide-containing vessel. High production rates for molybendum and other 4d transition metals are expected from uranium fission. Platinum was chosen because high production rates of tungsten are expected in spallation reactions.

Relative to the 20 cm-long foils, the converter is indented by 2.5 cm in the beam axis and direction. This layout is initially proposed to reduce the proton fluence, which emerges by scattering in the target container [32, 33,34]. The geometry parameters are listed in table 1, and chosen under consideration of typical ISOLDE target size limitations and recoil ranges, but without further optimization, which is out of the scope of this conceptual work. The geometry could be further optimized (*e.g.* towards higher production rates and lower energy deposition on the tungsten rod) depending on the outcome of experiments studying carbonyl decomposition in such a setup. The power deposted by the primary proton beam might require modification of the geometry or the development of a dedicated cooling concept to avoid heating of the gas-volume to temperatures above the decomposition threshold for transition metal carbonyl compleses. The foil thickness was chosen based on expected recoil range and commercial availability.

As will be discussed in sect. 2.2, the recoil energy of tungsten isotopes obtained in spallation reactions is lower than that of uranium fission products. Thus, a dense arrangement of thin (2 µm) platinum foils is desired. While the design is mechanically challenging, dense foil arrangements have already been realized by either using dimpled foils or dedicated spacers between the layers [35]. The proposed quantity of platinum foils (26 m^2) might be cost-prohibitive or require a custom manufacturing process. Further investigations towards a different type of platinum-containing material, *e.g.* films deposited on backing foils [36], could be subject of further studies. The replacement of platinum foils by gold foils could equally be considered.

The number of desired isotopes produced inside the target material per µC of primary beam N_0 was investigated with the FLUKA particle tracking code [37,38]. The 1.4 GeV proton beam was assumed to have a Gaussian profile with $\sigma = 0.35$ cm, which is the common irradiation mode for an ISOLDE proton beam focused on the target container. The resulting proton and neutron fluences are shown in fig. 3. Due to scattering of the high energy proton beam on the converter, the beam broadens to form a plume. Using the proton-to-neutron converter reduces the proton fluence in the region of the gas-filled container by two orders of magnitude, in comparison to direct proton irradiation. The neutrons emerge isotropically from the tungsten rod. Overall, the uranium foils are exposed to a neutron fluence exceeding $2 \times 10^{11}\,\mathrm{cm}^{-2}\,\mathrm{s}^{-1}$, if the neutron converter is bombarded with 2.0 µA of protons. fig. 4 shows the in-target production yield of molybdenum and rhodium as 4d elements, and tungsten as 5d element. The plot contains simulation results for two different target materials and geometries, which are summarized in table 1.

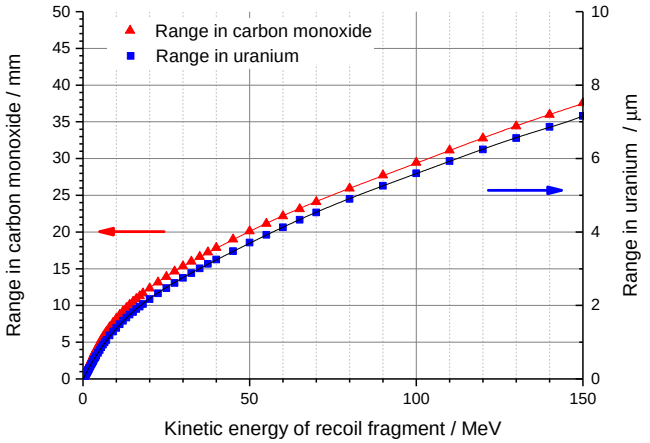

Fig. 5. Range of a ^{105}Mo fission fragment in a carbon monoxide atmosphere at 1 bar (abs.) and a metallic uranium, obtained by SRIM [39,40]. The lines show a polynomial fit

The in-target yields for molybdenum in the U(n,f) reaction reach a maximum for ^{105}Mo ($T_{1/2} = 36$ s) and decrease towards heavier and lighter isotopes. The yields on the outermost of the three foils are somewhat reduced due to the lower solid angle coverage and particle fluences. The yields of ^{105}Mo compute to $1.4 \times 10^8\,\mu\mathrm{C}^{-1}$ for the innermost foil, $1.3 \times 10^8\,\mu\mathrm{C}^{-1}$ (middle foil) and $1.1 \times 10^8\,\mu\mathrm{C}^{-1}$ (outermost foil), reaching a total yield of $3.8 \times 10^8\,\mu\mathrm{C}^{-1}$. For comparison, the in-target production of ^{105}Mo in a typical uranium carbide target at ISOLDE (ca. 50 g cm^{-2} of ^{238}U), irradiated directly with the proton beam, is computed to $5.4 \times 10^9\,\mu\mathrm{C}^{-1}$ by FLUKA [8].

The yields of the heavier element rhodium are in the same order of magnitude as molybdenum yields. The maximum yield of the tungsten isotopic chain in the Pt(n,spall) reaction, is found near ^{174}W. The total yield of this isotope produced in the platinum foil assembly is predicted to be $4.5 \times 10^8\,\mu\mathrm{C}^{-1}$.

2.2 Recoil range, thermalization and molecule formation

After production, the radionuclide propagates through the target material foil. Subsequently, it is crucial to thermalize the hot reaction products in the surrounding gas atmosphere to avoid implantation into the next foil or the

container. The projected ranges in the respective materials depend on the kinetic energy of the recoil ion, which in turn depends on the underlying nuclear reaction, and the associated kinetic energy of the projectile. In addition, the projected range decreases with carbon monoxide pressure in the target container. In the following a pressure of 1 bar (abs.) inside the target container, and a pure carbon monoxide atmosphere are assumed.

Protons and neutrons have been considered as projectiles inducing nuclear reactions, and their fluences in the target foils were obtained with FLUKA. Other secondary reaction channels are typically negligible and are not considered in in-target production simulations [41]. Folding the computed energy-differential projectile fluences with cross sections for isotope production computed by different codes, allows to identify the predominant reaction channel and finally, its associated recoil energy. For the low energy part (below 200 MeV) of the incident particle spectra, TALYS [42,43] and GEF [44,45] were used. Higher energies were addressed with the ABRABLA code [46]. The energy distribution of spallation neutrons originating from a neutron converter in similar geometry has already been experimentally investigated and is in agreement with FLUKA simulations [30]. The cross sections given by ABRABLA have also been benchmarked with experimental results obtained at ISOLDE [41,47].

The neutron energy spectra obtained within this work follow a broad distribution with a maximum at ca. 3 MeV (evaporation neutron peak) and extend to ca. 1.4 GeV, which is the energy of the incident proton [48]. The spectra of protons have a maximum at ca. 100 MeV, and also extend to 1.4 GeV.

From simulations with the GEF code in the energy range from 100 keV to 20 MeV for incident neutrons impinging on a ^{238}U target, the mean kinetic energy of ^{105}Mo fission recoils is expected to be between 90 and 100 MeV. ABRABLA equally predicts a recoil energy of ca. 90 MeV for 100 MeV neutrons. Excitation functions for the production of ^{174}W from ^{195}Pt have been calculated and folded with the proton and neutron fluence spectra. Incident particles from ca. 100 MeV on, significantly contribute to tungsten production. In total, the contribution of protons and neutrons to the production of ^{174}W, computes to 59% and 41%, respectively. The distribution maximum for the recoil energy of ^{174}W is near 1 MeV. It exhibits an exponentially decreasing tail towards higher energies.

The recoil ranges in the target foils and carbon monoxide gas have been calculated with SRIM [39,40] and fitted with a polynomial function. The results for molybdenum in uranium foils are shown in fig. 5 and indicate that a ^{105}Mo fission fragment has a range of ca. 6 µm in a metallic uranium foil. The range of a fission fragment emerging from the uranium foil in carbon monoxide depends on its energy after it emerges from the foil. To account for energy losses in the uranium foil and the target geometry, Monte-Carlo simulations were performed. Energy losses in the foil have been estimated by inversion of the obtained range function.

Within each foil, the fission events were generated uniformly. The relative number of production events per each foil was chosen based on the data obtained by FLUKA. The distribution of polar angle ϕ and azimuthal angle θ of the fission fragment trajectories were chosen such that the distribution in the solid angle $\mathrm{d}w = \sin\theta\ \mathrm{d}\theta\ \mathrm{d}\phi$ was uniform.[1] In vector representation, the trajectory of the fission fragment is given by

$$\begin{pmatrix} x \\ y \\ z \end{pmatrix} = \begin{pmatrix} x_0 \\ y_0 \\ z_0 \end{pmatrix} + \beta \begin{pmatrix} \sin\theta\,\cos\phi \\ \sin\phi\,\cos\phi \\ \cos\theta \end{pmatrix}, \tag{3}$$

where x_0, y_0 and z_0 are the coordinates of the fission event, and x, y and z the coordinates of intersection with a foil, after propagating a distance of β. Each uranium foil is described by two cylinders, defining the the inner and outer surface of the foil, respectively. The cylinders are defined by radius r and length $\mu_{\max}$.

$$\forall\, \mu \in \{0, \mu_{\max}\} : \begin{pmatrix} x \\ y \\ z \end{pmatrix} = \begin{pmatrix} x \\ \pm\sqrt{r^2 - x^2} \\ 0 \end{pmatrix} + \mu \begin{pmatrix} 0 \\ 0 \\ 1 \end{pmatrix} \tag{4}$$

Thus, equalizing the equations 3 and 4 yields an expression for β, which represents the maximum free flight path.

[1] Deviations from the uniform distribution could be seen in angle distributions obtained by ABRABLA, especially in the case of tungsten produced from platinum foils. Nonetheless, the effect of non-uniformly distributed nuclear reaction recoils only decreases the extraction and stopping efficiency by no more than 10% and is neglected.

Table 1. Assumed target foil geometries for in-target production and extraction efficiencies. A sketch is shown as part of fig. 2.

	Unit	Uranium foils	Platinum foils
converter radius	cm	1.4	
converter length	cm	20.0	
target container radius	cm	7.0	
number of foils		3	483
thickness	µm	25	2.5
length	cm	20	20
radii	cm	1.9, 3.0, 4.0	1.90 to 6.73
total surface area	m^2	0.11	26.1

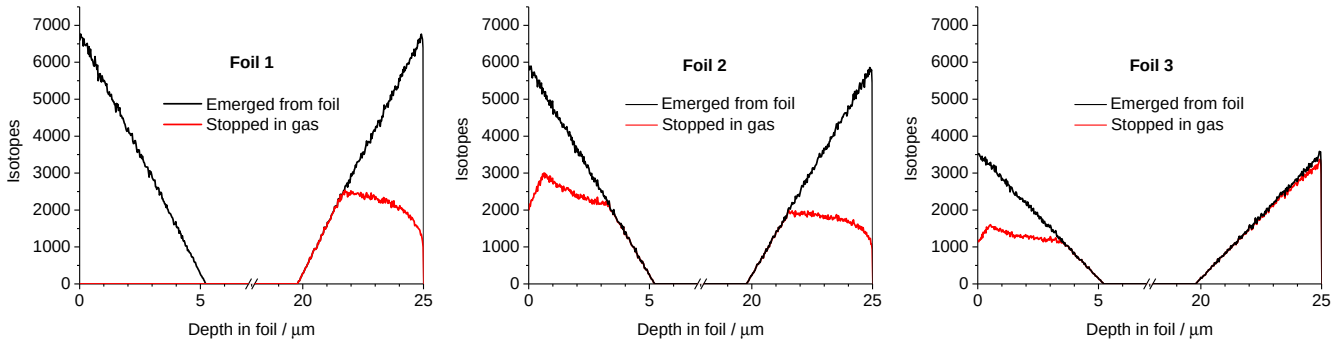

Fig. 6. Fraction of ^{105}Mo fission recoils which emerge from a 25 µm uranium foil, and which are stopped in a carbon monoxide gas before a confining wall is reached in dependency of the position of the fission event in the foil. A kinetic energy of 90 MeV is assumed, along with the target geometry outlined in sect. 2. The ratio of counts in the respective foils represents the ratio of the in-target production rates obtained by FLUKA.

The value was calculated to be

$$\begin{aligned}\beta = &- x_0 \cos\phi \csc\theta - y_0 \sin\phi \csc\theta \\ &\pm \left[\csc^2\theta \, \left(r^2 - y_0^2 \cos^2\phi \right.\right. \\ &\left.\left. + 2\, x_0\, y_0 \cos\phi \sin\phi \, + \left(r^2 - x_0^2\right) \sin^2\phi\right)\right]^{1/2},\end{aligned} \tag{5}$$

under the condition that $|y_0 \cos\phi - x_0 \sin\phi| < r$ [49]. The fraction of ^{105}Mo fission recoils emerging from the uranium foil in dependence of the depth of the fission event location from inside the foil is shown in fig. 6. Due to shallow angles, only a small fraction can emerge from the foil, if the point of fission exceeds a distance perpendicular to the surface of 5 µm. Assuming a typical thickness of commercially available uranium foils of 25 µm, in total $\epsilon^{\mathrm{Mo}}_{\mathrm{extr}} = 10\%$ of all ^{105}Mo fission recoils emerge from the foil. For comparison, a released fraction of 22% from an uranium oxide target at 1140 °C within 60 minutes was reported for Mo [50]. Release data at higher temperatures, as they are standard for uranium carbide targets, are not available and also difficult to predict due to the susceptibility of uranium oxide targets to undergo sintering.

The remaining recoil energy after propagating through the foil and the free flight path till the next surface determine if the recoil is thermalized in the gas or lost, due to implantation in a solid. The simulation predicts that $\epsilon^{\mathrm{Mo}}_{\mathrm{stop}} = 49\%$ of the emerging fragments are thermalized in carbon monoxide gas at 1 bar (abs.), leading to about 5% of all produced ^{105}Mo fragments being thermalized in gas. The bulk target material could be reduced by integration of thinner foils of *e.g.* 10 µm thickness, which would not decrease the total yield. Within the geometry assumed for platinum foils, $\epsilon^{\mathrm{W}}_{\mathrm{extr}} = 1.6\%$ emerge from the foil and thereof $\epsilon^{\mathrm{W}}_{\mathrm{stop}} = 21\%$ are thermalized in the gas.

After thermalization of the recoils in carbon monoxide gas, the carbonyl compounds form readily. Measurements have shown that in gas mixtures with inert gases, the chemical yield increases with the partial pressure of carbon monoxide. Using pure carbon monoxide gas, the chemical efficiency ϵ_{form} was found to be ca. 80% for the formation of $Mo(CO)_6$ and 30% for $W(CO)_6$ [21].[2]

2.3 Gas separation

A carbon monoxide partial pressure of 1 bar (abs.) inside the target container is desirable to achieve a high chemical yield, and is also crucial for efficient stopping of the fission recoils. However, ion sources typically operate under high vacuum conditions, and often a pressure of 1×10^{-3} mbar may already prevent efficient ionization. Thus, the separation of radioactive carbonyl compounds from the excess gas atmosphere is required. Since carbon monoxide, exhibiting a boiling point of −191 °C [51], is by far more volatile than carbonyl compounds, the two components are separable by chromatography. The implementation of a suitable cryogenic trap coupled to an ion source was already evaluated for the transport of carbon monoxide in a carrier gas by Powell *et al.* [52], and Katagiri *et al.* have also shown the feasibility of the integration into the process of radioactive ion beam production [23]. The option of neutral CO injection via a cryogenic trap into an electron beam ion source for charge breeding is also considered for medical applications [53,54,55].

Adsorption enthalpies of carbonyl compounds have been measured on SiO_2, gold, Fluorinated Ethylene Propylene (FEP) and PolyTetraFluoroEthylene (PTFE) surfaces by isothermal chromatography and by thermochromatography [56,27,57,58]. In isothermal studies with radiotracers from a ^{249}Cf source, an adsorption enthalpy for $Mo(CO)_6$ on SiO_2 surfaces of $-\Delta H_{\mathrm{ads}} = 42.5(25)\,\mathrm{kJ\,mol^{-1}}$ was determined [21]. In thermochromatography experiments, the same quantity was found to be $-\Delta H_{\mathrm{ads}} = 36(8)\,\mathrm{kJ\,mol^{-1}}$. Later experiments by Wang *et al.* reported values in agreement with earlier findings. Adsorption enthalpies of other

[2] The given efficiency for molybdenum was obtained as ratio between transport by carbonyl formation and aerosol transport of atomic species attached to clusters. An absolute efficiency is given for tungsten.

transition metal carbonyl complexes (technetium, tungsten, rhenium, osmium, iridium) could also be deduced, all ranging in the same order of magnitude and indicating a physisorption interaction. For the following considerations, $Mo(CO)_6$ was chosen as a model case, and an adsorption enthalpy of $-40\,\mathrm{kJ\,mol^{-1}}$ was assumed as average value of the measurements.

The system for cryogenic gas separation must be designed such that the total gas flow rate into the ion source does not exceed its maximum acceptable gas load and the pumping capacity of the vacuum system. A typical upper limit of $1 \times 10^{-3}\,\mathrm{mbar\,L\,s^{-1}}$ was estimated for gas injection into an ion sources operated at ISOLDE. In addition, the time needed to reach this condition should be as low as possible to minimize decay losses. The proposed setup is shown in fig. 2b, which is operated in a batch-mode. During irradiation, the target container is filled with carbon monoxide at atmospheric pressure. After a defined irradiation time, which depends on the half-life of the desired isotope, the gas inventory is pumped by a roughing pump through a cooled quartz tube which retains the less volatile carbonyl compounds. After a certain fraction is evacuated from the target container, the latter is isolated from the chromatographic system by closing the reservoir valve. The residual pressure in the chromatographic tube is further reduced, till the maximum flow rate into the ion source is reached. Finally, the quartz tube is heated by a resistive heating element to ambient temperature allowing carbonyl compounds to be fed into the ion source, where they are ionized and electrostatically extracted. The time required for allowing the temperature to raise, is assumed to be short in comparison to the half-life of the model isotopes discussed within this concept ($\ll 35\,\mathrm{s}$) and neglected in the calculation of the expected yield. In parallel to the heating of the quartz tube, the irradiation of the next batch can take place, so that the heating period is not included in the cycle time $\nu_{\mathrm{batch}}^{-1}$ of the batch process.

A Monte-Carlo model proposed by Zvara [59] was used to investigate the feasibility of the concept, which was also similar to the model used by Even *et al.* for the adsorption enthalpy measurements [56]. The model takes into account the temperature dependent sojourn times (cf. eq. 1) and gas flow conditions. Assuming that the chromatographic tube is connected to an evacuated vessel (choked flow), the evaluation of Reynolds numbers for tube diameters from 0.5 mm to 3.5 mm suggests turbulent flow conditions. The time dependent pressure in the reservoir $p_{\mathrm{target}}(t)$ can be estimated following the evaluation of the pV-flowrate q_{pV}, given by

$$q_{pV} = V\frac{\mathrm{d}p}{\mathrm{d}t} = A\,a\,p_{\mathrm{crit}}\ , \tag{6}$$

where V is the volume of the target container, A the cross sectional area of the tube, a the speed of sound in the medium and p_{crit} the critical pressure, which is given by

$$p_{\mathrm{crit}} = 1.92\,\frac{1}{a\,d}\left(\frac{\bar{c}^{\,6}}{\eta}\right)^{1/7}\left(\frac{d^3\,p_{\mathrm{target}}^2}{2\,l}\right)^{4/7}\ , \tag{7}$$

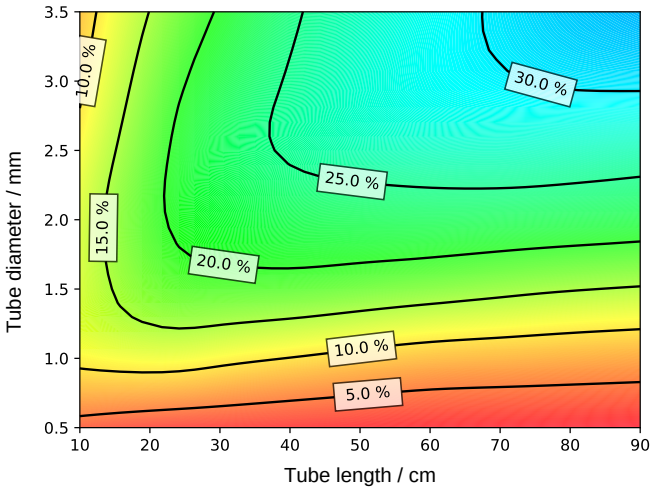

Fig. 7. Dependence of the cryogenic gas separation efficiency ϵ_{sep} on the dimensions of the chromatographic tube for ^{105}Mo, which is determined by decay losses during extraction of the reservoir inventory and consideration of irreversible processes obtained by simulation (see text). The figure shows interpolated data.

where d and l are inner diameter and length of the tube, respectively, $\bar{c}$ the mean thermal particle speed and η the temperature-dependent dynamic viscosity, which was calculated with the Jones equation [60]. It was assumed that the tube was kept at a constant temperature. The equations hold under the approximation that $p_{\mathrm{target}}^2 \approx p_{\mathrm{target}}^2 - p_{\mathrm{crit}}^2$ [61]. Solution of the equations yields the time-dependent pressure in the reservoir, which was initially ($t = 0$) kept at the pressure $p_{\mathrm{target},0}$.

$$p_{\mathrm{target}}(t) = \frac{823543\;p_{\mathrm{target},0}\;V^7}{\left(k\;p_{\mathrm{target},0}^{1/7}\;t + 7V\right)^7} \tag{8}$$

The simulation generates particles with a random lifetime, which is sampled from a distribution according to the given half-life. Subsequently, the propagation of the particle through the chromatographic system is simulated. The length of a displacement is typically approximated by the variance of the zone profile of the chromatographic peak, and expressions have been obtained for laminar flow *e.g.* ref. [62]. Within this work, the mean length of a displacement δ was approximated by the diffusional deposition length in developed turbulent flow, which depends on Reynolds number $Re = Q\,d\,\rho/(A\,\eta)$, Schmidt number $Sc = \eta/(\rho\,D)$, the mutual diffusion constant D and the volume flowrate Q. The density ρ is derived from the pressure, and the diffusion constant is obtained by the approximation proposed by Gilliland [63]. Assuming a uniform distribution of particles at the inlet, the expression for the mean displacement length holds for the first contact with a wall and was sampled from an exponential distribution [64].

$$\delta = \frac{43.5\;Q}{\pi\;D\;Re^{0.83}\;Sc^{0.3}} \tag{9}$$

According to Zvara, the mean number of real wall collisions within a long displacement step Z can be calculated by the flowrate, the mean thermal particle speed and the surface per unit length S of the column as

$$Z = \frac{\bar{c}\, S}{4\, Q}\, \delta. \tag{10}$$

After each displacement, the time spent by the particle in the system and its position are evaluated. At the end of the time required to extract a defined fraction from the reservoir, it is computed, if the particle has either decayed, was retained on the column surface, or has been eluted.

The separation efficiency is given by a linear combination of i) the fraction of carbonyl compounds evacuated from the reservoir ii) the ratio of molecules which are inside the quartz column (*i.e.* not decayed and not eluted) after the desired fraction was extracted from the reservoir, to the number of molecules fed into the column and iii) an additional factor to account for decay losses during the time required to reach a flow rate below 10^{-3} mbar L s^{-1}, which was estimated to be ca. 5 seconds. The input variables of the simulation were the fraction of carbonyl compounds extracted from the reservoir and fed into the quartz tube as well as its dimensions and temperature.

For each geometry of the separation channel the respective highest efficiencies ϵ_{sep} have been determined. At elevated flowrates, longer channels are required due to the increase in the diffusional deposition length (eq. 9). The results for ^{105}Mo are shown in fig. 7. The simulation predicts that efficiencies above 60% are in reach. Using the same geometry boundary conditions, the maximum efficiency for ^{108}Mo (1.11 s) is calculated to be above 0.6%. Typical temperatures are in the range of -130 ± 40 °C. Further details of the Monte-Carlo simulation are discussed in ref. [64].

In addition to radioactive decay, further losses have to be considered, such as irreversible sticking after decomposition of the volatile compound or reactions with impurities. The extent of such additional losses can be estimated based on typical capillary transport losses, which could be in the order of 50% [22]. Decay losses for the long-lived isotope ^{174}W ($T_{1/2} = 31$ min) are negligible, and an efficiency of $\epsilon_{\mathrm{sep}}^{\mathrm{W}} = 50\%$ is assumed. The separation efficiency of ^{105}Mo computes to $\epsilon_{\mathrm{sep}}^{\mathrm{Mo}} = 30\%$.

2.4 Ionization

A review about ion sources for radioactive ion beam production can be found in ref. [65]. In contrast to ion sources designed to deliver stable isotope beams, additional requirements arise for the ionization of radionuclides. Due to their limited availability compared to stable isotopes, the ionization efficiency is one of the most important figures of merit. For exotic isotopes with very short half-lives ($\lesssim 100$ ms), the residence time also needs to be considered. A compact design is required to meet constraints imposed by robot-handling of the target and ion source unit and resistance to the strong radiation field of the driver beam is mandatory.

The three main processes for ion generation are i) surface ionization ii) photo-induced ionization and iii) electron-impact ionization. Surface ionization in hot cavities is applied for elements with low ionization potential (IP) of up to ca. 6 eV like the alkaline or alkaline earth metals. For elements with elevated IP, resonant laser ionization can be used if laser systems are available to excite suitable transitions [66]. Electron impact ionization is the underlying process in electron beam (arc-discharge) ion sources and radio-frequency driven plasma ion sources. Via electron impact ionization, almost all elements and molecules can be ionized efficiently. Plasma sources are typically used for volatile species only.

The ionization of carbonyl compounds is a crucial step towards ion beam production. The method of ionization must be chosen carefully with respect to the properties of the compound. The ionization potential of $Mo(CO)_6$ was measured to be in the range from 8.2 eV to 8.5 eV [67, 68, 69, 70]. The first bond dissociation energy (FBDE) is significantly lower and was determined to be 1.7 eV by pyrolysis with a pulsed CO_2-laser in a gas cell [71], in agreement with data obtained by thermal decomposition on a silver surface [24, 25] and theoretical studies [72]. In comparison to typical candidates for molecular beams at ISOLDE, the compound is delicate, and decomposition on hot surfaces is expected. For species with high ionization potential, Forced Electron Beam Induced Arc-Discharge (FEBIAD) ion sources [73], like the VADIS (Versatile Arc-Discharge Ion Source) [74] are commonly used. However, the high operating temperature is expected to decompose the carbonyl compounds even before they reach the ion source volume. Thus, ion sources operated below decomposition temperature, favoring high electron energies for ionization and efficient ion extraction over breakup, are the preferred choice.

2.4.1 ECR sources

The Metal Ions from VOlatile Compounds (MIVOC) method, where volatile metallic compounds are fed into an Electron Cyclotron Resonance (ECR)-heated plasma ion source, is a well established method for the extraction of non-radioactive metal beams [75, 76]. The residence time of an element in the ion source is an important parameter for radioactive ion beam sources. This data is not yet available for MIVOC ion sources.

The production of molybdenum beams by injection of molybdenum hexacarbonyl is reported by Nakagawa *et al.* [77] at the RIKEN 18 GHz ECRIS. The reported ion currents I_ν on each charge state ν along with the material consumption allow a rough estimation of the ionization efficiency. For ferrocene, the material consumption $q_{\mathrm{m}}^{\mathrm{Fe}} = 2\,\mathrm{mg\,h^{-1}}$ is explicitly reported. Based on the respective vapour pressures of molybdenum hexacarbonyl p_{Mo} and ferrocene p_{Fe}, the material consumption of $Mo(CO)_6$ can be estimated here, under the assumption that the control valve between MIVOC chamber and ion source

was adjusted to the same conductance. The ionization efficiency is given by

$$\epsilon_{\mathrm{ion}} = \frac{\sum_\nu I_\nu/\nu}{e\, q_{\mathrm{n}}} = \frac{M_{\mathrm{Fe}} \sum_\nu I_\nu/\nu}{q_{\mathrm{m}}^{\mathrm{Fe}}\, \mathrm{F}} \frac{p_{\mathrm{Fe}}}{p_{\mathrm{Mo}}}\,, \qquad (11)$$

where e is the elementary charge, q_{n} the neutral particle flow into the ion source, $M_{\mathrm{Fe}} = 55.8\,\mathrm{g\,mol^{-1}}$ the molar mass of iron and F the Faraday constant. Assuming vapour pressures at 300 K of 1 Pa for ferrocene [78], and 25 Pa for molybdenum hexacarbonyl [79], ion currents, and ferrocene material consumption as given in ref. [77], the ionization efficiency of $Mo(CO)_6$ computes to 0.03%. The ionization efficiency for iron from ferrocene computes to 4.3%. Ionization efficiencies could possibly be improved by using a gas mixture as buffer gas [80]. Given that currents were not reported for all charge states, the calculated efficiency is a lower limit.

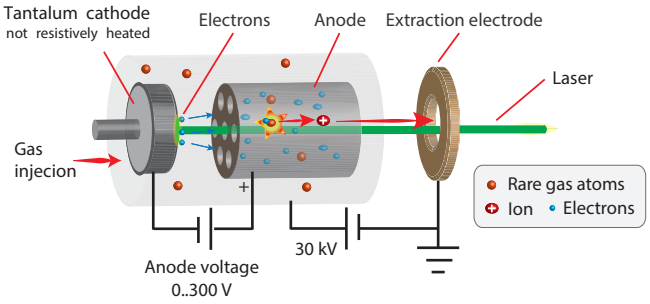

Fig. 8. Principle of the exploratory experiment exploiting electron generation by a laser beam in a cold environment. The electrons are liberated from the cathode and accelerated through a grid into the positively biased anode body, where volatile species are ionized in collisions.

2.4.2 Arc-discharge ion sources

In arc-discharge ion sources, electrons are emitted from a cathode and accelerated to an energy of ca. 100 eV to 200 eV that matches the maximum ionization cross section. The electrons are typically emitted thermionically. Arc-discharge ion sources, in contrast to compact radio-frequency plasma ion sources, offer the advantage of a narrow electron energy distribution and relatively high electron energies. The latter avoid favouring breakup over ionization due to insufficient electron energy. Thus, the application of electron impact ionization in a cold environment presents an interesting asset. Penescu *et al.* proposed eq. 12 to model the ionization efficiency of FEBIAD-type ion sources [81]. The ionization efficiency ϵ_{ion} depends on the rate of ionization per unit volume R_{ioniz}, the volume of the ionization region V, the number of neutral particles injected per unit time n_{in} and an additional factor f to account for the probability of ion extraction, electron confinement and higher order effects. The rate of ionization can be expressed as a linear combination of the number densities of neutral particles N_n, electrons N_e, the ionization cross section σ and the relative velocity of electrons and neutral particles v_{el}.

$$\epsilon_{\mathrm{ion}} = \frac{R_{\mathrm{ioniz}} V}{n_{\mathrm{in}}} f, \quad \text{where} \quad R_{\mathrm{ioniz}} = N_n\, N_e\, \sigma\, v_{\mathrm{el}} \qquad (12)$$

Unfortunately, absolute partial ionization cross sections for molybdenum hexacarbonyl or its fragments have not yet been published. It is interesting to note that also the ionization cross section of molybdenum has not yet been measured due to the refractory nature of the element and only theoretical calculations are available [82].

Due to the lack of available data, we conducted a comparative study of the ionization efficiency of the noble gas krypton and molybdenum hexacarbonyl in a cold environment. We chose to use a laser to liberate electrons out of the tantalum cathode of a standard VADIS source equipped with a water cooled transfer line (VD7). In contrast to common operation of the VADIS ion source, the source was not resistively heated. The laser pulses impinging on the cathode induce a local raise of temperature during the laser pulse. However, the heat is dissipated quickly to the water-cooled assembly [83]. The laser power used in our experiment is not expected to raise the average temperature of the cathode significantly. Thus, thermal decomposition of carbonyl compounds on the cathode is negligible.

The candidate mechanisms for electron generation in the interaction of the laser beam and the tantalum cathode are either extraction from a plasma plume, thermionic electron emission or the photo-electric effect. As discussed in the next paragraph, the used fluences were most likely insufficient for ablation and plasma formation. Time-dependent heat transfer and thermionic electron emission models for tantalum are available [84], but require more precise knowledge of pulse fluence as available from our experiment to be applied. Since the single photon energies were below the material work function, the absorption of multiple photons is required to release electrons by the photo-electric effect. Efficient multiphoton photoemission has been observed with ultrashort ($\tau_{\mathrm{p}} = 80$ fs) laser pulses [85] but data on quantum efficiency is not available for the conditions present in our experiments. Nonetheless, in both scenarios electrons are extracted in an environment that is (on average) at ambient temperature.

Experimental A sketch of the ion source is shown in fig. 8. UV light (343 nm) supplied by a Pharos laser at 50 kHz repetition rate and pulse length of 265 fs was guided through the ion beam outlet aperture on the tantalum cathode. The laser power before entering the vacuum system was measured to be 4.5 W. The dimensions of the laser spot were estimated with the bare eye and measured to be ca. 5 mm in diameter. Due to the limited ion beam outlet aperture of only 1.5 mm in diameter, only a fraction of the beam power reached the cathode. An upper limit for the fluence per pulse computes to $\phi_l < 5 \times 10^{-3}\,\mathrm{J\,cm^{-2}}$.

Table 2. Ionization efficiency estimation of the exploratory cold electron impact ion source shown in fig. 8. The efficiency is given for the most abundent fragment of $Mo(CO)_6$, and corrected for isotope abundance. The aim of the experiment was to deduce the *relative* ionization efficiency of the two species.

Nuclide	Isotope abundance	Current	Injected neutrals	Ionization efficiency
^{98}Mo	24.3%	33 pA	2238 pnA	0.0015%
^{84}Kr	57.0%	200 pA	8999 pnA	0.0022%

The minimum laser fluence needed for ablation (threshold fluence) was estimated in ref. [86] to be $0.17\,\mathrm{J\,cm^{-2}}$ at $\lambda_l = 750\,\mathrm{nm}$ and a pulse length of $\tau_\mathrm{p} = 8.5\,\mathrm{fs}$. Thus, the source in our experiment was most likely not operated in an ablation regime.[3]

Krypton (Carbagas, 99.998%) and molybdenum hexacarbonyl (Schuchardt München, TA Mo 36.33%, C 27.18%, Fe 0.005%, Cu 0.0008%) were supplied through a common transfer line into the ion source. The krypton flow rate was controlled with a calibrated leak, which was measured to be $1.15 \times 10^{-5}\,\mathrm{mbar\,L\,s^{-1}}$ for 1 bar (abs.) of helium. The setup for the controlled injection of molybdenum hexacarbonyl consisted of an evaporation chamber, connected to the common transfer line via a regulation valve (Pfeiffer EVR116). The evaporation chamber was equipped with a capacitance diaphragm gauge (Pfeiffer CMR 373) to monitor the pressure. The residual gas composition was monitored by a residual gas analyzer (Pfeiffer PrismaPlus) at the extraction site of the ion source.

[3] Attempts to further focus the laser beam with a telescope caused high voltage breakdowns and damage on the cathode surface. However, in the experiments described in this work, the focusing telescope was not used.

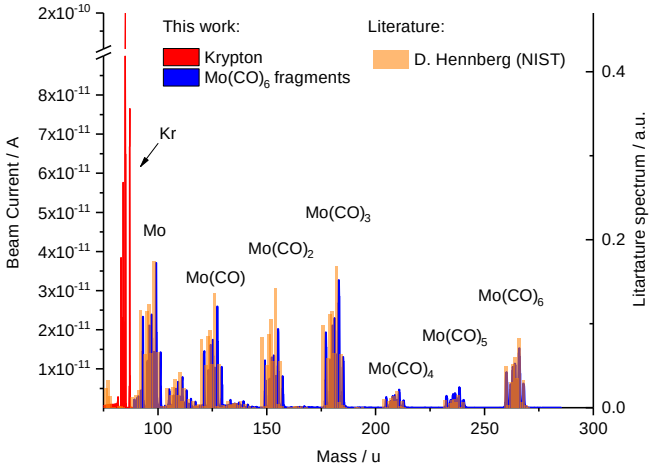

Fig. 9. Typical mass spectrum of Kr and $Mo(CO)_6$ measured simultaneously with the cold electron impact source. A mass spectrum of $Mo(CO)_6$ obtained also by electron impact ionization by D. Henning in [87] is shown for comparison. Minor deviations in the fragment distribution might arise from different electron energies or source characteristics.

After introduction of a solid $Mo(CO)_6$ sample into the evaporation chamber, the latter was evacuated with a turbo-molecular pump, backed by a dry scroll pump, to a pressure below $1 \times 10^{-2}\,\mathrm{mbar}$. Subsequently, the valve to the pumping group was closed. The sample quickly evaporates untill the saturation vapour pressure is reached inside the reservoir. Successive opening of the regulation valve allowed controlled injection into the transfer line. The material consumption was estimated by allowing the complete evaporation of a known amount, which was monitored via the pressure of the evaporation chamber and by the residual gas composition. The material consumption was measured to be $88^{+5}_{-21}\,\mathrm{\mu g\,h^{-1}}$. The relatively large error is due to consideration of material losses during the initial evacuation.

The results of the relative efficiency measurement of Kr and $Mo(CO)_6$ are listed in table 3 and an obtained mass spectrum is shown in fig. 9. The ionization efficiencies of krypton and molybdenum compute to 0.0022% and 0.0015%, respectively. The result of the experiment shows that the ionization efficiencies of Kr and $Mo(CO)_6$ are in the same order of magnitude. While these ionization efficiencies in combination with high in-target production rates, or vaporization of a radioactive $Mo(CO)_6$ sample obtained by other means, would already allow a range of nuclear physics experiments, a higher efficiency is desirable.

Proposed design of a cold photo-cathode driven ion source In the following, we explore the feasibility of an electron-impact ion source exploiting the photo-electric effect for electron release. Basic design parameters for a novel photo-cathode driven ion source will be derived that aims at an ionization efficiency of $\sim$ 1% for $Mo(CO)_6$. First, the general assumptions are presented, then the space-charge limitations of an electron current passing through the gap between cathode and anode are discussed and finally the basic requirements of a suitable laser system are given.

The efficiency estimate of the new design is based on the assumption that the measured ionization efficiency obtained in our exploratory experiment linearly scales with the electron current. This is expected in a first approximation, since the rate of ionization linearly depends on the electron density. The probability of ion extraction, which is included besides other effects in the factor f of equation 12, is affected by source geometry. However, in contrast to the required increase of several orders of magnitude on the electron current, the extraction factor is typically only affected to some minor extend [81], which could be subject of further studies.

The electron currents in our experiment have been obtained as drain current of the anode power supply. However, the instantaneous currents might have exceeded acceptable values for the used pico-amperemeter. To avoid underestimating the electron current, which would lead to overestimation of the photo-cathode source efficiency, we assume a space-charge limited current in following considerations. The measured electron currents were about fac-

Table 3. Parameters of a proposed cold electron-impact ion source that exploits a photo-cathode as source of electrons and is expected to reach an ionization efficiency of 1% for $Mo(CO)_6$. The ionization efficiency of the proposed source is estimated by scaling the measured ionization efficiency of $Mo(CO)_6$ obtained in an exploratory experiment by the respective calculated electron currents. In the experiment, electrons were liberated by a laser, however the exact mechanism of electron production could not be identified. The increase in electron current (*cf.* eq. 13) can be achieved by adaptation of the geometry which allows higher bunch charges without virtual cathode formation and an increase in the repetition rate of the laser. An anode potential of $V_g = 120\,\mathrm{V}$ is assumed. See text for details.

Parameter	Symbol	Unit	Exploratory Experiment	Proposed Photo-cathode source
1. Geometry and calculated critical bunch charge				
laser spot diameter †	$2\,r_{\mathrm{em}}$	mm	1.5	12
anode-cathode distance	d_{g}	mm	1.5	3
critical bunch charge §	q_{c}	pC	2	45
2. Cathode and laser wavelength				
cathode material			Ta	Cu
center wavelength	λ_{l}	nm	343	257
quantum efficiency at λ_{l}	ϵ_{q}	%	– ‡	0.014 [88]
3. Required laser system				
pulse repetition rate	ξ	MHz	0.05	2
average power	P_{l}	W	< 4.5 ‖	3.7
pulse energy	E_{l}	µJ	< 90 ‖	1.9 #
fluence per pulse	ϕ_{l}	$\mu\mathrm{J\,cm^{-2}}$	< 5093 ‖	1.6
4. Calculated mean electron current and ionization efficiency				
mean electron current	I_{m}	µA	0.09	90
ionization efficiency	ϵ_{ion}	%	0.001	1

† circular area on the cathode that is illuminated and emits electrons

§ calculated maximum charge that can be transported in a short pulse between cathode and anode without virtual cathode formation

‡ data on multiphoton quantum efficiency not available and mechanism of electron production unclear

‖ An upper limit is given based on the measured laser power before entering the vacuum system.

Chosen to match critical charge q_{c}

tor two below the calculated space-charge limited current at a typical anode potential of 120 V. The observation of saturation effects of electron current with laser pulse energy might also indicate operation in proximity of a space-charge limited regime.

The maximum current density J_{p} that can pass a gap of length d_{g} with a potential difference of V_{g} is classically given by the Child-Langmuir law [89,90]. If the transition time of electrons between cathode and anode grid is long compared to the laser pulse of duration τ_{p}, a single sheet approximation can be applied [91]. Corrections for the two-dimensional geometry have been proposed in ref. [92]. The maximum mean current I_{m} (without virtual cathode formation occurring) is given by

$$I_{\mathrm{m}} = J_{\mathrm{p}}\,\pi r_{\mathrm{em}}^2\,\xi\,\tau_{\mathrm{p}} = \left(1 + \frac{d_{\mathrm{g}}}{4r_{\mathrm{em}}}\right)\frac{\epsilon_0 \pi r_{\mathrm{em}}^2 V_{\mathrm{g}}}{d_{\mathrm{g}}}\,\xi, \qquad (13)$$

where ξ is the pulse repetition rate and r_{em} the radius of the electron-emitting surface. To allow higher electron currents, the repetition rate of the laser or the diameter of the electron-emitting surface can be increased. Increasing the anode potential V_{g} would push the ionization cross section into an unfavorable regime, and the further reduction of anode-cathode distance (typically 1.5 mm) reduces the reliability of the ion source since a minor displacement is sufficient to cause an electrical contact between anode and cathode.[4]

The laser driver is most effective if the resulting electron pulse charge does not the exceed the critical limit $q_{\mathrm{c}} = I_{\mathrm{m}}\xi^{-1}$. The characteristic parameters, such as mean power P_{l}, pulse energy $E_{\mathrm{l}} = P_{\mathrm{l}}\xi^{-1}$ and pulse energy fluence $\phi_{\mathrm{l}} = E_{\mathrm{l}}\pi^{-1}r_{\mathrm{em}}^{-2}$ can be estimated by the quantum efficiency ϵ_q, *i.e.* the ratio of emitted electrons to photons hitting the surface, as

$$E_{\mathrm{l}} = \frac{h\,c}{\lambda_{\mathrm{l}}}\frac{q_{\mathrm{c}}}{\epsilon_{\mathrm{q}}\,e}, \qquad (14)$$

where h is the Planck constant, and λ_{l} the photon wavelength. Many high-quantum-efficiency materials are semiconductors, like cesium telluride. They require sophisticated vacuum systems (pressures below 10^{-9} mbar) to reach

[4] Such issues were observed for resistively heated cathodes of VADIS at ISOLDE.

their nominal performance [93]. On the other hand, metal cathodes have a lower quantum efficiency but can operate at higher pressures. Thus, a copper cathode was chosen for the estimations which has a quantum efficiency of ca. 0.014% at 266 nm and a residual pressure of 10^{-7} mbar [88,93].

A set of design parameters for a cold photo-cathode driven ion source and laser system is proposed in table 3. Following the previous discussion, the parameters are chosen such that an ionization efficiency of 1% for $Mo(CO)_6$ could be reached under the assumption that the measured ionization efficiency scales linearly with the space-charge-limited electron current. The proposed design assumes a laser spot diameter of $2r_{\mathrm{em}} = 12$ mm which is equal to the size of the VADIS cathode. In our preparatory experiment (*c.f.* fig. 8), the laser beam was guided through the ion beam outlet hole on the cathode. An increase of the outlet hole diameter from currently 1.5 mm to 12 mm might significantly decrease the source efficiency because it reduces the residence time of neutral species in the anode body. Thus, we propose to introduce the laser beam perpendicular to the electron beam, a trajectory that was recently developed for the perpendicularly-illuminated LIST ion source [94]. The aforementioned laser path is estimated to require an increased anode-cathode distance of ca. 3 mm. The required pulse energy fluence computes to $1.9\,\mu\mathrm{J\,cm^{-2}}$ which is well below the ablation threshold of $0.77\,\mathrm{J\,cm^{-2}}$ even for short (10 fs) pulses [95]. Other factors contributing to damage of photo-cathodes have been identified. In ref. [96], the damage threshold for copper photo cathodes was estimated by simulation and a fluence of less than $40\,\mathrm{mJ\,cm^{-2}}$ is recommended. The reliability and efficiency of such a photo-cathode source might be impacted by condensation of molecule fragments on the cathode or the residual pressure of carbon monoxide. Its behavior needs to be experimentally verified.

A deep ultra violet (DUV) laser is required for efficient release of electrons from metal photo-cathodes. Due to the limited bunch charge, high repetition rates are beneficial. As listed in table 3, the desired efficiency of ca. 1% for $Mo(CO)_6$ could be reached with 3.7 W average power at a wavelength of 257 nm and repetition rate of 2 MHz. A recent review about DUV laser generation is given in ref. [97]. The required laser system could be based on fourth harmonic generation of a 1 µm Yb fiber laser. Besides pulsed lasers, also continuous wave (cw) lasers could be considered [98,99,100]. For the latter, additional considerations apply for ionization efficiency estimates, as will be discussed in the following paragraphs.

Continous thermionic source efficiency The spatial separation of a resistively heated cathode and ionization volume provides an alternative path towards a cold electron impact ion source. A thermionic electron source could be placed remotely in an actively cooled environment, with no line of sight to the ionization volume to avoid radiative heating. The achievable ionization efficiencies of $Mo(CO)_6$ in such a configuration can be estimated from krypton efficiencies, which are in the range of 30% for known FEBIAD-type sources [73,101].

For this, our experimental results are compared to the aforementioned model (eq. 12). While the ionization cross-section of a given compound is independent of the ion source, the extraction factors f of a continuously operated thermionic emission ion source and a pulsed laser-induced emission source are expected to differ, even if the geometry of the cavity is similar. In the first case, the continous release of electrons generates an electric field in the ionization volume which influences the extraction of ions. It was proposed that this is due to the formation of a potential well [101,102,103,104]. In comparison to the immediate extraction of a nascent ion guided by a favourable field, a potential well might also increase the number of wall collisions of an ion before extraction. The latter would decrease the extraction factor f, particularly for condensible species which are lost to surfaces upon collision. The pulsed electron generation in our experiments is expected to significantly reduce the aforementioned hindrance due to the limited life-time of electrons [81]. On the other hand, the electric field present in sources with continuous electron emission might guide produced ions towards the outlet. In an electron-free environment, the operation at room temperature contributes to a more efficient ion extraction. The field produced by the grounded extraction electrode penetrates into the anode volume and decreases the potential near the outlet aperture. Ions created in this region are guided along the decreasing field towards the outlet hole. To overcome the gradient to the outlet hole, a certain ion energy is required. Thus, as argued in ref. [81], the region of direct extraction (active volume) decreases with increasing ion energy.

By evaluation of the parameters given in eq. 12 similar to the derivation discussed in [81], it can be written as

$$\epsilon_{\mathrm{ion}} = \frac{I}{\mathrm{e}\,S_{\mathrm{out}}} \sqrt{\frac{2\,\pi\,M}{\mathrm{R}\,T}}\,\sigma\,l\,f, \tag{15}$$

where I is the electron current, e the elementary charge, S_{out} the cross-sectional area of the outlet hole, T the temperature of the ion source, M the molar mass of the neutral species, R the universal gas constant, l the length of the ionization volume in the axial direction and σ the ionization cross-section. As in eq. 12, the probability of ion extraction (and other effects) is solely included in the factor f. As already discussed, the electron current I was approximated with the theoretical space charge-limited current, estimated for short pulses [91] and corrected for the limited emitter surface [92].

The dependence of the extraction factor f on the anode potential is shown in fig. 10 for krypton beams from the exploratory cold ion source (*cf.* fig. 8) using evaluated cross sections [105], along with data obtained for argon from FEBIAD-type sources [81]. For this measurement, light at a wavelength of 515 nm was used. The extraction factor is given as linear combination $f = f_{\mathrm{no-mag}}\,f_{\mathrm{mag}}$. The factor $f_{\mathrm{no-mag}}$ is directly obtained from a measurement with disabled source magnet. The factor f_{mag} is calculated by dividing the extraction factor with enabled mag-

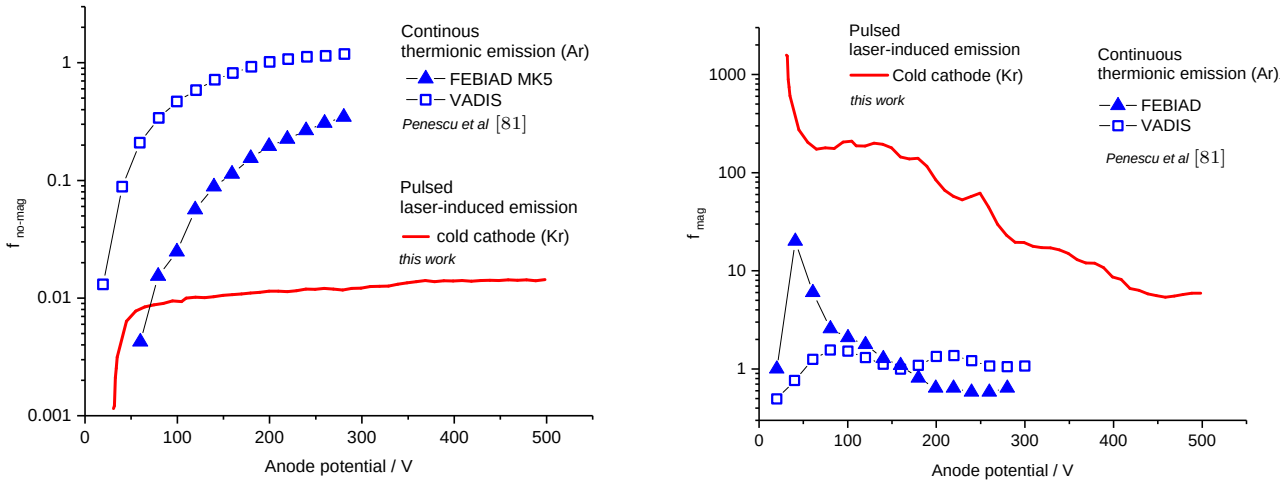

(a) Extraction without source magnet

(b) Contribution of source magnet

Fig. 10. Contributions to the extraction factor $f = f_{\mathrm{no-mag}}\, f_{\mathrm{mag}}$, according to eq. 15, for the exploratory cold ion source shown in fig. 8 used in this work, in comparison to data from FEBIAD sources, which were taken from [81]. The magnet currents in (b) were 4.5 A and 6 A for the continuous thermionic source and the pulsed laser-induced emission source, respectively. See text for details.

net by the previously obtained factor $f_{\mathrm{no-mag}}$. As can be seen from fig. 10, the similarity in the curves for pulsed laser-induced and continous thermionic electron emission indicates that in both cases electron impact ionization is observed. As discussed in more detail in ref. [81], the factor $f_{\mathrm{no-mag}}$ increases with anode potential, which can be attributed to a reduced space-charge repulsion at higher electron velocities leading to a better electron confinement. For FEBIAD-type sources, the ion extraction might also be favored at higher voltages due to a reduced Debye-length and increased active volume. The magnetic field increases the electron density, an effect which is significantly more pronounced for the laser-induced electron emission ion source. Deviations between the cold exploratory ion source and FEBIAD-type sources arise not only due to the laser induced, pulsed release of electrons, but also due to a different geometry of electron extraction. While the whole cathode surface (ca. 12 mm diameter) emits electrons in thermionic mode, the laser spot is defined by the diameter of the outlet aperture of the source, which is 1.5 mm only. Seeing the similar shape of the curves, an order-of-magnitude estimation of the extraction factor for the VADIS source in the ionization process of molybdenum hexacarbonyl is proposed in the following, provided the cathode heating and the ionization volume with the anode can be decoupled as already discussed.

Due to unknown ionization cross sections of $Mo(CO)_6$, the extraction factor f cannot be experimentally obtained from an efficiency measurement. However, the short lifetime of electrons after a laser pulse, in comparison to longer extraction times of ions, suggests that the hindrance of extraction by electrostatic fields inside the cold exploratory ion source is low. Thus, as first approximation it is assumed that the krypton extraction factor $f^{\mathrm{L}}_{\mathrm{Kr}}$ is equal to the extraction factor of molybdenum hexacarbonyl $f^{\mathrm{L}}_{\mathrm{Mo(CO)_6}}$ in the cold exploratory ion source.[5] The situation in the VADIS source is different, and the extraction factor of $Mo(CO)_6$ is approximated with the extraction factor of carbon monoxide, which suffers from similar electron-beam induced decomposition issues as $Mo(CO)_6$ inside the source. Under these assumptions, the ionization efficiency of $Mo(CO)_6$ in a cavity with only cold surfaces (*i.e.* no thermal decomposition), computes to[6]

$$\mathcal{E}^{\mathrm{VD}}_{\mathrm{Mo(CO)_6}} \sim \mathcal{E}^{\mathrm{L}}_{\mathrm{Mo(CO)_6}} \frac{\mathcal{E}^{\mathrm{VD}}_{\mathrm{Kr}}\, f^{\mathrm{VD}}_{\mathrm{CO}}}{\mathcal{E}^{\mathrm{L}}_{\mathrm{Kr}}\, f^{\mathrm{VD}}_{\mathrm{Kr}}} \sim 2\%. \qquad (16)$$

The ion source proposed here is exposed to a significant partial pressure of residual carbon monoxide. While in some cases results have been obtained, indicating that residual carbon monoxide might increase the ionization efficiency for elements with lower ionization potential [102], experimental results for molybdenum hexacarbonyl are not available.

A drawback of ion sources exploiting electron impact ionization is the lack of selectivity. Separation of isobaric contaminants in the radioactive ion beam has been achieved by element-dependent adsorption on quartz columns [107, 108]. Unfortunately, this technique might not be suitable to separate different carbonyl compounds, as their adsorption enthalpies are in the same range [109]. An alternative

[5] A mass dependence of the extraction factor has been observed, however even the ratio of xenon and argon extraction factors was found to only be $\frac{f^{\mathrm{VD}}_{\mathrm{Xe}}}{f^{\mathrm{VD}}_{\mathrm{Ar}}} \approx 1.8$ [81].

[6] The calculation assumes a typical ionization efficiency of 1% for carbon monoxide, an ionization cross section of ca. $1.9 \times 10^{-20}\,\mathrm{m}^2$ at 120 V anode potential [106], space-charge limited electron current, and a distance between anode and cathode of 1.5 mm.

approach could be based on differences in compound stabilities. Carbonyl complexes of Tc, Ru and Rh readily decompose on gold surfaces already at ambient temperature (30 °C to 50 °C), whereas Mo complexes have a survival probability of 60% in the same setup [24]. Differences in the ionization fragmentation patterns could be exploited for additional selectivity.

2.4.3 Laser ionization

Resonant laser ionization is a powerful tool for element-selective ionization. However, the technique is typically only applied to single atoms. Recently, a resonant laser ionization scheme for molybdenum was developed and tested online at ISOLDE [111]. Exploiting this scheme for carbonyl compounds requires first to strip the molybdenum atom of its carbonyl ligands. Laser induced breakup of the compound [112,113] is widely discussed in literature and resonant breakup is also reported in ref. [114]. The concept of laser-induced neutral dissociation followed by resonant laser ionization is further discussed in ref. [115]. While the efficiency of laser induced breakup and ionization has not yet been quantified, the method would allow element-selective ionization.

3 Conclusions and Implementation at ISOLDE

Within the previous sections, we have provided a concept for a gas-filled recoil target, which can be used at ISOL facilities. Thin metallic foils acting as target material are placed around a tungsten rod, which serves as a spallation neutron source. Instead of diffusion, the recoil energy of the reaction product is exploited to extract the radioisotopes from the foil. They are subsequently thermalized in carbon monoxide gas. Volatile carbonyl complexes form at ambient temperature and pressure. The carbonyl complexes are chromatographically separated from the carbon monoxide gas and fed into an ion source. Following the discussion in the previous section, the estimated efficiency for each step is listed in table 4. Experimentally obtained ionization efficiencies in a proof-of-principle setup along with expected values after successful ion source development are given. In the former case, intensities in the order of $51\,\mathrm{s}^{-1}$ for ^{105}Mo from uranium foils and $6\,\mathrm{s}^{-1}$ for ^{174}W from platinum foils can be expected. After successful development of the proposed ion source, a total intensity of $3.4 \times 10^4\,\mathrm{s}^{-1}$ for ^{105}Mo and $3.9 \times 10^3\,\mathrm{s}^{-1}$ for ^{174}W is expected. Typically, intensities in this order of magnitude are compatible with post-acceleration within the HIE-ISOLDE linac [116].[7]

The implementation at ISOLDE can be achieved with two different approaches. Standard target units already combine a class of target material, some chromatography setup and an ion source [107]. Following this approach, a compact setup is mandatory that is also suitable to operate in strong radiation fields. The dimensions and weight of the setup are limited by the maximum permitted load for the robot operating the target unit and the design of the target stations. Due to the low temperatures required for gas separation, needs arise to either implement a cryostat system at the target stations, or follow an alternative strategy for gas separation.

The second approach splits the setup in two assemblies. The gas-filled target remains installed at the target station, while the chromatographic setup is installed remotely, *e.g.* in the ISOLDE experimental hall. The carbonyl compounds are extracted as neutrals in a carbon monoxide stream to the remote location, which is an efficient and established technique, commonly used in transactinide synthesis to transport the compound over a distance of several meters in short times [109]. The split installation circumvents size and weight limitations of the chromatographic setup and the operation of the latter in radiation environments.

4 Outlook

Following this study, we have started to experimentally investigate the feasibility of the concept. A target unit was built, which allows the characterization of the neutron converter setup and the in-target production rates along with beam-induced breakup of carbonyl compounds.

The recently started development of a two chamber approach for the synthesis of carbonyl compounds is not yet included in the considerations of this work [117]. Within this approach, the target foils can be directly irradiated by the proton beam. The nuclear reaction products are flushed with an inert gas stream into a second chamber, in which the radioactive atoms are allowed to react with carbon monoxide to form carbonyl compounds. In this setup a transport efficiency between the two chambers of more than 50% was measured. The spatial separation of isotope production and molecule formation would allow benefiting from higher in-target production rates and avoids exposure of delicate compounds to strong radiation fields at the same time.

5 Acknowledgments

We would like to thank F. Wenander, U. Köster, A. Andreyev and R. Heinke for their comments and fruitful discussions regarding the target concept. We also thank M. Götz for the insights into his ongoing development work of the two-chamber approach for carbonyl compound production. We appreciate support for simulation codes from R. Dos Santos Augusto (FLUKA), A. Kelic-Heil and J. Klimo (ABRABLA) and Ch. Duchemin (TALYS and FLUKA). The target unit used in the ionization studies has been manufactured by the ISOLDE workshop (E. Barbero, B. Crepieux, M. Owen, and A. Viéitez Suárez). This

[7] The actual intensity of the post-accelerated beam depends on additional factors such as presence of isobaric contaminants, molecular break-up and charge state distribution in the electron-beam ion source (charge breeder).

Table 4. Estimation of expected ion beam yields of ^{105}Mo from uranium foils, and ^{174}W from platinum foils.

Symbol	Unit	Description	^{105}Mo		^{174}W		ref.
$T_{1/2}$	s	half life	36		1860		[110]
Predominant production reaction			U(n,f)		Pt(n,spall)		sect. 2.1
N_0	μC^{-1}	in-target production	3.8×10^8		4.5×10^8		sect. 2.1
t_{irr}	s	irradiation time	50		400		sect. 2
I_p	µA	proton current	2.0		2.0		[5]
N_0^{batch}		isotopes per batch	2.4×10^{10}		3.3×10^6		eq. 2
$\nu_{\mathrm{batch}}^{-1}$	s	cycle time	83		454		sect. 2
ϵ_{extr}	%	extraction eff.	10		1.6		sect. 2.2
ϵ_{stop}	%	stopping eff.	49		21		sect. 2.2
ϵ_{form}	%	chemical eff.	80		30		[21]
ϵ_{sep}	%	gas-separation eff.	30		50		sect. 2.3
ϵ_{ion}	%	ionization eff.†	1	0.0015	1	0.0015	sect. 2.4
N	s^{-1}	average ion rate	3.4×10^4	51	3.9×10^3	6	eq. 2

† Two ionization efficiencies are given. The lower efficiency was measured in an exploratory experiment with a cold VADIS, in which electrons were released by a laser. The higher efficiency is an estimated value that is believed to be in reach after development of a cold FEBIAD-type ion source (cf. sect. 2.4).

project has received funding from MEDICIS-Promed and the European Union's Horizon 2020 research and innovation program under grant agreement No 654002.

6 Authors contributions

All the authors were involved in the preparation of the manuscript. All authors have read and approved the final manuscript.

References

1. O. Kofoed-Hansen, K. Nielsen, Dan. Mat.Fys.Medd **26**, no. 7 (1951)
2. J. Koch, O. Kofoed-Hansen, P. Kristensen, W. Drost-Hansen, Physical Review **76**, 279 (1949)
3. J. Ramos, Nuclear Instruments and Methods in Physics Research Section B: Beam Interactions with Materials and Atoms **463**, 201 (2020)
4. J. Lettry, R. Catherall, G. Cyvoct, P. Drumm, A. Evensen, M. Lindroos, O. Jonsson, E. Kugler, J. Obert, J. Putaux et al., Nuclear Instruments and Methods in Physics Research Section B: Beam Interactions with Materials and Atoms **126**, 170 (1997)
5. R. Catherall, W. Andreazza, M. Breitenfeldt, A. Dorsival, G.J. Focker, T.P. Gharsa, G.T. J, J.L. Grenard, F. Locci, P. Martins et al., Journal of Physics G: Nuclear and Particle Physics **44**, 094002 (2017)
6. L. Zanini, M. Andersson, P. Everaerts, M. Fallot, H. Frånberg, F. Gröschel, C. Jost, T. Kirchner, Y. Kojima, U. Köster et al., AIP Conference Proceedings **769**, 1525 (2005)
7. C. Elschenbroich, Organometallchemie, Teubner Studienbücher Chemie (Vieweg+Teubner Verlag, 2009), ISBN 9783835192232
8. The ISOLDE yield database, `http://isolde.web.cern.ch` (2018), [Online; accessed 24-August-2018]
9. C.F. Liang, P. Paris, D. Bucurescu, S. Della Negra, J. Obert, J.C. Putaux, Zeitschrift für Physik A Atoms and Nuclei **309**, 185 (1982)
10. Y.I. Frenkel, Statisticheskaya Fizika (Statistical physics) (Izd Akad Nauk SSSR, Moskva, 1948)
11. J. Frenkel, Zeitschrift für Physik **26**, 117 (1924)
12. M. Schädel, D. Shaughnessy, eds., The Chemistry of Superheavy Elements (Springer Berlin Heidelberg, 2014), `https://doi.org/10.1007/978-3-642-37466-1`
13. U. Köster, P. Carbonez, A. Dorsival, J. Dvorak, R. Eichler, S. Fernandes, H. Frånberg, J. Neuhausen, Z. Novackova, R. Wilfinger et al., The European Physical Journal Special Topics **150**, 285 (2007)
14. U. Köster, O. Arndt, E. Bouquerel, V. Fedoseyev, H. Frånberg, A. Joinet, C. Jost, I. Kerkines, R. Kirchner, Nuclear Instruments and Methods in Physics Research Section B: Beam Interactions with Materials and Atoms **266**, 4229 (2008)
15. J. Ballof, C. Seiffert, B. Crepieux, Ch.E. Düllmann, M. Delonca, M. Gai, A. Gottberg, T. Kröll, R. Lica, M.M. Flores et al., The European Physical Journal A **55**, 65 (2019)
16. C.F. Liang, P. Paris, M.G. Porquet, J. Obert, J.C. Putaux, Zeitschrift für Physik A Atoms and Nuclei **321**, 695 (1985)
17. P. Kunz, The ISAC yield database, `http://mis.triumf.ca/science/planning/yield/beam` (2020), [Online; accessed 22-April-2020]
18. F. Baumgärtner, P. Reichold, Z. Naturforsch. **16a**, 945 (1961)
19. G.K. Wolf, W. Fröschen, Tech. Rep. KFK 1783, Kernforschungszentrum Karlsruhe, Zyklotron-Laboratorium, Karlsruhe (1973)
20. K. Bächmann, Chemical Problems of the On-Line Separation of Short-Lived Nuclides, in Proceedings of the 7th international conference on electromagnetic isotope

separators and the technique of their applications (1970), p. 126
21. J. Even, A. Yakushev, Ch.E. Düllmann, J. Dvorak, R. Eichler, O. Gothe, W. Hartmann, D. Hild, E. Jäger, J. Khuyagbaatar et al., Radiochimica Acta **102**, 1093 (2014)
22. J. Even, A. Yakushev, Ch.E. Düllmann, J. Dvorak, R. Eichler, O. Gothe, D. Hild, E. Jäger, J. Khuyagbaatar, J.V. Kratz et al., Inorganic Chemistry **51**, 6431 (2012)
23. K. Katagiri, A. Noda, K. Suzuki, K. Nagatsu, A.Y. Boytsov, D.E. Donets, E.D. Donets, E.E. Donets, A.Y. Ramzdorf, M. Nakao et al., Review of Scientific Instruments **86**, 123303 (2015)
24. I. Usoltsev, R. Eichler, Y. Wang, J. Even, A. Yakushev, H. Haba, M. Asai, H. Brand, A.D. Nitto, Ch.E. Düllmann et al., Radiochimica Acta **104**, 141 (2016)
25. I. Usoltsev, R. Eichler, A. Türler, Radiochimica Acta **104**, 531 (2016)
26. Ch.E. Düllmann, K.E. Gregorich, G.K. Pang, I. Dragojevic, R. Eichler, C.F. III, M.A. Garcia, J.M. Gates, D. Hoffman, S.L. Nelson et al., Radiochimica Acta **97** (2009)
27. Y. Wang, Z. Qin, F.L. Fan, S.W. Fan, F.-Y.and Cao, X.L. Wu, X. Zhang, J. Bai, X.J. Yin, L.L. Tian, L. Zhao et al., Radiochimica Acta **102** (2014)
28. Y. Wittwer, R. Eichler, D. Herrmann, A. Türler, Radiochimica Acta **109**, 243 (2021)
29. R. Catherall, J. Lettry, S. Gilardoni, U. Köster, Nuclear Instruments and Methods in Physics Research Section B: Beam Interactions with Materials and Atoms **204**, 235 (2003)
30. T. Stora, E. Noah, R. Hodak, T.Y. Hirsh, M. Hass, V. Kumar, K. Singh, S. Vaintraub, P. Delahaye, H. Frånberg-Delahaye et al., EPL (Europhysics Letters) **98**, 32001 (2012)
31. J. Ramos, M. Ballan, L. Egoriti, D. Houngbo, S. Rothe, R. Augusto, A. Gottberg, M. Dierckx, L. Popescu, S. Marzari et al., Nuclear Instruments and Methods in Physics Research Section B: Beam Interactions with Materials and Atoms **463**, 357 (2020)
32. R. dos Santos Augusto, L. Buehler, Z. Lawson, S. Marzari, M. Stachura, T. Stora, CERN-MEDICIS collaboration, Applied Sciences **4**, 265 (2014)
33. R. Luis, J.G. Marques, T. Stora, P. Vaz, L. Zanini, The European Physical Journal A **48** (2012)
34. A. Gottberg, T. Mendonca, R. Luis, J. Ramos, C. Seiffert, S. Cimmino, S. Marzari, B. Crepieux, V. Manea, R. Wolf et al., Nuclear Instruments and Methods in Physics Research Section B: Beam Interactions with Materials and Atoms **336**, 143 (2014)
35. J. Bennett, C. Densham, P. Drumm, W. Evans, M. Holding, G. Murdoch, V. Panteleev, Nuclear Instruments and Methods in Physics Research Section B: Beam Interactions with Materials and Atoms **126**, 117 (1997)
36. D. Stoychev, A. Papoutsis, A. Kelaidopoulou, G. Kokkinidis, A. Milchev, Materials Chemistry and Physics **72**, 360 (2001)
37. T.T. Böhlen, F. Cerutti, M.P.W. Chin, A. Fassò, A. Ferrari, P.G. Ortega, A. Mairani, P.R. Sala, G. Smirnov, V. Vlachoudis, Nuclear Data Sheets **120**, 211 (2014)
38. A. Ferrari, P.R. Sala, A. Fassò, J. Ranft, FLUKA: A multi-particle transport code, CERN Yellow Reports: Monographs (CERN, Geneva, 2005), `http://cds.cern.ch/record/898301`
39. J.F. Ziegler, M. Ziegler, J. Biersack, Nuclear Instruments and Methods in Physics Research Section B: Beam Interactions with Materials and Atoms **268**, 1818 (2010), 19th International Conference on Ion Beam Analysis
40. J.F. Ziegler, SRIM – The Stopping Range of Ions in Matter , `http://www.srim.org` (2018), [Online; accessed 24-August-2018]
41. S. Lukić, F. Gevaert, A. Kelić, M. Ricciardi, K.H. Schmidt, O. Yordanov, Nuclear Instruments and Methods in Physics Research Section A: Accelerators, Spectrometers, Detectors and Associated Equipment **565**, 784 (2006)
42. A. Koning, D. Rochman, Nuclear Data Sheets **113**, 2841 (2012), special Issue on Nuclear Reaction Data
43. A. Koning, S. Hilaire, S. Goriely, Talys-1.95, a nuclear reaction program, `https://www.talys.eu`
44. K.H. Schmidt, B. Jurado, C. Amouroux, Tech. rep., Organisation for Economic Co-Operation and Development (2014)
45. K.H. Schmidt, B. Jurado, GEF – A General Description of Fission Observables, `http://www.khs-erzhausen.de/GEF.html`, version 2019/1.1, [Online; accessed 21-February-2019]
46. A. Kelic, M.V. Ricciardi, K.H. Schmidt, ABLA07 - towards a complete description of the decay channels of a nuclear system from spontaneous fission to multifragmentation, in Joint ICTP-IAEA Advanced Workshop on Model Codes for Spallation Reactions Trieste, Italy, February 4-8, 2008 (2009), `0906.4193`
47. T.E. Cocolios, B.A. Marsh, V.N. Fedosseev, S. Franchoo, G. Huber, M. Huyse, A.M. Ionan, K. Johnston, U. Köster, Y. Kudryavtsev et al., Nuclear Instruments and Methods in Physics Research Section B: Beam Interactions with Materials and Atoms **266**, 4403 (2008)
48. D. Filges, F. Goldenbaum, Handbook of Spallation Research (Wiley VCH Verlag GmbH, 2009), ISBN 3527407146
49. Wolfram Research Inc., Mathematica, Version 11.3, Champaign, IL, 2018
50. B. Eichler, V.P. Domanov, Journal of Radioanalytical Chemistry **28**, 143 (1975)
51. W.M. Haynes, Handbook of chemistry and physics; 91th ed. (CRC Press, New York, NY, 2010)
52. J. Powell, F.Q. Guo, P.E. Haustein, R. Joosten, R.M. Larimer, C. Lyneis, D.M. Moltz, E.B. Norman, J.P. O'Neil, M.W. Rowe et al., BEARS: radioactive ion beams at LBNL, in Exotic nuclei and atomic masses (ENAM 98) (ASCE, 1998)
53. J. Pitters, M. Breitenfeldt, H. Pahl, A. Pikin, F. Wenander, Nuclear Instruments and Methods in Physics Research Section B: Beam Interactions with Materials and Atoms **463**, 198 (2020)
54. A.Y. Boytsov, D.E. Donets, E.D. Donets, E.E. Donets, K. Katagiri, K. Noda, D.O. Ponkin, A.Y. Ramzdorf, V.V. Salnikov, V.B. Shutov, Review of Scientific Instruments **86**, 083308 (2015)
55. J. Pitters, M. Breitenfeldt, F.J.C. Wenander, H. Pahl, A. Pikin, Tech. rep. (2018), `http://cds.cern.ch/record/2648691`
56. J. Even, Ph.D. thesis, Johannes Gutenberg-Universität Mainz (2011)
57. S. Cao, Y. Wang, Z. Qin, F. Fan, H. Haba, Y. Komori, X. Wu, C. Tan, X. Zhang, Physical Chemistry Chemical Physics **18**, 119 (2016)

58. Y. Wang, Z. Qin, F.L. Fan, H. Haba, Y. Komori, S.W. Cao, X.L. Wu, C.M. Tan, Physical Chemistry Chemical Physics **17**, 13228 (2015)
59. I. Zvara, Radiochim. Acta **38**, 95 (1985)
60. H.L. Johnston, E.R. Grilly, The Journal of Physical Chemistry **46**, 948 (1942)
61. K. Jousten, Wutz Handbuch Vakuumtechnik: Theorie und Praxis; 9th ed. (Vieweg, Wiesbaden, 2006), https://cds.cern.ch/record/1125847
62. J.C. Giddings, Dynamics of chromatography (Marcel Dekker, Inc., New York, 1965)
63. E.R. Gilliland, Industrial & Engineering Chemistry **26**, 681 (1934)
64. I. Zvára, The Inorganic Radiochemistry of Heavy Elements (Springer Netherlands, 2008), https://doi.org/10.1007/978-1-4020-6602-3
65. T. Stora, Radioactive Ion Sources, in CAS-CERN Accelerator School: Ion Sources, Senec, Slovakia, 29 May - 8 June 2012, edited by R. Bailey (2014), p. 19, http://cds.cern.ch/record/1693046
66. B. Marsh, Resonance Ionization Laser Ion Sources, in CAS-CERN Accelerator School: Ion Sources, Senec, Slovakia, 29 May - 8 June 2012, edited by R. Bailey (2014), p. 61, http://cds.cern.ch/record/1693046
67. Y.J. Chen, C.L. Liao, C.Y. Ng, The Journal of Chemical Physics **107**, 4527 (1997)
68. S. Masuda, Y. Harada, The Journal of Chemical Physics **96**, 2469 (1992)
69. B.E. Bursten, D.J. Darensbourg, G.E. Kellogg, D.L. Lichtenberger, Inorganic Chemistry **23**, 4361 (1984)
70. G.D. Michels, G.D. Flesch, H.J. Svec, Inorganic Chemistry **19**, 479 (1980)
71. K.E. Lewis, D.M. Golden, G.P. Smith, Journal of the American Chemical Society **106**, 3905 (1984)
72. A.W. Ehlers, G. Frenking, Journal of the American Chemical Society **116**, 1514 (1994)
73. R. Kirchner, E. Roeckl, Nuclear Instruments and Methods **133**, 187 (1976)
74. L. Penescu, R. Catherall, J. Lettry, T. Stora, Review of Scientific Instruments **81**, 02A906 (2010)
75. I.G. Brown, The Physics and Technology of Ion Sources; 2nd ed. (Wiley, Weinheim, 2004), https://cds.cern.ch/record/1113300
76. H. Koivisto, J. Ärje, M. Nurmia, Nuclear Instruments and Methods in Physics Research Section B: Beam Interactions with Materials and Atoms **94**, 291 (1994)
77. T. Nakagawa, J. Ärje, Y. Miyazawa, M. Hemmi, T. Chiba, N. Inabe, M. Kase, T. Kageyama, O. Kamigaito, A. Goto et al., Nuclear Instruments and Methods in Physics Research Section A: Accelerators, Spectrometers, Detectors and Associated Equipment **396**, 9 (1997)
78. M.A. Da Silva, M.J. Monte, Thermochimica Acta **171**, 169 (1990)
79. A. Baev, V. Bludilina, I. Gajdym, Zhurnal Fizicheskoj Khimii **54**, 338 (1980)
80. R. Geller, Electron cyclotron resonance ion sources and ECR plasmas (IOP, Bristol, 1996), https://cds.cern.ch/record/381888
81. L.C. Penescu, Techniques to produce and accelerate radioactive ion beams. tehnici de producere si accelerare a fasciculelor radioactive (2009), presented 2009, http://cds.cern.ch/record/2259078
82. D.H. Kwon, Y.J. Rhee, Y.K. Kim, International Journal of Mass Spectrometry **245**, 26 (2005)
83. J.C. Jaeger, **11**, 132 (1953)
84. C.M. Verber, A.H. Adelman, Journal of Applied Physics **36**, 1522 (1965)
85. P. Musumeci, L. Cultrera, M. Ferrario, D. Filippetto, G. Gatti, M.S. Gutierrez, J.T. Moody, N. Moore, J.B. Rosenzweig, C.M. Scoby et al., Physical Review Letters **104**, 084801 (2010)
86. S. Mittelmann, J. Oelmann, S. Brezinsek, D. Wu, H. Ding, G. Pretzler, Applied Physics A **126** (2020)
87. P.W.E. Acree, NIST Chemistry WebBook, NIST Standard Reference Database 69 (National Institute of Standards and Technology, 1997), chap. Mass Spectra
88. T. Srinivasan-Rao, J. Fischer, T. Tsang, Journal of Applied Physics **69**, 3291 (1991)
89. C.D. Child, Physical Review (Series I) **32**, 492 (1911)
90. I. Langmuir, Physical Review **2**, 450 (1913)
91. Á. Valfells, D.W. Feldman, M. Virgo, P.G. O'Shea, Y.Y. Lau, Physics of Plasmas **9**, 2377 (2002)
92. Y.Y. Lau, Physical Review Letters **87** (2001)
93. S. Kong, J. Kinross-Wright, D. Nguyen, R. Sheffield, Nuclear Instruments and Methods in Physics Research Section A: Accelerators, Spectrometers, Detectors and Associated Equipment **358**, 272 (1995)
94. R. Heinke, T. Kron, S. Raeder, T. Reich, P. Schönberg, M. Trümper, C. Weichhold, K. Wendt, Hyperfine Interactions **238** (2016)
95. C.S.R. Nathala, A. Ajami, W. Husinsky, B. Farooq, S.I. Kudryashov, A. Daskalova, I. Bliznakova, A. Assion, Applied Physics A **122** (2016)
96. L.M. Zheng, Y.C. Du, C.X. Tang, W. Gai, Chinese Physics C **41**, 067002 (2017)
97. H. Xuan, H. Igarashi, S. Ito, C. Qu, Z. Zhao, Y. Kobayashi, Applied Sciences **8**, 233 (2018)
98. R. Zhao, X. Fu, L. Zhang, S. Fang, J. Sun, Y. Feng, Z. Xu, Y. Wang, Applied Optics **56**, 8973 (2017)
99. Z. Burkley, A.D. Brandt, C. Rasor, S.F. Cooper, D.C. Yost, Applied Optics **58**, 1657 (2019)
100. Z.N. Burkley, Ph.D. thesis, Colorado State University (2019), https://hdl.handle.net/10217/195311
101. L. Penescu, R. Catherall, J. Lettry, T. Stora, Review of Scientific Instruments **81**, 02A906 (2010)
102. Y. Martinez Palenzuela, Characterization and optimization of a versatile laser and electron-impact ion source for radioactive ion beam production at ISOLDE and MEDICIS. (2019), Doctoral Thesis, https://cds.cern.ch/record/2672954
103. F.M. Millan, T. Day Goodacre, A. Gottberg, Nuclear Instruments and Methods in Physics Research Section B: Beam Interactions with Materials and Atoms **463**, 302 (2020)
104. Y. Martinez Palenzuela, B. Marsh, J. Ballof, R. Catherall, K. Chrysalidis, T. Cocolios, B. Crepieux, T. Day Goodacre, V. Fedosseev, M. Huyse et al., Nuclear Instruments and Methods in Physics Research Section B: Beam Interactions with Materials and Atoms **431**, 59 (2018)
105. M.J. Higgins, J.G. Hughes, H.B. Gilbody, F.J. Smith, M.A. Lennon, K.L. Bell, A.E. Kingston, Atomic and molecular data for fusion ; 3, recommended cross sections and rates for electron impact ionization of atoms and ions: copper to uranium (Culham Lab., Abingdon, 1989), https://cds.cern.ch/record/203081

106. Y. Itikawa, Journal of Physical and Chemical Reference Data **44**, 013105 (2015)
107. E. Bouquerel, R. Catherall, M. Eller, J. Lettry, S. Marzari, T. Stora, I. Collaboration, The European Physical Journal Special Topics **150**, 277 (2007)
108. E. Bouquerel, Atomic beam merging and suppression of alkali contaminants in multi body high power targets: Design and test of target and ion source prototypes at ISOLDE (2009), http://cds.cern.ch/record/1259908, Doctoral Thesis
109. J. Even, A. Yakushev, Ch.E. Düllmann, H. Haba, M. Asai, T.K. Sato, H. Brand, A.D. Nitto, R. Eichler, F.L. Fan et al., Science **345**, 1491 (2014)
110. S. Chu, L.P. Ekström, R.B. Firestone, The Lund/LBNL nuclear data search, [Online; accessed 30-April-2020], `http://nucleardata.nuclear.lu.se/toi/`
111. K. Chrysalidis, Ph.D. thesis (2019), presented 29 Nov 2019, `http://cds.cern.ch/record/2703661`
112. D.G. Leopold, V. Vaida, Laser Chemistry **3**, 49 (1983)
113. R.C. Dunbar, in Gas Phase Inorganic Chemistry, edited by D.H. Russell (Springer Nature, 1989), pp. 323–352, ISBN 0306429721
114. L. Windhorn, T. Witte, J.S. Yeston, D. Proch, M. Motzkus, K.L. Kompa, W. Fuß, Chemical Physics Letters **357**, 85 (2002)
115. C. Seiffert, J. Ballof, Extraction of refractory elements by laser induced breakup and ionisation of molybdenum carbonyls (2017), Letter of Intent to the INTC, INTC-I-178, `https://cds.cern.ch/record/2241995`
116. A. di Pietro, K. Riisager, P. van Duppen, Journal of Physics G: Nuclear and Particle Physics **44**, 044013 (2017)
117. M. Götz, S. Götz, J.V. Kratz, J. Ballof, Ch.E. Düllmann, K. Eberhardt, C. Mokry, D. Renisch, J. Runke, T.K. Sato et al., Radiochimica Acta **109**, 153 (2021)

7 Conclusion and outlook

This thesis addressed multiple aspects of molecular sideband formation at ISOL facilities with the aim to facilitate radioactive ion beam production. It could be shown that radioactive boron beams can be produced by *in-situ* synthesis of boron fluorides in reaction of radiogenic boron with injected sulfur hexafluoride or carbon tetrafluoride. The release properties were analyzed and could be fitted to a model covering diffusion in the solid matrix and effusion from the target container to the ion source. The extracted ^{8}B beams were already used in successful experiments, *e.g.*, investigation of the electron capture and β-decay of ^{8}B into the highly excited states of ^{8}Be using the ISOLDE decay station setup [255] or to probe proton halo effects in collision with ^{64}Zn around the Coulomb barrier [256].

The formation of carbonyl selenide beams was studied in online experiments and with stable tracers at the ISOLDE offline 1 separator. Selenium beams are demanded by facility users, *e.g.*, for investigations in astrophysics [257]. Due to the present contaminations (like gallium), selenium is often extracted as carbonyl selenide (COSe). Motivated by a depletion of the carbonyl sideband that renders impossible experiments with post-accelerated beams, the formation of the molecule was studied. Previously, it was proposed that injection of oxygen or carbon monoxide into the target unit fosters the molecule formation. Following the results presented within this thesis, both proposals seem unlikely. First indication was found that injection of carbon tetrafluoride could recover the depleted sidebands. Further experiments are required to develop a more robust way for the extraction of COSe. These experiments could include synthesis of the compound under controlled conditions, matrices and possible catalytic surface effects.

The extraction of refractory elements by the ISOL method presents a challenge. Despite a more than 60 years long history of ISOL, most of the refractory elements are still not available as ISOL beam. Following recent developments in the field of superheavy elements [251], it was investigated by detailed calculations, simulations and exploratory experiments if the carbonyl-method could be applied to ISOL facilities. The efficient synthesis of volatile transition metal carbonyl compounds has been demonstrated by thermalization of fission recoils or fusion-evaporation residues in a carbon monoxide containing atmosphere ($\sim 1 \times 10^{3}$ mbar) at ambient temperature and pressure. For radioactive ion beam production, an additional separation step is required to remove the gas atmosphere since ion sources operate typically in a low pressure regime ($\sim 1 \times 10^{-5}$ mbar or lower). Ion beam yields for the isotopes ^{105}Mo and ^{174}W were estimated by consideration of production rates in the target material, the probability of extraction

by the recoil effect, molecule formation, separation from the residual gas atmosphere and ionization.

The ionization of $Mo(CO)_6$ was studied in available ion sources at ISOLDE, *i.e.*, VADIS (electron impact ionization in a hot environment with a forced electron beam), COMIC (microwave plasma) and Helicon (RF plasma) ion source. The available ion sources did not yield satisfactory efficiency for radioactive ion beam production, due to irreversible decomposition of the compound. Following the results, exploratory experiments exploiting electron impact ionization in a cold environment were conducted. These yielded, for the first time, similar ionization efficiency of the noble gas krypton and $Mo(CO)_6$. Instead of thermionic electron emission, the required electrons were liberated by a laser. Based on the experiment, design parameters for a photocathode-driven ion source were derived in calculations. It was estimated that an ionization efficiency of ca. 1% for $Mo(CO)_6$ could be reached. The ion beam yield of $^{105}Mo(CO)_6$ produced from a uranium foils target and $^{174}W(CO)_6$ obtained from a platinum foils target were estimated to be in the order of $1 \times 10^4\,s^{-1}$ and $1 \times 10^3\,s^{-1}$, respectively. Thus, the yields would be sufficient for conducting experiments requiring post accelerated beams at HIE-ISOLDE.

To verify the production rates of transition metal carbonyl compounds at ISOLDE, a setup has been designed, built and tested. The setup was designed to be compatible with handling by the available Kuka robot system and the ISOLDE hot-cells. The system allows for the first time the irradiation of a sample with spallation neutrons obtained from a proton-to-neutron converter without manual handling, which typically involves radiological risks and doses. The experiment has passed the safety audits and risk analysis, and is ready to be conducted after successful commissioning of the hot-cells.

Towards efficient ionization of fragile carrier molecules

A

Contents

Since the early days of ISOL developments, a variety of carrier molecules has been proposed for most of the known elements. Unfortunately, only the thermally most stable molecules could be extracted. This is mostly due to the high temperatures present in the target and ion source unit. Cold target methods have been proposed, but no means of ionization is available for efficient ionization of fragile carrier molecules. This chapter discusses attempts to ionize the fragile molecule $Mo(CO)_6$ with radiofrequency-heated plasma and arc-discharge ion sources with thermionic electron generation. The sources discussed within this chapter did not offer sufficiently high ionization efficiency. A promising approach via cold electron-impact ionization is discussed in Chapter 6.

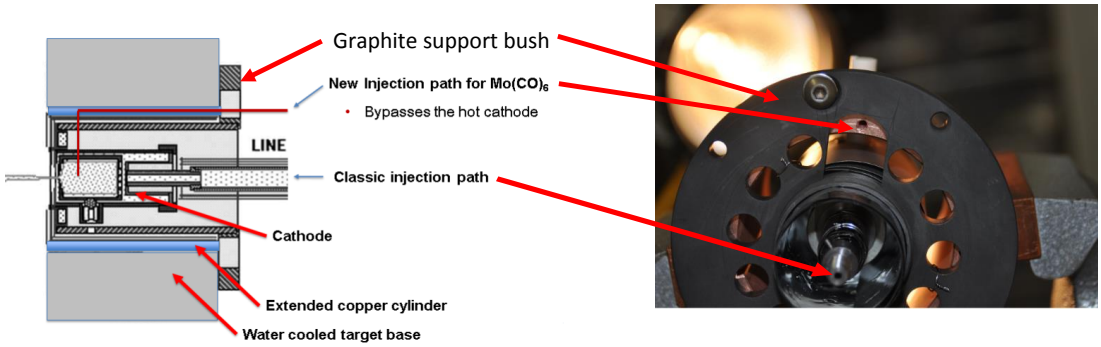

Figure A.1: Modified VADIS source with cold injection. Schematics (left) and photo from the neutral injection side (right). The classic injection path of a hot (VD5) ion source is indicated for reference.

A.1 Forced electron beam ion sources

In this section, experiments towards ionization of the delicate compound $Mo(CO)_6$ in a VADIS are summarized. First, the existing transfer lines, connecting target container and ion source, are briefly discussed with respect to survival of fragile molecules. Thereafter, the methods of carbonyl injection are described and finally, the obtained results are presented. All experiments have been conducted at the ISOLDE offline 1 separator that was previously described in sect. 2.4.1.

The available transfer lines were discussed in sect. 1.2.3. The hot transfer line (VD5) is designed to operate at the maximum achievable temperature. It is heated along with the ion source. Neutrals reach the ionization volume through the hollow cathode and an orifice in its electron-emitting surface. The cold version (VD7, *cf.* fig. 1.13) connects a water-cooled transfer line to a region in proximity to the ionization volume but not directly inside the ionization volume. Volatile species that have passed the cooled transfer line diffuse via the anode grid into the ionization volume. Due to the proximity of hot cathode and anode grid, collisions of neutral species with the hot cathode are inevitable. Thus, both transfer line configurations are not well suited for fragile compounds. To minimize exposure of fragile compounds to heat, the transfer line shown in fig. A.1 was built. A ceramic tube (boron nitride) guided the carbonyl compounds directly into the anode volume. The tube was connected to a copper piece that was in contact with the water-cooled aluminum target base. Nonetheless, parts of the ceramic tube might have been exposed to temperatures above the decomposition temperature of the compound.

Two methods for injection of molybdenum hexacarbonyl (a colorless crystalline solid at ambient temperature) into the ion source were tested. Solid samples are typically introduced via a tantalum tube that is ohmically heated (mass markers) [63]. The method is not suited for species with high vapour pressure since already in the absence of a heating current, the indirect heating from the cathode is sufficient to cause uncontrolled evaporation. Gases are usually supplied via a calibrated leak (1×10^{-7} to 1×10^{-3} mbar L s^{-1}) that is backed by gas at atmospheric pressure. To reach the pressure required for injection via a calibrated leak, a glass-reservoir containing $Mo(CO)_6$, along with its connection to the calibrated leak, were heated to ca. 140 °C. A total pressure of ca. 200 mbar could be reached, however, metallic mirrors revealed that

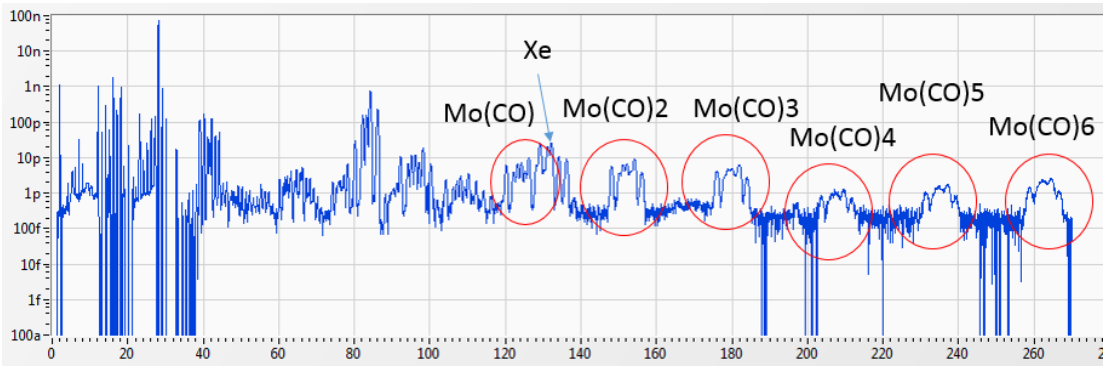

Figure A.2: Mass spectrum of molybdenum hexacarbonyl obtained with a modified VADIS operated at a cathode temperature of 1700°.

the compound decomposed on hot spots and a partial pressure of carbon monoxide was present in the system. A more reliable injection could be achieved without calibrated leak, following an approach similar to the evaporation system used for MIVOC sources [254]. The solid sample was placed in a reservoir at ambient or reduced temperature (−11 °C to 20 °C). After the initial evacuation of the reservoir, the sample sublimes till its saturation vapour pressure $p_{\mathrm{vap}}(0\,^{\circ}\mathrm{C}) \approx 1 \times 10^{-2}$ mbar [258] is reached. The flow rate into the ion source is given by $Q_{pV} = C_{\mathrm{g}} \left(p_{\mathrm{vap}} - p_{\mathrm{extr}}\right) \approx C_{\mathrm{g}} p_{\mathrm{vap}}$ [259], where the conductance C_{g} is a constant of the experimental setup.

A mass spectrum obtained with the ion source at $T_{\mathrm{cath}} \approx 1700°$ is shown in fig. A.2. The isotopic pattern of molybdenum allows identification of $\mathrm{Mo(CO)}_x^+$ with $1 \leqslant x \leqslant 6$. The beam composition is dominated by a species of mass 28 u (very likely carbon monoxide), which arises from trace impurities in the target and ion source system or by decomposition of $\mathrm{Mo(CO)_6}$. Decomposition products of the boron nitride tube could also contribute to the peak.

The temperature was successively increased from $T_{\mathrm{cath}} = 1700\,^{\circ}\mathrm{C}$ to 2100 °C while the current of $\mathrm{Mo(CO)_6}^+$ was monitored. At the same time, the sample temperature increased from $T_{\mathrm{res}} = -11\,^{\circ}\mathrm{C}$ to $-1\,^{\circ}\mathrm{C}$. Upon heating the cathode, the ion current showed an immediate response. Its highest value was found at the highest tested temperature of $T_{\mathrm{cath}} \approx 2100\,^{\circ}\mathrm{C}$ ($T_{\mathrm{res}} = -1°$). The pressure on the extraction side remained between $p_{\mathrm{extr}} = 1.1 \times 10^{-6}$ mbar and 1.4×10^{-6} mbar. After reaching the maximum cathode temperature, the ion current decreased below background level. The vanishing current could be attributed to a leak that developed during the experiment in the gas injection system. It caused rupture of a gas connection tube inside the target unit. The maximum observed current allows to estimate the ionization efficiency. The sample in the reservoir (120 mg) was allowed to fully evaporate at ambient temperature, which required ca. 37 hours. The flow rate Q_{pV} of $\mathrm{Mo(CO)_6}$ is proportional to its vapour pressure since the conductance between sample reservoir and ion source remained unchanged. At room temperature (20 °C), Q_{pV} is ca. 10 times higher compared to the conditions used in the ionization experiment. An efficiency of $\epsilon_{\mathrm{ion}} \approx 3 \times 10^{-6}$ was estimated which is typically considered insufficient for radioactive ion beam applications.

The low ionization efficiency can be explained by thermal decomposition which takes place i) in the ion source and ii) in the gas injection line connected to the ion source.

While the latter is more difficult to asses by calculation, the former can be estimated by consideration of the mean ionization length, *i.e.*, the average free path of a neutral before its ionization. The walls of the anode body (ionization volume) are in proximity to the hot cathode. Their temperature well exceeds the decomposition temperature of carbonyl compounds. Thus, the maximum travel distance of injected $Mo(CO)_6$ is limited by its first wall encounter. The length is in the order of the diameter of the anode body, *i.e.*, ca. 1 cm. Expressions for the ionization length and typical values for a VADIS are given in [176]. Its precise calculation for $Mo(CO)_6$ is not possible because the ionization cross sections are not known. Typical values for xenon are in the order of 3 m at 1900 °C. For the same species, electron density and electron velocity, the ionization length λ_{ion} is proportional to the ion velocity v_i, which in turn depends on the temperature and mass of the ion

$$\lambda_{\text{ion}} \propto v_i \propto \sqrt{\frac{T}{m_i}}. \tag{A.1}$$

Assuming that the ionization cross section of $Mo(CO)_6$ is in the same order of magnitude as Xe and an ion temperature of 100 °C, the ionization length is in the order of $\lambda_{\text{ion,Mo(CO)}_6} \sim 1\,\text{m}$. Within this estimation, the vast majority of the neutrals arriving in the ionization volume suffer a wall encounter and decomposition instead of their ionization. Additional losses arise from the probability of thermal decomposition prior to arrival in the ionization volume. Metallic mirrors could be seen on the joint between the copper cylinder shown in fig. A.2 and the tantalum tube connected to the copper part, indicating that the present temperatures did exceed decomposition temperatures prior to injection. To increase the ionization efficiency, a significant reduction of the surface temperatures in the ionization volume would be required along with an active cooling of the injection path. These major modifications are challenging due to the proximity to the hot cathode.

A.2 Radio frequency heated sources

The radio frequency heated plasma ion sources have been briefly described in sect. 1.2.3. In contrast to forced electron beam ion sources, they do not require a hot cathode and operate close to room temperature. These ion sources have been developed with the goal of efficient ionization of volatile molecules, like CO and CO_2.

A.2.1 COMIC source

The injection of $Mo(CO)_6$ was achieved in the same way as described for the VADIS in the previous section A.1. The molybdenum hexacarbonyl fragments could be identified in the mass spectrum. A photo of the plasma, as seen through the laser window, and mass spectra of selected fragments are shown in fig. A.3. The ion source was operated with krypton as buffer gas. It ignited at 70 W forward power and a pressure of $p_{\text{extr}} = 1.0 \times 10^{-5}\,\text{mbar}$. The krypton gas load was reduced after ignition by a leak valve till a pressure of $p_{\text{extr}} = 5.5 \times 10^{-6}\,\text{mbar}$ was reached. The sample was allowed to warm up from −43 °C to 47 °C. First indication of $Mo(CO)_3{}^+$ (5 pA) was found at ca. −4 °C. The highest measured current of 37 pA was obtained at 24 °C, where also the

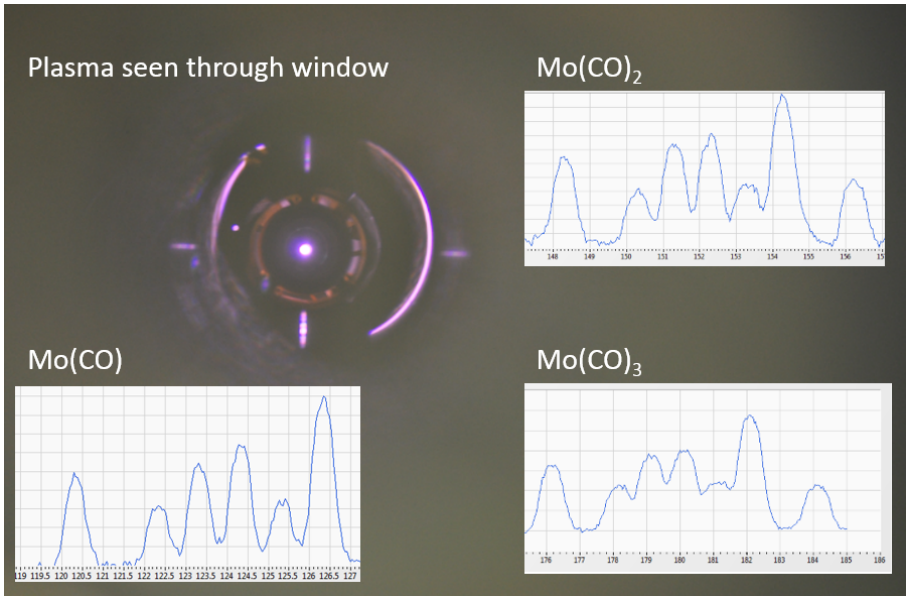

Figure A.3: COMIC krypton plasma as seen through the laser window of the offline 1 separator and selected mass spectra of $Mo(CO)_6$ fragments.

highest pressure of $p_{extr} = 1.4 \times 10^{-5}$ mbar was measured. At higher temperatures, the current first decreased and finally, the plasma extinguished and could not be reignited.

A lower limit for the efficiency obtained by integration of the $Mo(CO)_3^+$ current and sample weight (120 mg) computes to $\epsilon_{ion} > 1 \times 10^{-8}$. Assuming similar evaporation conditions as discussed in sect. A.1, an efficiency of $\epsilon_{ion} \sim 1 \times 10^{-7}$ is obtained at the temperature of $-4\,°C$. Within the same experiment, the ionization efficiency of krypton was determined to be 0.6%, which is well below the previously reported value of 34% [109]. The issue could later be attributed to a failure to bias the intermediate extraction electrode which remained floating. The absence of voltage led to insufficient beam focusing. Nevertheless, the obtained ionization efficiencies are well below values acceptable for radioactive beam applications.

A photo of the previously cleaned ionization chamber of the COMIC source is shown in fig. A.4a. Black and metallic deposits (most likely carbon and molybdenum) could be found in the quartz chamber and inside a PolyTetraFluoroEthylene (PTFE) tube through which vapours of molybdenum hexacarbonyl were supplied. The deposits were most abundant around the injection region and the central antenna rod. Despite the quartz chamber being tightly embedded in a water-cooled copper piece, the temperature of the quartz injection tube reached temperatures of ca. 100 °C at 25 W of absorbed microwave power. The temperature inside the the quartz chamber, particularly at the RF-antenna, is difficult to assess but expected to be significantly higher. To investigate, if $Mo(CO)_6$ is mostly decomposed thermally or by electron collisions in the plasma, the concentration of $Mo(CO)_6$ in the residual gas of the offline 1 separator was measured by a RGA (*c.f.* fig. 2.11 and sect. 2.4.1) while a constant flux of $Mo(CO)_6$ was supplied to the ion source and the microwave power varied. During the experiment, the plasma in the ion source was not ignited. The results are shown in fig. A.4b. The partial pressure of $Mo(CO)_6$ in the residual gas decreases steeply with microwave power. At a power of 7 W the original

(a) Previously cleaned COMIC ionization chamber after the experiment

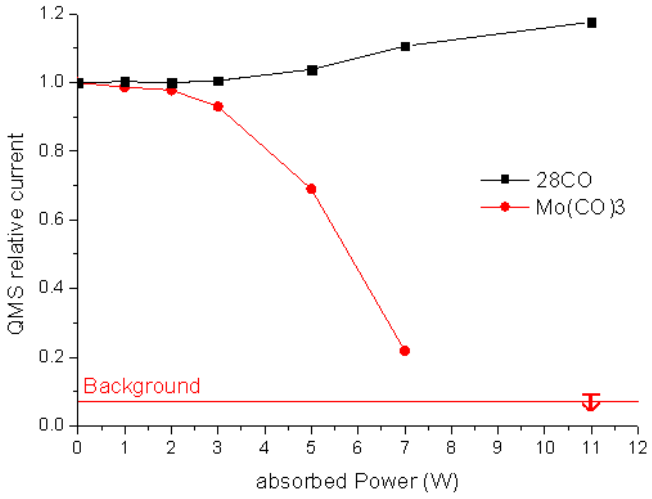

(b) Destruction of $Mo(CO)_6$ with microwave power

Figure A.4: Decomposition of $Mo(CO)_6$ in the COMIC ion source. The ionization chamber contains black and metallic deposits. The spatial distribution of the deposits indicates that decomposition mostly takes place in the vicinity of the neutral injection tube. The destruction of $Mo(CO)_6$ with microwave power was investigated by monitoring their partial pressure in the residual gas after passing through the COMIC source, which was not ignited.

signal reduced by ca. 80%, at 11 W no signal above background could be detected. The typical microwave power required for operation is ca. 20 W to 50 W. Thus, it can be assumed that the majority of $Mo(CO)_6$ is decomposed already by microwave power in the absence of a plasma. An additional issue arises from the geometry of the ionization chamber. The volume from which the ion of a refractory compound can be extracted must be in line-of-sight to the outlet aperture. This volume is limited by the hot central antenna rod and only a few mm in depth. Overall, the COMIC ion source in present design does not seem suitable for ionization of fragile compounds.

A.2.2 Helicon source

Similar to the COMIC ion source, the Helicon ion source exploits ionization in an RF-heated plasma. The source is operated in the frequency range of 100 MHz to 200 MHz. The quartz ionization volume is surrounded by an antenna that is connected via an impedance matching box to the RF source (*cf.* sect. 1.2.3, 2.3 and [114]). As shown in fig. A.5, the $Mo(CO)_6$ sample was placed inside the target unit (vacuum vessel). To avoid contact with metallic surfaces, the sample holder and the capillary connecting the latter to the ion source, were made of PTFE. A peltier element allowed cooling to ca. $-20\,°C$. At this temperature, no fragments of $Mo(CO)_6$ could be detected in the residual gas composition. The vapour pressure is expected to be $p_{vap}(-20\,°C) = 7 \times 10^{-4}$ mbar. Prevention of evaporation due to ice formation with residual humidity can also not be excluded.

The source was operated with helium buffer gas, for which the highest molecule ionization efficiencies are expected [114]. It ignited at a pressure of $p_{extr} = 3.5 \times 10^{-5}$ mbar

(a) Antenna coil, quartz ionization tube and aluminum back plate (scale bar shown for comparison).

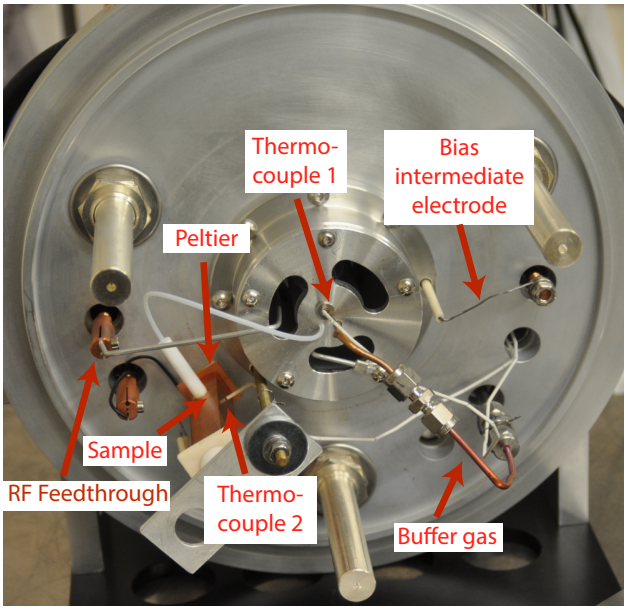

(b) Target base (open vacuum vessel) with mounted ionization chamber in the center.

Figure A.5: The Helicon ion source and cold mass marker setup. The $Mo(CO)_6$ sample was placed in a hollow PTFE cylinder that was embedded in a copper block. A peltier element allowed cooling the copper block to ca. $-20\,°C$. The sample vapours reach the ion source via a PTFE tube. The magnet array surrounding the quartz tube is not shown (*cf.* fig. 1.12).

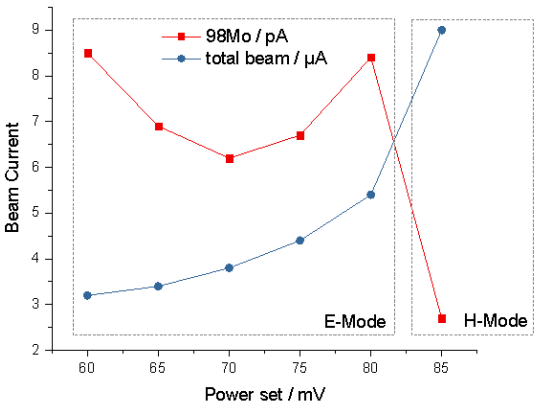

(a) Evolution of beams with RF power

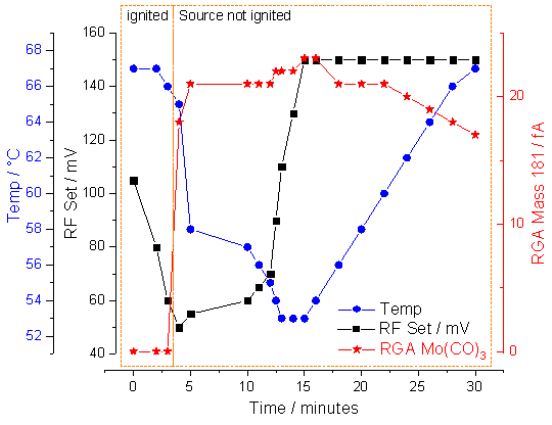

(b) Decomposition of $Mo(CO)_6$ with RF power

Figure A.6: $Mo(CO)_6$ ionization in the Helicon source. The dependence of beam currents on RF power indicates that the ionization efficiency of $Mo(CO)_6$ is higher in a capacitively coupled plasma. The decomposition of $Mo(CO)_6$ was studied by monitoring their partial pressure in the residual gas after passing through the ion source. The RF amplitude of the signal generator is given before amplification. The resulting forward power measured by an SWR meter was in the range from 30 W (50 mV) to 140 W (150 mV). Ca. 50% to 80% power reflected.

(a) Helicon chamber after use

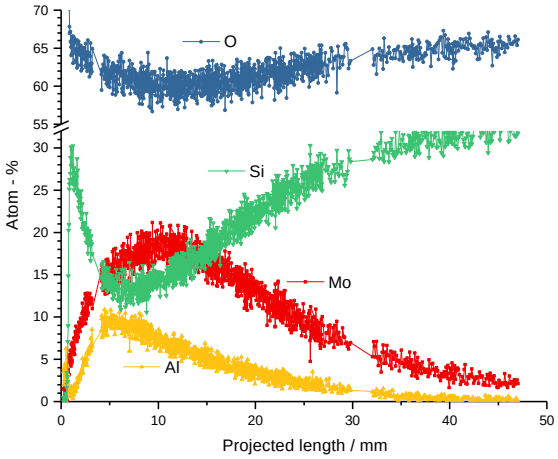

(b) Element composition (EDX) of the surface

Figure A.7: The Helicon quartz tube (plasma chamber) after usage. The neutrals were injected from the left side. Grey deposits formed on the surface near the injection region. The deposits were analyzed by EDX. See text for details.

and 14 W forward power at 164 MHz. Prior to injection of $Mo(CO)_6$, the efficiencies of krypton and xenon were determined to be ca. 2% and 4%, respectively. After allowing the sample to warm up to 20 °C, the fragments of $Mo(CO)_6$, as observed in earlier experiments with other ion sources, could be identified. The dependence of ion beam with RF power was studied (see fig. A.6a). In contrast to noble gas efficiencies, the highest efficiency for Mo^+, which was the best resolved framgment in the mass spectrum, was found at low RF power in capacitive mode. A possible reason might be a higher voltage gradient that promotes sputtering of deposits on the chamber walls. From the highest measured current (12 pA), the initial weight of the sample (7.5 mg) and an estimated evaporation time of one day, an efficiency in the order of $\epsilon_{\text{ion}} \sim 4 \times 10^{-7}$ could be estimated.

The decomposition of $Mo(CO)_6$ was investigated in the same way as reported for the COMIC source in sect. A.2.1. During operation of the source, no fragments were observed in the residual gas. The temperature measured at the back plate of the source (thermocouple 1 in fig. A.5b) was ca. 67 °C during operation at ca. 70 W to 100 W forward power. The RF power was successively reduced while the temperature and the $Mo(CO)_3^+$ RGA ion current were monitored (*cf.* fig. A.6b). At a forward power of ca. 30 W, the plasma extinguished and $Mo(CO)_x$ fragments appeared in the mass spectrum of the RGA. To estimate the fraction of sample molecules decomposed by RF heating, the power was increased without ignited plasma to the previous operational level of 100 W. The current on the RGA reduced by ca. 74% which indicates that this fraction is decomposed by heating effects. The remaining fraction is likely decomposed in electron collisions in the plasma.

The quartz tube was inspected after the experiment and the elemental composition on its surface was studied with Energy-Dispersive X-ray spectroscopy (EDX). Grey deposits are visible near the entrance region of the neutrals (fig. A.7a), indicating that the majority of the neutral $Mo(CO)_6$ could not reach the ion extraction region. The EDX spectrum (5 keV electron energy) revealed the maximum of molybdenum deposition

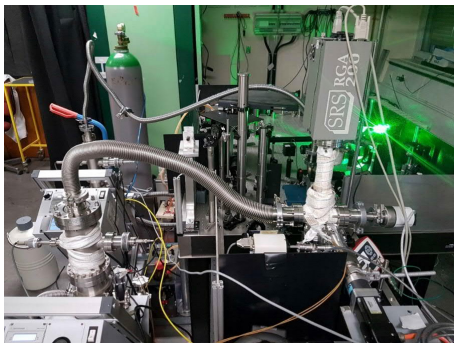

(a) Photo of the setup

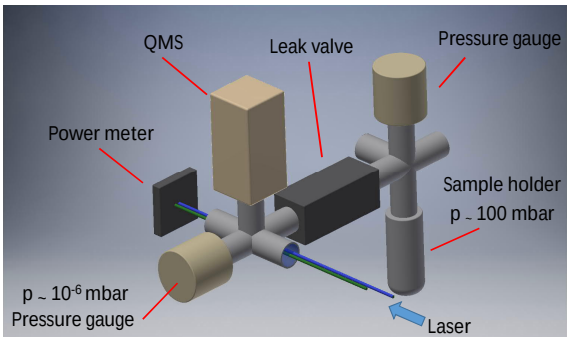

(b) Schematic drawing

Figure A.8: The setup to study breakup of $Mo(CO)_6$. Vapours of $Mo(CO)_6$ were injected via a leak valve into a chamber equipped with two windows through which a laser beam was guided. The gas composition was monitored with a residual gas analyzer. Schematic drawing courtesy of Ch. Seiffert.

at ca. 1 cm from the entrance. Aluminum could be found closer to the entrance, likely originating from the aluminum back plate confining the plasma chamber. Carbon could not be unambiguously identified in the EDX spectrum. The results suggested that injection of the sample closer to the extraction region would increase the efficiency, which was, however, not the case.

A.3 Experiments involving laser beams

Two different experiments involving lasers were conducted. In one experiment it was investigated, if $Mo(CO)_6$ can be efficiently decomposed by available laser systems in a geometry similar to an ion source. The breakup of the molecule is typically considered a required step for resonant laser ionization of the naked atom. The second experiment was conducted within the framework of experiments towards electron impact ionization in a cold environment with laser-induced electron emission (*cf.* Chapter 6).

A.3.1 Laser breakup

The breakup of $Mo(CO)_6$ was studied in a setup with geometry similar to an ion source. The setup is shown in fig. A.8. The solid sample was placed in a stainless steel chamber. A steady flow of $Mo(CO)_6$ vapours was injected via a leak valve into a CF16 6-way cross equipped with two laser windows. The length of the interaction region was ca. 8 cm. Laser beams with pulse length in the order of tens of nanoseconds and wavelength 355 nm, 523 nm and 266 nm were guided subsequently through the chamber. Their power was measured after passing through the chamber. The gas composition was monitored with an RGA. A depletion of the Mo(CO)x signals was found at the wavelength of 266 nm, as shown in fig. A.9. At the other wavelengths no response could be detected. The results are in agreement with the UV-vis absorption spectrum of $Mo(CO)_6$ [260]. At a laser power of ca. 0.7 W ca. 15% of continuously injected $Mo(CO)_6$ was decomposed. Following the obtained results, the investigation of a combination of resonant ionization and breakup was proposed [261].

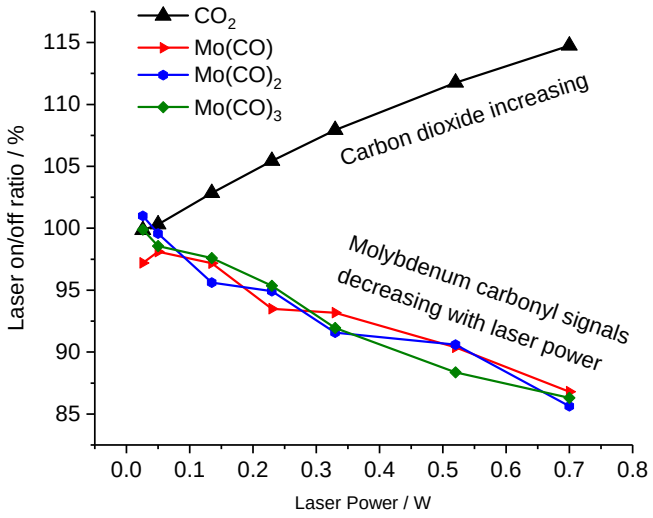

Figure A.9: Plot of selected ion currents measured with a residual gas analyzer versus power of the laser beam at 266 nm passing through a chamber with vapours of $Mo(CO)_6$.

A.3.2 Non-resonant laser ionization and further measurements

Along with the experiments towards ionization in a cold VADIS (Chapter 6), a direct ionization with a laser beam was observed which yields a fragmentation pattern different from that of electron impact ionization (see fig. A.10). The obtained ion beam currents were below these measured in electron impact ionization. The modes could be switched by setting the anode voltage and target magnet current to 0 V and 0 A, respectively. As can be seen in fig. A.10, the direct laser ionization mode is not capable of ionizing the noble gas krypton but only loosely bound compounds like $Mo(CO)_6$. The used setup is described in Chapter 6. It consists of a VADIS kept at ambient temperature which is illuminated by a femtosecond laser (265 fs pulse length), 343 nm wavelength, power of 4.5 W and 50 kHz repetition rate.

In addition to the data included in the publication in Chapter 6, the ion currents of $Mo(CO)_6$ fragments were measured in dependence of the anode voltage. These measurements allow to deduce the relative appearance potential of the fragment. The results are shown in fig. A.11. As can be seen from the graph, the appearance potentials increase with number of ligands for $Mo(CO)_x$ with $0 \leq x \leq 5$. The curve for $Mo(CO)_6^+$ deviates from the other fragments which is likely due to a different mechanism of ionization which is non-dissociative. The absolute values of the respective appearance potentials could not be obtained due to the unknown energy distribution at 0 V anode potential. For comparison, the ionization potential of krypton is shown in fig. A.11 which cannot be trivially obtained from the measured curve.

A.4 Contributions

The experiments involving the VADIS (sect. A.1), COMIC (sect. A.2.1) and Helicon (sect. A.2.2) ion sources were prepared, conducted and analyzed by myself. The EDX

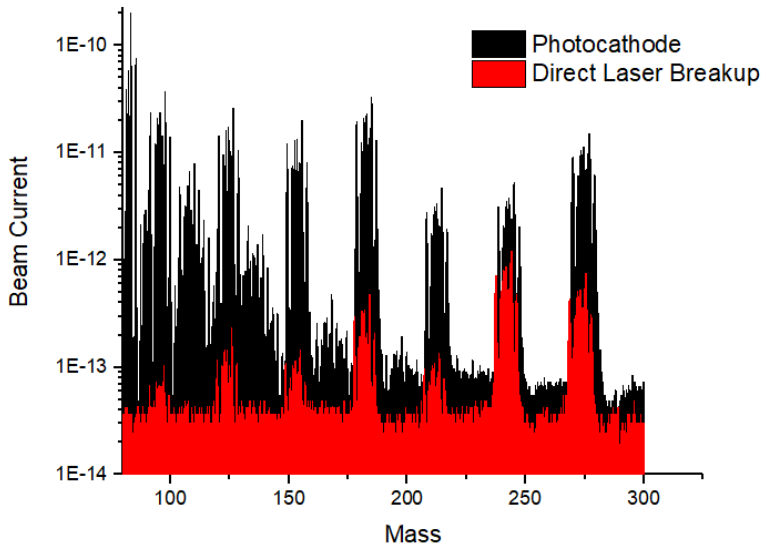

Figure A.10: $Mo(CO)_6$ fragmentation pattern in electron impact and direct laser ionization

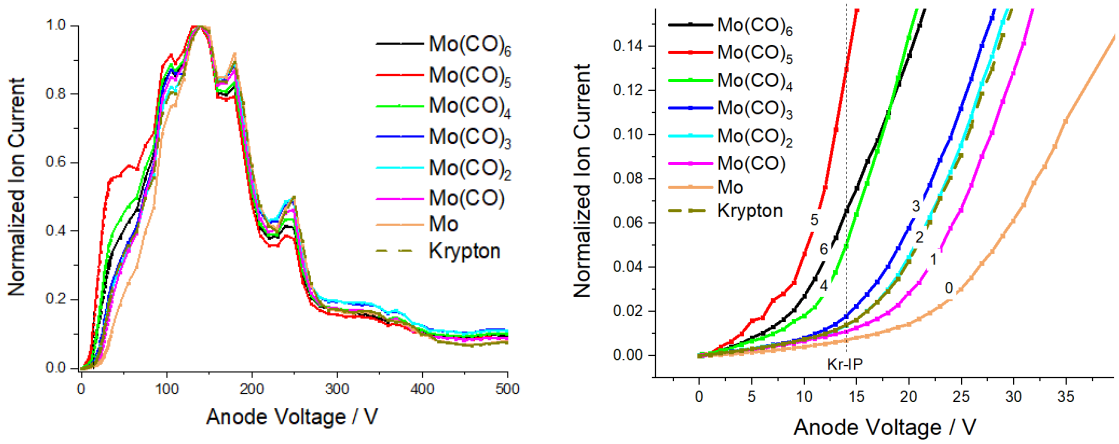

(a) full measurement range

(b) onset region

Figure A.11: Normalized beam current of the Mo(CO)x fragments versus anode voltage as measured in a VADIS at ambient temperature.

spectrum of the Helicon ion source was measured by J.P. Ramos. The laser breakup experiment (sect. A.3.1) was jointly prepared and conducted in collaboration with Ch. Seiffert. The data was mostly analyzed by Ch. Seiffert. The non-resonant laser ionization experiment (sect. A.3.2) was conducted within the collaboration as stated in Chapter 6. The resulting data was analyzed by myself.

Towards experimental study of transition metal carbonyl formation at ISOLDE

B

Contents

The formation of radioactive carbonyl compounds has been demonstrated from recoils obtained in neutron-induced or spontaneous fission and from fusion-evaporation reactions after separation from the intense primary beam. At ISOLDE the situation is different. The scattered primary beam causes a certain fluence of charged particles (mostly protons) in the region of molecule formation. The experiment proposed in this chapter was designed to study, if carbonyl formation at ISOLDE is efficient. The components for the experiment have been designed, built and tested, however the experiment could not yet be conducted within this theses. The attached documents describe scientific aspects, the designed and built equipment and the forseen operational procedures.

B.1 Contributions

The first attached document (Experiment proposal) was written by myself. The second document was drafted by J. Riegert and myself based on a setup developed by myself in collaboration of specialists for hot-cell handling and safety, as indicated in the document. The risk assessment was led by J. Riegert.

Experiment proposal to study transition metal carbonyl formation at ISOLDE

J. Ballof[1,2], V. Barozier[1], F. Boix Pamies[1], R. Catherall[1], Ch. E. Düllmann[2,3,4], P. G. Harwood[1], D. Phan[1], J.P. Ramos[1], J. M. Riegert[1], S. Rothe[1], T. Stora[1], and A. Yakushev[3]

[1] *CERN, 1211 Geneva 23, Switzerland*
[2] *Johannes Gutenberg - Universität Mainz, Institut für Kernchemie, Fritz-Strassmann-Weg 2, 55128 Mainz, Germany*
[3] *GSI Helmholtzzentrum für Schwerionenforschung, 64291, Darmstadt, Germany*
[4] *Helmholtz-Institut Mainz, 55099 Mainz, Germany*

October 9, 2018

Abstract

This document gives an overview of a proposed experiment at the ISOLDE and MEDICIS facilities aiming at formation and survival of volatile multi-carbonyl carriers for refractory elements. The experiment is a crucial step towards extraction of refractory element beams like molybdenum, technetium, ruthenium and rhodium at ISOLDE. For this experiment, a versatile irradiation unit was designed, which is also available for future neutron and proton irradiation experiments. It allows sample handling by the ISOLDE and MEDICIS KUKA robots, in the hot cells and the rail conveyor system to ensure the lowest possible dose for the operating staff conducting irradiation experiments.

1 Introduction, Motivation and Justification

Despite the manifold new developments introduced to ISOL target units within the last 60 years, the beam extraction of elements with very high boiling points (refractory elements) remains a very challenging topic. Due to their vanishingly low volatility, radionuclides of these elements generated by the driver beam are captured within the target and suffer from hampered release [1].

However, following new developments, which came up in the field of superheavy element chemistry within the last years [2], a new compound class might open up new perspectives for the extraction of the most refractory elements. Highly volatile carbonyl complexes M(CO)x, x=5-6 of suitable elements were found to form already at ambient temperature and pressure upon thermalizing fission fragments emerging from a thin uranium foil in a carbon monoxide-containing atmosphere. The ISOLDE Periodic Table of Elements shown in Figure 1 demonstrates the potential of the "carbonyl method". Nine out of fifteen transition metals, which are not yet available as beam, form volatile carbonyl compounds. Despite their potential as volatile carriers, transition metal carbonyls are delicate compounds, and decomposition in beam-induced plasmas and at elevated temperatures is expected. [3–5]. The synthesis of carbonyl compounds has been demonstrated at a TRIGA reactor and in fusion reactions, where the evaporation

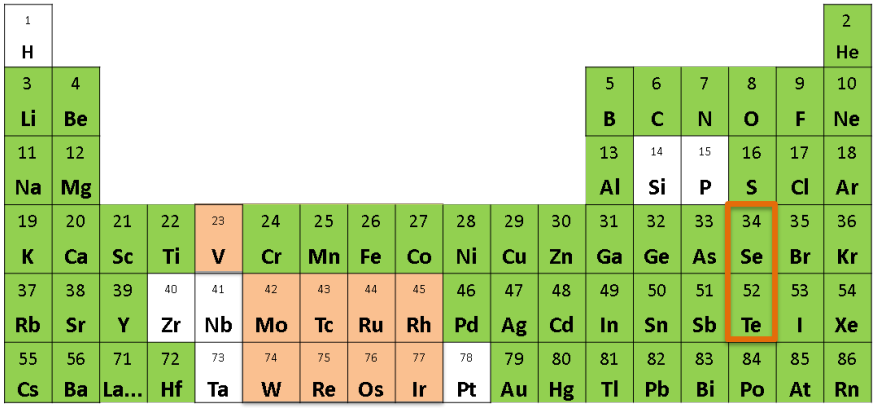

Figure 1: Periodic Table of elements showing available beams at ISOLDE (green / dark grey), Non-available Elements, which form transition metal carbonyls (red background /light grey) and carbonyl chalcogenides (red frame).

residues haven been physically separated from the beam prior to carbonyl formation [6]. The intense proton beam at ISOLDE is expected to induce a plasma, similar to the induction of a plasma by the primary beam used in fusion-evaporation reactions. We have therefore designed a target unit, equipped with an improved neutron converter, which allows to conduct neutron irradiation of a sample in a regime of very low residual proton current. In addition, the target unit is equipped with a second irridiation postion in a region of higher proton fluence. The latter allows us to quantitatively investigate the carbonyl decomposition by impacting protons. To deduce the total chemical efficiency of the process, which is an important factor for the beam extraction in an ISOLDE production unit, a catcher foil will be used to determine the total number of recoiling isotopes, which recoil out of the uranium foil. The fraction of fission recoils forming carbonyl compounds can be distinguished from their elemental counterparts by their volatility. While carbonyl compounds are known to be easily transported by a gas stream, the refrectory metals in elemental form stay deposited on surfaces. By retaining the volatile species on a charcoal trap, and subjecting it to gamma spectroscopy, the inventory of volatile species is obtained.

2 Experimental Setup

2.1 The ISOLDE hot cells

The layout of the ISOLDE hot cells is shown in Fig. 2. The facility consists of two separate cells, which are connected through a transfer channel. The right cell, as seen from the operator (cell 1), is equipped with an access lock, which allows the introduction and evacuation of an ISOLDE target unit. The target unit can be transported by a crane to the target table, which serves as support and fixation device. The exterior walls are shielded with the equivalent of 15 cm lead. The ventillation system is designed for a maximum flow volume of 85 m^3/h [7]. Both cells are equipped with vacuum and pressurized gas lines leading to a panel at the rear outside wall.

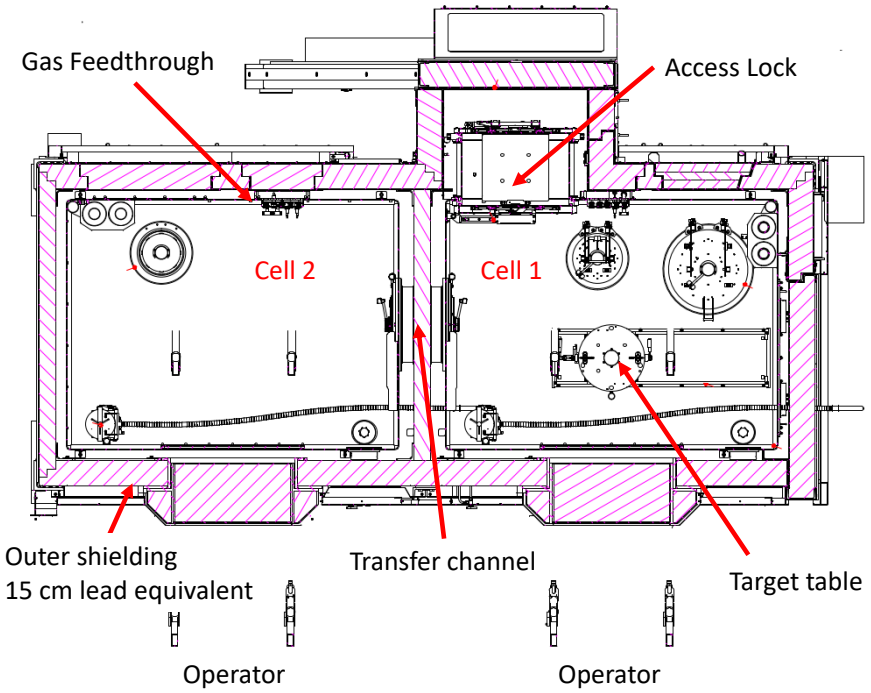

Figure 2: The ISOLDE hot cells

2.2 The versatile irradiation unit

The irradiation unit (cf. Fig. 3) serves as support for the sample assembly and is equipped with a tungsten rod as spallation neutron source. The proton beam of the PSB can be focused either on the tungsten rod to irradiate the sample with secondary neutrons, or directly on the sample. The neutron converter is kept in an enclosure under vacuum to resemble the design of the standard ISOLDE target unit. The volume between neutron converter and its cover can be evacuated through the target valve. The arrangement of the sample assembly was optimized to reduce the proton fluence to a minimum, if the beam is focused on the converter.

2.3 The sample assembly

The sample assembly consists of two gas containers equipped with a handle for the KUKA-robot. A schematic view of a sample container is shown in Fig. 4. The sample container is made of PEEK polymer, which is a radiation hard, low outgassing, and mechanically robust material. The container consists of two parts, which are held together by a KF-type clamp. The upper part of the container does not contain bigger metallic parts, and is therefore ideally suited to be taken out of the hot cell. It will contain a catcher foil, which is made of a plastic material, or a very thin metallic foil.

The lower part will not be handled manually, and is equipped with two quick connectors and valves for gas-related operations, fixtures for attaching the assembly to a target base, and a 25 μm thick uranium foil in the center of each container.

2.4 The transfer unit

The irradiation unit is directly exposed to the proton beam and especially the neutron converter rod, made of tungsten, is getting highly activated. Hence, the introduction of

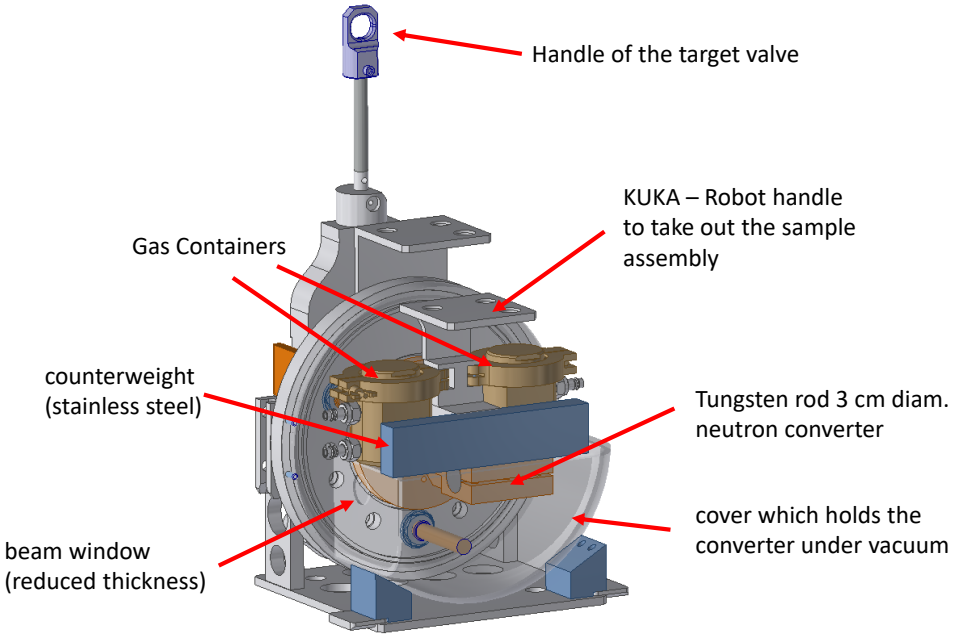

Figure 3: Sketch of the irradiation unit including sample assembly

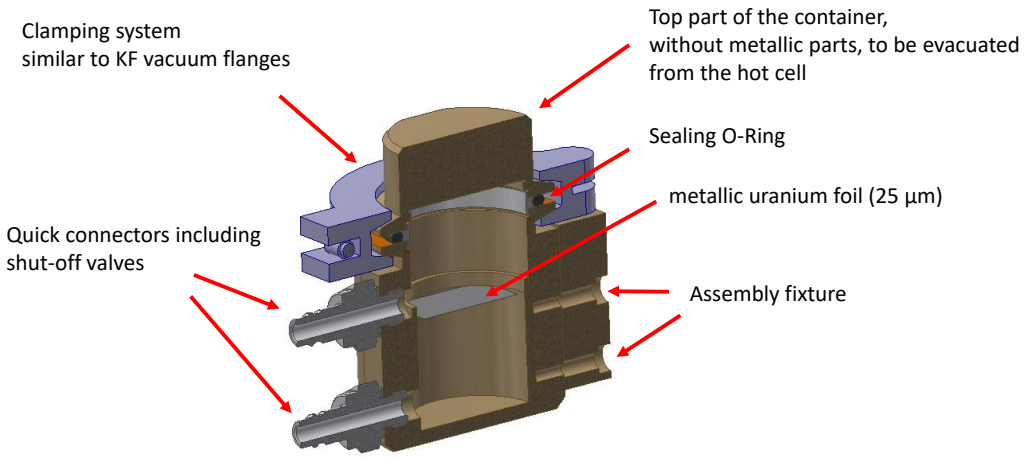

Figure 4: Sketch of a gas container. Two containers, supporting parts and a KUKA robot handle are combined to form the sample assembly.

the irradiation unit into the hot cells should be avoided. However, after separation of the sample assembly from the irradiation unit, the former still needs to be transported via KUKA robot and rail conveyor system to the hot cell. As mean of transport, a dedicated transfer unit was designed. It resembles the dimension of a standard target base, and is equipped with a fixture to attach the sample assembly.

2.5 The gas system

A simple, telemanipulator operable gas-system is installed inside hot cell 2, which allows to

- evacuate the gas container,
- purify the gas prior to irradiation using scrubber cartridges,
- circulate gas through the container and to
- fill the container with gas.

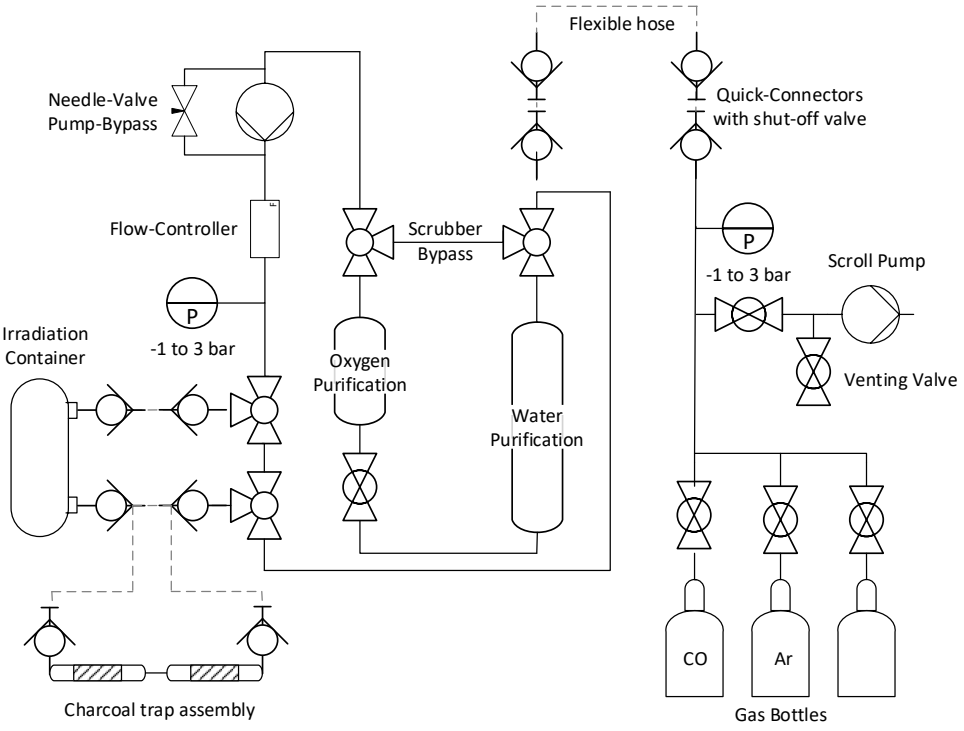

Figure 5: Scheme of the gas system for hot cell 2

Two pumps are used within or nearby hot cell 2. In any case is the exhaust gas fed into the hot cell volume. A scroll pump serves as vacuum source to evacuate container as well as tubing and a membrane pump allows to force gas in a loop. Two purification cartridges are part of the loop, which allow the reduction of residual oxygen and water prior to filling the gas containers and irradiation. After irradiation, two options for the extraction of volatile compounds out of the gas container volume and into the charcoal trap are available. The gas is either evacuated over the charcoal trap assembly till a rough vacuum pressure level is reached, or a gas is circulated through charcoal trap and

container at ambient pressure. Small gas bottles (1 L, 200 bar) and tubing are placed either in or nearby the hot cells.

The schema of the gas system is shown in Fig. 5. Swagelok quarter turn plug valves are used, which have been tested to be compatible with telemanipulation. The charcoal trap assembly consists of two charcoal traps in series. While the first trap is intended to collect the sample, the second trap is used to monitor if species are able to pass the first trap. Each trap is made up of a PTFE tube, filled with granular charcoal which is held in place by quartz wool plugs on either side of the tube. The assembly is equipped with quick connectors for fast connection, which also have been tested for compatibility with remote handling. The partially assembled system is shown in Fig. 6.

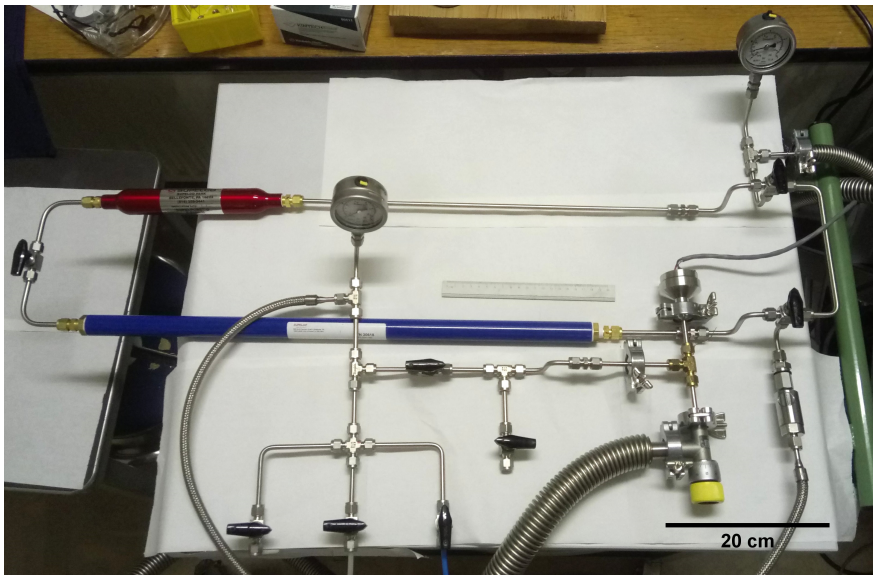

Figure 6: Photo of the partially assembled system during tests

3 Experimental Procedure

3.1 Pre-irradiation operations in the hot cells

Prior to irradiation, the gas container is prepared in hot cell 2. The clamps of the gas containers are opened, and a lid with a new catcher foil is mounted. Subsequently, the gas system is connected to the container using the quick couplings. The container is first evacuated, tested for leak-tightness and filled with a gas, which is typically carbon monoxide, an inert gas or a mixture of oxygen and an inert gas. The sequence is repeated for the second gas container. After isolating the containers from the gas system, the sample assembly is transferred through the transfer channel to hot cell 1. The assembly is attached to the transport unit which in turn is evacuated from the hot cell through the access lock by crane and the MEDICIS KUKA-Robot.

3.2 Transfer and irradiation

An overview of the target area is shown in Fig. 7. The transfer unit including gas containers is transported from the hot cell access lock to the MEDICIS rail conveyor system by the MEDICIS robot and placed on a trailer. The trailer is moved to the GPS

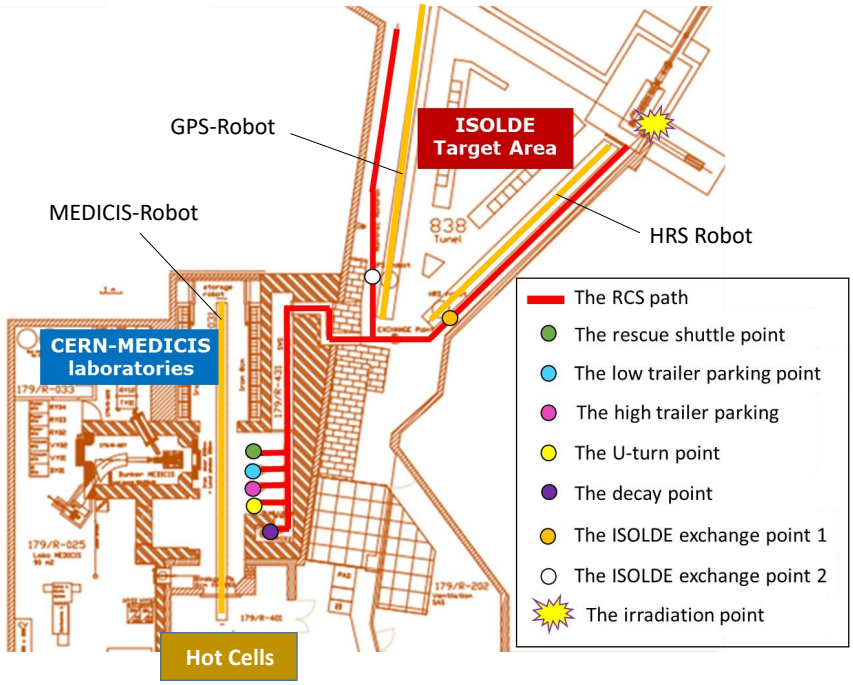

Figure 7: The ISOLDE Target area (adapted from EDMS Document 1541088)

or HRS exchange point, where the container assembly is transferred by a KUKA robot to the irradiation unit, which will then be placed on an ISOLDE frontend for irradiation. The target is clamped to the frontend and water cooling is started, however, the target vacuum valve remains closed to avoid the need for venting the frontend sector before decoupling, which would significantly delay the procedure. After irradiation, the steps are followed in reverse order to bring the transfer unit including the irradiated sample assembly inside the hot cell, while leaving the irradiation unit at the exchange point.

3.3 Post-irradiation operations in the hot cells

Within the post-irradiation procedure, the catcher foils need to be recovered and the produced radioactive species inside the gas volume have to be transferred to a charcoal trap. Since the gas system is installed in hot cell 2, the sample assembly is transferred to the neighboring cell through the transfer channel and connected via quick couplings to the charcoal traps and the gas system (cf. Fig. 5). The gas is evacuated over the charcoal trap. Optionally, the sample assembly is heated to ca. 100 °C and the gas loop is filled with a gas which is circulated through container and charcoal trap. Subsequently, the pressure inside the gas container is regulated to atmospheric pressure. After removal of the container clamp which holds both parts of the gas container together, it is visually verified, that the uranium foil in the lower part of the gas container remained intact. The upper part of the gas container (lid), containing the catcher foil, is taken out of the hot cell where the catcher foil is removed and subjected to gamma spectroscopy. The charcoal trap assembly is also evacuated from the hot cell and the decay radiation is recorded.

4 Radioprotection aspects

FLUKA simulations were performed to estimate the expected dose rates at each step of the experiment. The FLUKA model takes into account the geometry of the irradiation unit to correctly reproduce the proton beam interactions, in particular with the neutron converter and it's aluminum cover. However, only the sample assembly is transported to the hot cell. Thus, the dose rates discussed in the following sections are only considering the dose due to activation of the sample assembly. The dose for items confined in the hot cell is calculated as photon dose using EWT74 tables. For items evacuated from the hot cells, also particles (excluding heavy ions) were taken into account.

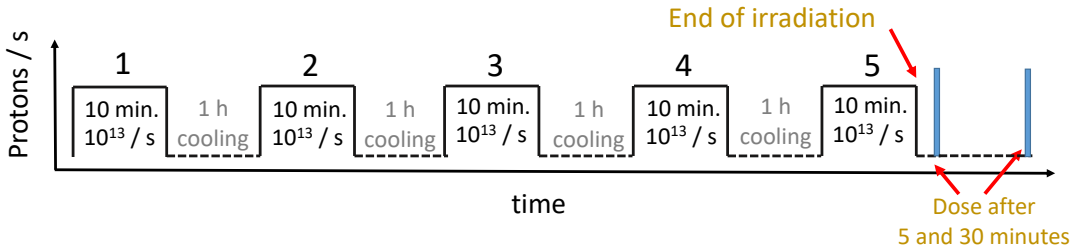

Figure 8: Irradiation profile assuming five consecutive irradiation experiments for dose rate simulations.

The irradiation pattern for the simulations is shown in Fig. 8. It assumes 5 consecutive irradiation experiments, where the irradiation unit is exposed to 10^{13} protons per second for 10 minutes followed by one hour of cooling time between each experiment. The dose rate is evaluated 5 and 30 minutes after the last irradiation.

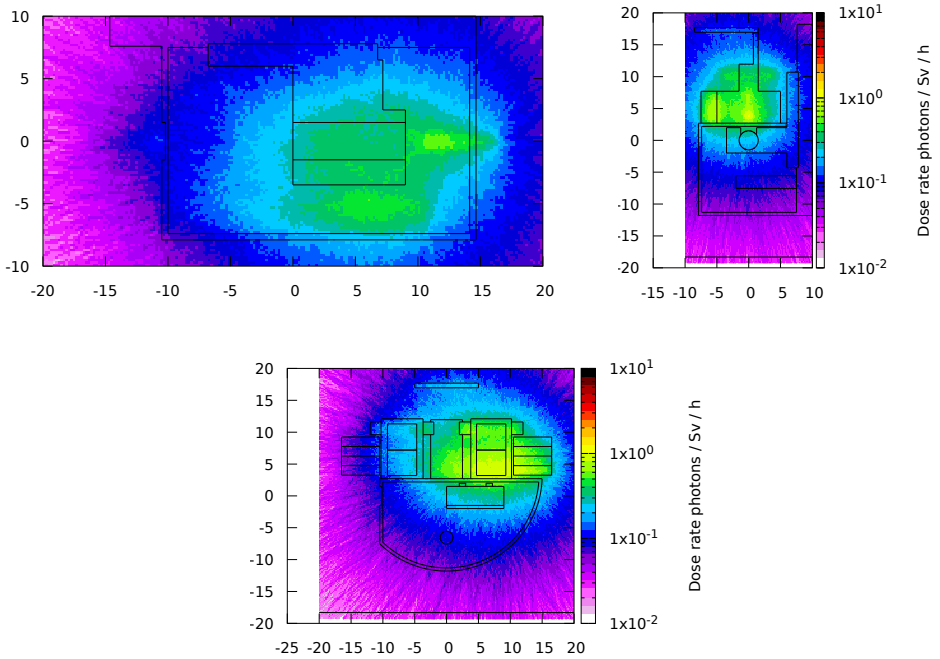

Figure 9: Effective photon dose rate of the sample assembly based on EWT74 conversion coefficients (worst possible geometry) for the target unit scored 5 minuted after the end of the irradiation sequence. The length is given in units of cm.

CERN
CH1211 Geneva 23
Switzerland

EN Engineering Department

EDMS NO.	REV.	VALIDITY
2043742	**2**	**Draft for discussion**

REFERENCE

Date: 2018-10-22

OPERATIONAL PROCEDURE

EXPERIMENT PROPOSAL TO STUDY TRANSITION METAL CARBONYL FORMATION

CERN-MEDICIS

DOCUMENT PREPARED BY:	DOCUMENT CHECKED BY:	DOCUMENT APPROVED BY:
J. RIEGERT/EN-STI J. BALLOF/EN-STI	A-P. BERNARDES / EN-STI P. HARWOOD / EN-STI D. JAILLET / EN-EA E. AUBERT / HSE-RP A. DORSIVAL / HSE-RP F. POZZI / HSE-RP A. HENRIQUE / HSE-OHS J. GULLEY / HSE-OHS	R.CATHERALL/ EN-STI T. STORA / EN-STI

Diffusion: A. PARDONS / EN-EA

HISTORY OF CHANGES

REV. NO.	DATE	PAGES	DESCRIPTIONS OF THE CHANGES
1	2018-10-22	-	Creation of the document
2	2018-11-05	All	Integration of comments made on EDMS from F. POZZI, J. GULLEY and comments from D. JAILLET

TABLE OF CONTENTS

FIGURE LIST

TABLE LIST

GLOSSARY

MEDICIS: MEDical Isotopes Collected from ISOLDE

REFERENCES

[1] J.BALLOF "*Experiment proposal to study transition metal carbonyl formation at ISOLDE*" **EDMS 2036665**
[2] ITD "*Technical Documentation – ISOLDE ALPHA-GAMMA LEAD HOT CELL*" **EDMS 2043740**
[3] B. CONDE FERNANDEZ "*CERN-MEDICIS safety file-demonstrative part*" **EDMS 1626873**
[4] B. CONDE FERNANDEZ "*Risk and failure analysis – MEDICIS MONTRAC*" **EDMS 1474203**
[5] J. RIEGERT "*RISK ASSESSMENT FOR THE USE OF PPE IN CERN-MEDICIS*" **EDMS 1903417**
[6] J. BALLOF, J.RIEGERT **"***Carbon-monoxide Gas bottle operations"* **EDMS 2045068**

1. INTRODUCTION

This experiment at the ISOLDE and MEDICIS facilities aims at formation and survival of volatile multi-carbonyl carriers for refractory elements. The experiment is a crucial step towards extraction of refractory element beams like molybdenum, technetium, ruthenium and rhodium at ISOLDE. For this experiment, a versatile irradiation unit is designed, which is also available for future neutron and proton irradiation experiments.

2. EQUIPMENT

Equipment	Description
The versatile irradiation unit and the sample assembly (removable part) 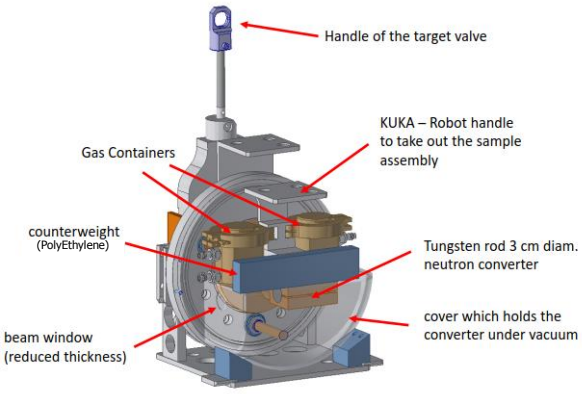 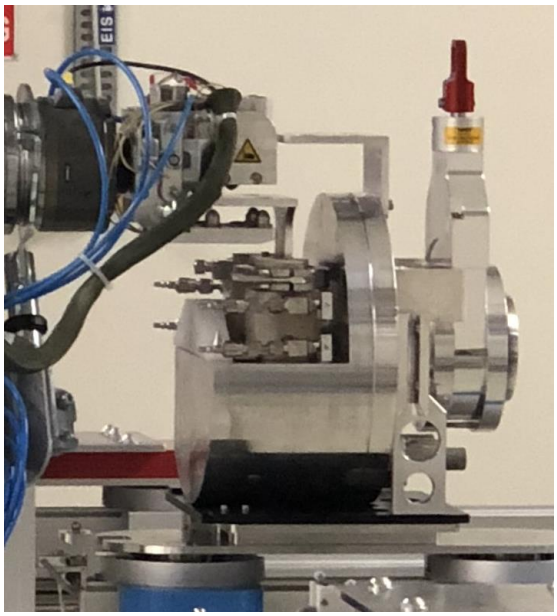	The irradiation unit servers as support for the sample assembly and is equipped with a tungsten rod as spallation neutron source.

Equipment	Description
Detail of the sample assembly 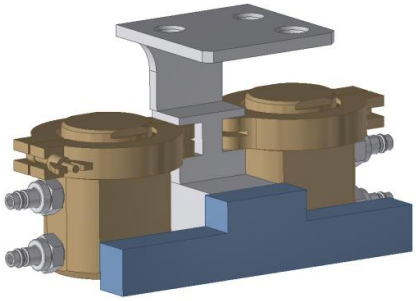 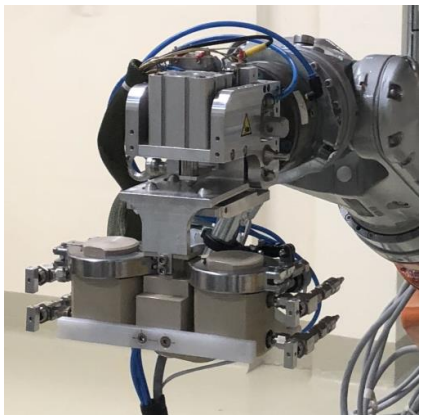	The sample assembly consists of two gas containers equipped with a handle for the KUKA-robot.
Detail of the gas containers 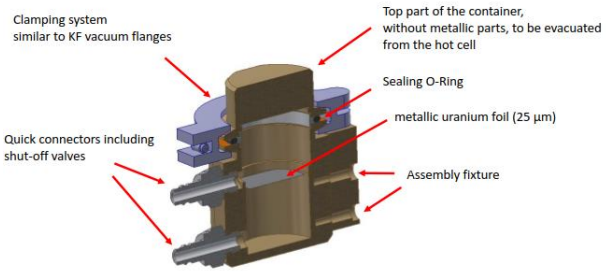 	The lower part is equipped with two quick connectors and valves for gas-related operations, fixtures for attaching the assembly to a target base. Each gas container has 2 foils : - A uranium foil that emit the recoils. This foil is not changed during experiments and stays inside the gas container. - A 25-µm thick catcher foil (*Carbon*) that capture recoils emitted by the Uranium foil. This foils is removed and changed during the experiment for spectrometric analysis.

Equipment	Description
The transfer unit and the sample assembly 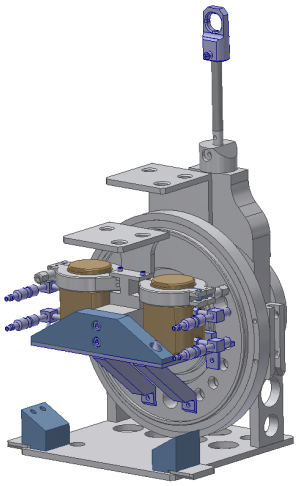 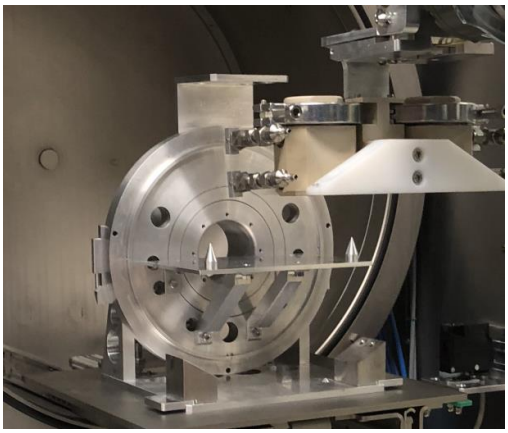	Base to transfer the sample assembly from the ISOLDE target area to the MEDICIS hot cell. Element with the dimension of a standard target base, and equipped with a fixture to attach the sample assembly.
Gas system 	The gas system is installed in the hot cell. It is operable with telemanipulators and allows to : • Evacuate the gas container, • Purify the gas prior to irradiation using scrubber cartridges, • Circulate gas through the container and to fill the container with gas.

Equipment	Description
Charcoal trap 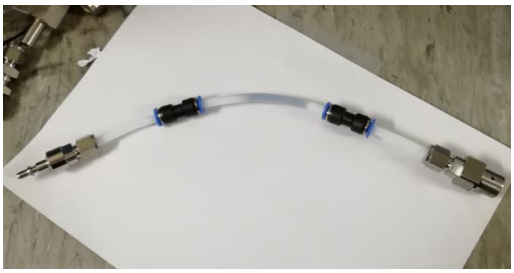	Adsorb volatile species in case of irradiation with gas inside the gas containers when evacuating the gas inside the gas setup
Tray 	Prevent hot cell contamination during removal of the catcher foils
Gas bottles	Fills the gas containers with : - CO - Ar The gas bottles are installed outside the hot cell (MEDICIS sector 1) and are connected to the hot cell Gas Feedthrough.
Pumps x3	3 pumps are used within or nearby hot cell 2 (connection to the hot cell feedthrough : • A scroll pump outside the hot cell (179/R-401) serves as vacuum source to evacuate container as well as tubing. • A pressure pump inside the hot cell is used to pressurize the exhaust gas inside the gas tank. • A membrane pump inside the hot cell allows to force gas in a loop.

Table 1: List of the equipment needed

3. PROCEDURE OF INTERVENTION

3.1 PREPARATION OF INTERVENTION

1. Preparation of equipment inside the hot cell :
   a. Installation of the gas setup.
   b. Installation and connection of pumps and gas bottles to hot cell feedthroughs.

3.2 FIRST PART: IRRADIATION WITHOUT GAS INSIDE THE GAS CONTAINERS

NOTA: Operations inside the hot cell are performed with telemanipulators.
For the first part of this experiment, 2 catcher foils will be used (one for each gas container).

3.2.1 Transfer of the irradiation unit to the MEDICIS area, and introduce the transfer unit with the sample assembly into the hot cell

2. Transfer on a trolley the irradiation unit without the sample assembly to the MEDICIS sector 2.
3. Install manually the irradiation unit without the sample assembly on the MEDICIS High (or Low) trailer.

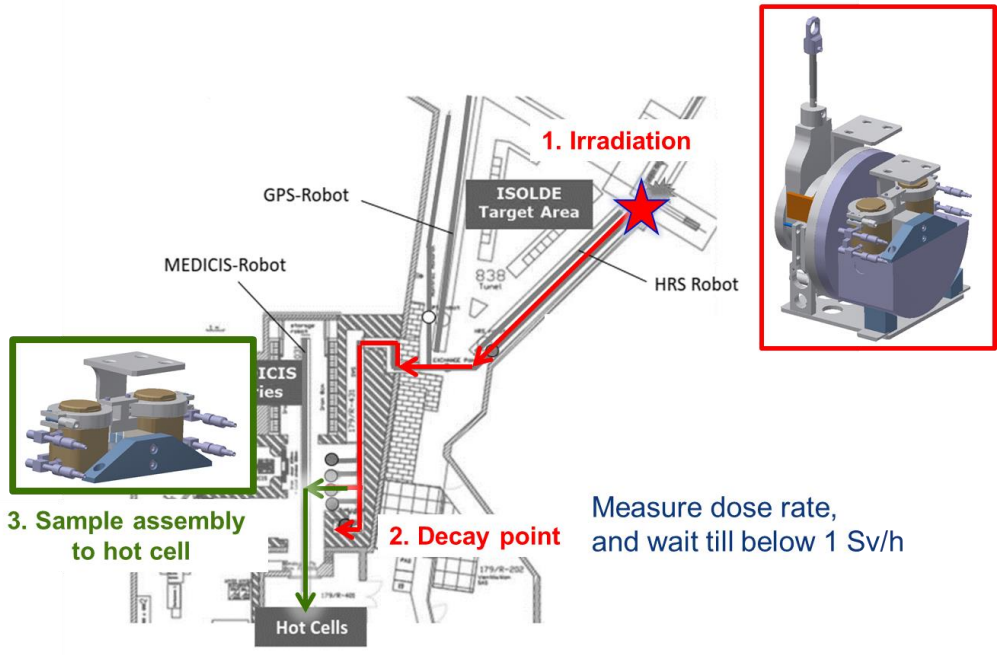

Figure 1: Global view of the transfer steps of the sample assembly after irradiation

4. Place the transfer unit including sample assembly manually on the sliding table of the hot-cell access lock.

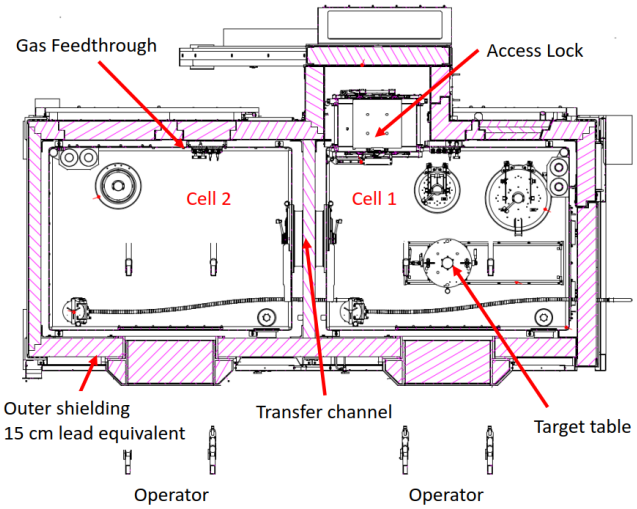

Figure 2: View of the hot cell

5. Opening of the material lock and installation of the transfer unit and the sample assembly on the movable sliding table *(only one door opened at a given time).*

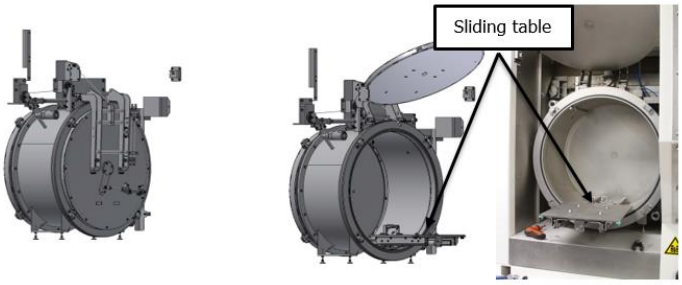

Figure 3: Opening of the material lock

6. Allow the movable access lock table to slide inside hot cell 1.
7. Retrieval of the transfer unit and the sample assembly with the crane.
8. Closure of the material lock.
9. Installation of the transfer unit and the sample assembly on the target table.

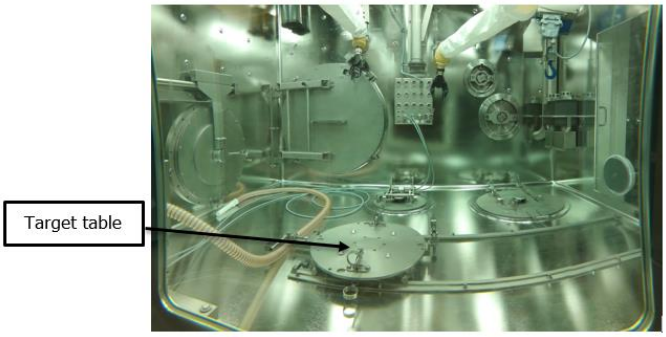

Figure 4: View of the target table

3.2.2 Pumping of the gas container

10. Connect the gas setup to the gas containers of the sample assembly.

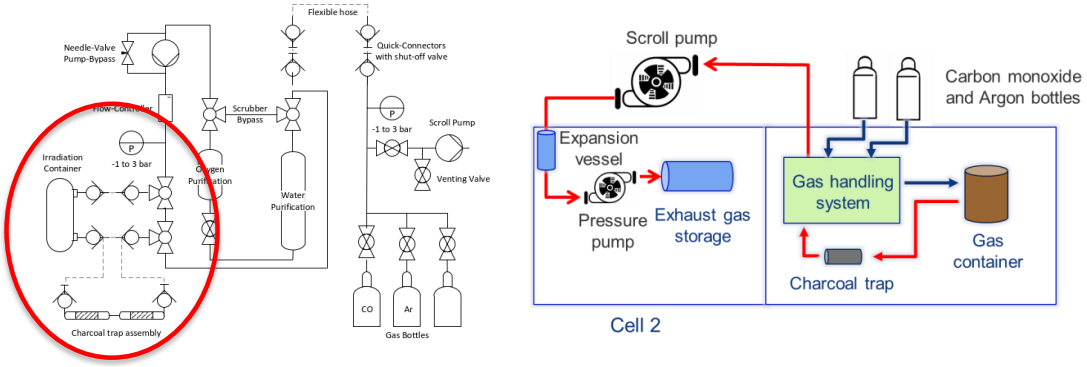

Figure 5: Gas setup drawing

11. Pump the gas containers.
12. Disconnection of the sample assembly from the gas setup.

3.2.3 Transfer of the irradiation unit and the sample assembly to the HRS or GPS Front-End for irradiation

13. Retrieval of the transfer unit and the sample assembly with the crane.
14. Opening of the material lock *(only one door opened at a given time).*
15. Installation of the transfer unit and the sample assembly on the sliding table.
16. Retrieval of the sample assembly only with the MEDICIS KUKA robot.
17. Closure of the material lock.
18. Transfer of the sample assembly to the irradiation unit, waiting on the high (or low) shuttle at MEDICIS sector 2.
19. Transfer of the irradiation unit including sample assembly to HRS or GPS exchange point (ISOLDE exchange point 2 or 1) with the MONTRAC system.
20. With the ISOLDE KUKA robot, retrieval of the irradiation unit with its sample assembly.
21. Transfer of the irradiation unit with its assembly to the HRS or GPS front-end.

22. **Irradiation of the irradiation base with the sample assembly.**

3.2.4 Transfer of the sample assembly to the hot cell

23. Transfer of the irradiation unit with its sample assembly to the HRS or GPS exchange point.
24. Transfer of the irradiation unit including sample assembly to the decay point with the MONTRAC.
25. Wait until the dose rate reaches the maximum level of 1 Sv/h, measured with the radiation monitor at the decay point.
26. Transfer of the sample assembly on its irradiation unit to MEDICIS sector 2 with the MONTRAC
27. With the MEDICIS KUKA robot, retrieval of the sample assembly and transfer to the transfer unit, waiting on hot cell the material lock.

3.2.5 Retrieval of the catcher foils for spectrometry gamma

28. Put to atmosphere the gas containers by opening their valves :
    a. Fill the gas containers and the lines with Argon
    b. Circulate Argon in the loop over a charcoal trap to filter volatile radionuclides
    c. Pump and collect the gas in the gas tank

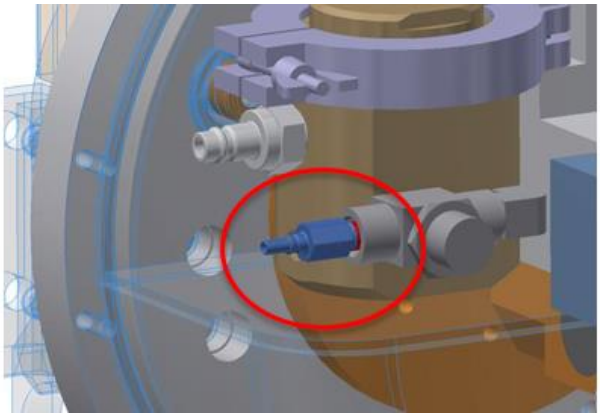

Figure 6: View of the principle of the valve on the gas containers

29. Opening of the gas containers clamps by unscrewing their wing nuts.

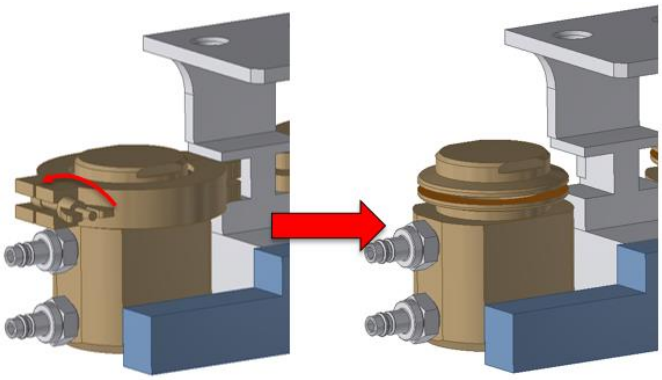

Figure 7: removal of the wing nuts

30. Removal of the container lid.

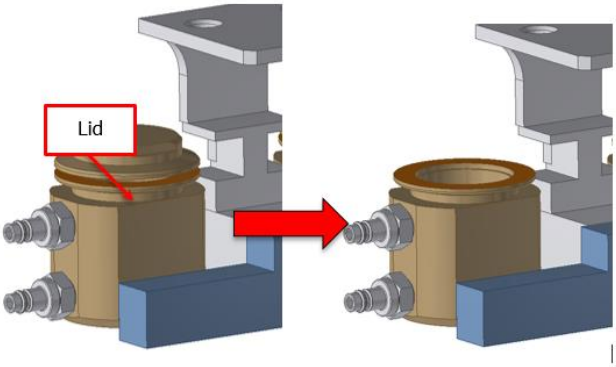

Figure 8: removal of the lid

31. Retrieval of the catcher foils on their support. The operation is done above a tray in order to prevent contamination of the hot cell.

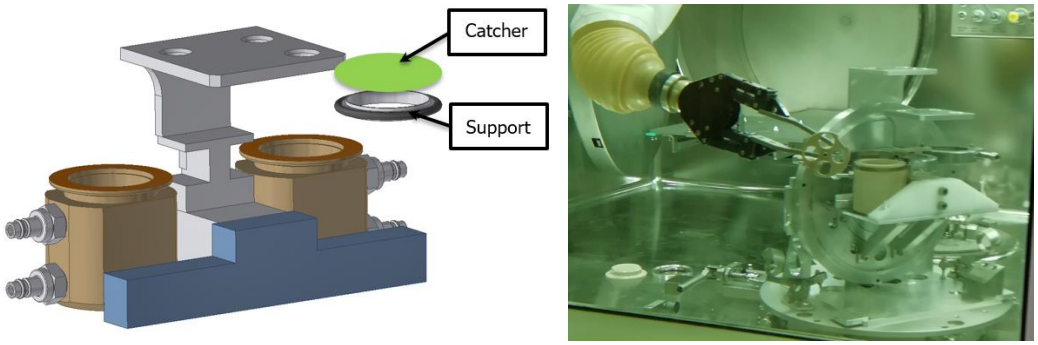

Figure 9: retrieval of the catcher foils on their support

32. Put it in bag through the rear access port and transfer using a grasper and a trolley with lead bricks for shielding, from the hot cell to the measurement room at MEDICIS 179/R-023 for spectrometry gamma.

Figure 10: View of the rear access port

3.2.6 Conditioning old catcher foils in wastes

33. Conditioning of old catcher foils in wastes under the fume hood (179/R-002).

3.2.7 Installation of new catcher foils in the gas container

34. Put new catcher foils on the support.
35. Put the lid of the gas container.
36. Put the gas containers clamps by screwing wing nuts.

3.3 SECOND PART: IRRADIATION WITH GAS INSIDE THE GAS CONTAINERS

These following points will be followed:

- The sample assembly is supposed to be with its transfer unit on the target table inside the hot cell
- The irradiation unit is on the exchange point in the ISOLDE target area
- Operations inside the hot cell are performed with the telemanipulators
- All gas operations are detailed in a specific procedure [6].
- No catcher foils are used during this second part of this experiment.
- 2 irradiations with gas are performed. One is with CO and the other with Ar.
- For each irradiation with gas, 2 charcoal traps will be used.
- Operation inside the hot cell can start only when the hot cell is totally inerted with Ar.

3.3.1 Pumping of the gas container and injection of Carbon monoxide gas inside

37. Repeat steps 10 to 11.
38. Open valves to the gas bottles.
39. Inject the gas mixture into the gas containers after pumping.
40. Close valves to gas bottles.

3.3.2 Transfer of the irradiation unit with the sample assembly to the ISOLDE exchange point

41. Repeat steps 12 to 19 for the irradiation unit with its sample assembly.

3.3.3 Transfer of the irradiation unit and the sample assembly to the HRS or GPS Front-End for irradiation)

42. With the ISOLDE KUKA robot, transfer the irradiation unit with the sample assembly to the HRS or GPS front-end and irradiation.

3.3.4 Transfer of the sample assembly to the hot cell

43. Repeat steps 23 to 27.

3.3.5 Evacuation of the gas over the charcoal trap

44. Connect the charcoal trap assembly between the gas containers and the gas setup.
45. Evacuate the gas over the charcoal trap. The exhaust of the setup is connected to the gas tank. The gas is stored for decay inside the hot cell.

3.3.6 Retrieval of the charcoal trap gamma for Spectrometry gamma

46. Disconnect the charcoal trap from the gas containers and the gas setup.
47. Put it in bag through rear access material and transfer, using a grasper and a trolley with lead bricks for shielding, from the hot cell to the measurement room at MEDICIS 179/R-023 for spectrometry gamma. Conditioning in wastes under the fume hood.

3.4 END OF INTERVENTION

3.4.1 Transfer of the sample assembly to the irradiation unit

48. Repeat steps 13 to 19 for the sample assembly.

3.4.2 Storage of the irradiation base with the sample assembly into the storage shelves

49. With the ISOLDE KUKA robot, transfer the irradiation base with its sample assembly to the storage shelves.

3.4.3 Storage of the transfer unit into the storage shelves

50. Manually retrieve the transfer unit from the hot cell access lock and store it into the 179/R-006 cupboard.

3.4.4 Evacuation of the gas tank inside the fume hood

51. After decay, remove from the hot cell the gas tank and transfer it into the fume hood of the lab 179/R-002.
52. Transfer the gas tank into the fume hood
53. Connect the exhaust to the ventilation pipe to release gas from the gas tank mixed with a neutral gas [6]
NOTA: The mixture CO + neutral gas will be proportionate so as to ensure that the mixture becomes non-flammable.

Figure 11 : ventilation pipe to exhaust gas

4. OPERATORS DURING EXPERIMENT

The number of participants will be limited to the strict minimum during operations.

OPERATOR	ROLE	CONTACT
G. LILLI / EN-SMM	- KUKA robot and MONTRAC handling	166621
P. HARWOOD / EN-SMM or B. CREPIEUX	- Hot cell expert - Retrieval of the charcoal traps and catcher foils from the hot cell	166604
J. BALLOF / EN-STI	- Manual transfer of charcoal traps and catcher foils for spectrometry and conditioning - Spectrometry measurements of the catchers foils and the charcoal traps - Conditioning of the catchers foils and the charcoal traps	167601
1 operator EN-STI with ATEX Level 1 training (to determinate)	- Opening and closure of the CO gas bottles	/
R. Catherall or A-P. BERNARDES / EN- STI (alternatively)	- Technical and safety supervision	163022 or 164255
J. RIEGERT / EN- STI	- Safety supervision	162276
E. AUBERT, A. DORSIVAL, M. DESCHAMPS	- RP supervision	169097, 164834, 161472

5. HAZARD SUMMARY

The most relevant hazards are described as well as the preventive and protective measures implemented related to this experiment only.

The risk analysis related to the MEDICIS facility is given in the following document "Safety File for CERN-MEDICIS - DEMONSTRATIVE PART"- **EDMS 1626873** [3].

The risk analysis related to the MONTRAC system is given in the following document "Risk and failure analysis – MEDICIS MONTRAC"- **EDMS 1474203** [4].

5.1 RADIOLOGICAL HAZARDS

5.1.1 Irradiation

During this experiment, there is an irradiation hazard as soon as the sample assembly with the irradiation base have been irradiated.

Normal scenario		Incidental scenario		
Step	**Risk reduction**	**Event during step**	**Risk reduction**	**Action if risk occurs**
Transfer of the sample assembly, the irradiation base between the hot cell and the front end	• Operations are controlled remotely	• Failure of the robot with the sample assembly at the level of the door to corridor 179/R-201	• Signs in front of the R-401 door to prevent any movement towards the door during the decay (1 day) [1]	• RP supervision • RP stop the activity • Blocking access to corridor R-201 • Wait for decay, retrieve manually the sample assembly for robot maintenance
While moving the transfer unit with the sample assembly to the hot cell, it passes a unshielded door to corridor 179/R-201 and gives an estimated dose rate of 0.2mSv at the level of the door	• Signs in front of the R-401 door to prevent any movement towards the door during the transfer • Transitory period (~2min)			

Normal scenario		Incidental scenario		
Step	**Risk reduction**	**Event during step**	**Risk reduction**	**Action if risk occurs**
Operation inside the hot cell : - Pumping of the gas containers - Gas injection inside the gas containers - Retrieval of the catcher foils - Retrieval of the charcoal traps	• Operations are done with telemanipulators inside the hot cell shielded with the equivalent of 15cm of lead. • The simulation gives a dose rate below 10 µSv/h with the shielding [1] – see Annex 1. Operations in the hot cell will last about 1 hour maximum after each irradiation. • Rehearsal of work steps to be done	• During the vacuum, breaking of the catcher foils and transfer into the charcoal traps that will increase the dose rate of them	• Rehearsal of work steps to be done • Regulation valve on the setup • Dose rate measurement before evacuation of the charcoal traps out of the cell	• RP supervision • RP stop the activity • Wait for decay if dose rate too high for manual handling for spectrometry
Evacuation out of the cell the catcher foils and the charcoal traps for spectrometry gamma through rear material lock. Conditioning in wastes.	• The operator is exposed directly to : o The charcoal trap : 2mSv/h at contact; o The catcher foils : around 3mSv/h at contact **Consequently** : • The catcher foils and the charcoal trap the will be manipulated at distance with a grasper • They are transferred on a trolley behind lead bricks. • Wait for decay before conditioning manually in waste • Rehearsal of work steps to be done			

Table 2: Irradiation hazard table

5.1.2 Contamination

Normal scenario		Incidental scenario		
Step	**Risk reduction**	**Event during step**	**Risk reduction**	**Action if risk occurs**
• Transfer of the sample assembly, the irradiation base between the hot cell and the front end	• Leak test done on the gas containers of the sample assembly	• During transfer, the sample assembly falls in the MEDICIS area. The gas container opens and the catcher foils are damaged and falls out of the container	• Programing and testing of trajectories with the robot before intervention • Rehearsal of work steps to be done	• RP supervision • RP stop the activity • Wearing of the full face mask in case of intervention in the target area to retrieve the elements
• Installation of the irradiation base on the Front end	• Rehearsal of the work step to be done to check if the handle of the sample assembly would be contaminated after installation of the irradiation base on the Front-End	• Contamination of the handle of the sample assembly that implies the contamination of telemanipulators grippers. And by consequence, the contamination of all elements inside the hot cell touched by the telemanipulators	• Smear tests on the handle of the sample assembly after introduction inside the hot cell , cleaning if possible to limit contamination of the equipment inside hot cell	• RP supervision • Smear test inside the hot cell at the end of the experiment and cleaning
• Operation inside the hot cell : ○ Gas injection inside the gas containers ○ Retrieval of the catcher foils ○ Retrieval of the charcoal traps	• Operation done inside the hot cell • The gas containers are flushed before opening to retrieve their catcher foils • The retrieval of the catcher foil is done above a tray to prevent contamination of the hot cell • The catcher foil and the charcoal trap are placed inside a prepared bag before evacuation from the hot cell through the rear access lock • Rehearsal of work steps to be done	• Breaking of the catcher foils or the charcoal trap with the telemanipulators inside the hot cell	• Operation done inside the hot cell • A rod with a sticky ending is used in case of foil rupture to recuperate fragments of the catcher foils • Rehearsal of work steps to be done	• RP supervision • RP stop the activity • The list of elements that could be released are listed in annex 2 – part a): “Expected Inventory in carbon catcher foils”. The total activity expected is around 2MBq. Non-volatile isotopes are retained in foil and volatile species should mostly disappear through ventilation. However, assuming

Normal scenario		Incidental scenario		
Step	**Risk reduction**	**Event during step**	**Risk reduction**	**Action if risk occurs**
				adsorption of all volatile species gives 1 kBq after 2 weeks left. • Wait for decay and cleaning with a vacuum cleaner
Conditioning of the charcoal traps and catcher foils in wastes	• Operation done inside the fume hood (179/R-002)	• Contamination outside the fume hood	• Conditioning of the charcoal traps and the catcher foils after a decay time • Rehearsal of work steps to be done	• RP supervision • RP stop the activity • Wearing of the full face mask in case of contamination released out of the fume hood

Table 3: Contamination hazard table

5.1.3 Radioactive gas

Normal scenario		Incidental scenario		
Step	**Risk reduction**	**Event during step**	**Risk reduction**	**Action if risk occurs**
• Irradiation of the sample assembly in the target area	• Leak test and test of pressure (validated by HSE) made on the gas containers : ○ The expected gas pressure inside the containers for an estimated temperature of 200 degrees is 2.2bars (see evaluation in Annex 3). The gas containers will be tested to support at least 3.3 bars (1,5 times 2.2bars) • 4 Thermocouples will be installed on the irradiation base to check the temperature, if the temperature exceeds 200°, the irradiation will be stopped.	• Overpressure inside the gas container, failure of valves and quick connectors and leak of the gas inside the target area during irradiation	• Rehearsal of work steps to be done • Same as for normal scenario	• RP supervision • RP stop the activity • The list of elements that could be released are listed in annex 2 – part b): "Expected Inventory in charcoal traps". The total activity expected is around 1MBq and this is low compared to the activity already existing in the target area *(to be confirmed by HSE-RP)*. • Wait for decay : within two days, the activity decays by a factor of ca. 140 [1]
• Evacuation of the gas over the charcoal trap inside the hot cell	• Leak test and test of pressure made on the gas setup	• Leak on the setup during the evacuation of the gas over the charcoal trap inside the hot cell	• Leak test of the gas setup before intervention • Ventilation of the hot cell during operation (depression) • Rehearsal of work steps to be done	• RP supervision • RP stop the activity • The list of elements that could be released are listed in annex 2 – part b): "Expected Inventory in charcoal traps". The total activity expected is around 1MBq. • Stop the pumping and wait for decay if leak inside the hot cell • In case of release of contamination in the room 179/R-401, close the valve located in the hot cell from
		• Contamination of the hot cell with the gas exhausted	• The exhaust of the setup is connected to a gas tank. Gas are stored for decay and then are released inside the ventilation pipe (179/R-002)	

Normal scenario		Incidental scenario		
Step	**Risk reduction**	**Event during step**	**Risk reduction**	**Action if risk occurs**
			• Rehearsal of work steps to be done	room 179/R-003 to stop the pumping • Wearing of the full face mask in case of contamination to access room 179/R-401 • Put sign in front of door 179/R-401 to forbid access during decay.
		• Contamination in the sector 1 during the pumping of the gas with the scroll pump due to a leak	• Leak test on line including the scroll pump • Checking the pressure values on the manometer • Rehearsal of work steps to be done	
Irradiated gas release of the gas tank (Co, Ar)	• The decay tank is placed inside the fume hood (179/R-002). The exhaust is connected to the ventilation pipe in room 179/R-002 • Leak test and pressure test of the gas release setup • Gas released after decay time • Low flow rate	• Contamination outside the fume hood	• Same as normal scenario	• RP supervision • RP stop the activity • Wearing of the full face mask in case of contamination in room 179/R-002 and closure of the release valve

Table 4: Radioactive gas hazard table

5.1.4 Radioactive waste

Normal scenario		Incidental scenario		
Step	**Risk reduction**	**Event during step**	**Risk reduction**	**Action if risk occurs**
• Conditioning in wastes the catcher foils and the charcoal traps	• The charcoal traps and catcher foils are given a suitable cooling time and then are conditioned in waste [1] • Operations done under the fumehood with tools for working at distance			
• Storage of the irradiation unit, transfer unit and sample assembly in order to be reused	• The units are temporarily stored in the MEDICIS shelves. After a suitable cooling time the dose rate is assessed. The irradiation unit and sample assembly are stored in the ISR, the transfer unit is not expected to be activated. In case of contamination e.g. by volatile I-131, further decay is awaited [1]			

Table 5: Radioactive wastes hazard table

5.2 CHEMICAL HAZARDS

During this experiment, the chemicals hazards (CMR and Toxic) are due to the use of the carbon monoxide – see safety data sheet in Annex 4.

Risk reduction	Action if risk occurs
Following the meeting with HSE-OHS and EN-EA : • See safety form SF-C-0-0-1 - **EDMS 2042265** • Procedure to use the gas bottle (connection, disconnection) with emergency procedure (*ongoing*) • Leak test of the lines connected to the gas bottles and the gas setup • Pressure test of lines used with CO • Use of a portable carbon monoxide detector to detect any leaks in the room 179/R-401 where the bottles are stored	• If a leak is detected, or if there is a ventilation failure, closure of the bottles valves if possible and evacuation of the room/building

Table 6: Chemical hazards table

5.3 MECHANICAL HAZARDS

Normal scenario		Incidental scenario		
Step	**Risk reduction**	**Event during step**	**Risk reduction**	**Action if risk occurs**
Mechanical energy (moving parts)				
Use of the KUKA robot, and MONTRAC systems to move the irradiation unit, transfer unit and sample assembly during transfer and handling steps	• See CERN-MEDICIS safety file – demonstrative part [3]			
Use of telemanipulators during hot cell operations	• See Risk assessment for the use of PPE in CERN-MEDICIS [5]			
Lifting of equipment (Falling)				
Use of crane inside the hot cell to lift the irradiation and transfer unit with the sample assembly	• Crane qualifies to lift 40Kg (weight of the sample assembly + transfer unit : below 25 kg) • Limit the height during transfer inside the hot cell • Rehearsal of work steps to be done	• Falling of the transfer unit with the sample assembly inside the hot cell in case of crane failure	• Same as for normal scenario	• Damage limited as the height during the lifting will be at the minimum possible • Check the status of the element that has fallen. If the element is damaged, the element is repaired if possible or the operation is stopped.

Normal scenario		Incidental scenario		
Step	**Risk reduction**	**Event during step**	**Risk reduction**	**Action if risk occurs**
Use of telemanipulators during operations inside the hot cell	• Equipment designed to be handled with the telemanipulators • Use of specific tools designed to handle the equipment with the telemanipulators • Button on the telemanipulators to lock the closure of the pincers and avoid the unintentionally dropping of elements handled • Limit the height of working inside the hot cell • Rehearsal of work steps to be done	• Falling of the equipment handled with telemanipulators	• Same as for normal scenario	• Damage limited as the height during the lifting will be at the minimum possible • Check the status of the element that has fallen. If the element is damaged, the element is repaired if possible or the operation is stopped.
Pressure				
• Use of two gas bottles of carbon monoxide connected to the hot cell. during experiment	• The use of 2 CO gas bottles (1l - 200 bars) has been assessed by EN/EA, and the measures asked in the safety form C-2-0-1 (submitted to HSE) - **EDMS 2038401** - will be followed.	• Damage on the gas bottles	• Following the meeting with HSE-OHS and EN-EA, the gas bottle will be attached on an structure element of the building (metallic beam) • The access of this room is limited. An operator *(with ATEX level 1 training)* enters in the room R-401 during the experiment only to open and close the valves. • The bottles are not situated under the trajectory of the robot. Consequently, a	• Evacuation of the building

Normal scenario		Incidental scenario		
Step	**Risk reduction**	**Event during step**	**Risk reduction**	**Action if risk occurs**
			mechanical shock strong enough to damage them is highly unlikely.	

	• There are 2 safety valves for the overpressure risk :
	  ○ One is the pressure regulator gas bottle that limits pressure to 10 bars
	  ○ One is situated just after the bottle outside the hot cell just before the feedthrough. It limits pressure to 2 bars
		• Overpressure and CO gas release in the room	• Checking the pressure values on the manometers
			• Use of a carbon monoxide detector that can detect CO leaks
			• Test of the bottles and the line before operation, use of a certified tube between gas bottles and hot cell
				• Stop the intervention and closure of the bottles

• Injection of the gas (Co, Ar inside the gas containers	• There are 1 safety valve for the overpressure risk : ○ Another safety valve is located inside the hot cell just after the feedthrough. It limits also the pressure to 2 bars inside the gas setup	• Overpressure and CO gas release in the hot cell	• Checking the pressure values on the manometer • Test of the gas setup before operation • Pressure test of the line validated by HSE	• Stop the intervention and closure of the bottles

Normal scenario		Incidental scenario		
Step	**Risk reduction**	**Event during step**	**Risk reduction**	**Action if risk occurs**
• Exhaust of the gas inside the gas tank *(used for decay)* after circulation over the charcoal trap	• There are 1 safety valve and an expansion vessel for the overpressure risk : ○ The safety valve is situated at the level of the gas tank and limits the pressure inside to 4 bars ○ The tank between the scroll pump and the pressure pump (cf. Figure 5) is an expansion vessel to prevent the risk of overpressure at the level of the pressure pump •	• Overpressure and CO gas release in the hot cell		• Stop exhaust of the gas inside the gas tank
• Irradiation in the target area of the sample assembly filled with the CO gas	• Cf.5.1.3	• Gas under pressure inside the gas containers (carbon monoxide, noble gases) during irradiation : Overpressure during irradiation	• Cf.5.1.3	

Table 7: Mechanical hazards table

5.4 FIRE HAZARDS

During this experiment, the fire hazard (flammable and explosive hazard) is due to the use of the carbon monoxide – see safety data sheet in Annex 4.
The ATEX risk level is 2 - 30cm in all direction around the gas connections (see safety form C-2-0-2 (submitted to HSE) - **EDMS 2038401)**

Risk reduction	Action if risk occurs

Following the meeting with HSE-OHS and EN-EA :
• The use of 2 CO gas bottles has been assessed by EN/EA, and the measures asked in the safety form C-2-0-1 (submitted to HSE) - **EDMS 2038401** - will be followed :
  ○ Leak test before the filling of system with CO (performed)
  ○ Pressure test of the line validated by HSE (performed)
  ○ Grounding of all equipment used with CO (ongoing) + Electrical safety inspection (performed)
  ○ Written operating instruction connection/replacing of CO bottles and manipulation with the CO in the hot cell with emergency procedure - **EDMS 2045068**
  ○ Purge air in the circuit before introducing CO
  ○ Labelling (Ex) next the bottles (performed)
  ○ ATEX lv1 training for the people involved in the manipulation of CO
• Hot cell filled with argon gas before starting and during the second part of the experiment
• Use of different manometers along the gas setup in order to detect any leak
• Use of a portable carbon monoxide detector to detect any leaks in the room R201 where are stored the bottles
• For the gas released inside the ventilation pipe (179/R-002), the flow rate will be low and the CO gas will be mixed with an inert gas
	• In case of leak (inside or outside the hot cell), the intervention is stop and the pumps are switched off
	• If a leak is detected outside the hot cell (room 179/R-401), or if there is a ventilation failure (alarm), actions will depend on the values measured by the carbon monoxide detector and the CO exposure limits:
	  ○ 30ppm for the VME/TWA (Time Weighted Average, over 8 hours) : Closure of the bottles, evacuate the building and call the firefighters
	  ○ 60 ppm for the VLE/STEL (Short Term Exposure Limit, 15 minutes): Closure of the bottles by not staying more than 15min inside the room (if it is not possible in 15min, evacuate the room), evacuate the building and call the firefighters
	  ○ 1200ppm for the IDLH (Immediately Dangerous to Life or Health): entry strictly prohibited in the room, evacuate immediately the room, evacuate the building and call the firefighters
	• Firefighters are informed of the presence of these gas bottles inside the room 179/R-401 in case of emergency

Table 8: Fire hazards table

ANNEX 1: EFFECTIVE DOSE USING "EWT74" TABLES

After 5 irradiations at 1e13 pps for 10 minutes each
60 minutes cooling between irradiations
30 minutes cooling after last irradiation

1. Irradiation unit at decay point

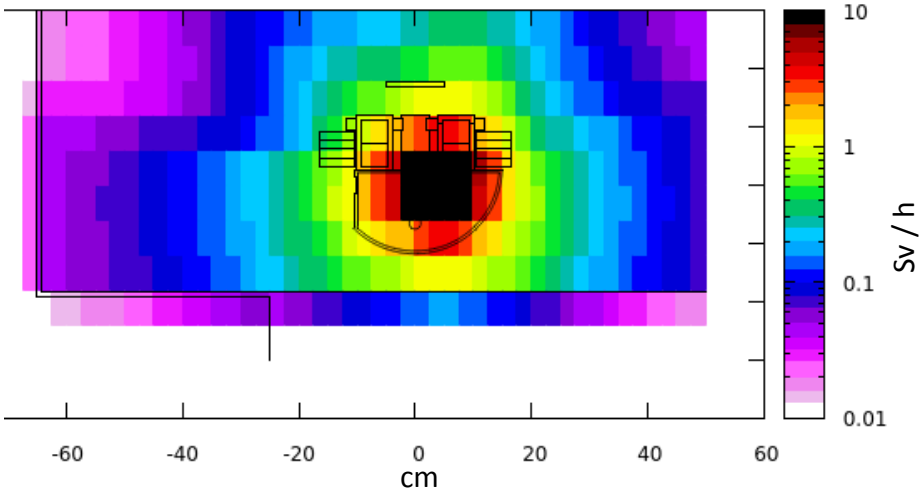

Dose rate less than 1 Sv/h at decay point expected

2. Sample assembly in hot cell

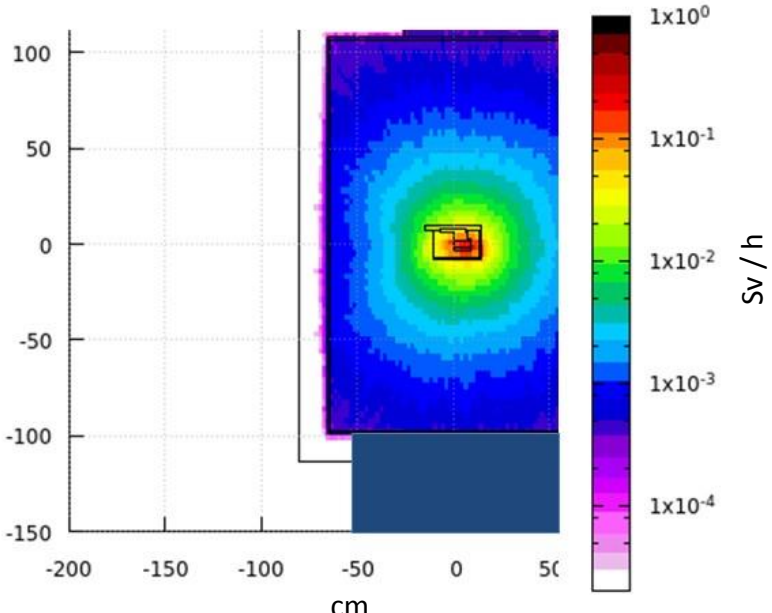

Less than 10 uSv/h outside the hot cell

ANNEX 2: LIST OF ELEMENT FORESEEN, ACTIVITY AND DOSE RATE SIMULATION

1. Produced radioisotopes

Evaluated after 10 minutes of irradiation at 1013 pps and 30 minutes of cooling. Radionuclides above 1 Bq are given.

a. Expected Inventory in carbon catcher foils

Inventory of catcher foil is arising from activation of the foil and implantation of caught uranium fission recoils. Assuming, that 10% of all elements produced by fission are released. All elements having 20 <= Z <= 70 are considered to be fission products. This value of 10% is estimated by the recoil energy, range and thickness of the foil. Most of the recoils don't leave the foil, because their kinetic energy is too low to propagate through the foil. The range was estimated with SRIM. The recoil energy by experimental data and ABRABLA simulations. 105Mo was used as model system.

Mass	Element	Type	Bq
11	C	Activation	1.77E+05
101	Tc	Implantation	1.35E+05
94	Y	Implantation	8.23E+04
138	Cs	Implantation	8.20E+04
101	Mo	Implantation	8.17E+04
104	Tc	Implantation	7.64E+04
141	Ba	Implantation	7.09E+04
134	Te	Implantation	6.93E+04
102	Tc	Implantation	6.30E+04
102	Mo	Implantation	6.25E+04
138	Xe	Implantation	6.07E+04
89	Rb	Implantation	5.61E+04
143	La	Implantation	5.55E+04
146	Pr	Implantation	5.44E+04
107	Rh	Implantation	5.40E+04
95	Y	Implantation	5.30E+04
134	I	Implantation	5.00E+04
139	Ba	Implantation	4.85E+04
131	Te	Implantation	4.61E+04
131	Sb	Implantation	4.60E+04
139	Cs	Implantation	4.27E+04
142	Ba	Implantation	4.07E+04
133	Te	Implantation	3.82E+04
142	La	Implantation	3.64E+04
146	Ce	Implantation	3.58E+04
111	Pd	Implantation	3.13E+04
147	Pr	Implantation	3.03E+04
93	Sr	Implantation	2.75E+04
92	Sr	Implantation	2.53E+04

Mass	Element	Type	Bq
115	Ag	Implantation	2.45E+04
105	Tc	Implantation	2.44E+04
118	In	Implantation	2.43E+04
118	Cd	Implantation	2.43E+04
87	Kr	Implantation	2.00E+04
130	Sb	Implantation	1.86E+04
84	Br	Implantation	1.77E+04
141	La	Implantation	1.46E+04
105	Ru	Implantation	1.45E+04
135	I	Implantation	1.36E+04
88	Kr	Implantation	1.31E+04
88	Rb	Implantation	1.19E+04
149	Nd	Implantation	1.14E+04
128	Sn	Implantation	9.09E+03
145	Pr	Implantation	8.92E+03
151	Nd	Implantation	8.68E+03
152	Pm	Implantation	8.44E+03
93	Y	Implantation	8.18E+03
91	Sr	Implantation	7.49E+03
117	Cd	Implantation	6.34E+03
113	Ag	Implantation	6.30E+03
129	Te	Implantation	5.91E+03
97	Zr	Implantation	5.60E+03
152	Nd	Implantation	5.54E+03
81	Se	Implantation	5.11E+03
129	Sb	Implantation	4.71E+03
83	Br	Implantation	4.02E+03
83	Se	Implantation	3.62E+03
127	Sn	Implantation	3.57E+03
117	In	Implantation	3.55E+03
92	Y	Implantation	3.37E+03
97	Nb	Implantation	3.32E+03
133	I	Implantation	2.95E+03
109	Pd	Implantation	2.83E+03
137	Xe	Implantation	2.80E+03
108	Rh	Implantation	2.70E+03
108	Ru	Implantation	2.53E+03
155	Sm	Implantation	2.02E+03
132	I	Implantation	1.83E+03
112	Pd	Implantation	1.79E+03
143	Ce	Implantation	1.77E+03
99	Mo	Implantation	1.58E+03

Mass	Element	Type	Bq
135	Xe	Implantation	1.55E+03
107	Ru	Implantation	1.42E+03
128	I	Implantation	1.33E+03
79	As	Implantation	1.30E+03
119	In	Implantation	1.25E+03
112	Ag	Implantation	1.04E+03
121	Sn	Implantation	1.00E+03
132	Te	Implantation	9.83E+02
153	Pm	Implantation	8.50E+02
78	Ge	Implantation	8.27E+02
89	Kr	Implantation	5.41E+02
115	Cd	Implantation	5.22E+02
145	Ce	Implantation	5.09E+02
128	Sb	Implantation	4.42E+02
158	Eu	Implantation	4.31E+02
144	Pr	Implantation	3.82E+02
151	Pm	Implantation	3.71E+02
78	As	Implantation	3.50E+02
75	Ge	Implantation	3.50E+02
140	Ba	Implantation	2.86E+02
157	Sm	Implantation	2.80E+02
130	I	Implantation	2.44E+02
90	Rb	Implantation	2.32E+02
127	Sb	Implantation	2.17E+02
120	Sb	Implantation	2.05E+02
127	Te	Implantation	1.91E+02
130	Sn	Implantation	1.81E+02
159	Eu	Implantation	1.80E+02
130	Cs	Implantation	1.68E+02
84	Se	Implantation	1.67E+02
156	Sm	Implantation	1.56E+02
105	Rh	Implantation	1.54E+02
74	Ga	Implantation	1.35E+02
111	Ag	Implantation	1.29E+02
153	Sm	Implantation	1.25E+02
85	Br	Implantation	1.20E+02
147	Nd	Implantation	1.20E+02
131	I	Implantation	1.10E+02
103	Ru	Implantation	1.03E+02
136	La	Implantation	9.11E+01
116	Ag	Implantation	8.98E+01
149	Pm	Implantation	8.90E+01

Mass	Element	Type	Bq
133	Sb	Implantation	8.54E+01
112	In	Implantation	7.06E+01
158	Sm	Implantation	6.51E+01
69	Zn	Implantation	6.45E+01
73	Ga	Implantation	6.07E+01
96	Nb	Implantation	5.67E+01
95	Zr	Implantation	5.53E+01
119	Cd	Implantation	5.22E+01
162	Tb	Implantation	5.22E+01
7	Be	Activation	5.17E+01
157	Eu	Implantation	4.83E+01
114	Ag	Implantation	4.77E+01
114	Pd	Implantation	4.61E+01
132	Sb	Implantation	4.42E+01
148	Pr	Implantation	4.31E+01
125	Sn	Implantation	4.19E+01
140	La	Implantation	4.17E+01
80	Br	Implantation	3.95E+01
150	Pm	Implantation	3.94E+01
89	Sr	Implantation	3.55E+01
77	Ge	Implantation	2.95E+01
77	As	Implantation	2.41E+01
122	Sb	Implantation	2.35E+01
117	Sb	Implantation	2.30E+01
133	Xe	Implantation	2.25E+01
149	Pr	Implantation	2.06E+01
162	Gd	Implantation	1.86E+01
70	Ga	Implantation	1.80E+01
163	Tb	Implantation	1.60E+01
104	Rh	Implantation	1.53E+01
106	Ag	Implantation	1.35E+01
65	Ni	Implantation	1.34E+01
61	Co	Implantation	1.28E+01
134	La	Implantation	1.21E+01
133	La	Implantation	1.18E+01
129	Sn	Implantation	1.18E+01
136	Cs	Implantation	1.18E+01
144	Ce	Implantation	9.88E+00
82	Br	Implantation	9.52E+00
141	Nd	Implantation	9.01E+00
159	Gd	Implantation	8.74E+00
126	Sb	Implantation	8.67E+00

Mass	Element	Type	Bq
123	I	Implantation	8.53E+00
119	Sb	Implantation	8.30E+00
131	La	Implantation	7.74E+00
115	Sb	Implantation	7.41E+00
139	Pr	Implantation	7.35E+00
116	Sb	Implantation	7.29E+00
137	Pr	Implantation	6.73E+00
136	Pr	Implantation	6.59E+00
106	Ru	Implantation	6.51E+00
106	Rh	Implantation	6.51E+00
139	Nd	Implantation	6.50E+00
121	I	Implantation	6.45E+00
141	Pm	Implantation	6.11E+00
135	La	Implantation	6.07E+00
121	In	Implantation	5.99E+00
165	Dy	Implantation	5.42E+00
142	Pr	Implantation	5.40E+00
141	Ce	Implantation	5.37E+00
127	Cs	Implantation	4.74E+00
72	Zn	Implantation	4.17E+00
129	Cs	Implantation	4.09E+00
56	Mn	Implantation	4.03E+00
137	Ce	Implantation	3.79E+00
159	Ho	Implantation	3.63E+00
90	Y	Implantation	3.49E+00
161	Tm	Implantation	3.44E+00
49	Sc	Implantation	3.31E+00
132	Cs	Implantation	3.24E+00
72	Ga	Implantation	3.19E+00
129	Ba	Implantation	3.14E+00
98	Nb	Implantation	3.12E+00
160	Ho	Implantation	3.06E+00
99	Nb	Implantation	2.99E+00
125	Xe	Implantation	2.91E+00
135	Pr	Implantation	2.89E+00
130	La	Implantation	2.88E+00
125	Cs	Implantation	2.81E+00
117	Te	Implantation	2.76E+00
78	Br	Implantation	2.74E+00
66	Cu	Implantation	2.71E+00
61	Fe	Implantation	2.65E+00
123	Xe	Implantation	2.63E+00

Mass	Element	Type	Bq
76	As	Implantation	2.61E+00
132	La	Implantation	2.41E+00
68	Ga	Implantation	2.24E+00
163	Er	Implantation	2.23E+00
136	Nd	Implantation	2.21E+00
157	Ho	Implantation	2.12E+00
143	Pr	Implantation	2.09E+00
124	Sb	Implantation	1.97E+00
3	H	Activation	1.92E+00
64	Ho	Implantation	1.85E+00
161	Gd	Implantation	1.73E+00
91	Y	Implantation	1.73E+00
124	I	Implantation	1.73E+00
127	Ba	Implantation	1.70E+00
126	I	Implantation	1.70E+00
162	Tm	Implantation	1.64E+00
159	Er	Implantation	1.61E+00
163	Tm	Implantation	1.60E+00
131	Cs	Implantation	1.55E+00
111	Sn	Implantation	1.55E+00
137	Nd	Implantation	1.50E+00
142	Pm	Implantation	1.44E+00
142	Sm	Implantation	1.43E+00
162	Ho	Implantation	1.39E+00
118	Sb	Implantation	1.38E+00
167	Ho	Implantation	1.37E+00
167	Yb	Implantation	1.30E+00
134	Pr	Implantation	1.29E+00
123	Sn	Implantation	1.28E+00
140	Pr	Implantation	1.24E+00
135	Ce	Implantation	1.20E+00
56	Cr	Implantation	1.19E+00
128	Cs	Implantation	1.19E+00
133	Ce	Implantation	1.16E+00
87	Zr	Implantation	1.13E+00
161	Ho	Implantation	1.12E+00
158	Ho	Implantation	1.12E+00
104	Ag	Implantation	1.10E+00
67	Cu	Implantation	1.10E+00
122	I	Implantation	1.09E+00

b. Expected Inventory in charcoal traps

Inventory of charcoal traps arising from volatile fission products. Noble gases, Se, the halogens Br and I, (earth) alkaline metals Rb, Sr, Cs as well as candidates for carbonyl formation Zr to Ru (4d metals) and Hf to Ir (5d metals) have been considered as volatile.

Mass	Element	Bq
101	Tc	1.35E+05
138	Cs	8.20E+04
101	Mo	8.17E+04
104	Tc	7.64E+04
102	Tc	6.30E+04
102	Mo	6.25E+04
138	Xe	6.07E+04
89	Rb	5.61E+04
107	Rh	5.40E+04
134	I	5.00E+04
139	Cs	4.27E+04
93	Sr	2.75E+04
92	Sr	2.53E+04
105	Tc	2.44E+04
87	Kr	2.00E+04
84	Br	1.77E+04
105	Ru	1.45E+04
135	I	1.36E+04
88	Kr	1.31E+04
88	Rb	1.19E+04
91	Sr	7.49E+03
97	Zr	5.60E+03
81	Se	5.11E+03
83	Br	4.02E+03
83	Se	3.62E+03
97	Nb	3.32E+03
133	I	2.95E+03
137	Xe	2.80E+03
108	Rh	2.70E+03
108	Ru	2.53E+03
132	I	1.83E+03
99	Mo	1.58E+03
135	Xe	1.55E+03
107	Ru	1.42E+03
128	I	1.33E+03
218	Rn	8.05E+02
89	Kr	5.41E+02
217	Rn	2.53E+02
130	I	2.44E+02
90	Rb	2.32E+02
212	Rn	2.11E+02
130	Cs	1.68E+02
84	Se	1.67E+02

Mass	Element	Bq
105	Rh	1.54E+02
209	Rn	1.21E+02
85	Br	1.20E+02
131	I	1.10E+02
208	Rn	1.09E+02
103	Ru	1.03E+02
210	Rn	6.76E+01
96	Nb	5.67E+01
95	Zr	5.53E+01
207	Rn	4.20E+01
80	Br	3.95E+01
89	Sr	3.55E+01
133	Xe	2.25E+01
104	Rh	1.53E+01
136	Cs	1.18E+01
206	Rn	1.10E+01
82	Br	9.52E+00
211	Rn	9.35E+00
123	I	8.53E+00
180	Re	6.62E+00
106	Ru	6.51E+00
106	Rh	6.51E+00
121	I	6.45E+00
182	Ir	6.38E+00
183	Ir	5.99E+00
180	Os	5.87E+00
179	Re	5.43E+00
127	Cs	4.74E+00
129	Cs	4.09E+00
178	Re	4.03E+00
132	Cs	3.24E+00
98	Nb	3.12E+00
171	Ta	3.00E+00
99	Nb	2.99E+00
168	Hf	2.95E+00
125	Xe	2.91E+00
179	W	2.90E+00
175	W	2.85E+00
125	Cs	2.81E+00
78	Br	2.74E+00
216	Rn	2.67E+00
123	Xe	2.63E+00
174	W	2.24E+00
177	Re	2.20E+00
184	Ir	2.02E+00
170	Ta	1.80E+00
124	I	1.73E+00
126	I	1.70E+00

Mass	Element	Bq
179	Os	1.57E+00
181	Os	1.56E+00
131	Cs	1.55E+00
128	Cs	1.19E+00
87	Zr	1.13E+00
172	Ta	1.10E+00
122	I	1.09E+00

2. Activity and dose rate simulation

Dose rates and simulation details are discussed in “Experiment proposal to study transition metal carbonyl formation at ISOLDE” **EDMS 2036665.**

ANNEX 3: TEMPERATURE DEPENDENCE OF PRESSURE IN GAS CONTAINER

Initially, the gas containers are filled with a maximum pressure of 1.0 bar above atmospheric pressure. Upon proton irradiation, moderate heating of the target unit is expected. The Expected pressure increase with temperature is shown below (ideal gas law).

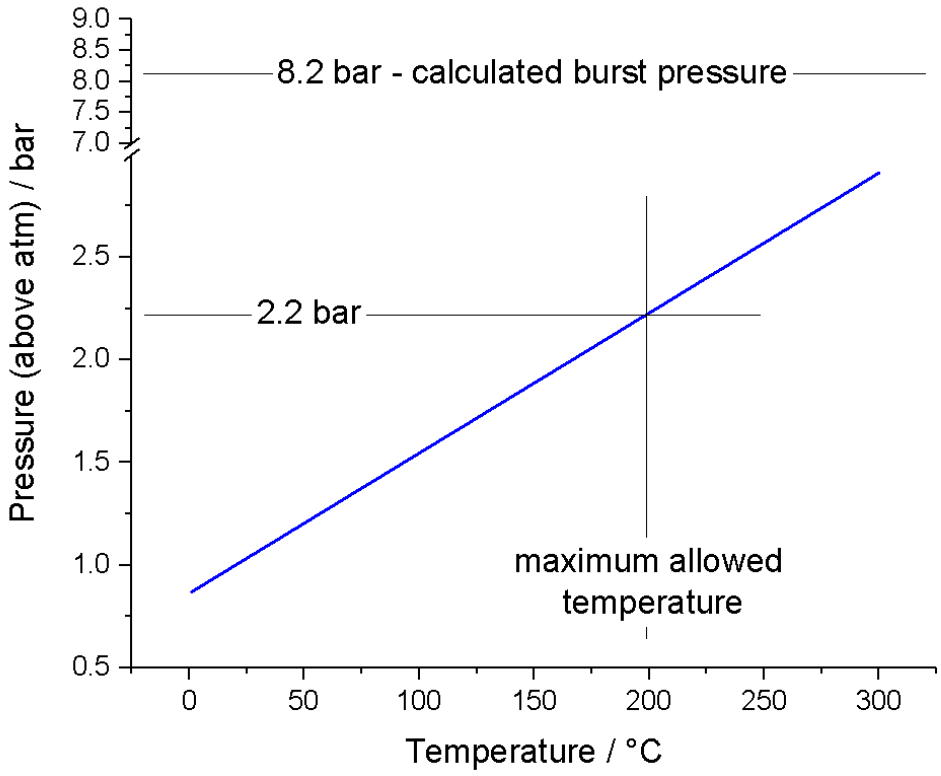

ANNEX 4: SAFETY DATA SHEET OF THE CARBON MONOXIDE

Carbagas AIR LIQUIDE	FICHE DE DONNEES DE SECURITE	Page : 1 / 6 Edition révisée n° : 0 Date : 13 / 12 / 2010 : 0 / 0 / 0
	Monoxyde de carbone	CG019

Danger

1 Identification de la substance/du mélange et de la société/l'entreprise

Identificateur de produit

Nom commercial	: Monoxyde de carbone
N° FDS	: CG019
Description chimique	: Monoxyde de carbone No CAS :000630-08-0 No CE :211-128-3 No Index :006-001-00-2
Formule chimique	: CO
N° d'enregistrement	: Limite d'enregistrement non atteinte
Usage	: Industriel et professionnel Faire une analyse des risques avant utilisation
Identification de la société	: Carbagas AG HOFGUT CH-3073 GUEMLIGEN Switzerland
Numéro d'appel d'urgence	: Tel.: 031 950 50 50

2 Identification des dangers

Classification de la substance ou du mélange

Classe de Risque et catégorie de code réglementaire CE 1272/2008 (CLP)	
• Dangers physiques	: Gaz inflammables - Catégorie 1 - Danger (H220) Gaz sous pression - Gaz comprimés - Attention (H280)
• Dangers pour la santé	: Toxicité aiguë, par inhalation - Catégorie 3 - Danger (H331) Toxicité pour le système reproductif - Foetus - Catégorie 1A - Danger (H360D) Toxicité spécifique pour certains organes cibles - Exposition répétée - Catégorie 1 - Danger (H372)
Classification CE 67/548 ou CE 1999/ 45	: F+; R12 Repr. Cat. 1; R61 T; R23-R48/23

Éléments d'étiquetage

Carbagas AIR LIQUIDE	FICHE DE DONNEES DE SECURITE	Page : 2 / 6 Edition révisée n° : 0 Date : 13 / 12 / 2010 : 0 / 0 / 0
	Monoxyde de carbone	**CG019**

2 Identification des dangers (suite)

Règlement d'Etiquetage CE 1272/2008 (CLP)

• Pictogrammes de danger

• Pictogrammes de danger

• Mention d'avertissement : Danger

• Mention de danger : H331 : Toxique par inhalation.
H220 : Gaz extrêmement inflammable.
H360 : Peut nuire à la fertilité ou au fœtus.
H372 : Risque avéré d'effets graves pour les organes à la suite d'expositions répétées ou d'une exposition prolongée.
H280 : Contient un gaz sous pression; peut exploser sous l'effet de la chaleur.

• Mentions de mise en garde

- Prévention : P260 : Ne pas respirer les gaz, vapeurs.
P210 : Tenir à l'écart de la chaleur/des étincelles/des flammes nues/des surfaces chaudes. – Ne pas fumer.
P202 : Ne pas manipuler avant d'avoir lu et compris toutes les précautions de sécurité.

- Intervention : P304+P340+P315 : EN CAS D'INHALATION: transporter la victime à l'extérieur et la maintenir au repos dans une position où elle peut confortablement respirer. Consulter immédiatement un médecin.
P308+P313 : EN CAS d'exposition prouvée ou suspectée: consulter un médecin.
P377 : Fuite de gaz enflammé: Ne pas éteindre si la fuite ne peut pas être arrêtée sans risque.
P381 : Éliminer toutes les sources d'ignition si cela est faisable sans danger.

- Stockage : P405 : Garder sous clef.
P403 : Stocker dans un endroit bien ventilé.

Etiquetage CE 67/548 ou CE 1999/45

Symbole(s) : F+ : Extrêmement inflammable

: T : Toxique

Phrase(s) R : R61 : Risque pendant la grossesse d'effets néfastes pour l'enfant.
R12 : Extrêmement inflammable.
R23 : Toxique par inhalation.
R48/23 : Toxique : risque d'effets graves pour la santé en cas d'exposition prolongée par inhalation.

Phrase(s) S : S45 : En cas d'accident ou de malaise, consulter immédiatement un médecin (si possible lui montrer l'étiquette).
S53 : Eviter l'exposition - se procurer des instructions spéciales avant l'utilisation.

Autres dangers

Autres dangers : Aucun(e).

Carbagas AIR LIQUIDE	FICHE DE DONNEES DE SECURITE	Page : 3 / 6 Edition révisée n° : 0 Date : 13 / 12 / 2010 : 0 / 0 / 0
	Monoxyde de carbone	**CG019**

3 Composition/informations sur les composants

Substance / Préparation : Substance.

Nom de la substance		Contenance	No CAS	No CE	No Index	No. Enregistrement	Classification
Monoxyde de carbone	:	100 %	630-08-0	211-128-3	006-001-00-2	NOTE 2	F+; R12 Repr. Cat. 1; R61 T; R23-48/23 Flam. Gas 1 (H220) Repr. 1A (H360d) Acute Tox. 3 (H331) STOT RE 1 (H372) Press. Gas (H280)

Ne contient pas d'autres composants ni impuretés qui pourraient modifier la classification du produit.
Note 1: Listé dans l'Annexe IV/V de Reich, exempté d'enregistrement
Note 2: Limite d'enregistrement non atteinte
Voir le texte complet des Phrases-R au chapitre 16

4 Premiers secours

Premiers secours

- Inhalation : Toxique par inhalation.
Les symptômes peuvent être des étourdissements, des maux de tête, des nausées et une perte de coordination.
Déplacer la victime dans une zone non contaminée, en s'équipant d'un appareil respiratoire autonome. Laisser la victime au chaud et au repos. Appeler un médecin. Pratiquer la respiration artificielle si la victime ne respire plus.

- Ingestion : L'ingestion n'est pas considérée comme un mode d'exposition possible.

5 Mesures de lutte contre l'incendie

Risques spécifiques : L'exposition prolongée au feu peut entraîner la rupture et l'explosion des récipients.

Produits de combustion dangereux : Aucun(e).

Moyens d'extinction

- Agents d'extinction appropriés : Tous les agents d'extinction connus peuvent être utilisés.

Méthodes spécifiques : Si possible, arrêter le débit gazeux.
S'éloigner du récipient et le refroidir avec de l'eau depuis un endroit protégé.
Ne pas éteindre une fuite de gaz enflammée, sauf si absolument nécessaire. Une réinflammation spontanée et explosive peut se produire. Eteindre les autres feux.

Equipements de protection spéciaux pour pompiers : Utiliser un appareil respiratoire autonome.

6 Mesures à prendre en cas de dispersion accidentelle

Précautions pour les personnes : Evacuer la zone.
Eliminer les sources d'inflammation.
Assurer une ventilation d'air appropriée.
Porter un appareil respiratoire autonome pour entrer dans la zone, à moins d'avoir contrôlé que celle-ci est sûre.

Précautions pour la protection de l'environnement : Essayer d'arrêter la fuite.

Méthodes de nettoyage : Ventiler la zone.

Carbagas AIR LIQUIDE	FICHE DE DONNEES DE SECURITE	Page : 4 / 6 Edition révisée n° : 0 Date : 13 / 12 / 2010 : 0 / 0 / 0
Monoxyde de carbone		CG019

7 Manipulation et stockage

Manipulation : Prendre des mesures de précaution contre les décharges électrostatiques.
Empêcher l'aspiration d'eau dans le récipient.
Purger l'air de l'installation avant d'introduire le gaz.
Interdire les remontées de produits dans le récipient.
Utiliser seulement l'équipement spécifié approprié à ce produit et à sa pression et température d'utilisation. Contacter votre fournisseur de gaz en cas de doute.
Maintenir à l'écart de toute source d'inflammation (y compris de charges électrostatiques).
Se reporter aux instructions du fournisseur pour la manipulation du récipient.

Stockage : Stocker le récipient dans un endroit bien ventilé, à température inférieure à 50°C.
Entreposer à l'écart des gaz oxydants et des autres oxydants.

8 Contrôles de l'exposition/protection individuelle

Protection individuelle : Assurer une ventilation appropriée.
Ne pas fumer pendant la manipulation du produit.
Disposer d'un appareil respiratoire autonome, prêt à être utilisé en cas d'urgence.

Limites d'exposition professionnelle : Monoxyde de carbone : TLV© -TWA [mg/m³] : 25
Monoxyde de carbone : TLV© -TWA [ppm] : 25

9 Propriétés physiques et chimiques

Etat physique à 20 °C	: Gaz.
Couleur	: Incolore.
Odeur	: Non détectable à l'odeur.
Masse moléculaire	: 28
Point de fusion [°C]	: -205
Point d'ébullition [°C]	: -192
Température critique [°C]	: -140
Pression de vapeur [20°C]	: Non applicable.
Densité relative, gaz (air=1)	: 1
Densité relative, liquide (eau=1)	: 0,79
Solubilité dans l'eau [mg/l]	: 30
Domaine d'inflammabilité [%vol dans l'air]	: 10,9 à 74
Température d'autoinflammation [°C]	: 620

10 Stabilité et réactivité

Produits de décomposition dangereux : Aucun(e).

Matières incompatibles : Peut former un mélange explosif avec l'air.
Peut réagir violemment avec les oxydants.
Air, Oxydant.

Conditions à éviter : Tenir à l'écart de la chaleur/des étincelles/des flammes nues/des surfaces chaudes. – Ne pas fumer.

Carbagas AIR LIQUIDE	FICHE DE DONNEES DE SECURITE	Page : 5 / 6 Edition révisée n° : 0 Date : 13 / 12 / 2010 : 0 / 0 / 0
Monoxyde de carbone		CG019

11 Informations toxicologiques

Informations toxicologiques : Destruction des globules rouges (poison hémolytique).
Inhalation (rat) CL50 [ppm/4h] : 1880

12 Informations écologiques

Information relative aux effets écologiques : Pas d'effet écologique connu causé par ce produit.
Potentiel de réchauffement global [CO2=1] : 1

13 Considérations relatives à l'élimination

Généralités : Eviter de rejeter à l'atmosphère.
Ne pas rejeter dans tout endroit où son accumulation pourrait être dangereuse.
Ne pas évacuer dans les endroits où il y a un risque de former un mélange explosif avec l'air. Le gaz rejeté doit être brûlé dans un brûleur approprié équipé d'un arrêt anti-retour de flamme.
Contacter le fournisseur si des instructions sont souhaitées.

14 Informations relatives au transport

Numéro ONU : 1016
• Etiquetage ADR, IMDG, IATA

: 2.1 : gaz inflammable.
2.3 : Gaz toxique.

Transport terrestre

ADR/RID
I.D. n° : 263
Nom d'expédition des Nations unies : MONOXYDE DE CARBONE COMPRIMÉ
Classe(s) de danger pour le transport : 2
- Code de classification ADR/RID : 1 TF
- Packing Instruction(s) - General : P200
- Tunnel Restriction : B/D : Transport en citerne: Passage interdit dans les tunnels des catégories B, C, D et E; Autre transport : Passage interdit dans les tunnels de catégorie D et E.

Transport par mer

- Code IMO-IMDG
• Désignation officielle pour le transport : MONOXYDE DE CARBONE COMPRIMÉ
• ADR : 2.3
- Groupe d'emballage IMO : P200

Carbagas AIR LIQUIDE	FICHE DE DONNEES DE SECURITE	Page : 6 / 6 Edition révisée n° : 0 Date : 13 / 12 / 2010 : 0 / 0 / 0
	Monoxyde de carbone	**CG019**

14 Informations relatives au transport (suite)

- **Emergency Schedule (EmS) - Fire** : F-D
- **Emergency Schedule (EmS) - Spillage** : S-U
- **Instructions - Packing** : P200

Transport aérien

- **ICAO/IATA**
- **Désignation officielle de transport** : CARBON MONOXIDE, COMPRESSED
- **ADR** : 2.3
- **IATA-Passenger and Cargo Aircraft** :
- **Cargo Aircraft only** :

Eviter le transport dans des véhicules dont le compartiment du chargement n'est pas séparé de la cabine de conduite.
S'assurer que le conducteur du véhicule connaît les dangers potentiels du chargement ainsi que les mesures à prendre en cas d'accident ou autres éventualités.
Avant de transporter les récipients :
- S'assurer que les récipients sont fermement arrimés.
- S'assurer que le robinet de bouteille est fermé et ne fuit pas.
- S'assurer que le bouchon de protection de sortie du robinet (quand il existe) est correctement mis en place.
- S'assurer que le dispositif de protection du robinet (quand il existe) est correctement mis en place.
- Assurer une ventilation convenable.
- Se conformer à la réglementation en vigueur.

15 Informations réglementaires

Restrictions : Réservé à l'usager professionnel.

Réglementations/législation particulières à la substance ou au mélange en matière de sécurité, de santé et d'environnement : S'assurer que toutes les réglementations nationales ou locales sont respectées.

Seveso regulation 96/82/EC : Listé

16 Autres informations

S'assurer que les opérateurs comprennent bien les risques d'inflammabilité.
Les utilisateurs d'appareils respiratoires doivent être formés.
S'assurer que les opérateurs comprennent bien le risque de toxicité.

Liste du texte complet des Phrases-R en section 3 : R12 : Extrêmement inflammable.
R23 : Toxique par inhalation.
R48/23 : Toxique : risque d'effets graves pour la santé en cas d'exposition prolongée par inhalation.
R61 : Risque pendant la grossesse d'effets néfastes pour l'enfant.

La présente Fiche de Données de Sécurité a été établie conformément aux Directives Européennes en vigueur et est applicable à tous les pays qui ont traduit les Directives dans leur droit national.

DENEGATION DE RESPONSABILITE : Malgré le soin apporté à sa rédaction, aucune responsabilité ne saurait être acceptée en cas de dommage ou d'accident résultant de son utilisation. Les informations données dans ce document sont considérées comme exactes au moment de son impression. Avant d'utiliser ce produit pour une expérience ou un procédé nouveaux, examiner attentivement la compatibilité et la sécurité du matériel mis en oeuvre.

Fin du document

Carbagas AG
HOFGUT CH-3073 GUEMLIGEN Switzerland

En cas d'urgence : Tel.: 031 950 50 50

Bibliography

[1] E. Rutherford, *The Scattering of α and β Particles by Matter and the Structure of the Atom*, Phil. Mag **21**, 669 (1911)

[2] I. Curie, F. Joliot, *Un noveau type de radioactivite*, Compt. Rend. Acad. Sci. **198**, 254 (1934)

[3] G.G. Adamian, N.V. Antonenko, A. Diaz-Torres, S. Heinz, *How to extend the chart of nuclides?*, The European Physical Journal A **56** (2020)

[4] M. Thoennessen, B. Sherrill, *From isotopes to the stars*, Nature **473**, 25 (2011)

[5] M. Thoennessen, *The Discovery of Isotopes* (Springer International Publishing, 2016)

[6] J. Erler, N. Birge, M. Kortelainen, W. Nazarewicz, E. Olsen, A.M. Perhac, M. Stoitsov, *The limits of the nuclear landscape*, Nature **486**, 509 (2012)

[7] M. Wang, G. Audi, F.G. Kondev, W. Huang, S. Naimi, X. Xu, *The AME2016 atomic mass evaluation (II). Tables, graphs and references*, Chinese Physics C **41**, 030003 (2017)

[8] E.C. Simpson, *Interactive nuclide chart*, [Online] `http://people.physics.anu.edu.au/~ecs103/chart/`, accessed 09.09.2020

[9] E.C. Simpson, M. Shelley, *Nuclear cartography: patterns in binding energies and sub-atomic structure*, Physics Education **52**, 064002 (2017)

[10] Y. Blumenfeld, T. Nilsson, P.V. Duppen, *Facilities and methods for radioactive ion beam production*, Physica Scripta **T152**, 014023 (2013)

[11] M. Borge, M. Kowalska, T. Stora, *Motivations to receive a 2 GeV proton beam at ISOLDE / HIE-ISOLDE: Impact on radioisotope beam availability and physics program*, Tech. rep., Geneva (2012), `http://cds.cern.ch/record/1482729`

[12] T. Stora, *Recent developments of target and ion sources to produce ISOL beams*, Nuclear Instruments and Methods in Physics Research Section B: Beam Interactions with Materials and Atoms **317**, 402 (2013)

[13] D.J. Morrissey, B.M. Sherrill, *In-Flight Separation of Projectile Fragments*, in *The Euroschool Lectures on Physics with Exotic Beams, Vol. I* (Springer Berlin Heidelberg, 2004), pp. 113–135

[14] H. Suzuki, T. Kubo, N. Fukuda, N. Inabe, D. Kameda, H. Takeda, K. Yoshida, K. Kusaka, Y. Yanagisawa, M. Ohtake et al., *Production cross section measurements*

of radioactive isotopes by BigRIPS separator at RIKEN RI Beam Factory, Nuclear Instruments and Methods in Physics Research Section B: Beam Interactions with Materials and Atoms **317**, 756 (2013)

[15] T. Kubo, M. Ishihara, N. Inabe, H. Kumagai, I. Tanihata, K. Yoshida, T. Nakamura, H. Okuno, S. Shimoura, K. Asahi, *The RIKEN radioactive beam facility*, Nuclear Instruments and Methods in Physics Research Section B: Beam Interactions with Materials and Atoms **70**, 309 (1992)

[16] T. Kubo, *In-flight RI beam separator BigRIPS at RIKEN and elsewhere in Japan*, Nuclear Instruments and Methods in Physics Research Section B: Beam Interactions with Materials and Atoms **204**, 97 (2003)

[17] H. Geissel, P. Armbruster, K. Behr, A. Brünle, K. Burkard, M. Chen, H. Folger, B. Franczak, H. Keller, O. Klepper et al., *The GSI projectile fragment separator (FRS): a versatile magnetic system for relativistic heavy ions*, Nuclear Instruments and Methods in Physics Research Section B: Beam Interactions with Materials and Atoms **70**, 286 (1992)

[18] R. Anne, A.C. Mueller, *LISE 3: a magnetic spectrometer—Wien filter combination for secondary radioactive beam production*, Nuclear Instruments and Methods in Physics Research Section B: Beam Interactions with Materials and Atoms **70**, 276 (1992)

[19] M. Winkler, H. Geissel, H. Weick, B. Achenbach, K.H. Behr, D. Boutin, A. Brünle, M. Gleim, W. Hüller, C. Karagiannis et al., *The status of the Super-FRS in-flight facility at FAIR*, Nuclear Instruments and Methods in Physics Research Section B: Beam Interactions with Materials and Atoms **266**, 4183 (2008)

[20] H. Geissel, H. Weick, M. Winkler, G. Münzenberg, V. Chichkine, M. Yavor, T. Aumann, K. Behr, M. Böhmer, A. Brünle et al., *The Super-FRS project at GSI*, Nuclear Instruments and Methods in Physics Research Section B: Beam Interactions with Materials and Atoms **204**, 71 (2003)

[21] M.V. Ricciardi, S. Lukić, A. Kelić, K.H. Schmidt, M. Veselsky, *Secondary-beam production: Protons versus heavy ions*, The European Physical Journal Special Topics **150**, 321 (2007)

[22] O. Kofoed-Hansen, K. Nielsen, *Measurements on shortlived radioactive krypton isotopes from fission after isotopic separation*, Dan. Mat.Fys.Medd **26**, no. 7 (1951)

[23] J. Koch, O. Kofoed-Hansen, P. Kristensen, W. Drost-Hansen, *Measurements on Ratioactive Krypton Isotopes from Fission after Mass-Spectrographic Separation*, Physical Review **76**, 279 (1949)

[24] H.L. Ravn, B.W. Allardyce, *On-line mass separators*, in *Treatise on heavy ion science* (Springer, 1989), pp. 363–439

[25] R. Catherall, W. Andreazza, M. Breitenfeldt, A. Dorsival, G.J. Focker, T.P. Gharsa, G.T. J, J.L. Grenard, F. Locci, P. Martins et al., *The ISOLDE facility*, Journal of Physics G: Nuclear and Particle Physics **44**, 094002 (2017)

[26] M.J.G. Borge, B. Jonson, *ISOLDE past, present and future*, Journal of Physics G: Nuclear and Particle Physics **44**, 044011 (2017)

[27] W. Mittig, *The spiral project at GANIL and future opportunities*, Journal of Physics G: Nuclear and Particle Physics **24**, 1331 (1998)

[28] A.C.C. Villari, F.L. Pellemoine, C. Barué, G. Gaubert, S. Gibouin, Y. Huguet, P. Jardin, S.K. Rody, N. Lecesne, R. Leroy et al., *RNB production at SPIRAL/GANIL*, AIP Conference Proceedings **576**, 254 (2001), https://aip.scitation.org/doi/pdf/10.1063/1.1395297

[29] F. Azaiez, S. Essabaa, F. Ibrahim, D. Verney, *The ALTO Facility in Orsay*, Nuclear Physics News **23**, 5 (2013)

[30] S. Essabaa, J. Arianer, P. Ausset, O. Bajeat, J. Baronick, F. Clapier, L. Coacolo, C. Donzaud, M. Ducourtieux, S. Galès et al., *Photo-fission for the production of radioactive beams ALTO project*, Nuclear Instruments and Methods in Physics Research Section B: Beam Interactions with Materials and Atoms **204**, 780 (2003)

[31] R. Catherall, J. Lettry, S. Gilardoni, U. Köster, *Radioactive ion beams produced by neutron-induced fission at ISOLDE*, Nuclear Instruments and Methods in Physics Research Section B: Beam Interactions with Materials and Atoms **204**, 235 (2003)

[32] J. Ballof, J. Ramos, A. Molander, K. Johnston, S. Rothe, T. Stora, Ch.E. Düllmann, *The upgraded ISOLDE yield database – A new tool to predict beam intensities*, Nuclear Instruments and Methods in Physics Research Section B: Beam Interactions with Materials and Atoms **463**, 211 (2020)

[33] O. Bajeat, P. Delahaye, C. Couratin, M. Dubois, H. Franberg-Delahaye, J. Henares, Y. Huguet, P. Jardin, N. Lecesne, P. Lecomte et al., *Development of target ion source systems for radioactive beams at GANIL*, Nuclear Instruments and Methods in Physics Research Section B: Beam Interactions with Materials and Atoms **317**, 411 (2013)

[34] P. Chauveau, P. Delahaye, M. Babo, H. Bouzomita, O. Bajeat, M. Dubois, R. Frigot, G. Grinyer, J. Grinyer, P. Jardin et al., *A new FEBIAD-type ion source for the upgrade of SPIRAL1 at GANIL*, Nuclear Instruments and Methods in Physics Research Section B: Beam Interactions with Materials and Atoms **376**, 35 (2016)

[35] P. Delahaye, M. Dubois, L. Maunoury, A. Annaluru, J. Angot, O. Bajeat, B. Blank, J. Cam, P. Chauveau, R. Frigot et al., *New exotic beams from the SPIRAL 1 upgrade*, Nuclear Instruments and Methods in Physics Research Section B: Beam Interactions with Materials and Atoms (2019)

[36] P. Jardin, O. Bajeat, C. Couratin, P. Delahaye, M. Dubois, C. Feierstein, F. Pellemoine, P. Lecomte, P. Lehérissier, L. Maunoury et al., *Status of the SPIRAL I upgrade at GANIL*, Review of Scientific Instruments **83**, 02A911 (2012)

[37] V. Kuchi, P. Jardin, C. Michel, L. Maunoury, M. Dubois, P. Delahaye, O. Bajeat, S. Hormigos, V. Métayer, M. MacCormick et al., *High efficiency ISOL system to produce neutron deficient short-lived alkali RIBs on GANIL/SPIRAL 1 facility*, Nuclear Instruments and Methods in Physics Research Section B: Beam Interactions with Materials and Atoms **463**, 163 (2020)

[38] R. Klapisch, R. Bernas, *The detection of the short-lived lithium isotopes 8Li and 9Li by preliminary experiments with an on-line mass spectrometer*, Nuclear Instruments and Methods **38**, 291 (1965)

[39] M.C. Mhamed, C. Lau, S. Essabaa, *Two-dimensional/three-dimensional simulations for the optimization of an electron-beam-generated-plasma-based-type ion source*, Review of Scientific Instruments **79**, 02B911 (2008)

[40] J. Dilling, R. Krücken, L. Merminga, *ISAC and ARIEL: the TRIUMF radioactive beam facilities and the scientific program* (Springer, 2014)

[41] G. Prete, A. Andrighetto, J. Esposito, P. Mastinu, J. Wyss, *The SPES project: a second generation ISOL facility*, Physics Procedia **26**, 274 (2012)

[42] A.A. Prof., D.B. Dr., M.D. Dr., R.F. Dr., L.P. Dr., M.S. Dr., A.S. Dr., den Eynde Prof., D.V. Dr., *Myrrha accelerator driven system programme: recent progress and perspectives*, Izvestiya Wysshikh Uchebnykh Zawedeniy, Yadernaya Energetika **2019**, 29 (2019)

[43] H.J. Woo, B.H. Kang, K. Tshoo, C.S. Seo, W. Hwang, Y.H. Park, J.W. Yoon, S.H. Yoo, Y.K. Kim, D.Y. Jang, *Overview of the ISOL facility for the RISP*, Journal of the Korean Physical Society **66**, 443 (2015)

[44] J. Äystö, *Development and applications of the IGISOL technique*, Nuclear Physics A **693**, 477 (2001)

[45] G. Savard, A. Levand, B. Zabransky, *The CARIBU gas catcher*, Nuclear Instruments and Methods in Physics Research Section B: Beam Interactions with Materials and Atoms **376**, 246 (2016)

[46] J. Äystö, T. Eronen, A. Jokinen, A. Kankainen, I.D. Moore, H. Penttilä, eds., *Three decades of research using IGISOL technique at the University of Jyväskylä* (Springer Netherlands, 2014)

[47] I. Moore, T. Eronen, D. Gorelov, J. Hakala, A. Jokinen, A. Kankainen, V. Kolhinen, J. Koponen, H. Penttilä, I. Pohjalainen et al., *Towards commissioning the new IGISOL-4 facility*, Nuclear Instruments and Methods in Physics Research Section B: Beam Interactions with Materials and Atoms **317**, 208 (2013)

[48] D. Gorelov, H. Penttilä, A. Al-Adili, T. Eronen, J. Hakala, A. Jokinen, A. Kankainen, V. Kolhinen, J. Koponen, M. Lantz et al., *Developments for neutron-induced fission at IGISOL-4*, Nuclear Instruments and Methods in Physics Research Section B: Beam Interactions with Materials and Atoms **376**, 46 (2016)

[49] K. Peräjärvi, J. Cerny, J. Hakala, J. Huikari, A. Jokinen, P. Karvonen, J. Kurpeta, D. Lee, I. Moore, H. Penttilä et al., *New ion-guide for the production of beams of neutron-rich nuclei between Z=20–28*, Nuclear Instruments and Methods in Physics Research Section A: Accelerators, Spectrometers, Detectors and Associated Equipment **546**, 418 (2005)

[50] P. Karvonen, I. Moore, T. Sonoda, T. Kessler, H. Penttilä, K. Peräjärvi, P. Ronkanen, J. Äystö, *A sextupole ion beam guide to improve the efficiency and beam quality at IGISOL*, Nuclear Instruments and Methods in Physics Research Section B: Beam Interactions with Materials and Atoms **266**, 4794 (2008)

[51] P. Hansen, *The SC: Isolde and Nuclear Structure*, in *History of CERN*, edited by J. Krige (1996), Vol. 3, p. 327

[52] B. Jonson, A. Richter, *More than three decades of ISOLDE physics*, **129**, 1 (2000)

[53] E. Kugler, D. Fiander, B. Johnson, H. Haas, A. Przewloka, H. Ravn, D. Simon, K. Zimmer, *The new CERN-ISOLDE on-line mass-separator facility at the PS-Booster*, Nuclear Instruments and Methods in Physics Research Section B: Beam Interactions with Materials and Atoms **70**, 41 (1992)

[54] M. Turrión, M. Eller, R. Catherall, L.M. Fraile, U. Herman-Izycka, U. Köster, J. Lettry, K. Riisager, T. Stora, *Management of ISOLDE yields*, Nuclear Instruments and Methods in Physics Research Section B: Beam Interactions with Materials and Atoms **266**, 4674 (2008)

[55] R. dos Santos Augusto, L. Buehler, Z. Lawson, S. Marzari, M. Stachura, T. Stora, C.M. collaboration, *CERN-MEDICIS (Medical Isotopes Collected from ISOLDE): A New Facility*, Applied Sciences **4**, 265 (2014)

[56] J. Cruikshank, S. Marzari, L. Lambert, K. Chrysalidis, S. Wilkins, S. Rothe, V. Samothrakis, J. Ballof, R. Heinke, D. Leimbach et al., *ISOLDE Facility Upgrades and Developments*, in *ISOLDE Newsletter 2020* (2020), p. 7, `https://isolde.web.cern.ch/sites/isolde.web.cern.ch/files/ISOLDE%20Newsletter%202020.pdf`

[57] J. Ramos, *Thick solid targets for the production and online release of radioisotopes: The importance of the material characteristics – A review*, Nuclear Instruments and Methods in Physics Research Section B: Beam Interactions with Materials and Atoms **463**, 201 (2020)

[58] A. Gottberg, *Target materials for exotic ISOL beams*, Nuclear Instruments and Methods in Physics Research Section B: Beam Interactions with Materials and Atoms **376**, 8 (2016)

[59] U. Köster, *ISOLDE target and ion source chemistry*, Radiochimica Acta **89** (2001)

[60] G. Alton, Y. Zhang, Y. Kawai, *Prescriptions for optimizing intensities of short-lived RIBs at ISOL based research facilities*, Applied Radiation and Isotopes **64**, 1574 (2006)

[61] E. Aitken, *Some Comments Regarding Sintering Characteristics in a Radiation Environment*, in *Symposium on Radiation Effects in Refractory Fuel Compounds* (ASTM International, 1962)

[62] J. Lettry, R. Catherall, G. Cyvoct, P. Drumm, A. Evensen, M. Lindroos, O. Jonsson, E. Kugler, J. Obert, J. Putaux et al., *Release from ISOLDE molten metal targets under pulsed proton beam conditions*, Nuclear Instruments and Methods in Physics Research Section B: Beam Interactions with Materials and Atoms **126**, 170 (1997), international Conference on Electromagnetic Isotope Separators and Techniques Related to Their Applications

[63] H. Ravn, S. Sundell, L. Westgaard, *Target Techniques for the isolde on-line isotope separator*, Nuclear Instruments and Methods **123**, 131 (1975)

[64] M. Delonca, Ph.D. thesis, *Development of new target concepts for proton beams at CERN/ISOLDE.* (2015), presented 14 Dec 2015, https://cds.cern.ch/record/2230047

[65] F.B. Pamies, T. Stora, E. Barbero, V. Barozier, A. Bernardes, R. Catherall, B.C. Fernandez, B. Crepieux, M. Delonca, M. Dierckx et al., *The LIEBE high-power target: Offline commissioning results and prospects for the production of 100Sn ISOL beams at HIE-ISOLDE*, Nuclear Instruments and Methods in Physics Research Section B: Beam Interactions with Materials and Atoms **463**, 128 (2020)

[66] D. Houngbo, A. Bernardes, J. David, M. Delonca, K. Kravalis, S. Lahiri, R. Losito, C. Maglioni, A. Marchix, T. Mendonca et al., *Development of a liquid Pb-Bi target for high-power ISOL facilities*, Nuclear Instruments and Methods in Physics Research Section B: Beam Interactions with Materials and Atoms **376**, 57 (2016)

[67] U. Köster, U.C. Bergmann, D. Carminati, R. Catherall, J. Cederkäll, J.G. Correia, B. Crepieux, M. Dietrich, K. Elder, V.N. Fedoseyev et al., *Oxide fiber targets at ISOLDE*, Nuclear Instruments and Methods in Physics Research Section B: Beam Interactions with Materials and Atoms **204**, 303 (2003)

[68] J. Ramos, A. Gottberg, T. Mendonça, Ch. Seiffert, A. Senos, H. Fynbo, O. Tengblad, J. Briz, M. Lund, G. Koldste et al., *Intense 31–35Ar beams produced with a nanostructured CaO target at ISOLDE*, Nuclear Instruments and Methods in Physics Research Section B: Beam Interactions with Materials and Atoms **320**, 83 (2014)

[69] J. Ramos, A. Gottberg, R. Augusto, T. Mendonca, K. Riisager, Ch. Seiffert, P. Bowen, A. Senos, T. Stora, *Target nanomaterials at CERN-ISOLDE: synthesis and release data*, Nuclear Instruments and Methods in Physics Research Section B: Beam Interactions with Materials and Atoms **376**, 81 (2016), proceedings of the XVIIth International Conference on Electromagnetic Isotope Separators and Related Topics (EMIS2015), Grand Rapids, MI, U.S.A., 11-15 May 2015

[70] M.N. Rahaman, *Ceramic processing and sintering* (CRC press, 2003)

[71] M. Dombsky, J.M. D'Auria, *Zeolite target development at TISOL*, AIP Conference Proceedings **392**, 365 (1997), https://aip.scitation.org/doi/pdf/10.1063/1.52482

[72] M. Dombsky, L. Buchmann, J. D'Auria, P. McNeely, G. Roy, H. Sprenger, J. Vincent, *Targets and ion sources at the TISOL facility*, Nuclear Instruments and Methods in Physics Research Section B: Beam Interactions with Materials and Atoms **70**, 125 (1992)

[73] S. Fernandes, Ph.D. thesis, *Submicro and Nano Structured Porous Materials for the Production of High-Intensity Exotic Radioactive Ion Beams*, École Polytechnique féd'erale de Lausanne (2010), http://cds.cern.ch/record/1312950

[74] J.P. Ramos, Ph.D. thesis, *Titanium carbide-carbon porous nanocomposite materials for radioactive ion beam production: processing, sintering and isotope release properties*, École Polytechnique féd'erale de Lausanne (2017), http://cds.cern.ch/record/2243566

[75] Ch. Seiffert, Ph.D. thesis, *Production of radioactive molecular beams for CERN-ISOLDE*, Technische Universität Darmstadt (2014), http://cds.cern.ch/record/2064456

[76] B. Wolf, *Handbook of Ion Sources* (CRC Press, 2017)

[77] I. Langmuir, K.H. Kingdon, E. Rutherford, *Thermionic effects caused by vapours of alkali metals*, Proceedings of the Royal Society of London. Series A, Containing Papers of a Mathematical and Physical Character **107**, 61 (1925)

[78] J.B. Taylor, I. Langmuir, *The evaporation of atoms, ions and electrons from caesium films on tungsten*, Physical Review **44**, 423 (1933)

[79] R. Kirchner, *On the thermoionization in hot cavities*, Nuclear Instruments and Methods in Physics Research Section A: Accelerators, Spectrometers, Detectors and Associated Equipment **292**, 203 (1990)

[80] T.K. Sato, M. Asai, A. Borschevsky, T. Stora, N. Sato, Y. Kaneya, K. Tsukada, C.E. Düllmann, K. Eberhardt, E. Eliav et al., *Measurement of the first ionization potential of lawrencium, element 103*, Nature **520**, 209 (2015)

[81] J. Rumble, ed., *CRC Handbook of Chemistry and Physics* (Taylor & Francis, 2020), ISBN 0367417243

[82] R. Kirchner, *Release studies of elementary and metal-fluoride ions at the GSI on-line mass separator*, Nuclear Instruments and Methods in Physics Research Section B: Beam Interactions with Materials and Atoms **126**, 135 (1997), international Conference on Electromagnetic Isotope Separators and Techniques Related to Their Applications

[83] V. Fedosseev, K. Chrysalidis, T. Day Goodacre, B. Marsh, S. Rothe, r. Seiffert, K. Wendt, *Ion beam production and study of radioactive isotopes with the laser ion source at ISOLDE*, Journal of Physics G: Nuclear and Particle Physics **44**, 084006 (2017)

[84] S. Kuhn, *Determination of axial steady-state potential distributions in collisionless single-ended Q-machines*, Plasma Physics **21**, 613 (1979)

[85] M. Huyse, *Ionization in a hot cavity*, Nuclear Instruments and Methods in Physics Research **215**, 1 (1983)

[86] V.N. Panteleev, A.E. Barzakh, D.V. Fedorov, A.M. Ionan, V.S. Ivanov, F.V. Moroz, S.Y. Orlov, Y.M. Volkov, *Enhancement of ionization efficiency of surface, electron bombardment and laser ion sources by axial magnetic field application*, Review of Scientific Instruments **75**, 1585 (2004)

[87] *RILIS elements*, [Online] http://riliselements.web.cern.ch/, accessed 02.10.2020

[88] D. Fink, S. Richter, B. Bastin, K. Blaum, R. Catherall, T. Cocolios, D. Fedorov, V. Fedosseev, K. Flanagan, L. Ghys et al., *First application of the Laser Ion Source and Trap (LIST) for on-line experiments at ISOLDE*, Nuclear Instruments and Methods in Physics Research Section B: Beam Interactions with Materials and Atoms **317**, 417 (2013)

[89] R. Kirchner, E. Roeckl, *Investigation of gaseous discharge ion sources for isotope separation on-line*, Nuclear Instruments and Methods **133**, 187 (1976)

[90] O. Almén, K. Nielsen, *Systematic investigation of a magnetic ion source for an electromagnetic isotope separator*, Nuclear Instruments **1**, 302 (1957)

[91] R. Kirchner, E. Roeckl, *Investigation of small-volume gaseous discharge ion sources for isotope separation on-line*, Nuclear Instruments and Methods **131**, 371 (1975)

[92] S. Sundell, H. Ravn, *Ion source with combined cathode and transfer line heating*, Nuclear Instruments and Methods in Physics Research Section B: Beam Interactions with Materials and Atoms **70**, 160 (1992)

[93] L. Penescu, R. Catherall, J. Lettry, T. Stora, *Development of high efficiency Versatile Arc Discharge Ion Source at CERN ISOLDE*, Review of Scientific Instruments **81**, 02A906 (2010)

[94] Y. Martinez Palenzuela, T.E. Cocolios, P. Van Duppen, T. Stora, Ph.D. thesis, *Characterization and optimization of a versatile laser and electron-impact ion source for radioactive ion beam production at ISOLDE and MEDICIS.*, KU Leuven, Arenberg Doctoral School (2019), presented 26 Apr 2019, `https://cds.cern.ch/record/2672954`

[95] Y. Martinez Palenzuela, B.A. Marsh, J. Ballof, R. Catherall, K. Chrysalidis, T.E. Cocolios, B. Crepieux, T. Day Goodacre, V.N. Fedosseev, M.H. Huyse et al., *Enhancing the extraction of laser-ionized beams from an arc discharge ion source volume*, Nuclear Instruments and Methods in Physics Research Section B: Beam Interactions with Materials and Atoms **431**, 59 (2018)

[96] T. Day Goodacre, J. Billowes, R. Catherall, T.E. Cocolios, B. Crepieux, D.V. Fedorov, V.N. Fedosseev, L.P. Gaffney, T. Giles, A. Gottberg et al., *Blurring the boundaries between ion sources: The application of the RILIS inside a FEBIAD type ion source at ISOLDE*, Nuclear Instruments and Methods in Physics Research Section B: Beam Interactions with Materials and Atoms **376**, 39 (2016)

[97] R. Eder, H. Grawe, E. Hagebø, P. Hoff, E. Kugler, H. Ravn, K. Steffensen, *The production yields of radioactive ion-beams from fluorinated targets at the ISOLDE online mass separator*, Nuclear Instruments and Methods in Physics Research Section B: Beam Interactions with Materials and Atoms **62**, 535 (1992)

[98] A. Kronenberg, E. Spejewski, H. Carter, B. Mervin, C. Jost, D. Stracener, S. Lapi, T. Bray, *Molecular sidebands of refractory elements for ISOL*, Nuclear Instruments and Methods in Physics Research Section B: Beam Interactions with Materials and Atoms **266**, 4252 (2008)

[99] R. Kirchner, O. Klepper, D. Marx, G.E. Rathke, B. Sherrill, *An ion source with storage capability for bunched beam release and controlled chemical separation*, Nuclear Instruments and Methods in Physics Research Section A: Accelerators, Spectrometers, Detectors and Associated Equipment **247**, 265 (1986)

[100] R. Kirchner, *An ion source with bunched beam release*, Nuclear Instruments and Methods in Physics Research Section B: Beam Interactions with Materials and Atoms **26**, 204 (1987)

[101] N. Lecesne, *On-line ECR ion sources: Present and future*, Nuclear Instruments and Methods in Physics Research Section B: Beam Interactions with Materials and Atoms **266**, 4338 (2008)

[102] F. Wenander, W. Farabolini, G. Gaubert, P. Jardin, J. Lettry, *First ECR-ionized noble gas radioisotopes at ISOLDE*, Nuclear Physics A **746**, 659 (2004)

[103] H. Franberg, Ph.D. thesis, *Production of exotic, short lived carbon isotopes in ISOL-type facilities*, Bern U. (2008), https://cds.cern.ch/record/1136904

[104] P. Jardin, W. Farabolini, G. Gaubert, J. Pacquet, T. Drobert, J. Cornell, C. Barue, C. Canet, M. Dupuis, J.L. Flambard et al., *Optimization of ECR singly-charged ion sources for the radioactive ion beam production*, Nuclear Instruments and Methods in Physics Research Section B: Beam Interactions with Materials and Atoms **204**, 377 (2003)

[105] G. Gaubert, C. Baru, C. Canet, J. Cornell, M. Dupuis, W. Farabolini, J.L. Flambard, P. Gorel, P. Jardin, N. Lecesne et al., *Minimono: An ultracompact permanent magnet ion source for singly charged ions*, Review of Scientific Instruments **74**, 956 (2003)

[106] J.Y. Pacquet, R. Leroy, Patent, *Magnetic system, particularly for ECR sources, for producing closed surfaces of equimodule B of form dimensions*, US 6194836B1 (2001)

[107] F. Wenander, J.L. and, *MECRIS: A compact ECRIS for ionization of noble gas radioisotopes at ISOLDE*, Review of Scientific Instruments **75**, 1627 (2004)

[108] P. Sortais, T. Lamy, J. Médard, J. Angot, L. Latrasse, T. Thuillier, *Ultracompact/ultralow power electron cyclotron resonance ion source for multipurpose applications*, Review of Scientific Instruments **81**, 02B314 (2010)

[109] P. Suominen, T. Stora, P. Sortais, J. Médard, *Ionization efficiency of a COMIC ion source equipped with a quartz plasma chamber*, in *XIXth International Workshop on ECR Ion Sources (ECRIS 2010)* (2010), p. MOPOT006

[110] P. Sortais, T. Lamy, Patent, *Low-power Gaseous Plasma Source*, PCT/FR2009/051986 (2020)

[111] B. deB. Darwent, *Bond dissociation energies in simple molecules*, Tech. rep., National Standard Reference Data System (1970), NSRDS-NBS 31

[112] S.G. Lias, *Ionization Energy Evaluation*, in *NIST Chemistry WebBook, NIST Standard Reference Database Number 69*, edited by E.P. Linstrom, W. Mallard (2020)

[113] P. Suominen, *Plasma ion sources for 1+ molecular radioactive ion beams*, ARIS 2011, Leuven, Belgium

[114] M. Kronberger, A. Gottberg, T. Mendonca, J. Ramos, C. Seiffert, P. Suominen, T. Stora, *Production of molecular sideband radioisotope beams at CERN-ISOLDE using a Helicon-type plasma ion source*, Nuclear Instruments and Methods in Physics Research Section B: Beam Interactions with Materials and Atoms **317**, 438 (2013)

[115] P. Suominen, T. Stora, *Target and Ion Source Development*, in *ISOLDE Newsletter 2011* (2011), p. 20, https://isolde.web.cern.ch/sites/isolde.web.cern.ch/files/April%202011.pdf

[116] T. Bjørnstad, E. Hagebø, P. Hoff, O.C. Jonsson, E. Kugler, H.L. Ravn, S. Sundell, B. Vosicki, the ISOLDE Collaboration, *Methods for Production of Intense Beams of Unstable Nuclei: New Developments at ISOLDE*, Physica Scripta **34**, 578 (1986)

[117] E. Bouquerel, R. Catherall, M. Eller, J. Lettry, S. Marzari, T. Stora, I. Collaboration, *Purification of a Zn radioactive ion beam by alkali suppression in a quartz line target prototype*, The European Physical Journal Special Topics **150**, 277 (2007)

[118] E.J.A. Bouquerel, Ph.D. thesis, *Atomic Beam Merging and Suppression of Alkali Contaminants in Multi Body High Power Targets: Design and Test of Target and Ion Source Prototypes at ISOLDE* (2009), presented on 10 Dec 2009, http://cds.cern.ch/record/1259908

[119] J. Lettry, R. Catherall, P. Drumm, A. Evensen, O.C. Jonsson, E. Kugler, J. Obert, J.C. Puteaux, J.S.M. Toule-monde, *Experience with ISOLDE molten metal targets at the CERN PS-Booster*, in *13th Meeting of the International Collaboration on Advanced Neutron Sources* (1995), http://www.neutronresearch.com/parch/1995/01/199501005950.pdf

[120] G. Friedlander, J.W. Kennedy, E.S. Macias, J.M. Miller, *Nuclear and Radiochemistry* (John Wiley & Sons, 1981), ISBN 047186255X

[121] A. Ferrari, P.R. Sala, *The Physics of High Energy Reactions*, in *Proceedings of the Workshop on Nuclear Reaction Data and Nuclear Reaction Physics, Design and Safety* (World Scientific, 1998), Vol. 2, pp. 424–532

[122] F.G. Detlef Filges, *Handbook of Spallation Research* (Wiley VCH Verlag GmbH, 2009), ISBN 3527407146

[123] J.C. David, *Spallation reactions: A successful interplay between modeling and applications*, The European Physical Journal A **51** (2015)

[124] J. Klimo, J.P. Ramos, J. Ballof, T. Stora, *Simulations of production cross section of isotopes produced in spallation reaction using ABRABLA07 code*, Tech. rep. (2016), (unpublished)

[125] *Iaea benchmark of spallation models*, [Online] https://www-nds.iaea.org/spallations/, accessed 07.11.2020

[126] M. Ricciardi, A. Kelic, K.H. Schmidt, *Results obtained with ABLA07*, Tech. rep. (2009), http://cds.cern.ch/record/1355323

[127] A. Kelic, M.V. Ricciardi, K.H. Schmidt, *ABLA07 - towards a complete description of the decay channels of a nuclear system from spontaneous fission to multifragmentation*, in *Proceedings of the Advanced Workshop on Model Codes for Spallation Reactions, ICTP Trieste, Italy, 4-8 February 2008*, edited by D. Filges, S. Leray, Y. Yariv, A. Mengoni, A. Stanculescu, G. Mank (IAEA, 2009), pp. 181–221, INDC(NDS)-530, https://www-nds.iaea.org/publications/indc/indc-nds-0530/

[128] T.T. Böhlen, F. Cerutti, M.P.W. Chin, A. Fassò, A. Ferrari, P.G. Ortega, A. Mairani, P.R. Sala, G. Smirnov, V. Vlachoudis, *The FLUKA Code: Developments and Challenges for High Energy and Medical Applications*, Nuclear Data Sheets **120**, 211 (2014)

[129] A. Ferrari, P.R. Sala, A. Fassò, J. Ranft, *FLUKA: A multi-particle transport code* , CERN Yellow Reports: Monographs (CERN, Geneva, 2005), http://cds.cern.ch/record/898301

[130] J.J. Gaimard, K.H. Schmidt, *A reexamination of the abrasion-ablation model for the description of the nuclear fragmentation reaction*, Nuclear Physics A **531**, 709 (1991)

[131] J. Benlliure, A. Junghans, B. Jurado, M.V. Ricciardi, K.H. Schmidt, *Calculated fission-product yields from collisions of ^{238}U with protons and heavy ions*, in *GSI Scientific Report 1999* (Gesellschaft für Schwerionenforschung mbH Darmstadt, 2000), http://repository.gsi.de/record/53532/files/GSI-Report-2000-1.pdf

[132] M.V. Ricciardi, P. Armbruster, J. Benlliure, M. Bernas, A. Boudard, S. Czajkowski, T. Enqvist, A. Kelić, S. Leray, R. Legrain et al., *Light nuclides produced in the proton-induced spallation ofU238at 1 GeV*, Physical Review C **73** (2006)

[133] S. Lukić, F. Gevaert, A. Kelić, M. Ricciardi, K.H. Schmidt, O. Yordanov, *Systematic comparison of ISOLDE-SC yields with calculated in-target production rates*, Nuclear Instruments and Methods in Physics Research Section A: Accelerators, Spectrometers, Detectors and Associated Equipment **565**, 784 (2006)

[134] A. Heikkinen, P. Kaitaniemi, A. Boudard, *Implementation of INCL cascade and ABLA evaporation codes in Geant4*, Journal of Physics: Conference Series **119**, 032024 (2008)

[135] F. Cerutti, A. Ferrari, A. Mairani, P.R. Sala, *New developments in FLUKA*, in *Proceedings of the 13th international conference on nuclear reaction mechanisms*, edited by F. Cerutti, M. Chadwick, A. Ferrari, T. Kawano, S. Bottoni, L. Pellegri (CERN, 2012), p. 469, https://cds.cern.ch/record/1537387

[136] F. Ballarini, G. Battistoni, F. Cerutti, A. Empl, A. Fassò, A. Ferrari, E. Gadioli, M.V. Garzelli, A. Ottolenghi, L.S. Pinsky et al., *Nuclear Models in FLUKA: Present Capabilities, Open Problems, and Future Improvements*, AIP Conference Proceedings **769**, 1197 (2005), https://aip.scitation.org/doi/pdf/10.1063/1.1945222

[137] G. Battistoni, J. Bauer, T.T. Boehlen, F. Cerutti, M.P.W. Chin, R.D.S. Augusto, A. Ferrari, P.G. Ortega, W. Kozłowska, G. Magro et al., *The FLUKA Code: An Accurate Simulation Tool for Particle Therapy*, Frontiers in Oncology **6** (2016)

[138] G. Battistoni, F. Cerutti, A. Fassò, A. Ferrari, S. Muraro, J. Ranft, S. Roesler, P.R. Sala, *The FLUKA code: description and benchmarking*, AIP Conference Proceedings **896**, 31 (2007), https://aip.scitation.org/doi/pdf/10.1063/1.2720455

[139] A. Fasso, A. Ferrari, S. Roesler, P. Sala, F. Ballarini, A. Ottolenghi, G. Battistoni, F. Cerutti, E. Gadioli, M. Garzelli et al., *The physics models of FLUKA: status and recent development.* , in *Conference for Computing in High-Energy and Nuclear Physics* (2003), Vol. C0303241, p. 10, https://cds.cern.ch/record/625976

[140] R.M. dos Santos Augusto, Ph.D. thesis, *On the feasibility of using radioactive ion beams in hadrontherapy: dosimetric and imaging studies*, Lud-

wig–Maximilians–Universität München (2018), presented 11 Jul 2018, http://cds.cern.ch/record/2637861

[141] R. Luis, J.G. Marques, T. Stora, P. Vaz, L. Zanini, *Optimization studies of the CERN-ISOLDE neutron converter and fission target system*, The European Physical Journal A **48** (2012)

[142] T. Stora, E. Noah, R. Hodak, T.Y. Hirsh, M. Hass, V. Kumar, K. Singh, S. Vaintraub, P. Delahaye, H. Franberg-Delahaye et al., *A high intensity 6 He beam for the β-beam neutrino oscillation facility*, EPL (Europhysics Letters) **98**, 32001 (2012)

[143] J.F. Ziegler, J.P. Biersack, M.D. Ziegler, *SRIM: the stopping and range of ions in matter* (Cadence Design Systems, Raleigh, NC, 2008), http://cds.cern.ch/record/1525729

[144] P. Sigmund, *Particle Penetration and Radiation Effects*, *General Aspects and Stopping of Swift Point Charges*, Vol. 1 (Springer Berlin Heidelberg, 2006), ISBN 978-3-540-31713-5

[145] P. Sigmund, *Particle Penetration and Radiation Effects*, *Penetration of Atomic and Molecular Ions* (Springer International Publishing, 2014), ISBN 978-3-319-05563-3

[146] P. Sigmund, *Stopping Power: Wrong Terminology*, in *ICRU News 2000* (International Commission on Radiation Units & Measurements, 2000), https://www.icru.org/images/pdf/n_001_4.pdf

[147] N. Bohr, *II. On the theory of the decrease of velocity of moving electrified particles on passing through matter*, The London, Edinburgh, and Dublin Philosophical Magazine and Journal of Science **25**, 10 (1913)

[148] J.F. Ziegler, *SRIM2013 - the stopping and range of ions in matter*, [Online] http://www.srim.org/, accessed 12.11.2020

[149] S.M. Seltzer, D.T. Bartlett, D.T. Burns, G. Dietze, H.G. Menzel, H.G. Paretzke, A. Wambersie, *Fundamental Quantities and Units for Ionizing Radiation (revised)*, Journal of the ICRU **11** (2011)

[150] J.F. Ziegler, *Stopping of energetic light ions in elemental matter*, Journal of Applied Physics **85**, 1249 (1999)

[151] M. Fujioka, Y. Arai, *Diffusion of radioisotopes from solids in the form of foils, fibers and particles*, Nuclear Instruments and Methods in Physics Research **186**, 409 (1981)

[152] H. Fechtig, S. Kalbitzer, *The Diffusion of Argon in Potassium-Bearing Solids*, in *Potassium Argon Dating* (Springer Berlin Heidelberg, Berlin, Heidelberg, 1966), pp. 68–107, ISBN 978-3-642-87895-4, https://doi.org/10.1007/978-3-642-87895-4_4

[153] M. Santana-Leitner, Ph.D. thesis, *A Monte Carlo code to optimize the production of Radioactive Ion Beams by the ISOL technique*, Technical University of Catalonia (2005), presented 29 Jul 2005, http://cds.cern.ch/record/905537

[154] J. Frenkel, *Theorie der Adsorption und verwandter Erscheinungen*, Zeitschrift für Physik **26**, 117 (1924)

[155] I. Zvára, *The Inorganic Radiochemistry of Heavy Elements* (Springer Netherlands, 2008)

[156] B. Eichler, *Das Flüchtigkeitsverhalten von Transactiniden im Bereich um Z = 114 (Vorhersage)*, Kernchemie **19**, 307 (1976)

[157] B. Eichler, H. Roßbach, *Adsorption of Volatile Metals on Metal Surfaces and its Application in Nuclear Chemistry*, Radiochimica Acta **33** (1983)

[158] H. Roßbach, B. Eichler, *Adsorption von Metallen auf metallischen Oberflächen und Möglichkeiten ihrer Nutzung in der Kernchemie - Ermittlung von Adsorptionsenthalpien mit dem Rechenprogramm AMO*, Report ZfK-527, Zentralinstitut für Kernforschung Rossendorf bei Dresden (1984)

[159] B. Eichler, S. Hübener, H. Roßbach, *Adsorption flüchtiger Metalle auf metallischen Oberflächen und ihre Anwendung in der Kernchemie - Berechnung der Adsorptionsenthalpien der Actinoide*, Report ZfK-560, Zentralinstitut für Kernforschung Rossendorf bei Dresden (1985)

[160] B. Eichler, S. Hübener, H. Roßbach, *Adsorption flüchtiger Metalle auf metallischen Oberflächen und ihre Anwendung in der Kernchemie - Berechnung der Adsorptionsenthalpien der Seltenerdmetalle*, Report ZfK-561, Zentralinstitut für Kernforschung Rossendorf bei Dresden (1985)

[161] G. Rudstam, *Project for an isotope separator on-line with the CERN synchro-cyclotron*, Nuclear Instruments and Methods **38**, 282 (1965)

[162] R. Kirchner, *On the release and ionization efficiency of catcher-ion-source systems in isotope separation on-line*, Nuclear Instruments and Methods in Physics Research Section B: Beam Interactions with Materials and Atoms **70**, 186 (1992)

[163] J. Lettry, R. Catherall, P. Drumm, P.V. Duppen, A. Evensen, G. Focker, A. Jokinen, O. Jonsson, E. Kugler, H. Ravn, *Pulse shape of the ISOLDE radioactive ion beams*, Nuclear Instruments and Methods in Physics Research Section B: Beam Interactions with Materials and Atoms **126**, 130 (1997)

[164] H. Zhang, *Ion sources* (Science Press Springer, New York, 1999), ISBN 9783540657477

[165] I.G. Brown, *The Physics and Technology of Ion Sources; 2nd ed.* (Wiley, Weinheim, 2004), https://cds.cern.ch/record/1113300

[166] A. Piel, *Plasma Physics* (Springer-Verlag GmbH, 2017), ISBN 3319634259, https://www.ebook.de/de/product/29471191/alexander_piel_plasma_physics.html

[167] P. Chabert, N. Braithwaite, *Physics of radio-frequency plasmas* (Cambridge University Press, 2011)

[168] R. Boswell, F. Chen, *Helicons-the early years*, IEEE Transactions on Plasma Science **25**, 1229 (1997)

[169] F. Chen, R. Boswell, *Helicons-the past decade*, IEEE Transactions on Plasma Science **25**, 1245 (1997)

[170] F.F. Chen, *Helicon discharges and sources: a review*, Plasma Sources Science and Technology **24**, 014001 (2015)

[171] Á. Valfells, D.W. Feldman, M. Virgo, P.G. O'Shea, Y.Y. Lau, *Effects of pulse-length and emitter area on virtual cathode formation in electron guns*, Physics of Plasmas **9**, 2377 (2002)

[172] Y.Y. Lau, *Simple Theory for the Two-Dimensional Child-Langmuir Law*, Physical Review Letters **87** (2001)

[173] R. Kirchner, *Untersuchung von Gasentladungs-Ionenquellen für die On-Line - Massentrennung*, Tech. Rep. GSI-P-76-1, GSI, Darmstadt (1976), http://cds.cern.ch/record/698782

[174] R. Kirchner, *Plasma and beam characteristics of FEBIAD - A low-intensity, high-efficiency ion source*, in *International Conference on Low-energy Ion Beams* (Institute of Physics, 1978), Vol. 38 of *Conference Series*, pp. 29–33, ISBN 0-85498-129-2

[175] D.A. Dunn, S.A. Self, *Static Theory of Density and Potential Distribution in a Beam-Generated Plasma*, Journal of Applied Physics **35**, 113 (1964)

[176] L.C. Penescu, Ph.D. thesis, *Techniques to produce and accelerate radioactive ion beams. Tehnici de producere si accelerare a fasciculelor radioactive* (2009), presented 2009, http://cds.cern.ch/record/2259078

[177] F.M. Millan, T. Day Goodacre, A. Gottberg, *Multiphysics simulation of a FEBIAD ion source*, Nuclear Instruments and Methods in Physics Research Section B: Beam Interactions with Materials and Atoms **463**, 302 (2020)

[178] S. Warren, T. Giles, C. Pequeno, A. Ringvall-Moberg, *Offline 2, ISOLDE's target, laser and beams development facility*, Nuclear Instruments and Methods in Physics Research Section B: Beam Interactions with Materials and Atoms **463**, 115 (2020)

[179] G. Wolf, T. Fritsch, J. Dreyer, *Experience with chemical compounds as targets for the production and isotope separation of carrier free nuclei*, in *Proc. 8th Int. EMIS Conf., SkSvde* (Chalmers Inst. of Techn, Sweden; Gothentmrg, 1973)

[180] J. Ballof, C. Seiffert, B. Crepieux, C.E. Düllmann, M. Delonca, M. Gai, A. Gottberg, T. Kröll, R. Lica, M.M. Flores et al., *Radioactive boron beams produced by isotope online mass separation at CERN-ISOLDE*, The European Physical Journal A **55** (2019)

[181] M.A. Molander, *Development of the ISOLDE Yield Database*, Report (2018), http://cds.cern.ch/record/2636715

[182] M. Athanasakis, S. Wilkins, G. Neyens, *Radioactive molecules at isolde*, Tech. rep., CERN, Geneva (2021), http://cds.cern.ch/record/2748712

[183] R.F.G. Ruiz, R. Berger, J. Billowes, C.L. Binnersley, M.L. Bissell, A.A. Breier, A.J. Brinson, K. Chrysalidis, T.E. Cocolios, B.S. Cooper et al., *Spectroscopy of short-lived radioactive molecules*, Nature **581**, 396 (2020)

[184] M. Fan, C. Holliman, X. Shi, H. Zhang, M. Straus, X. Li, S. Buechele, A. Jayich, *Optical Mass Spectrometry of Cold RaOH+ and RaOCH3+*, Physical Review Letters **126**, 023002 (2021)

[185] C. Babcock, Ph.D. thesis, *Collinear Laser Spectroscopy of Manganese Isotopes using the Radio Frequency Quadrupole Cooler and Buncher at ISOLDE* (2015), presented 03 Dec 2015, http://cds.cern.ch/record/2233219

[186] A. Mollaebrahimi, B. Anđelić, J. Even, M. Block, M. Eibach, F. Giacoppo, N. Kalantar-Nayestanaki, O. Kaleja, H. Kremers, M. Laatiaoui et al., *A setup to develop novel Chemical Isobaric SEparation (CISE)*, Nuclear Instruments and Methods in Physics Research Section B: Beam Interactions with Materials and Atoms (2019)

[187] J.H. Freeman, G. Sidenius, *The technology and chemistry of heavy ion sources*, in *Second international conference on ion sources, ICIS 2* (1972), p. 724, September 11 - 15, 1972, Vienna

[188] J. Freeman, G. Sidenius, *The technology and chemistry of heavy ion sources*, Nuclear Instruments and Methods **107**, 477 (1973)

[189] R. Kirchner, *Review of ISOL target–ion-source systems*, Nuclear Instruments and Methods in Physics Research Section B: Beam Interactions with Materials and Atoms **204**, 179 (2003)

[190] U. Köster, O. Arndt, E. Bouquerel, V.N. Fedoseyev, H. Frånberg, A. Joinet, C. Jost, I.S.K. Kerkines, R. Kirchner, *Progress in ISOL target–ion source systems*, Nuclear Instruments and Methods in Physics Research Section B: Beam Interactions with Materials and Atoms **266**, 4229 (2008)

[191] U. Köster, P. Carbonez, A. Dorsival, J. Dvorak, R. Eichler, S. Fernandes, H. Frånberg, J. Neuhausen, Z. Novackova, R. Wilfinger et al., *(Im-)possible ISOL beams*, The European Physical Journal Special Topics **150**, 285 (2007)

[192] E. Hagebø, P. Hoff, O. Jonsson, E. Kugler, J. Omtvedt, H. Ravn, K. Steffensen, *New production systems at ISOLDE*, Nuclear Instruments and Methods in Physics Research Section B: Beam Interactions with Materials and Atoms **70**, 165 (1992)

[193] D. Stracener, G. Alton, R. Auble, J. Beene, P. Mueller, J. Bilheux, *Targets used in the production of radioactive ion beams at the HRIBF*, Nuclear Instruments and Methods in Physics Research Section A: Accelerators, Spectrometers, Detectors and Associated Equipment **521**, 126 (2004)

[194] U. Köster, Ph.D. thesis, *Ausbeuten und Spektroskopie and radioaktiver Isotope and bei LOHENGRIN and und ISOLDE* (1999), presented on 30 Dec 1999, http://cds.cern.ch/record/494272

[195] H. Carter, J. Kormicki, D. Stracener, J. Breitenbach, J. Blackmon, M. Smith, D. Bardayan, *First on-line results for As and F beams from HRIBF target/ion sources*, Nuclear Instruments and Methods in Physics Research Section B: Beam Interactions with Materials and Atoms **126**, 166 (1997)

[196] H. Ravn, *Status and future development of ion sources for on-line mass separators*, Nuclear Instruments and Methods in Physics Research Section B: Beam Interactions with Materials and Atoms **70**, 107 (1992)

[197] D. Stracener, *Status of radioactive ion beams at the HRIBF*, Nuclear Instruments and Methods in Physics Research Section B: Beam Interactions with Materials and Atoms **204**, 42 (2003), 14th International Conference on Electromagnetic Isotope Separators and Techniques Related to their Applications

[198] H.L. Ravn, S. Sundell, L. Westgaard, *Short-lived Isotopes of Alkali and Alkaline-earth Elements Studied by On-line Isotope Separator Techniques*, .L inorg, nucl. Chem **37**, 383 (1975)

[199] C.F. Liang, P. Paris, D. Bucurescu, S. Della Negra, J. Obert, J.C. Putaux, *Selective on-line separation of new Ta, Zr and Sr isotopes*, Zeitschrift für Physik A Atoms and Nuclei **309**, 185 (1982)

[200] Y. Kawase, K. Okano, M. Shibata, A. Taniguchi, *Fluorination method for the surface ionization of Sr and Ba with a helium-jet type ISOL*, Nuclear Instruments and Methods in Physics Research Section B: Beam Interactions with Materials and Atoms **70**, 146 (1992)

[201] P.L. Reeder, L.J. Alquist, J. Lin, J.F. Wright, *Separation of alkaline earth from alkali metal fission products in the solar on-line mass spectrometer*, Nuclear Instruments and Methods **133**, 501 (1976)

[202] P. Hoff, L. Jacobsson, B. Johansson, P. Aagaard, G. Rudstam, H.U. Zwicky, *Production of molecular ions in the integrated target/ion-source of an isotope-separation-on-line system*, Nuclear Instruments and Methods **172**, 413 (1980)

[203] J. Putaux, J. Obert, L. Kotfila, B. Roussiere, J. Sauvage-Letessier, C. Liang, A. Peghaire, P. Paris, *Target ion source systems at the Orsay isocele 2 separator*, Nuclear Instruments and Methods in Physics Research **186**, 321 (1981)

[204] M. Hellström, B. Fogelberg, L. Jacobsson, L. Spanier, G. Rudstam, *Some studies of molecular ions obtained from a $U + C$ target at $> 2100°C$*, Nuclear Instruments and Methods in Physics Research Section B: Beam Interactions with Materials and Atoms **70**, 142 (1992)

[205] P. Delahaye, *Radioactive ion beam R & D with SPIRAL 1*, in *Beamlab meeting (EURISOL - ENSAR2)* (2018), `https://indico.cern.ch/event/714382/`

[206] B. Roussière, I. Deloncle, N. Barré-Boscher, M.A. Cardona, M.C. Mhamed, T. Corbin, E. Cottereau, H. Croizet, B. Dimitrov, S. Essabaa et al., *Production of lanthanide molecular ion beams by fluorination technique*, Journal of Physics: Conference Series **724**, 012042 (2016)

[207] S. Essabaa, N. Barré-Boscher, M.C. Mhamed, E. Cottereau, S. Franchoo, F. Ibrahim, C. Lau, B. Roussière, A. Saïd, S. Tusseau-Nenez et al., *The radioactive beam facility ALTO*, Nuclear Instruments and Methods in Physics Research Section B: Beam Interactions with Materials and Atoms **317**, 218 (2013)

[208] C.F. Liang, P. Paris, G. Bastin, J. Obert, J.C. Putaux, *On-line separation of refractory hafnium and tantalum isotopes at the ISOCELE separator*, in *Proceeings of the 4th international conference on nuclei far from stability* (1981), p. 709, CERN 81-09

[209] J. Sauvage, C. Bourgeois, A. Caruette, P. Kilcher, J. Obert, J. Oms, J.C. Putaux, B. Roussiere, A. Ferro, J. Fournet et al., *The ISOCELE II separator: a general description,recent results, and future developments*, in *Proceedings of the TRIUMF-ISOL workshop*, edited by J. Crawford, J. D'Auria (1984)

[210] U. Köster, O. Arndt, R. Catherall, J.G. Correia, B. Crepieux, R. Eichler, P. Fernier, L.M. Fraile, S. Hennrich, K. Johnston et al., *ISOL beams of hafnium isotopes and isomers*, The European Physical Journal Special Topics **150**, 293 (2007)

[211] P. Kunz, *The ISAC yield database*, `http://mis.triumf.ca/science/planning/yield/beam` (2020), [Online; accessed 22-April-2020]

[212] H. Ravn, *Progress in targets and ion sources for on-line separators*, Nuclear Instruments and Methods **139**, 281 (1976)

[213] W. Kurcewicz, E. Ruchowska, P. Hill, N. Kaffrell, G. Nyman, *Collective states in 230Ra fed by β- decay of 230Fr*, Nuclear Physics A **464**, 1 (1987)

[214] P. Hill, N. Kaffrell, W. Kurcewicz, G. Nyman, *The new neutron-rich nuclei 231Fr and 231Ra*, Zeitschrift für Physik A Atoms and Nuclei **320**, 531 (1985)

[215] M. Dombsky, P. Kunz, *ISAC targets*, Hyperfine Interactions **225**, 17 (2013)

[216] M. Dombsky, P. Bricault, *High intensity targets for ISOL, historical and practical perspectives*, Nuclear Instruments and Methods in Physics Research Section B: Beam Interactions with Materials and Atoms **266**, 4240 (2008)

[217] C.F. Liang, P. Paris, M.G. Porquet, J. Obert, J.C. Putaux, *On-line separation of163Ta and162Ta*, Zeitschrift für Physik A Atoms and Nuclei **321**, 695 (1985)

[218] K.H. Burkhard, W. Dumanski, R. Kirchner, E. Roeckl, *Statusbericht der On-line-Massenseparator-Gruppe*, in *GSI Projektbericht GSI-PB-2-74* (1974)

[219] G. Sidenius, O. Skilbreid, *E.M. Separations with High Efficiency of Microgramme Quantities*, in *Electromagnetic Separation of Radioactive Isotopes* (Springer Vienna, 1961), pp. 243–249

[220] P. Jardin, M.G. Saint-Laurent, W. Farabolini, G. Gaubert, J.C. Cornell, M. Dubois, S. Gibouin, N. Lecesne, R. Leroy, J.Y. Pacquet et al., *Latest results obtained at GANIL with new target-source systems dedicated to radioactive ion production*, Review of Scientific Instruments **75**, 1617 (2004)

[221] H. Ravn, *Experiments with intense secondary beams of radioactive ions*, Physics Reports **54**, 201 (1979)

[222] H. Ravn, R. Catherall, J. Barker, P. Drumm, A. Evensen, E. Hagebø, P. Hoff, O. Jonsson, E. Kugler, J. Lettry et al., *Bunched release of gases from oxide targets*, Nuclear Instruments and Methods in Physics Research Section B: Beam Interactions with Materials and Atoms **126**, 176 (1997)

[223] P.V. Duppen, P. Decrock, M. Huyse, T. Delbar, W. Galster, P. Leleux, I. Licot, E. Liénard, P. Lipnik, M. Loiselet et al., *Production, acceleration and use of radioactive ion beams at Louvain-la-Neuve*, Nuclear Instruments and Methods in Physics Research Section B: Beam Interactions with Materials and Atoms **70**, 393 (1992)

[224] U. Köster, *Intense radioactive-ion beams produced with the ISOL method*, The European Physical Journal A **15**, 255 (2002)

[225] S. Ichikawa, T. Sekine, H. Iimura, M. Oshima, *Measurement of hold-up times in a thermal ion source for metallic and monoxide ions of lanthanum and cerium*, Nuclear Instruments and Methods in Physics Research Section B: Beam Interactions with Materials and Atoms **70**, 156 (1992)

[226] S. Ichikawa, T. Sekine, H. Iimura, M. Oshima, N. Takahashi, *Selective mass separation of light lanthanoids by means of ionization of their monoxides*, Nuclear Instruments and Methods in Physics Research Section A: Accelerators, Spectrometers, Detectors and Associated Equipment **274**, 259 (1989)

[227] K. Chrysalidis, J. Ballof, Ch.E. Düllmann, V.N. Fedosseev, C. Granados, B.A. Marsh, Y.M. Palenzuela, J.P. Ramos, S. Rothe, T. Stora et al., *Developments towards the delivery of selenium ion beams at ISOLDE*, The European Physical Journal A **55** (2019)

[228] M. Cheikh-Mhamed (Coordinator), *EURISOL JRA WP 14 Third periodic scientific report Beamlab, ENSAR2* (2021), in preparation, `https://eurisol-jra.in2p3.fr/documents/`

[229] K. Aleklett, P. Hoff, E. Lund, G. Rudstam, *Delayed neutron emission probabilities of the precursors 89,90,91Br and 139,140,141I*, Zeitschrift fr̈ Physik A Atoms and Nuclei **295**, 331 (1980)

[230] W. Kurcewicz, E. Ruchowska, N. Kaffrell, T. Björnstad, G. Nyman, *Collective excitations in the transitional nuclei 224, 226Ra*, Nuclear Physics A **356**, 15 (1981)

[231] U. Köster, V.N. Fedoseyev, A.N. Andreyev, U.C. Bergmann, R. Catherall, J. Cederkäll, M. Dietrich, H.D. Witte, D.V. Fedorov, L. Fraile et al., *On-line yields obtained with the ISOLDE RILIS*, Nuclear Instruments and Methods in Physics Research Section B: Beam Interactions with Materials and Atoms **204**, 347 (2003)

[232] J.H. Kusk, Master's thesis, *Gamma-rays in the dacay of* ^{31}Ar, ^{32}Ar, ^{33}Ar, Department of Physics and Astronomy Aarhus University, Denmark (2011)

[233] G.T. Koldste, Ph.D. thesis, *Deciphering drip-line decays - the case of* ^{31}Ar, Department of Physics and Astronomy Aarhus University, Denmark (2015), `http://cds.cern.ch/record/2103354`

[234] G. Herrmann, *Rapid radiochemical separations*, Arkiv för Fysik **36**, 111 (1967)

[235] M. Weber, N. Trautmann, G. Herrmann, *Volatilization of fission products from solid uranium tetrafluoride*, Radiochemical and Radioanalytical Letters (1971)

[236] P. Delahaye, F. Ames, I. Podadera, R. Savreux, F. Wenander, *Recent developments of the radioactive beam preparation at REX-ISOLDE*, in *The 4th International Conference on Exotic Nuclei and Atomic Masses* (Springer Berlin Heidelberg, 2005), pp. 739–741

[237] A. Roine, *HSC Chemistry 7.1*, `http://www.hsc-chemistry.net` (2010), [Online; accessed 19-July-2021]

[238] T.G. Pearson, P.L. Robinson, *83. Carbonyl selenide. Part I. Preparation and physical properties*, Journal of the Chemical Society (Resumed) p. 652 (1932)

[239] O. Glemser, T. Risler, *Kohlenoxydverbindungen der Nichtmetalle I*, Zeitschrift für Naturforschung B **3**, 1 (1948)

[240] K. Kondo, S. Yokoyama, N. Miyoshi, S. Murai, N. Sonoda, *A New Synthesis of Carbonyl Selenide*, Angewandte Chemie International Edition in English **18**, 691 (1979)

[241] R.H. Purcell, F.D. Zahoorbux, *217. The kinetics of the decomposition of carbonyl selenide on an allotropic selenium surface*, Journal of the Chemical Society (Resumed) p. 1029 (1937)

[242] R.S. BALDWIN, D.O. PROTO, L. B., *The Formation of OCSe from the Reaction of Recoil Selenium Atoms with Carbon Monoxide*, Radiochimica Acta **16** (1971)

[243] M. Wachsmuth, R. Eichler, L. Tobler, D. Jost, H.W. Gäggeler, M. Amman, *Online gas-phase separation of short-lived bromine nuclides from precursor selenium*, Radiochimica Acta **88** (2000)

[244] M. Wachsmuth, B. Eichler, L. Tobler, F. Hänssler, H. Gäggeler, M. Ammann, *Chemical characterization of short-lived selenium and their daughter isotopes from thermal neutron induced fission of 235U at a gas-jet facility*, Journal of radioanalytical and nuclear chemistry **254**, 201 (2002)

[245] M. Bavia, G.D. Lonardo, G. Galloni, A. Trombetti, *Molecular spectra of OCSe*, Journal of the Chemical Society, Faraday Transactions 2 **68**, 615 (1972)

[246] T. Wentink, *Triatomic Linear Molecules Containing Carbon and Oxygen, Sulfur, Selenium, or Tellurium. I. Vibrational Spectra of CS2, CSe2, SCSe, and SCTe*, The Journal of Chemical Physics **29**, 188 (1958)

[247] E.K.C. Lee, Y.N. Tang, F.S. Rowland, *The Gas Phase Reactions of Recoil Sulfur Atoms with Carbon Monoxide and Carbon Dioxide*, The Journal of Physical Chemistry **68**, 318 (1964)

[248] A.F. Novgorodov, M. Adilbish, N.G. Zaitseva, A. Kowalew, Z. Kovacs, *Investigation of the behaviour of nuclear reaction products at their volatilization from irradiated Ag and Au targets in dynamic vacuum (10-2–10-3 torr O2 or H2O)*, Journal of Radioanalytical Chemistry **56**, 37 (1980)

[249] P. Paris, V. Berg, A. Caruette, J. Obert, J. Putaux, J. Sarrouy, *Development of the ORSAY high current on-line separator ISOCELE*, Nuclear Instruments and Methods **139**, 251 (1976)

[250] G. Alton, Y. Liu, C. Williams, S. Murray, *A new concept kinetic-ejection negative-ion source for rib generation*, Nuclear Instruments and Methods in Physics Research Section B: Beam Interactions with Materials and Atoms **170**, 515 (2000)

[251] J. Even, A. Yakushev, Ch.E. Düllmann, J. Dvorak, R. Eichler, O. Gothe, D. Hild, E. Jäger, J. Khuyagbaatar, J.V. Kratz et al., *Rapid Synthesis of Radioactive Transition-Metal Carbonyl Complexes at Ambient Conditions*, Inorganic Chemistry **51**, 6431 (2012)

[252] C. Elschenbroich, *Organometallchemie* (Teubner, Wiesbaden, 2005), ISBN 9783519535010

[253] R. Crabtree, *The organometallic chemistry of the transition metals* (Wiley, Hoboken, New Jersey, 2014), ISBN 9781118138076

[254] H. Koivisto, J. Ärje, M. Nurmia, *Metal ion beams from an ECR ion source using volatile compounds*, Nuclear Instruments and Methods in Physics Research Section B: Beam Interactions with Materials and Atoms **94**, 291 (1994)

[255] S. Viñals, M.J.G. Borge, O. Tengblad, E. Nácher, J. Benito, P. Figuera, L.M. Fraile, H.O.U. Fynbo, A. Gad, J. Jensen et al., *The experiments to determine the electron capture and β-decay of 8B into the highly excited states of 8Be*, Journal of Physics: Conference Series **1643**, 012130 (2020)

[256] R. Spartà, A.D. Pietro, P. Figuera, O. Tengblad, A. Moro, I. Martel, J. Fernández-García, J. Lei, L. Acosta, M. Borge et al., *Probing proton halo effects in the 8B+64Zn collision around the Coulomb barrier*, Physics Letters B **820**, 136477 (2021)

[257] E. Nacher, A. Algora, J.A. Briz, B. Rubio, J.L. Taín, W. Gelletly, L.M. Fraile, *Beta decay along the rp-process path for accurate stellar weak-decay rates:* ^{68}*Se and* ^{70}*Se*, Tech. rep., CERN, Geneva (2020), `http://cds.cern.ch/record/2717982`

[258] T. Ohta, F. Cicoira, P. Doppelt, L. Beitone, P. Hoffmann, *Static Vapor Pressure Measurement of Low Volatility Precursors for Molecular Vapor Deposition Below Ambient Temperature*, Chemical Vapor Deposition **7**, 33 (2001)

[259] K. Jousten, *Wutz Handbuch Vakuumtechnik* (Springer Vieweg, Wiesbaden, Germany, 2018), ISBN 9783658133856

[260] M. Moghadam, S. Tangestaninejad, V. Mirkhani, I. Mohammadpoor-Baltork, N.S. Mirbagheri, *Molybdenum hexacarbonyl supported on functionalized multi-wall carbon nanotubes: Efficient and highly reusable catalysts for epoxidation of alkenes with tert-butyl hydroperoxide*, Journal of Organometallic Chemistry **695**, 2014 (2010)

[261] C. Seiffert, J. Ballof, *Extraction of refractory elements by laser induced breakup and ionisation of molybdenum carbonyls* (2017), Letter of Intent to the INTC, INTC-I-178, `https://cds.cern.ch/record/2241995`